

# Abstract

BAYATI, MOHAMMAD REZA. Structure and Properties of VO<sub>2</sub> and TiO<sub>2</sub> Based Epitaxial Heterostructures Integrated with Silicon and Sapphire Substrates. (Under the direction of Prof. Jagdish (Jay) Narayan and Prof. Roger J. Narayan.)

The main focus of this study was placed on structure-property correlation in TiO<sub>2</sub> and VO<sub>2</sub> based epitaxial heterostructures where the photochemical and electrical properties were tuned through microstructural engineering. In the framework of domain matching epitaxy, epitaxial growth of TiO<sub>2</sub> and VO<sub>2</sub> heterostructures on different substrates were explained. The  $\theta$ -2 $\theta$  and  $\varphi$  scan X-ray diffraction measurements and detailed high resolution electron microscopy studies corroborated our understanding of the epitaxial growth and the crystallographic arrangement across the interfaces. The influence of the laser and substrate variables on structural characteristics of the films was investigated using X-ray photoelectron spectroscopy, room temperature photoluminescence spectroscopy, and UV-Vis spectrophotometry. In addition, morphological studies were performed by atomic force microscopy. Photochemical properties of the heterostructures were assessed through measuring surface wettability characteristics and photocatalytic reaction rate constant of degradation of 4-chlorophenol under ultraviolet and visible irradiations. We also studied electrical properties employing 4-probe measurement technique. The effect of post treatment processes, such as vacuum annealing and laser treatment, on structure

and properties was investigated as well. The role of point defects and deviation from the stoichiometry on photochemical and electrical properties was addressed.

In this research,  $\text{TiO}_2$  epilayers with controlled phase structure, defect content, and crystallographic alignments were grown on sapphire and silicon substrates. Integration with silicon was achieved using cubic and tetragonal yttria-stabilized zirconia buffer layers. I was able to tune the phase structure of the  $\text{TiO}_2$  based heterostructures from pure rutile to pure anatase and establish an epitaxial relationship across the interfaces in each case. These heterostructures were used for two different purposes. First, their application in environmental remediation was taken into account. The photochemical efficiency of the samples was evaluated under ultraviolet and visible illuminations. I was able to establish a correlation between the growth conditions and the photocatalytic activity of single crystalline  $\text{TiO}_2$  thin films. Visible-light-responsive  $\text{TiO}_2$  films were fabricated via vacuum annealing of the samples where point defects, namely oxygen vacancies and titanium interstitial, are surmised to play a critical role. An ultrafast switching was observed in wetting characteristics of the single crystalline rutile  $\text{TiO}_2$  films from a hydrophobic state to a superhydrophilic state by single pulsed excimer laser annealing. It was observed that the laser annealing almost doubles the photocatalytic efficiency of the anatase epitaxial thin films. I was able to measure the photochemical properties of the rutile and the anatase  $\text{TiO}_2$  heterostructures in a controlled way due to the single crystalline nature of the films. Second, the rutile  $\text{TiO}_2$  epilayers with different out-of-plane orientations were deposited and used as a platform for  $\text{VO}_2$  based epitaxial heterostructures with the aim of manipulating of microstructure and electrical properties of the  $\text{VO}_2$  films.

Vanadium dioxide ( $\text{VO}_2$ ) is an interesting material due to the abrupt change in electrical resistivity and infrared transmittance at about 68 °C. The transition temperature can be tuned through microstructural engineering. It was the idea behind using rutile  $\text{TiO}_2$  with different crystallographic orientations as a template to tune the semiconductor to metal transition characteristics of the  $\text{VO}_2$  top layer. I successfully grew  $\text{VO}_2(001)$ ,  $\text{VO}_2(100)$ , and  $\text{VO}_2(\bar{2}01)$  epitaxial thin films on  $\text{TiO}_2(100)/c$ -sapphire,  $\text{TiO}_2(101)/r$ -sapphire, and  $\text{TiO}_2(001)/m$ -sapphire platforms, respectively. It was observed that tetragonal phase of  $\text{VO}_2$  was stabilized at lower temperatures leading to a significant decrease in the semiconductor to metal transition temperature. In other words, we were able to tune the transition temperature of the  $\text{VO}_2$  epitaxial heterostructures. This achievement introduces the  $\text{VO}_2$  based single crystalline heterostructures as a promising candidate for a wide range of applications where different transition temperatures are required. The epitaxial relationships were established and atomic arrangement across the interfaces was studied in detail.

© Copyright 2013 by Mohammad Reza Bayati

All Rights Reserved

Structure and Properties of VO<sub>2</sub> and TiO<sub>2</sub> Based Epitaxial Heterostructures  
Integrated with Silicon and Sapphire Substrates

by  
Mohammad Reza Bayati

A dissertation submitted to the Graduate Faculty of  
North Carolina State University  
in partial fulfillment of the  
requirements for the Degree of  
Doctor of Philosophy

Materials Science and Engineering

Raleigh, North Carolina

2013

APPROVED BY:

---

Prof. Jagdish Narayan

Co-Chair of the Advisory Committee

---

Prof. Roger J. Narayan

Co-Chair of the Advisory Committee

---

Prof. Mike J. Rigsbee

---

Prof. John T. Prater

# Dedication

To

My wife, this would have never been achieved without her kindness and support.

My mother, who taught me the meaning of patience.

And all people teaching me even a single word...

***Academic knowledge flourishes only when it is applied.***

# Biography

Mohammad Reza Bayati was born on Sep. 20, 1978 in Tehran the capital of Iran. He received his high school diploma in Mathematics and Physics from Allameh-Helli high school, Iranian National Organization for Developing Exceptional Talents (NODET) in 1996. Reza earned his B.S. degree in Materials Science and Engineering in 2000. Title of his thesis was "Influence of the austenite grain size on physical and mechanical properties of austempered AISI 4340 steels". Afterward, he joined Shiraz University to study for an M.Sc. degree. He worked on electrochemically grown black chromium solar selective absorbers as his thesis. The main goal of this project was optimizing the optical properties and thermal stability of the chromia coatings and fabrication of highly efficient solar absorbers. Then, he joined Iran University of Science and Technology, which is one of the highest ranking universities in the Middle East, in 2005 to pursue a Ph.D. degree. His Ph.D. dissertation was entitled "Growth of nano/micro-structured TiO<sub>2</sub> based combined porous layers via micro arc oxidation process for photocatalytic applications". Receiving a Ph.D. from an Iranian university did not satisfy him, so he decided to join NC State University to pursue another Ph.D. in 2011. Reza worked under the direction of Prof. Jay Narayan and Prof. Roger Narayan and received his second Ph.D. degree within about two and half years which is a record. He has been working on oxide semiconductors for more than ten years. Reza is married to Dr. Roya Molaei.

# Acknowledgements

First and foremost, I would like to express my sincere and heartfelt appreciation to Prof. Jagdish (Jay) Narayan and Prof. Roger J. Narayan due to their continuous encouragement, constructive advices, and invaluable support in the course of this project. I have been honored to have the chance to work in their group without which this dissertation would have never materialized.

I would like to cordially appreciate my advisory committee members, Prof. Mike J. Rigsbee, Prof. John T. Prater, and Prof. Korukonda Murty, for their time, constructive comments, and helpful discussions. Special thanks to Prof. C. Lew Reynolds for his kind collaboration and letting me have his valuable advice in my preliminary exam. Working with them enriched my knowledge and my research work.

I am indebted to undergraduate students, Jerry Ding (Zhejiang University, China), Mattao Cao (Zhejiang University, China) and especially Shivani Joshi (Amity Institute of Nanotechnology, India), whose contribution helped me a lot to complete my dissertation. I want to give special thanks to my present and past colleagues, Dr. Sudhakar Nori, Dr. Alok Gupta, Dr. Pranav Gupta, Namik Temizer, and Yi-Fang Lee, for every single day of my life in the past few years. Their support throughout my doctoral research has been invaluable and has made my stay at NC State University a really enjoyable experience and worthwhile.

I am grateful to my close collaborators, Dr. Thomas Rawdanowicz (NC State

University), Dr. Yi Liu (NC State University), Dr. Honghui Zhou (Oak Ridge National Laboratory), Dr. Steve Pennycook (Oak Ridge National Laboratory), Dr. Scott Misture (Alfred University), Dr. John Budai (Oak Ridge National Laboratory), Fred Stevie (NC State University), Chuck Mooney (NC State University), Roberto Garcia (NC State University), and Bahar Mohammad-Alipour (NC State University) for their contribution to my dissertation.

I would also like to thank the administrative staff in the department of Materials Science and Engineering at NC State University, particularly Edna Deas, for their prompt help in any official work.

From the bottom of my heart, I would like to thank my wife, Roya. She was the one who cheered me up when things did not look promising. With all honesty, I owe all my success to her and her unbridled support, love, and encouragement.

The financial support from the US National Science Foundation through grant numbers of DMR-1304607 and DMR-0803663 is highly appreciated.

# Table of Contents

<b>List of Tables.....</b>	<b>xv</b>
<b>List of Figures.....</b>	<b>xvi</b>
<b>Chapter 1: Introduction.....</b>	<b>1</b>
References.....	6
<b>Chapter 2: Background Knowledge.....</b>	<b>7</b>
2.1. Titanium dioxide ( $\text{TiO}_2$ ).....	7
2.1.1. Anatase.....	8
2.1.2. Rutile.....	10
2.1.3. Defect characteristics.....	12
2.2. Vanadium dioxide ( $\text{VO}_2$ ).....	16
2.2.1. Introduction.....	16
2.2.2. Applications of $\text{VO}_2$ thin films.....	18
2.2.3. Structural characteristics of $\text{VO}_2$ .....	19
2.2.4. Electronic characteristics of $\text{VO}_2$ .....	23
2.2.5. Thermodynamic model of SMT in $\text{VO}_2$ .....	25
2.2.5.1. Single-crystal films.....	26
2.2.5.2. Textured polycrystalline films.....	26

2.2.5.3. Random polycrystalline films.....	26
2.2.5.4. Amorphous films.....	27
2.3. Thin film epitaxy.....	27
2.3.1. Sources of strains.....	28
2.3.1.1. Lattice misfit strains.....	29
2.3.1.2. Thermal misfit strains.....	30
2.3.1.3. Microstructural and defect related strains.....	30
2.3.2. Lattice matching epitaxy.....	31
2.3.3. Domain matching epitaxy.....	33
2.4. Photocatalytic reactions.....	36
References.....	38

<b>Chapter 3: Experimental Techniques.....</b>	<b>46</b>
3.1. Substrates and buffer layers.....	46
3.1.1. Silicon.....	46
3.1.2. Sapphire (Aluminum oxide).....	47
3.1.3. Yttria-stabilized zirconia.....	48
3.2. Thin film growth.....	50
3.2.1. Advantages and disadvantages of PLD.....	52
3.2.2. Physics of the laser-solid interaction.....	54
3.2.2.1. Laser-solid interaction.....	54
3.2.2.2. Plasma formation and initial isothermal expansion.....	56

3.2.2.3. Adiabatic expansion of the plasma.....	58
3.2.3. Lasers used for PLD.....	60
3.3. Characterization techniques.....	61
3.3.1. Crystalline structure.....	61
3.3.2. Stoichiometry.....	63
3.3.3. Microstructure.....	64
3.3.4. Morphology.....	67
3.3.5. Optical characteristics.....	68
3.3.5.1. UV-Vis spectroscopy.....	68
3.3.5.2. Photoluminescence spectroscopy.....	69
3.3.6. Electrical properties.....	70
3.3.7. Photochemical activity.....	71
3.3.7.1. Photocatalytic properties.....	71
3.3.7.2. Wetting properties.....	72
References.....	72

## **Chapter 4: Control of Structure and Properties of Epitaxial TiO<sub>2</sub>/c-Sapphire**

<b>Thin Film Heterostructures.....</b>	<b>76</b>
4.1. Introduction.....	77
4.2. Experimental.....	79
4.3. Results and discussion.....	80
4.3.1. Microstructure.....	80

4.3.2. Epitaxial relationship and the DME details.....	85
4.3.3. Morphology.....	90
4.3.4. Stoichiometry.....	92
4.3.5. Optical properties.....	95
4.4. Conclusions.....	98
References.....	99

<b>Chapter 5: Structure-Property Correlation in Epitaxial Rutile Films Grown on Sapphire(0001) Substrates by Pulsed Laser Deposition.....</b>	<b>103</b>
5.1. Introduction.....	104
5.2. Experimental.....	105
5.3. Results and discussion.....	107
5.3.1. Phase structure.....	107
5.3.2. Optical properties.....	109
5.3.3. Stoichiometry.....	111
5.3.4. Epitaxial relationship.....	112
5.3.5. Morphology.....	116
5.3.6. Photocatalytic activity.....	117
5.4. Conclusions.....	119
References.....	120

## **Chapter 6: Domain Epitaxy in $\text{TiO}_2/\alpha\text{-Al}_2\text{O}_3$ Thin Film Heterostructure**

<b>with Ti<sub>2</sub>O<sub>3</sub> Transition Layer.....</b>	<b>123</b>
6.1. Introduction.....	123
6.2. Experimental.....	125
6.3. Results and discussion.....	126
6.4. Conclusions.....	131
References.....	132
<b>Chapter 7: Defect Mediated Photocatalytic Decomposition of 4-chlorophenol on Epitaxial Rutile Thin Films under Visible and UV Illuminations.....</b>	<b>135</b>
7.1. Introduction.....	136
7.2. Experimental.....	140
7.3. Results and discussion.....	141
7.3.1. Phase structure.....	141
7.3.2. Optical properties.....	144
7.3.3. Stoichiometry.....	146
7.3.4. Morphology.....	148
7.3.5. Thin film epitaxy.....	149
7.3.6. Photocatalytic activity.....	151
7.4. Conclusions.....	158
References.....	158

<b>Chapter 8: Phase Tuning, Thin Film Epitaxy, and Properties of YSZ-Buffered</b>	
<b>TiO<sub>2</sub> on Si(001) Substrate.....</b>	<b>161</b>
8.1. Introduction.....	162
8.2. Experimental.....	164
8.3. Results and discussion.....	166
8.3.1. Phase structure.....	166
8.3.2. Epitaxial relationship and the DME details.....	173
8.3.3. Morphology.....	181
8.3.4. Electrical properties.....	183
8.3.5. Photocatalytic properties.....	185
8.4. Conclusions.....	187
References.....	188
<b>Chapter 9: Nanosecond Switching in Wetting Properties of TiO<sub>2</sub>/c-</b>	
<b>YSZ/Si(001) Heterostructures Induced by Laser Irradiation.....</b>	<b>192</b>
9.1. Introduction.....	193
9.2. Experimental.....	195
9.3. Results and discussion.....	197
9.3.1. Microstructure and thin film epitaxy.....	197
9.3.2. Morphology.....	201
9.3.3. Stoichiometry.....	204
9.3.4. Wettability characteristics.....	206

9.4. Conclusions.....	209
References.....	210

## **Chapter 10: Enhancement of Photocatalytic Activity of Anatase TiO<sub>2</sub> Single**

### **Crystalline Thin Films by Nanosecond Pulsed Excimer Laser**

<b>Treatment.....</b>	<b>214</b>
10.1. Introduction.....	215
10.2. Experimental.....	218
10.3. Results and discussion.....	220
10.3.1. Microstructure and thin film epitaxy.....	220
10.3.2. Stoichiometry.....	229
10.3.3. Thermal stability of anatase in epitaxial heterostructures.....	231
10.3.4. Photocatalytic efficiency.....	234
10.4. Conclusions.....	236
References.....	237

## **Chapter 11: Role of Substrate Crystallographic Characteristics on Structure**

### **and Properties of Rutile Epilayers.....**

<b>241</b>	
11.1. Introduction.....	242
11.2. Experimental.....	239
11.3. Results and discussion.....	246
11.3.1. Microstructural studies.....	246

11.3.1.1. Rutile TiO <sub>2</sub> / <i>m</i> -sapphire heterostructure.....	246
11.3.1.2. Rutile TiO <sub>2</sub> / <i>r</i> -sapphire heterostructure.....	258
11.3.1.3. Rutile TiO <sub>2</sub> / <i>c</i> -sapphire heterostructure.....	264
11.3.2. Photocatalytic characteristics.....	272
11.4. Conclusions.....	276
References.....	276
<b>Chapter 12: Semiconductor to Metal Transition Characteristics in</b>	
<b>VO<sub>2</sub>/TiO<sub>2</sub>/Al<sub>2</sub>O<sub>3</sub> Thin Film Heterostructures.....</b>	<b>279</b>
12.1. Introduction.....	280
12.2. Experimental.....	282
12.3. Results and discussion.....	284
12.3.1. SMT characteristics.....	284
12.3.2. Microstructural studies.....	285
12.3.2.1. VO <sub>2</sub> /TiO <sub>2</sub> / <i>m</i> -sapphire heterostructure.....	285
12.3.2.2. VO <sub>2</sub> /TiO <sub>2</sub> / <i>r</i> -sapphire heterostructure.....	290
12.3.2.3. VO <sub>2</sub> /TiO <sub>2</sub> / <i>c</i> -sapphire heterostructure.....	294
12.3.3. Structure-property correlation characteristics.....	297
12.4. Conclusions.....	306
References.....	306
<b>Chapter 13: Summary and Suggestions for Future Works.....</b>	<b>309</b>

13.1. Concluding remarks.....	309
13.2. Suggestions for future works.....	313

# List of Tables

Tab. 3.1. Operating wavelengths of several excimer lasers.....	60
Tab. 4.1. Portion of the XPS peaks for different oxygen pressures.....	94
Tab. 5.1. Photocatalytic reaction rate constants as a function of the frequency....	118
Tab. 7.1. Portion of the XPS peaks for different oxygen pressures.....	148
Tab. 7.2. Photocatalytic reaction rate constants as a function of pressure.....	156
Tab. 8.1. Photocatalytic reaction rate constants of decomposition of 4CP .....	187
Tab. 11.1. Interplanar spacing for several family of planes of rutile(001)/ <i>m</i> -sapphire heterostructure obtained from high resolution θ-2θ scans.....	252
Tab. 11.2. Interplanar spacing for several family of planes of rutile(101)/ <i>r</i> -sapphire heterostructure obtained from high resolution θ-2θ scans.....	264
Tab. 11.3. Interplanar spacing for several family of planes of rutile(100)/ <i>c</i> -sapphire heterostructure obtained from high resolution θ-2θ scans.....	271
Tab. 12.1. SMT characteristics of VO <sub>2</sub> epilayers grown on several TiO <sub>2</sub> /sapphire platforms.....	285
Tab. 12.2. Details on thin film epitaxy of VO <sub>2</sub> /TiO <sub>2</sub> /sapphire heterostructures.....	298

# List of Figures

Fig. 1.1.	Positions of the valence and the conductance bands of TiO <sub>2</sub> vs NHE.....	2
Fig. 2.1.	Phase diagram of the Ti-O system.....	8
Fig. 2.2.	Redox potentials of valence and conduction bands and band-gap energies for various metal oxides.....	9
Fig. 2.3.	Schematic illustration of low-index faces of anatase TiO <sub>2</sub> : (a) (101), (b) (100), and (c) (001).....	10
Fig. 2.4.	Schematic illustration of low-index faces of rutile TiO <sub>2</sub> : (a) (110), (b) (100), and (c) (001).....	11
Fig. 2.5.	Band model of TiO <sub>2</sub> showing the energy levels of intrinsic lattice defects.....	15
Fig. 2.6.	Hysteresis curves of: (a) resistance and (b) reflection during SMT of VO <sub>2</sub> .....	17
Fig. 2.7.	Phase diagram of the V-O system.....	18
Fig. 2.8.	Illustration of crystallographic lattice of: (a) monoclinic (M <sub>1</sub> ) and (b) tetragonal VO <sub>2</sub> .....	20
Fig. 2.9.	Phase diagram of the Cr-doped VO <sub>2</sub> system.....	21
Fig. 2.10.	Crystallographic structure of the M <sub>2</sub> monoclinic phase.....	22
Fig. 2.11.	Schematic delineation of electron band structure of: (a) tetragonal and (b) monoclinic VO <sub>2</sub> .....	24

Fig. 2.12. <i>d</i> -electron band splitting by crystal fields and their orbitals.....	24
Fig. 2.13. Schematic illustration of lattice matching epitaxy.....	32
Fig. 2.14. Schematic illustration of domain matching epitaxy.....	34
Fig. 2.15. High-resolution TEM cross-section image from ZnO/sapphire interface.....	36
Fig. 2.16. High-resolution TEM cross-section image of GaN epilayer grown on sapphire substrate.....	36
Fig. 2.17. Schematic illustration of the photocatalytic reactions.....	37
Fig. 3.1. Diamond cubic lattice of silicon.....	47
Fig. 3.2. Delineation of several crystallographic planes of sapphire: (a) <i>c</i> -plane (b) <i>r</i> -plane, and (c) <i>m</i> -plane.....	48
Fig. 3.3. Crystal structure of zirconia: (a) monoclinic, (b) tetragonal, and (c) cubic structures.....	49
Fig. 3.4. Schematic illustration of a typical PLD chamber.....	51
Fig. 3.5. Different regimes during laser irradiation of the target.....	57
Fig. 3.6. (a) The initial elliptical shape of the plasma after the laser pulse is terminated, (b) Final shape of the plasma when it hits the substrate and (c) Shape of a YBCO film deposited on a Si substrate.....	59
Fig. 3.7. A schematic diagram showing $\theta$ , $\varphi$ , and $\psi$ axes.....	63
Fig. 3.8. Two operation modes of the TEM imaging system: (a) diffraction mode and (b) image mode.....	66
Fig. 3.9. Schematic illustration of the optic system and mechanical parts of	

AFM.....	68
Fig. 3.10. Delineation of a four point probe resistivity measurement setup.....	71
Fig. 4.1. XRD patterns of the TiO <sub>2</sub> layers grown at different temperatures.....	81
Fig. 4.2. XRD patterns of the TiO <sub>2</sub> layers grown under different pressures at (a) 450 and (b) 550 °C.....	82
Fig. 4.3. Effect of laser energy on phase structure of the TiO <sub>2</sub> layers grown at 450 °C under oxygen pressure of $5 \times 10^{-4}$ Torr.....	85
Fig. 4.4. XRD $\varphi$ -scan of the TiO <sub>2</sub> film grown at 450 °C under $5 \times 10^{-4}$ Torr oxygen pressure with energy density of 3.5-4.0 J.cm <sup>-2</sup> : (a) Sapphire(01 $\bar{1}$ 2) and (b) Rutile (110) reflections.....	86
Fig. 4.5. Schematic drawing of (a) sapphire (0001) plane, (b) rutile (001) plane, and (c) epitaxial relationship of rutile (200) on <i>c</i> -sapphire.....	87
Fig. 4.6. (a) Cross section TEM image of the rutile TiO <sub>2</sub> film on sapphire substrate and the indexed TEM-SAED pattern, and (b) High resolution STEM image of 2 adjacent rutile grains with two different in-plane orientations.....	88
Fig. 4.7. Schematic illustration of crystallographic orientation at the TiO <sub>2</sub> /Ti <sub>2</sub> O <sub>3</sub> interface.....	90
Fig. 4.8. Surface morphology of the TiO <sub>2</sub> films grown at 450 °C under various oxygen pressures: (a) $5 \times 10^0$ , (b) $5 \times 10^{-2}$ , (c) $5 \times 10^{-4}$ , and (d) $5 \times 10^{-6}$ Torr.....	91
Fig. 4.9. Surface morphology of the TiO <sub>2</sub> films grown at 450 °C and $5 \times 10^{-4}$ Torr	

with applying different laser energies: (a) 1.5-2.0, (b) 2.5-3.0, (c) 3.5-4.0, and (d) 4.5-5.0 J.cm <sup>-2</sup> .....	92
Fig. 4.10. XPS O(1s) core level binding energies in the TiO <sub>2</sub> films grown under oxygen pressures of: (a) 5×10 <sup>-2</sup> , (b) 5×10 <sup>-4</sup> , and (c) 5×10 <sup>-6</sup> Torr.....	93
Fig. 4.11. XPS O(1s) core level binding energies in the TiO <sub>2</sub> films grown under oxygen pressure of 5×10 <sup>-4</sup> at 450 °C with laser energies of: (a) 2.5-3.0 (b) 3.5-4.0, and (c) 4.5-5.0 J.cm <sup>-2</sup> .....	95
Fig. 4.12. Transmittance spectra of the layers grown at different substrate temperatures.....	95
Fig. 4.13. Transmittance spectra of the layers grown at various oxygen pressures.....	96
Fig. 4.14. Room temperature PL spectra of the TiO <sub>2</sub> films grown at 450 °C under various pressures.....	98
Fig. 5.1. Effect of the repetition rate on phase structure of the rutile films.....	108
Fig. 5.2. Room temperature PL spectra of the rutile films grown at different frequencies.....	109
Fig. 5.3. Transmittance spectra of the rutile films grown at different frequencies.....	110
Fig. 5.4. O(1s) XPS core level binding energy in the rutile films grown at different frequencies: (a) 1, (b) 20, and (c) 30 Hz.....	112
Fig. 5.5. XRD φ-scan of rutile(110) and sapphire (01̄12) reflection planes.....	113
Fig. 5.6. TEM bright field image and indexed SAED pattern of the	

film/substrate interface.....	114
Fig. 5.7. Schematic illustration of plausible growth mechanism of rutile TiO <sub>2</sub> on <i>c</i> -sapphire.....	115
Fig. 5.8. AFM surface morphology of the TiO <sub>2</sub> films grown at frequencies of: (a) 1, (b) 10, (c) 20, and (d) 30 Hz.....	116
Fig. 5.9. Photocatalytic activity of the rutile TiO <sub>2</sub> thin films: (a) normalized concentration of 4CP and (b) ln(C <sub>0</sub> /C) at different UV-irradiation times.....	117
Fig. 6.1. (a) θ-2θ XRD pattern of the rutile/sapphire heterostructure, (b) φ- scan XRD performed on rutile(110) and sapphire(01̄12) reflections and (c) Schematic illustration of crystallographic arrangement across the film/sapphire interface.....	127
Fig. 6.2. High angle angular dark field STEM cross section images from: (a) sapphire [10̄10], (b) and (c) sapphire [1̄210] direction.....	128
Fig. 6.3. Schematic illustration of crystallographic arrangement across the TiO <sub>2</sub> /Ti <sub>2</sub> O <sub>3</sub> interface.....	129
Fig. 6.4. Arrangement of the misfit dislocations across the TiO <sub>2</sub> /Ti <sub>2</sub> O <sub>3</sub> interface.....	130
Fig. 7.1. θ-2θ XRD patterns of the rutile films annealed under various pressures.....	142
Fig. 7.2. Diffraction angle (2θ) of the rutile(200) peak as a function of the annealing pressure.....	143

Fig. 7.3. Influence of the annealing pressure on the room temperature PL spectra of the rutile films.....	144
Fig. 7.4. Transmittance spectra of the layers annealed under various pressures.....	145
Fig. 7.5. XPS O(1s) core level binding energies in the TiO <sub>2</sub> films annealed under pressures of: (a) $5 \times 10^{-6}$ , (b) $5 \times 10^{-3}$ , (c) $5 \times 10^{+1}$ Torr, and (d) unannealed sample.....	147
Fig. 7.6. The effect of annealing pressure on AFM surface morphology of the TiO <sub>2</sub> films: (a) $5 \times 10^{-6}$ , (b) $5 \times 10^{-4}$ , (c) $5 \times 10^{-3}$ , (d) $5 \times 10^{-2}$ , (e) $5 \times 10^0$ and (f) $5 \times 10^{+1}$ Torr.....	148
Fig. 7.7. $\varphi$ -scan XRD pattern of the rutile TiO <sub>2</sub> sample on <i>c</i> -cut sapphire.....	150
Fig. 7.8. A high resolution ADF-STEM image showing: (a) [1 $\bar{2}$ 10] and (b) [10 $\bar{1}$ 0] zones of <i>c</i> -sapphire.....	151
Fig. 7.9. Photocatalytic activity of rutile TiO <sub>2</sub> films under UV illumination.....	152
Fig. 7.10. Schematic illustration of photo-degradation of 4CP on TiO <sub>2</sub> films.....	154
Fig. 7.11. Photocatalytic activity of the rutile TiO <sub>2</sub> films under visible illumination.....	155
Fig. 7.12. Dependence of the electrical resistivity on the annealing pressure.....	157
Fig. 8.1. XRD patterns of the TiO <sub>2</sub> films deposited on c-YSZ/Si(100) under various oxygen pressures at temperatures of: (a) 300, (b) 500, and (c) 700 °C.....	167

Fig. 8.2. Atomic arrangement on (a) Zr-terminated c-YSZ (200), (b) O-terminated c-YSZ(200), (c) O-terminated r-TiO <sub>2</sub> (200), and (d) Ti-terminated a-TiO <sub>2</sub> planes. Roughness of the Zr- and O-terminated planes of c-YSZ is compared and highlighted by triangles.....	168
Fig. 8.3. XRD data for the TiO <sub>2</sub> thin films grown under varying pressures for different times.....	169
Fig. 8.4. High resolution XPS O(1s) core level binding energy of the r-TiO <sub>2</sub> film grown at different temperatures: (a) 300, (b) 500, (c) 700 °C.....	172
Fig. 8.5. φ-scan XRD patterns of the (110) <sub>rutile</sub> , (202) <sub>YSZ</sub> , and (202) <sub>Si</sub> reflection of the heterostructure fabricated at 700 °C under oxygen pressure of 5×10 <sup>-4</sup> Torr.....	174
Fig. 8.6. Delineation of 4 equally probable orientations of r-TiO <sub>2</sub> on c-YSZ layer.....	175
Fig. 8.7. Schematic illustration of the atomic arrangement and the epitaxial relationship across the interface between O-terminated r-TiO <sub>2</sub> and Zr-terminated c-YSZ films.....	175
Fig. 8.8. TEM low magnification bright field image and the high resolution cross section images of the r-TiO <sub>2</sub> /c-YSZ/Si(001) heterostructure. The indexed SAED pattern shown in the inset of the BF image confirms the proposed epitaxial relationship.....	176
Fig. 8.9. φ-scan XRD patterns of the (101) <sub>anatase</sub> , (202) <sub>YSZ</sub> , and (202) <sub>Si</sub> reflections of the heterostructure fabricated at 300 °C under oxygen	

pressure of $5 \times 10^{-2}$ Torr.....	178
Fig. 8.10. Schematic illustration of the atomic arrangement and the epitaxial relationship at Ti-terminated a-TiO <sub>2</sub> and O-terminated c-YSZ interface.....	179
Fig. 8.11. TEM low magnification bright field image and the high resolution cross section images of the a-TiO <sub>2</sub> /c-YSZ/Si(001) heterostructure.....	180
Fig. 8.12. Surface morphology of the heterostructures grown under different conditions: (a) $5 \times 10^{-4}$ Torr and 300 °C, (b) $5 \times 10^{-4}$ Torr and 500 °C, (c) $5 \times 10^{-4}$ Torr and 700 °C, (d) $5 \times 10^{-2}$ Torr and 300 °C, (e) $5 \times 10^{-2}$ Torr and 500 °C, and (f) $5 \times 10^{-2}$ Torr and 700 °C.....	182
Fig. 8.13. Electrical resistance of the TiO <sub>2</sub> /c-YSZ/Si heterostructures fabricated at different temperatures under oxygen pressure of $5 \times 10^{-4}$ Torr.....	184
Fig. 8.14. Photocatalytic decomposition of 4CP under ultraviolet illumination by (a) r-TiO <sub>2</sub> /c-YSZ/Si and (b) a-TiO <sub>2</sub> /c-YSZ/Si heterostructures.....	186
Fig. 9.1. θ-2θ and φ patterns of the TiO <sub>2</sub> /YSZ/Si(001) heterostructure.....	198
Fig. 9.2. Schematic illustration of four equally probable orientations of the rutile film on the YSZ buffer.....	199
Fig. 9.3. (a) Bright field cross section micrograph and the selected area electron diffraction of the TiO <sub>2</sub> /YSZ/Si(001) heterostructures showing rutile[031], YSZ[110], and Si[110] zones, (b) High resolution image of the rutile/YSZ interface, and (c) High resolution image of YSZ/Si(001)	

interface.....	200
Fig. 9.4. Matching of integral multiples of planes to relax the misfit strain across the rutile/YSZ interface.....	201
Fig. 9.5. $\theta$ - $2\theta$ XRD patterns of laser annealed samples that were prepared using several laser energies.....	202
Fig. 9.6. Surface morphology of the laser annealed samples. Data for sample annealed at energies of: (a) 0.16, (b) 0.21, (c) 0.28, (d) 0.32 $\text{J.cm}^{-2}$ are shown.....	203
Fig. 9.7. Low magnification bright field TEM image obtained from a sample that was laser annealed with an energy density of 0.32 $\text{J.cm}^{-2}$ .....	203
Fig. 9.8. XPS high resolution O(1s) core level binding energy for the as deposited sample. The result of the wettability study is also shown in the inset.....	205
Fig. 9.9. XPS high resolution O(1s) core level binding energy for the laser annealed samples. Data are shown for samples annealed at energies of: (a) 0.16, (b) 0.21, (c) 0.28, and (d) 0.32 $\text{J.cm}^{-2}$ .....	206
Fig. 9.10. Results of the wettability studies for the laser annealed samples. Data are shown for samples annealed at energies of: (a) 0.16, (b) 0.21, (c) 0.28, and (d) 0.32 $\text{J.cm}^{-2}$ .....	207
Fig. 9.11. XPS O(1s) core level binding energies for the laser annealed sample after 24 hours. Data are shown for samples annealed at energies of (a) 0.16, (b) 0.21, (c) 0.28, and (d) 0.32 $\text{J.cm}^{-2}$ .....	208

Fig. 10.1. $\theta$ - $2\theta$ XRD pattern of the anatase/t-YSZ/Si(001) epitaxial heterostructure.....	220
Fig. 10.2. $\varphi$ -scan patterns taken from: (a) Si(202) and t-YSZ(101) and (b) anatase(101) reflection.....	221
Fig. 10.3. Illustration of the crystallographic arrangement across the t-YSZ(001)/Si(001) interface.....	222
Fig. 10.4. Schematic Illustration of the crystallographic arrangement across the anatase/t-YSZ interface.....	223
Fig. 10.5. TEM micrographs of the anatase(004)/t-YSZ(002)/Si(001) heterostructure: (a) Low magnification cross section image and the SAED pattern which belongs to the Si[110], t-YSZ[100], and anatase [100] zones, highlighted in yellow, green, and red, respectively, and (b) A domain boundary in the anatase epitaxial film.....	224
Fig. 10.6. (a) High resolution TEM image of the anatase/t-YSZ interface, and (b) Inverse FFT image of the anatase/t-YSZ interface.....	225
Fig. 10.7. (a) Low magnification cross section TEM image from the laser treated sample, (b) High resolution TEM micrograph acquired from the interface between the laser affected and the pristine regions.....	227
Fig. 10.8. $\theta$ - $2\theta$ scan XRD taken from the laser annealed anatase/t-YSZ/Si(001) heterostructure.....	228
Fig. 10.9. XPS O(1s) core level binding energy of the: (a) pristine and (b) laser annealed anatase/t-YSZ/Si(001) heterostructures.....	229

Fig. 10.10. XRD patterns collected from the anatase/t-YSZ/Si heterostructure at elevated temperatures.....	232
Fig. 10.11. Intensity of the anatase(004) and t-YSZ(002) characteristic peaks Inset shows $I_{\text{anatase}(004)}/I_{\text{t-YSZ}(002)}$ ratio at different temperatures.....	233
Fig. 10.12. Low magnification TEM cross section image and the SAED pattern of the anatase/t-YSZ/Si heterostructure annealed at 1100 °C for 4 hours.....	234
Fig. 10.13. Effect of laser annealing on the photocatalytic efficiency of the anatase/t-YSZ/Si(001) thin film heterostructure.....	235
Fig. 11.1. Illustration of low-index faces of rutile: (a) (110), (b) (100), (c) (001) and (d) (101).....	243
Fig. 11.2. (a) $\theta$ - $2\theta$ pattern acquired from the rutile $\text{TiO}_2(001)/\text{Al}_2\text{O}_3(10\bar{1}0)$ heterostructure and (b) Rocking curves taken from (002) reflection of rutile $\text{TiO}_2$ using several $\varphi$ -angle.....	247
Fig. 11.3. Results of $\varphi$ -scan XRD performed on rutile $\text{TiO}_2(001)/\text{Al}_2\text{O}_3(10\bar{1}0)$ heterostructure: (a) Rutile(101) reflection and (b) Alumina(10 $\bar{1}$ 4) reflection.....	248
Fig. 11.4. Results of $\varphi$ -scan XRD performed on rutile $\text{TiO}_2(001)/\text{Al}_2\text{O}_3(10\bar{1}0)$ heterostructure: (a) Rutile(301) reflection and (b) Alumina(03 $\bar{3}$ 0) reflection.....	249
Fig. 11.5. Stereographic projection showing: (a) Rutile $\text{TiO}_2(001)$ and (b) $\text{Al}_2\text{O}_3(10\bar{1}0)$ poles.....	251

Fig. 11.6. (a) Cross section TEM micrograph and indexed SAED pattern acquired from rutile/ <i>m</i> -sapphire heterostructure. The SAED pattern belongs to rutile[100] and sapphire[0001] zones, (b) High resolution TEM image from the rutile/ <i>m</i> -sapphire interface. Alternation of 19/18 and 18/17 domains across the film/substrate interface is shown in the inset.....	252
Fig. 11.7. High resolution $\theta$ -2 $\theta$ scans through: (a) $\text{TiO}_2(002)$ , (b) $\text{TiO}_2(111)$ , (c) $\text{TiO}_2(301)$ , and (d) $\text{TiO}_2(101)$ faces of rutile epilayer deposited on $\text{Al}_2\text{O}_3(10\bar{1}0)$ substrate.....	253
Fig. 11.8. Schematic illustration of the rutile $\text{TiO}_2$ unit cell and the $\frac{1}{2}[10\bar{1}](101)$ slip system.....	257
Fig. 11.9. (a) $\theta$ -2 $\theta$ pattern of the rutile $\text{TiO}_2(101)/\text{Al}_2\text{O}_3(01\bar{1}2)$ heterostructure and (b) Rocking curve taken from (101) reflection of rutile $\text{TiO}_2$ along different $\varphi$ -angles.....	258
Fig. 11.10. $\varphi$ -scan patterns taken from rutile $\text{TiO}_2(101)/\text{Al}_2\text{O}_3(01\bar{1}2)$ heterostructure: (a) Rutile(200), (b) Rutile(002), (c) Rutile(121) and (d) Alumina(0006) reflections.....	260
Fig. 11.11. Stereographic projection showing: (a) Rutile $\text{TiO}_2(101)$ and (b) $\text{Al}_2\text{O}_3(01\bar{1}2)$ poles.....	261
Fig. 11.12. (a) Cross section TEM image taken from rutile/ <i>r</i> -sapphire heterostructure. The inset shows the indexed SAED pattern belonging to typical rutile[100] and sapphire[2110] zones, (b) High resolution	

micrograph of the rutile/ <i>r</i> -sapphire interface. Matching of 28 planes of rutile with 27 planes of sapphire to accommodate the lattice misfit strain is evident in the inset.....	262
Fig. 11.13. High resolution $\theta$ - $2\theta$ scan obtained from: (a) $\text{TiO}_2(101)$ , (b) $\text{TiO}_2(002)$ , and (c) $\text{TiO}_2(121)/(211)$ faces of rutile epilayer grown on $\text{Al}_2\text{O}_3(01\bar{1}2)$ substrate.....	263
Fig. 11.14. (a) $\theta$ - $2\theta$ pattern taken from the rutile $\text{TiO}_2(001)/\text{Al}_2\text{O}_3(0001)$ heterostructure and (b) Rocking curve acquired from (200) reflection of rutile $\text{TiO}_2$ along several $\varphi$ -angles.....	265
Fig. 11.15. Results of $\varphi$ -scan XRD from rutile $\text{TiO}_2(001)/\text{Al}_2\text{O}_3(0001)$ heterostructure: (a) Rutile(110), (b) Rutile(101), (c) Rutile(111), and (d) Alumina( $02\bar{2}4$ ) reflections.....	266
Fig. 11.16. Stereographic projection showing: (a) Rutile $\text{TiO}_2(100)$ and (b) $\text{Al}_2\text{O}_3(0001)$ poles.....	268
Fig. 11.17. (a) Low magnification cross section TEM image taken from the rutile/ <i>c</i> -sapphire heterostructure. The inset shows SAED patterns from two different zones of the $\text{TiO}_2$ film and sapphire substrate and (b) High resolution image from the rutile/ <i>c</i> -sapphire interface along [2 $\bar{1}\bar{1}0$ ] direction.....	270
Fig. 11.18. High resolution $\theta$ - $2\theta$ scans performed through: (a) $\text{TiO}_2(110)$ , (b) $\text{TiO}_2(101)$ , (c) $\text{TiO}_2(200)$ , (d) $\text{TiO}_2(111)$ , (e) $\text{TiO}_2(210)/(120)$ , (f) $\text{TiO}_2(220)$ , (g) $\text{TiO}_2(121)$ , (h) $\text{TiO}_2(211)$ , (i) $\text{TiO}_2(130)$ , and (j)	

TiO <sub>2</sub> (130) faces of rutile epilayer grown on Al <sub>2</sub> O <sub>3</sub> (0001) substrate.....	273
Fig. 11.19. Role of out-of-plane orientation on photocatalytic decomposition rate of 4-chlorophenol by rutile TiO <sub>2</sub> epitaxial thin films under ultraviolet illumination.....	274
Fig. 11.20. XPS O(1s) core level binding energy in: (a) Rutile/ <i>m</i> -sapphire, (b) Rutile/ <i>r</i> -sapphire, and (c) Rutile/ <i>c</i> -sapphire heterostructures.....	275
Fig. 12.1. Resistance versus temperature in: (a) VO <sub>2</sub> /TiO <sub>2</sub> / <i>m</i> -sapphire, (b) VO <sub>2</sub> /TiO <sub>2</sub> / <i>r</i> -sapphire, and (c) VO <sub>2</sub> /TiO <sub>2</sub> / <i>c</i> -sapphire heterostructures...	284
Fig. 12.2. Results of θ-2θ scan conducted on VO <sub>2</sub> /TiO <sub>2</sub> / <i>m</i> -sapphire heterostructure.....	286
Fig. 12.3. High resolution θ-2θ scans performed on: (a) VO <sub>2</sub> ( $\bar{1}00$ ), (b) VO <sub>2</sub> ( $\bar{1}\bar{1}0$ )+VO <sub>2</sub> ( $\bar{1}11$ ), (c) VO <sub>2</sub> ( $\bar{1}02$ ), (d) TiO <sub>2</sub> (111) and VO <sub>2</sub> ( $\bar{2}12$ )+VO <sub>2</sub> ( $\bar{2}10$ ), (e) TiO <sub>2</sub> (211) and VO <sub>2</sub> ( $\bar{2}13$ )+VO <sub>2</sub> ( $\bar{2}22$ ), and (f) TiO <sub>2</sub> (031) and VO <sub>2</sub> ( $\bar{2}31$ )+VO <sub>2</sub> ( $\bar{2}0\bar{2}$ )+VO <sub>2</sub> ( $\bar{2}04$ ) reflections in VO <sub>2</sub> /TiO <sub>2</sub> / <i>m</i> -sapphire heterostructure.....	287
Fig. 12.4. φ-scan patterns acquired from several reflections in VO <sub>2</sub> /TiO <sub>2</sub> / <i>m</i> - sapphire heterostructure: (a) VO <sub>2</sub> ( $\bar{2}12$ )+VO <sub>2</sub> ( $\bar{2}10$ ), (b) VO <sub>2</sub> ( $\bar{1}02$ ), (c) VO <sub>2</sub> ( $\bar{2}11$ )+VO <sub>2</sub> ( $\bar{2}00$ ), (d) TiO <sub>2</sub> (101), and (e) Al <sub>2</sub> O <sub>3</sub> (10 $\bar{1}4$ ).....	289
Fig. 12.5. Result of θ-2θ scan performed on VO <sub>2</sub> /TiO <sub>2</sub> / <i>r</i> -sapphire heterostructure.....	290
Fig. 12.6. High resolution θ-2θ patterns acquired from VO <sub>2</sub> /TiO <sub>2</sub> / <i>r</i> -sapphire heterostructure: (a) VO <sub>2</sub> ( $\bar{1}11$ ), (b) TiO <sub>2</sub> (110) and VO <sub>2</sub> (011), (c)	

VO <sub>2</sub> ( $\bar{1}02$ ), (d) TiO <sub>2</sub> (011) and VO <sub>2</sub> ( $\bar{2}11$ ), (e) TiO <sub>2</sub> ( $\bar{1}11$ ) and VO <sub>2</sub> ( $\bar{2}12$ ) and (f) TiO <sub>2</sub> (211), and VO <sub>2</sub> (211) reflections.....	291
Fig. 12.7. Results of $\varphi$ -scan XRD conducted on: (a) VO <sub>2</sub> ( $\bar{2}11$ ), (b) VO <sub>2</sub> (220), (c) VO <sub>2</sub> (011), (d) TiO <sub>2</sub> (110), and (e) Al <sub>2</sub> O <sub>3</sub> (0006) reflections in VO <sub>2</sub> /TiO <sub>2</sub> / <i>r</i> -sapphire heterostructure.....	292
Fig. 12.8. $\theta$ -2 $\theta$ pattern taken from VO <sub>2</sub> /TiO <sub>2</sub> / <i>c</i> -sapphire heterostructure.....	295
Fig. 12.9. $\varphi$ -patterns of different reflections in VO <sub>2</sub> /TiO <sub>2</sub> / <i>c</i> -sapphire heterostructure: (a) VO <sub>2</sub> (220) at $\psi=43.14^\circ$ , (b) VO <sub>2</sub> (220) at $\psi=68.35^\circ$ (c) VO <sub>2</sub> (211), (d) VO <sub>2</sub> (200), and (e) TiO <sub>2</sub> (110), and (f) Al <sub>2</sub> O <sub>3</sub> (01 $\bar{1}$ 2).....	296
Fig. 12.10. Schematic illustration of VO <sub>2</sub> <sup>monoclinic</sup> /TiO <sub>2</sub> <sup>tetragonal</sup> interface in: (a) VO <sub>2</sub> /TiO <sub>2</sub> / <i>m</i> -sapphire, (b) VO <sub>2</sub> /TiO <sub>2</sub> / <i>r</i> -sapphire, and (c) VO <sub>2</sub> /TiO <sub>2</sub> / <i>c</i> -sapphire heterostructures. TiO <sub>2</sub> and VO <sub>2</sub> unit cells are displayed in blue and red, respectively. The arrows show crystallographic orientations of TiO <sub>2</sub> lattice.....	301
Fig. 12.11. Cross section bright field TEM micrographs taken from: (a) VO <sub>2</sub> /TiO <sub>2</sub> / <i>m</i> -sapphire, (b) VO <sub>2</sub> /TiO <sub>2</sub> / <i>r</i> -sapphire, and (c) VO <sub>2</sub> /TiO <sub>2</sub> / <i>c</i> -sapphire heterostructures.....	303
Fig. 12.12. High resolution TEM image of VO <sub>2</sub> /TiO <sub>2</sub> interface in: (a) VO <sub>2</sub> /TiO <sub>2</sub> / <i>m</i> -sapphire (b) VO <sub>2</sub> /TiO <sub>2</sub> / <i>r</i> -sapphire heterostructures.....	304
Fig. 12.13. Schematic delineation of: (a) VO <sub>2</sub> and (b) TiO <sub>2</sub> unit cells along their [0 $\bar{1}$ 0] and [ $\bar{1}$ 00] orientations.....	305

# **Chapter 1**

## **Introduction**

Thin film heterostructures constitute the backbone of solid state device technology. Next generation solid state devices will require integration of various functions on practical substrates, particularly on Si(100). This integration will necessitate epitaxial growth of materials of different functions on a single chip where total misfit could range from less than 1% to over 25% or even more. Managing such huge misfits, especially in complicated systems where two materials with totally different crystalline structures and chemical compositions are juxtaposed, and controlling the defect characteristics are the key features to fabricate highly efficient devices for novel applications.<sup>1,2</sup> This research was intended to epitaxially grow TiO<sub>2</sub> and TiO<sub>2</sub>/VO<sub>2</sub> based heterostructures on sapphire and buffered silicon substrates where their microstructure at the atomic scale and their photochemical and electrical properties were studied.

The first step of this research was dedicated to epitaxial integration of titanium dioxide with sapphire and silicon substrates where phase tuning, atomic arrangement across the interfaces, mechanism behind strain relaxation, and defect characteristics are discussed in detail. In this project, two different applications for the TiO<sub>2</sub> based heterostructures were taken into account. TiO<sub>2</sub> is one of the important semiconductor

materials which is widely used as an efficient photocatalyst, because it is chemically and biologically inert, photocatalytically stable, commercially available and inexpensive, and environmentally friendly.<sup>3,4</sup> According to Fig.1.1, the valence band (VB) of TiO<sub>2</sub>, versus natural hydrogen electrode, lies at deep levels and, thus, photogenerated holes have strong enough oxidizing power to create OH<sup>•</sup> radicals, which decompose most organic pollutants. Position of its conduction band (CB) is also high enough to reduce oxygen molecules adsorbed on the surface.<sup>5</sup> As a consequence, photogenerated electrons and holes can participate in almost any redox reaction.

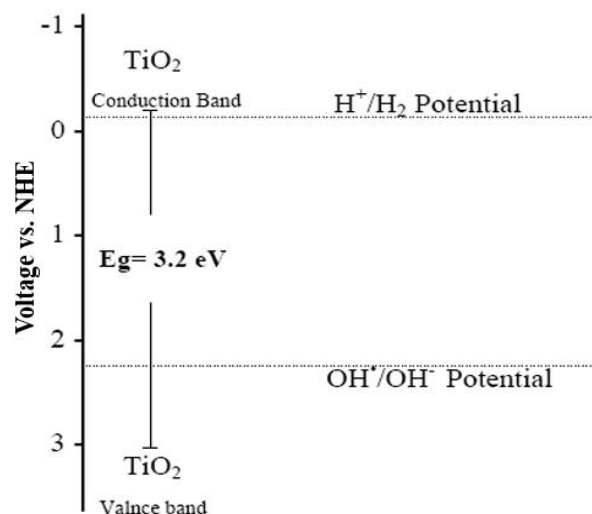


Fig.1.1. Positions of the valence and the conductance bands of TiO<sub>2</sub> vs. NHE.<sup>5</sup>

It is worth mentioning that higher energy consumption, which is a result of increasing the world population, gives rise to creating environmental pollutions and depleting the fossil fuel reservoirs; therefore, remediation of the environmental pollutants is necessary to keep the world clean for the next generations. Since now,

advanced oxidation technologies, in particular photocatalysis, have gained much attention by scientists. In their point of view, to counter environmental pollutions, a simple and comprehensive photonic reaction system which converts the solar energy into the chemical energy of a redox system, namely photocatalysis, would be helpful for the detoxification processes. Nowadays, heterogeneous photocatalysis is the most efficient method to destroy organic pollutants. This process is based on the use of ultraviolet or visible radiations to excite a semiconductor on whose surface the oxidation of the pollutants is performed. According to the importance of TiO<sub>2</sub> in the field of catalysis and environmental remediation, photocatalytic activity of the grown TiO<sub>2</sub> based epilayers was assessed in a controlled way and a correlation between the growth variables and the photocatalytic efficiency was established. The influence of vacuum and laser annealing on photochemical characteristics was studied as well. The results of this section of the present project are presented in chapters 4 to 11.

In the second step of this dissertation, TiO<sub>2</sub>/VO<sub>2</sub> epitaxial heterostructures were grown on silicon and sapphire substrates and the epitaxial relationship across the interfaces and the semiconductor-to-metal transition (SMT) characteristics were investigated. Vanadium dioxide crystallizes in two different states: high temperature tetragonal phase, with a metallic electrical behavior, and low temperature monoclinic phase which exhibits a semiconductor electrical behavior. It is one of the most extensively investigated correlated electron systems exhibiting a distinct semiconductor-to-metal transition due to a reversible fast phase transformation between the monoclinic and the tetragonal states at about 68 °C.<sup>6,7</sup> It is worth

mentioning that all the transition metal oxides exhibit the SMT behavior; however, VO<sub>2</sub> is distinguished by its thermal switching near room temperature transition. The characteristics associated with SMT in VO<sub>2</sub> are fascinating scientifically and are of immense technological importance for potential applications in sensor- and memory-type applications.<sup>8-11</sup> It is believed that the temperature of this transition can be modified by doping or stress. This belief was the main idea behind the second step of this dissertation where TiO<sub>2</sub> was used as a platform for VO<sub>2</sub> deposition and tuning the temperature at which the monoclinic to tetragonal phase transformation takes place. TiO<sub>2</sub> crystallizes in various structures where two of them, namely rutile and anatase, are the most important ones. Rutile has a tetragonal lattice with a P4<sub>2</sub>/mnm space group and lattice parameters of a=b=4.5933 and c=2.9592 Å.<sup>12</sup> On the other hand, the lattice constants of tetragonal VO<sub>2</sub> are a=b=4.554 and c=2.8557 Å. This information shows that the rutile TiO<sub>2</sub> and high temperature rutile VO<sub>2</sub> have very close structures.<sup>13-</sup><sup>15</sup> Thus, we expected to be able to stabilize the tetragonal state of VO<sub>2</sub> at temperatures lower than 68 °C through buffering by rutile TiO<sub>2</sub> and control the SMT temperature. In this step of the present research, TiO<sub>2</sub> epitaxial thin films with several out-of-plane orientations were used as a platform to manipulate the growth direction of VO<sub>2</sub> top layers and tune the SMT temperature. The results are presented in chapter 12.

This dissertation is organized into the following chapters:

Chapter 1: Introduction

Chapter 2: Background knowledge

Chapter 3: Experimental techniques

Chapter 4: Control of structure and properties of epitaxial  $\text{TiO}_2/c$ -sapphire thin film heterostructures

Chapter 5: Structure-property correlation in epitaxial rutile films grown on sapphire(0001) substrates by pulsed laser deposition

Chapter 6: Domain epitaxy in  $\text{TiO}_2/\alpha\text{-Al}_2\text{O}_3$  thin film heterostructures with  $\text{Ti}_2\text{O}_3$  transition layer

Chapter 7: Defect mediated photocatalytic decomposition of 4-chlorophenol on epitaxial rutile thin films under visible and UV illuminations

Chapter 8: Phase tuning, thin film epitaxy, and properties of YSZ-buffered  $\text{TiO}_2$  on Si(001) substrate

Chapter 9: Nanosecond switching in wetting properties of  $\text{TiO}_2/c\text{-YSZ/Si}(001)$  heterostructures induced by laser irradiation

Chapter 10: Enhancement of photocatalytic activity of anatase  $\text{TiO}_2$  single crystalline thin films by nanosecond pulsed excimer laser treatment

Chapter 11: Role of Substrate Crystallographic Characteristics on Structure and Properties of Rutile  $\text{TiO}_2$  Epilayers

Chapter 12: Semiconductor to Metal Transition Characteristics in  $\text{VO}_2/\text{TiO}_2/\text{Al}_2\text{O}_3$  Thin Film Heterostructures

Chapter 13: Summary and suggestions for future works

This research opens new opportunities for novel applications of  $\text{TiO}_2$  and  $\text{VO}_2$  based thin film heterostructures such as intelligent membranes, sensors, smart catalysts, and multifunctional devices.

## References

1. J. Narayan, *Acta Mater.* 61, 2703 (2013).
2. J. Narayan and B.C. Larson, *J. Appl. Phys.* 93, 27 (2003).
3. U. Diebold, *Surf. Sci. Rep.* 48, 53 (2003).
4. M. Miyauchi, A. Nakajima, T. Watanabe, and K. Hashimoto, *Chem. Mater.* 14, 2812 (2002).
5. Z. Ambrus, K. Mogyorosi, A. Szalai, T. Alapi, K. Demeter, A. Dombi, and P. Sipos, *Appl. Catal. A* 340, 153 (2008).
6. F.J. Morin, *Phys. Rev. Lett.* 3, 34 (1959).
7. J.B. Goodenough, *J. Solid State Chem.* 3, 490 (1971).
8. F. Chudnovskiy, S. Luryi, and B. Spivak, *Future Trends in Microelectronics: The Nano Millennium*, New York: Wiley Interscience (2002).
9. D.M. Newns, J.A. Misewich, C.C. Tsuei, A. Gupta, B.A. Scott, and A. Schrott, *Appl. Phys. Lett.* 73, 780 (1998).
10. H. Wang, X. Yi, S. Chen, and X. Fu, *Sens. Actuators A Phys.* 122, 108 (2005).
11. M.J. Lee, Y. Park, D.S. Suh, E.H. Lee, S. Seo, D.C. Kim, R. Jung, B.S. Kang, S.E. Ahn, C.B. Lee, D.H. Seo, Y.K. Cha, I.K. Yoo, J.S. Kim, and B.H. Park, *Adv. Mater.* 19, 3919 (2007).
12. N. Sbai, J. Perriere, W. Seiler, and E. Millon, *Surf. Sci.* 601, 5649 (2007).
13. D.B. McWhan, M. Marezio, J.P. Remeika, and P.D. Dernier, *Phys. Rev. B* 10, 490 (1974).
14. S. Westman, *Acta Chim. Scand.* 15, 217 (1961).
15. K. Rogers, *Powder Diffr.* 8, 240 (1993).

## Chapter 2

# Background Knowledge

### 2.1. Titanium dioxide ( $\text{TiO}_2$ )

Titanium dioxide ( $\text{TiO}_2$ ), also known as titania, is an *n*-type semiconductor and has been widely used in versatile applications owing to its technologically promising properties such as a large refractive index, a high dielectric constant, and a favorable photochemical characteristics. It is also chemically inert, photo-chemically stable, and non-toxic.<sup>1-4</sup>  $\text{TiO}_2$  crystallizes in three different polymorphs: anatase, rutile, and brookite.<sup>1,5</sup> Anatase is stable only at low temperatures and transforms into rutile upon heating. Rutile is the most thermodynamically stable phase. Brookite exists only in some extreme conditions, so it is not considered useful for practical applications. Other structures (e.g. Magneli phases, corundum sesquioxide, and so on) also exist under extreme conditions with no practical application.<sup>6-10</sup> Fig.2.1 shows the Ti-O phase diagram where formation conditions of all these states can be understood.<sup>11</sup> The structure of anatase  $\text{TiO}_2$  is considerably more open than that of rutile. Reduction, or removal of oxygen ions, facilitates the collapse from anatase to rutile, while the inclusion of interstitial titanium ions inhibits the same transformation. When the anatase to rutile phase transformation occurs, the relatively open anatase structure collapses in volume by about 8 %. The cell volumes of anatase and rutile are

approximately  $68 \text{ \AA}^3$  and  $62 \text{ \AA}^3$ , respectively. The collapse is accompanied by distortion of the oxygen framework, breaking of two of the six Ti-O bonds, and shifting of the  $\text{Ti}^{+4}$  ions. This sheds more light on the  $\text{TiO}_2$  polymorphs where their structure, properties, and defect characteristics are discussed.

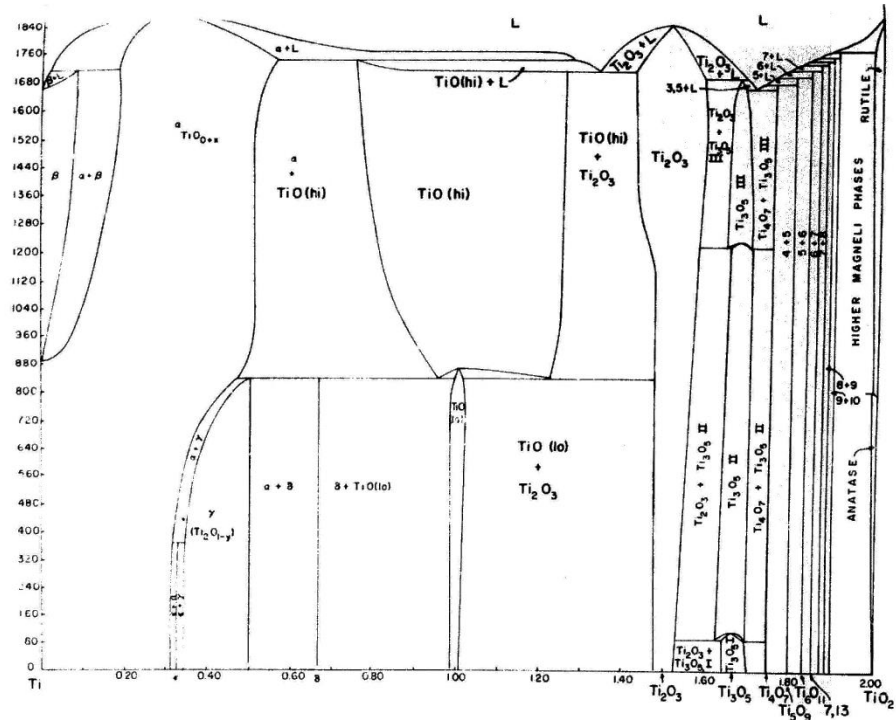


Fig. 2.1. Phase diagram of the Ti-O system.<sup>11</sup>

### 2.1.1. Anatase

Anatase has a tetragonal lattice with lattice parameters of  $a=b=3.7852$  and  $c=9.5139 \text{ \AA}$ . It belongs to the  $I4_1/\text{amd}$  space group.<sup>12</sup> The anatase  $\text{TiO}_2$  structure consists of a titanium atom surrounded by six oxygen atoms in a distorted octahedral configuration. The oxygen atoms are threefold coordinated. Its band gap and refractive

index are about 3.2 eV and 2.49,<sup>1,13</sup> respectively. Although anatase exhibits attractive properties as well, its relatively low thermal stability limits its applications to low temperatures. It is a metastable phase at temperatures below 800-900 °C and it transforms into rutile upon heating above this temperature in vacuum.<sup>14,15</sup> However, it is one of the most important known photocatalyst materials able to efficiently decompose almost any kind of environmental pollutants due to the position of its valence and conductance bands.<sup>16,17</sup> Fig.2.2 depicts the energy levels of the valence and conduction bands of various metal oxides versus the normal hydrogen electrode (NHE) along with the band-gap energies of these metal oxides at a pH of 7. Due to the positions of valence and conductance bands of TiO<sub>2</sub> with respect to the natural hydrogen electrode, it can reduce or oxidize almost all reactions.<sup>18</sup>

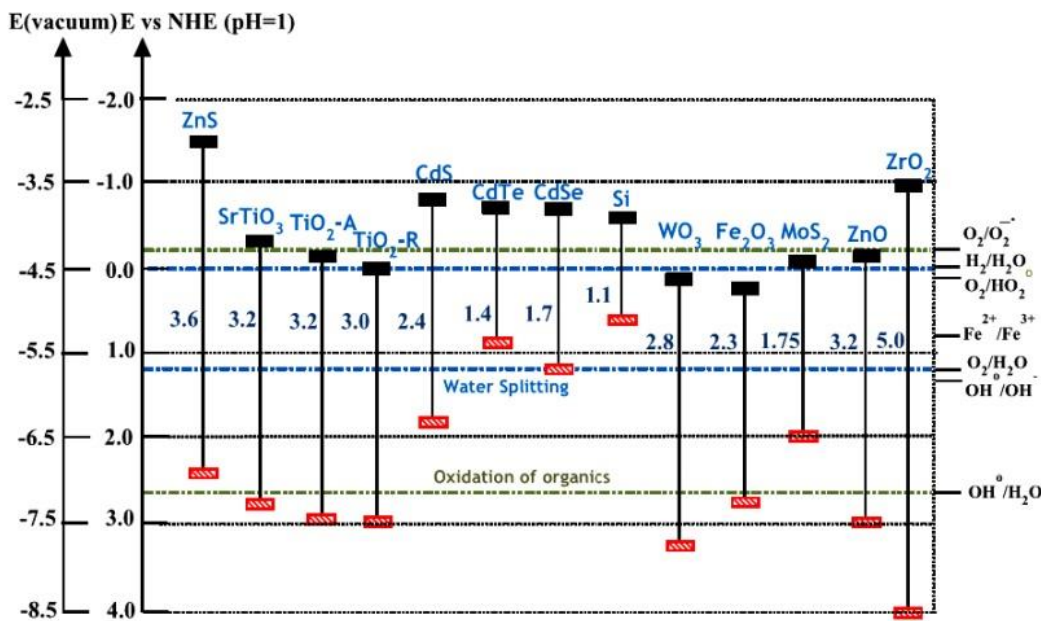


Fig.2.2. Redox potentials of valence and conduction bands and band-gap energies for various metal oxides. The redox potential positions of H<sup>+</sup>/H<sub>2</sub> and OH<sup>-</sup>/OH<sup>-</sup> are also illustrated.<sup>18</sup>

Anatase has two low energy surfaces which are shown in Fig.2.3. The (101) surface is corrugated with alternating rows of 5-coordinate Ti atoms and bridging oxygen which are at the edges of the corrugations. The (001) surface is rather flat and can undergo a (1×4) reconstruction. The (100) surface has double rows of 5-coordinate Ti atoms alternating with double rows of bridging oxygens. It can undergo a (1×2) reconstruction.<sup>19-22</sup> Anatase is used in anti-fogging and self-cleaning surfaces,<sup>23</sup> anti-bacteria agents,<sup>24</sup> hydrogen production,<sup>25</sup> sensors,<sup>26</sup> and Li-ion batteries.<sup>27</sup>

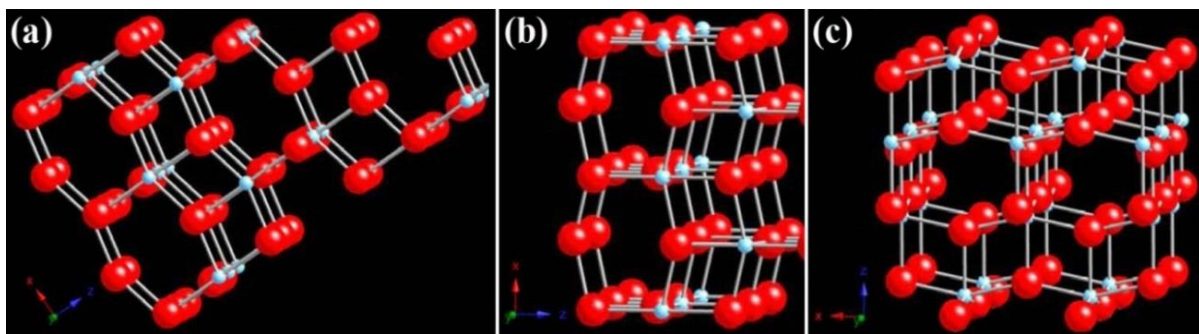


Fig.2.3. Schematic illustration of low-index faces of anatase  $\text{TiO}_2$ : (a) (101), (b) (100), and (c) (001).

### 2.1.2. Rutile

Rutile is the most thermodynamically stable state of  $\text{TiO}_2$  and has a band gap of 3.0 eV and a refractive index of about 2.9.<sup>1,13</sup> These properties along with its high thermal stability make it a promising candidate for many applications such as dye-sensitized solar cells,<sup>28</sup> anti-bacterial agents,<sup>13</sup> spintronic and magnetic devices,<sup>29</sup> photocatalysis,<sup>30</sup> sensors,<sup>31</sup> and microelectronics.<sup>32</sup> Rutile with a tetragonal lattice and parameters of  $a=b=4.5933$  and  $c=2.9592 \text{ \AA}$  belongs to the  $P4_2/mnm$  space group.<sup>4</sup> The rutile  $\text{TiO}_2$  structure consists of chains of  $\text{TiO}_6$  octahedra with each pair sharing opposite edges of

the unit cell. Each Ti atom is surrounded by six oxygen atoms, whereas each oxygen atom is surrounded by three metal atoms arranged as corners of an equilateral triangle. This tri-coordination (for nominally divalent O atoms) signifies the predominantly ionic character of bonding in rutile  $\text{TiO}_2$ . The octahedra within the structure are irregular; they show a slight orthorhombic distortion and are in contact with ten neighboring octahedra. Each oxygen atom in the rutile  $\text{TiO}_2$  structure is shared by three octahedra, leading the oxygen atoms to have a triangular planar coordination with respect to the titanium atoms. Rutile  $\text{TiO}_2$  has three main crystalline faces: (110), (100), and (001).<sup>1</sup> These crystallographic planes are depicted in Fig.2.4.

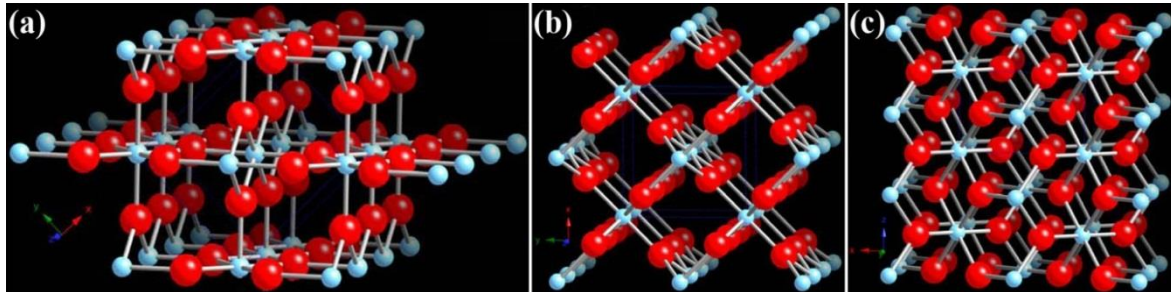


Fig.2.4. Schematic illustration of low-index faces of rutile  $\text{TiO}_2$ : (a) (110), (b) (100), and (c) (001).

The most thermally stable face is (110) which has been widely studied. It has rows of bridging oxygens connected to two 6-coordinated Ti atoms. Meanwhile, there are rows of 5-coordinated Ti atoms running parallel to the rows of bridging oxygens and alternating with them. The exposed Ti atoms are low in electron density. The (100) surface also has alternating rows of bridging oxygens and 5-coordinate Ti atoms existing in a different geometric relationship with each other. The (001) face is

thermally less stable restructuring above 475 °C.<sup>33</sup> There are double rows of bridging oxygens alternating with single rows of exposed Ti atoms which are of the equatorial type rather than the axial type.

### **2.1.3. Defect characteristics**

The electronic and optical properties of the nonstoichiometric oxides are critically dictated by defect structures existing within the material. Therefore, the study of the electronic structure in the presence of point defects is very important to understand the material properties of oxides. The defect chemistry may be used as a framework for the engineering of the functional properties of TiO<sub>2</sub>. There are six different kinds of point defects envisaged in the TiO<sub>2</sub> structure, namely titanium interstitial (Ti<sub>i</sub>), titanium vacancy (V<sub>Ti</sub>), oxygen interstitial (O<sub>i</sub>), oxygen vacancy (V<sub>O</sub>), and two anti-site defects, Ti<sub>O</sub> and O<sub>Ti</sub>. Each of these defects has specific formation energies ( $\Delta H$ ) under titanium and oxygen rich growth conditions. Theoretical estimation of formation energies of anti-site and titanium vacancy defects are too high; as a result, they form merely under extreme conditions. However, formation energies of Ti<sub>i</sub> and V<sub>O</sub> defects are about 2-3 eV under Ti-rich (low oxygen partial pressure) growth condition,<sup>34</sup> so these defects form easily in TiO<sub>2</sub> and may be converted to each other via reaction 2-1. Here, six Ti-O bonds have to be broken to free a titanium atom, while only three to free an oxygen atom. In addition, the number of possible sites for V<sub>O</sub> is twice of that for Ti<sub>i</sub>.<sup>34</sup> Therefore, the formation of oxygen vacancies is energetically favorable than the introduction of a titanium atom into an interstitial site.<sup>35</sup>



When an oxygen vacancy forms, two  $\text{Ti}^{4+}$  cations must convert to two  $\text{Ti}^{3+}$  cations to preserve the charge neutrality of the crystal. In addition, the  $\text{Ti}_i$  neutral atom donates three or four electrons to the host crystal and transforms to  $\text{Ti}^{3+}$  or  $\text{Ti}^{4+}$  ions.<sup>36</sup> It has been theoretically shown that formation of  $\text{Ti}_i^{3+}$  is more probable and a neutral  $\text{Ti}_i$  placed in an interstitial cavity of titania spontaneously transforms into a  $\text{Ti}^{3+}$  ion with nearly one electron localized on the 3d shell.<sup>36</sup> Therefore, the reduction of  $\text{TiO}_2$  is accompanied by the appearance of  $\text{Ti}^{3+}$  species. The  $\text{Ti}^{3+}$  defects play an important role in the optical and chemical activities of the material. The deviation from stoichiometry has been generally considered in terms of oxygen non-stoichiometry. Concordantly, the formula of titanium oxide has been assumed as  $\text{TiO}_{2-x}$ .<sup>37,38</sup> This suggestion has been supported by gravimetric studies.<sup>39-41</sup> According to the present state of understanding, however,  $x$  is the apparent oxygen deficit which should be considered in terms of the defects in both cation and oxygen sublattices as well as Ti interstitials.<sup>37</sup> The titanium interstitial, whose charge state has been the subject of much controversy, is preferentially located at an unoccupied octahedral site adjacent to its original lattice site. Configurations in which the Ti atom moves in the  $\langle 100 \rangle$  or  $\langle 010 \rangle$  direction to form the defect are more favorable than those in which the Ti interstitial moves along the  $\langle 001 \rangle$  direction. The presence of the interstitial titanium atoms causes additional distortion of the octahedra within the unit cell. Due to the open structure of the rutile phase along the [001] direction, relatively small relaxations are found around the Ti

interstitial compared to the case of the oxygen vacancy. A first-principles study showed that the closest Ti atoms relax away from the interstitial site by 13% of the bulk Ti-O bond length, while the nearest four O atoms pull in toward the cation interstitial by 10 %. Slight (< 1% relative change from bulk bond distance) differences in oxygen and titanium atom relaxations surrounding Ti interstitials in the (+4) versus (+3) charge state are calculated.<sup>38</sup> According to the Kroger-Vink notations, the formation of these point defects in TiO<sub>2</sub> may be described by the following equilibria:<sup>42-44</sup>



Considering reactions 2-2 to 2-4, it can be concluded that oxygen pressure plays a significant role in the formation or removal of all point defects in TiO<sub>2</sub> crystalline structure. Regarding these reactions, the concentration of the lattice defects may be expressed as a function of p(O<sub>2</sub>) though the following reactions:<sup>45</sup>

$$[V_0] \propto p(O_2)^{-\frac{1}{2}} \quad (2-5)$$

$$[Ti_i^{3+}] \propto p(O_2)^{-1} \quad (2-6)$$

$$[Ti_i^{4+}] \propto p(O_2)^{-1} \quad (2-7)$$

Taking equations 2-5 to 2-7 into closer consideration, it can be suggested that lowering the growth oxygen partial pressure results in an increase of concentration of

point defects, as will be shown in chapters 4 and 7. The ionic defects are responsible for the formation of donor and acceptor levels in the electronic structure of  $\text{TiO}_2$ . As seen in Fig.2.5, both oxygen vacancies and titanium interstitials form donor levels and titanium vacancies form acceptors. The effect of these defects on the concentrations of electronic charge carriers depends on their ionization degree.<sup>46-48</sup>

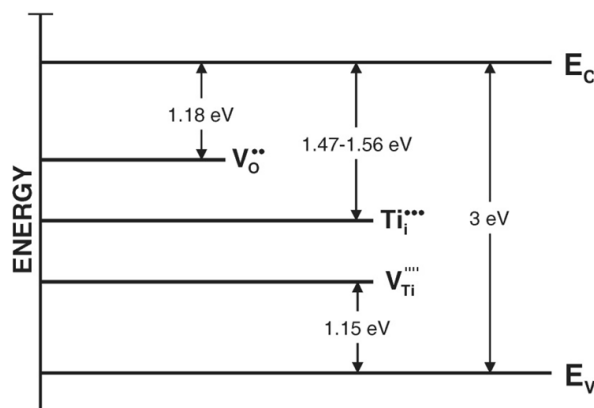


Fig.2.5. Band model of  $\text{TiO}_2$  showing the energy levels of intrinsic lattice defects.<sup>44</sup>

To touch briefly upon the defect chemistry in anatase versus rutile  $\text{TiO}_2$ , a recent paper addresses several features of the defect geometry in anatase that remain unexplored for rutile  $\text{TiO}_2$ . The three nearest-neighbor Ti atoms of the oxygen vacancy in anatase experience outward relaxations away from  $V_{\text{O}}^{2-}$  and towards its five remaining O neighbors.  $V_{\text{Ti}}^{-4}$ , a defect that arises in small concentrations, causes the surrounding O atoms to relax outwards substantially to a point halfway between their two remaining Ti neighbors. When  $Ti_i^{+4}$  is situated at an octahedral site, one vertical O neighbor moves towards the defect, while the surrounding Ti atoms relax outward as a

result of the electrostatic repulsion between positively charged Ti ions. In anatase  $\text{TiO}_2$ , the substitutional  $\text{O}_2$  molecule induces a small outward relaxation of the neighboring Ti atoms. The defect has a bond length of 1.46 Å, or about 21% greater than that of free  $\text{O}_2$ , 1.21 Å.<sup>38</sup>

## 2.2. Vanadium dioxide ( $\text{VO}_2$ )

### 2.1.1. Introduction

The strongly correlated electron systems exhibit fascinating behaviors such as high-temperature superconductivity, colossal magneto-resistance, exotic magnetic, charge and orbital ordering, and semiconductor-to-metal transition (SMT).<sup>49</sup> Vanadium dioxide ( $\text{VO}_2$ ) is one of the most attractive correlated electron systems exhibiting a distinct SMT at about 341 K (68 °C).<sup>50,51</sup> It belongs to the class of *smart materials*, which generally react to temperature variations, electric or magnetic fields, and pressure variations; thus, it has capabilities of sensing, actuating, and switching, relying on an intrinsic property of the material. This characteristic makes  $\text{VO}_2$  a promising candidate for novel electronics and electro-optic devices utilizing switches or memory elements. The mechanism behind the aforementioned SMT is a phase transformation from a monoclinic structure with semiconducting and infrared transparent characteristics to a tetragonal structure with metallic and infrared blocking properties. This phase transition is a reversible first order transformation taking place within about  $10^2$  femtoseconds.<sup>52-57</sup> It is worth mentioning that other vanadium oxides such as  $\text{VO}$ ,  $\text{V}_2\text{O}_3$ , and  $\text{V}_2\text{O}_5$  shows SMT at 125, 155, 530 K, respectively; however, the most outstanding

feature of  $\text{VO}_2$  is its near room-temperature transition.<sup>58-60</sup> As is shown in Fig.2.6, the semiconductor-to-metal transition in  $\text{VO}_2$  is characterized by abrupt orders of magnitude change in resistivity and increased reflectivity within the infrared region of spectrum ranging from 0.8 to 2.2  $\mu\text{m}$  where the SMT characteristics strongly depends on morphology, microstructure, defect content, strain, and doping.<sup>50,61</sup>

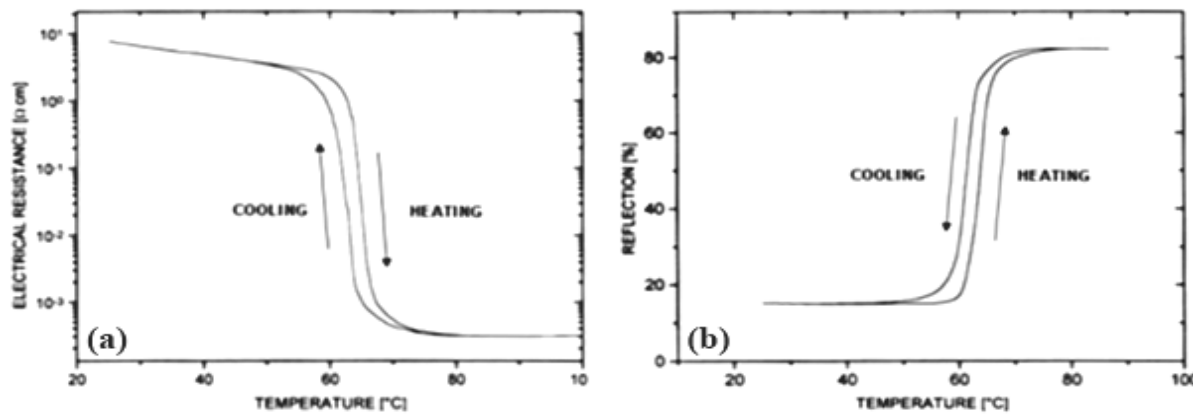


Fig.2.6. Hysteresis curves of: (a) resistance and (b) reflection during SMT of  $\text{VO}_2$ .<sup>84</sup>

In bulk  $\text{VO}_2$  crystals, the change in resistivity is of order  $\sim 10^3\text{-}10^5$ , with a hysteresis width of about  $1^{\circ}\text{C}$ . In thin films, hysteresis width may be in the range of  $10\text{-}15^{\circ}\text{C}$ , whereas in nanostructures it might be as broad as about  $30\text{-}35^{\circ}\text{C}$ . Even though the SMT characteristics of thin films and nanoparticles are not as favorable as those of bulk  $\text{VO}_2$ , thin films and nanostructures can better withstand the repeated thermal cycling. Meanwhile, their transition temperature can be tuned through microstructural manipulations.<sup>50,51,61-63</sup> It can be seen that there are as many as 15 to 20 other stable vanadium oxide phases, such as  $\text{V}_6\text{O}_9$ ,  $\text{V}_6\text{O}_{13}$ ,  $\text{V}_7\text{O}_{13}$  and others without any

semiconductor-to-metal transitions. Due to the formation of these rather stable compounds,  $\text{VO}_2$  only grows under a narrow range of oxygen pressure and temperature. Hence, growth of  $\text{VO}_2$  thin film is a challenge and it is necessary to elaborate an accurate synthesis procedure to ensure the formation of  $\text{VO}_2$  and to avoid formation of other undesirable vanadium oxides.<sup>61,64</sup> Under such circumstances, favorable SMT characteristics are achieved which open an avenue for new technological applications.

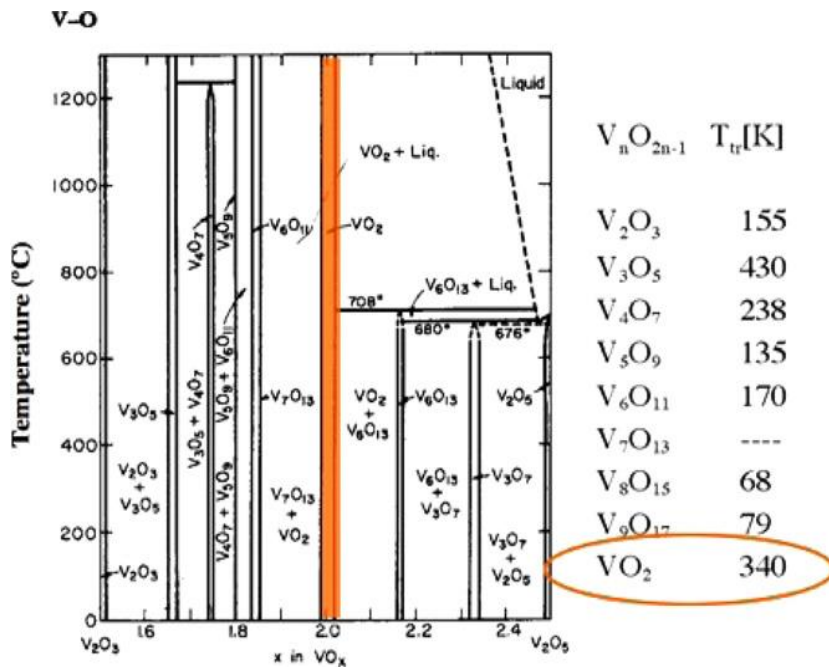


Fig.2.7. Phase diagram of the V-O system.<sup>64</sup>

### 2.2.2. Applications of $\text{VO}_2$ thin films

The large change in resistivity and transmittance/reflectivity during the SMT transition for  $\text{VO}_2$  occurs closer to room temperature than any other commonly-known

compounds and can also be conveniently depressed to about room temperature by microstructural and chemical manipulations.<sup>65</sup> In addition, VO<sub>2</sub> thin films are able to survive under the stress generated during repeated cycles of phase transformation<sup>66</sup> and are, therefore, suitable for various device applications including thermally activated thin films and nanoparticles for sensors and actuators,<sup>67-71</sup> optical switching<sup>72,73</sup>, beam limiting<sup>74</sup>, resistive switching<sup>75</sup>, thermal relays<sup>76</sup>, and energy management devices like solar cells<sup>77</sup> and smart windows<sup>78</sup>. VO<sub>2</sub> has been successfully employed in optical computing, variable reflectivity mirrors, light modulators, holographic recording media, high-speed solid-state optical displays, real-time coherent optical data processors, and fast random access scan lasers as well. VO<sub>2</sub> thin films also have potential applications in the millimeter-wave and microwave portions of the electromagnetic spectrum.<sup>79,80</sup>

### **2.2.3. Structural characteristics of VO<sub>2</sub>**

The SMT observed in VO<sub>2</sub> has its origin in a phase transformation from a high temperature tetragonal state to a low temperature monoclinic state. Across the transition temperature, changes in the electronic band structure are associated with atomic rearrangement between the more symmetric tetragonal (P4<sub>2</sub>/mnm) phase to the less symmetric monoclinic (P2<sub>1</sub>/c) phase. The lattice constants of tetragonal VO<sub>2</sub> are  $a=b=4.55 \text{ \AA}$  and  $c=2.87 \text{ \AA}$  and those for monoclinic VO<sub>2</sub> are  $a=5.743 \text{ \AA}$ ,  $b=4.517 \text{ \AA}$ ,  $c=5.375 \text{ \AA}$ , and  $\beta=122.6^\circ$ .<sup>50-52</sup> This VO<sub>2</sub> phase is called M<sub>1</sub>. Another monoclinic structure with different lattice parameters, called M<sub>2</sub>, can be possible upon light doping of VO<sub>2</sub>, application of a small uniaxial pressure, or peculiar synthesis condition.<sup>52</sup> The M<sub>2</sub> state

will be discussed in detail later on. The tetragonal and M<sub>1</sub> structures are shown in Fig.2.8.

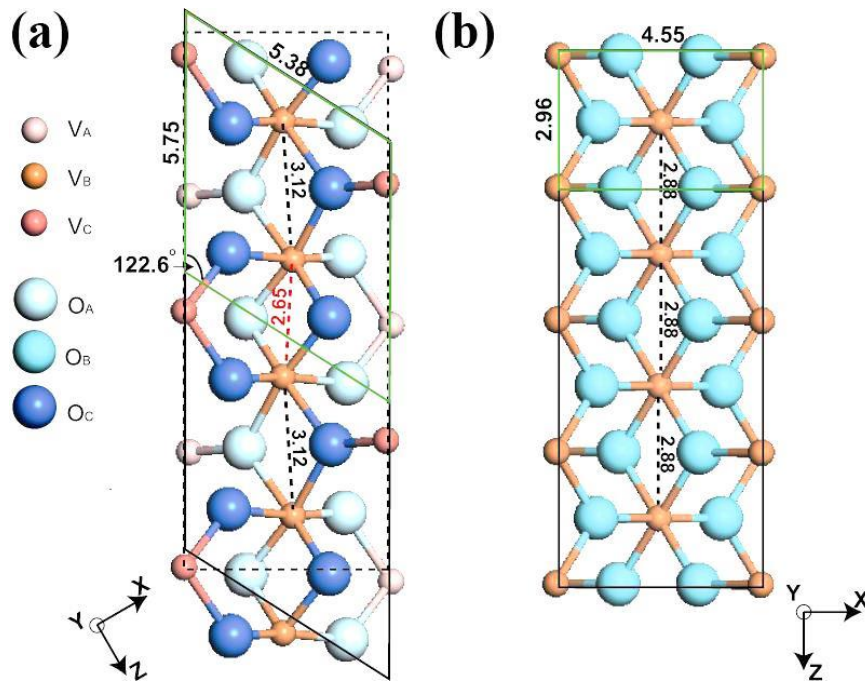


Fig.2.8. Illustration of crystallographic lattice of: (a) monoclinic (M<sub>1</sub>) and (b) tetragonal VO<sub>2</sub>.<sup>84</sup>

The key feature of the atomic rearrangement across the SMT is that monoclinic structure has the presence of V-V pairs along its *a*-axis where  $a_{\text{monoclinic}}=2c_{\text{tetragonal}}$ . During the phase transformation, the regular V-V separation of 0.287 nm in the tetragonal phase transforms to an alternate V-V separations of 0.265 nm and 0.312 nm leading to a doubling up of the unit cell. This is accompanied by a slight tilting with respect to the *c*-axis of the tetragonal structure to give one shortest vanadium-oxygen separation of 1.76 Å perpendicular to the tetragonal *c*-axis. The other cation-anion distance would be about 2 Å. The displacement of a cation toward one or more anions is

characteristic of a ferroelectric distortion. Thus, the driving mechanism responsible for this transition is an anti-ferroelectric one.<sup>81-84</sup> In addition to tetragonal and M<sub>1</sub> phases explained earlier, M<sub>2</sub> and T structures might form particularly upon doping. The lattice parameters of the M<sub>2</sub> monoclinic phase are a=9.06 Å, b=5.80 Å, c=4.25 Å, and β=91.8°.<sup>85</sup> These phases have been studies in the V<sub>1-x</sub>Cr<sub>x</sub>O<sub>2</sub> compound. The phase diagram of Cr-doped VO<sub>2</sub> by Pouget and Launois is shown in Fig.2.9. A similar phase diagram was also reported for the Al-doped VO<sub>2</sub> by Ghedira et al. As is observed, Cr-doped VO<sub>2</sub> enters the M<sub>2</sub> phase upon cooling through a first-order phase transition. On further lowering of the temperature, transition to the triclinic T phase occurs, followed by a first-order transition to the M<sub>1</sub> phase.<sup>52,81,86,87</sup>

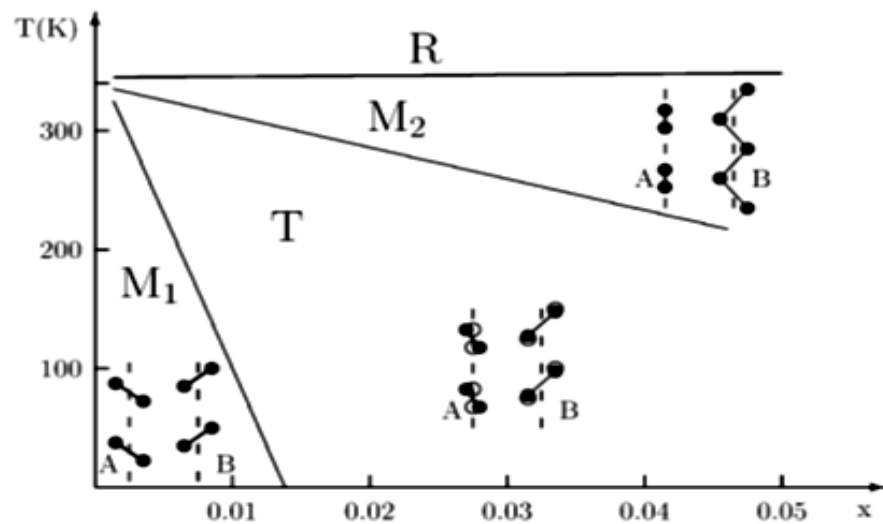


Fig.2.9. Phase diagram of the Cr-doped VO<sub>2</sub> system.<sup>81,84</sup>

The T phase is believed to be a triclinic lattice and is a transitional phase between M<sub>1</sub> and M<sub>2</sub>. This phase is sometimes called M<sub>3</sub>. The M<sub>2</sub> phase has a monoclinic lattice

which is different from  $M_1$  in that only half of the vertical (along  $c$ -axis) V-V chains are dimerized. In other words, V cations are displaced in the lateral (normal to the  $c$ -axis) direction so that the resulting vertical V chains have a zigzag pattern (Fig.2.10).<sup>81,84,88</sup>

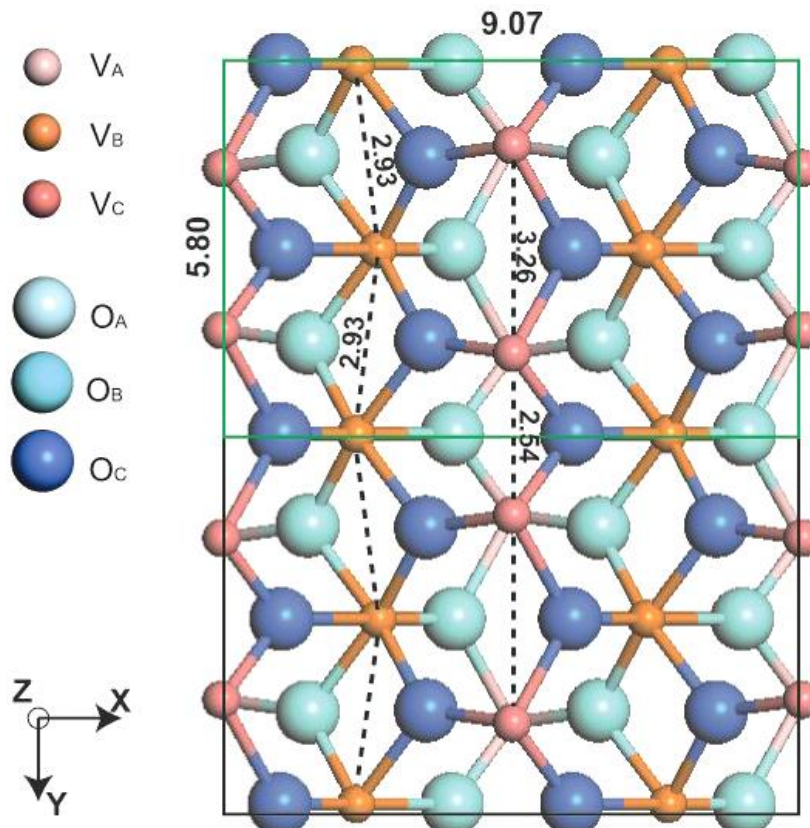


Fig.2.10. Crystallographic structure of the  $M_2$  monoclinic phase.<sup>84</sup>

The other half of vertical V chains in  $M_2$  remain straight, as it is in the metallic tetragonal phase. Uniaxial pressure applied to pure  $VO_2$  along  $[110]$  and  $[1\bar{1}0]$  directions can also give rise to  $M_2$  and T phases and leads to the phase diagram similar to that shown back in Fig.2.9.<sup>88</sup> Such uniaxial stress can be viewed as suppressing the zigzag-type displacements on those chains which have their tilting along the direction

of the applied stress, while the respective other chains are not affected. A study on electrical properties of M<sub>2</sub> and T showed that the conductivity changes only by 25% between the phases and both phases exhibit the same activation energy of 0.4 eV that is close to the activation energy in pure VO<sub>2</sub>, i.e. 0.45 eV. Therefore, the M<sub>2</sub> phase is regarded as a metastable modification of the M<sub>1</sub> phase, but the T phase appears as a transitional state exhibiting characteristics of both M<sub>1</sub> and M<sub>2</sub> phases. It has been pointed out that the critical uniaxial stress for appearance of the M<sub>2</sub> phase is so small that the free energies of the M<sub>1</sub> and M<sub>2</sub> phases in pure VO<sub>2</sub> must be extremely close at temperatures just below the SMT temperature.<sup>52,89</sup>

#### **2.2.4. Electronic characteristics of VO<sub>2</sub>**

The electronic band structure of VO<sub>2</sub>, in both tetragonal and monoclinic phase, was first explained quantitatively by Goodenough.<sup>83</sup> As shown in Fig.2.11, hybridization of V(3d) and O(2p) orbitals results in a distinct band structure which reflects the symmetry of atomic positions in the crystalline lattice. In the tetragonal state, the V atoms are surrounded by O-octahedral forming an edge-sharing chain along the [001] direction. The d-levels of the V ions are split into lower lying t<sub>2g</sub> states and e<sub>g</sub> states, as schematically illustrated in Fig.2.12. In this figure, the numbers in the parentheses are the number of degeneracy. The latter lie higher in energy and are empty. The e<sub>g</sub> orbitals are bridged by the O(2p) orbitals where the bonding assumes a σ-symmetry. The corresponding antibonding σ\* energy levels are positioned further away from the Fermi level.

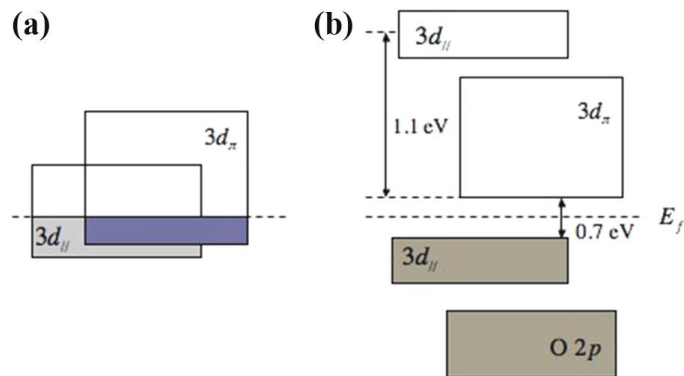


Fig.2.11. Schematic delineation of electron band structure of: (a) tetragonal and (b) monoclinic  $\text{VO}_2$ .<sup>83,84</sup>

The  $t_{2g}$  levels are grouped into the band  $\pi^*$  and  $d_{\parallel}$  that lie right near the Fermi level.<sup>90-92</sup> The  $d_{\parallel}$  orbitals are directed along the tetragonal  $c$ -axis with strong bonding of the V-V pair along this direction. In the monoclinic state, the pairing and tilting of the V atoms with respect to the tetragonal  $c$ -axis causes the splitting of the  $d_{\parallel}$  bands into bonding  $d_{\parallel}$  and antibonding  $d_{\parallel}^*$  bands and the shift of  $\pi^*$  band away from the Fermi level. Hence, a band gap opens between the top of  $d_{\parallel}$  and the bottom of  $\pi^*$ . The  $d_{\parallel}$  splitting, the optical band gap, and the rise of the  $\pi^*$  were determined to be 2.5, 0.7, and 0.5 eV, respectively.<sup>52,90-92</sup>

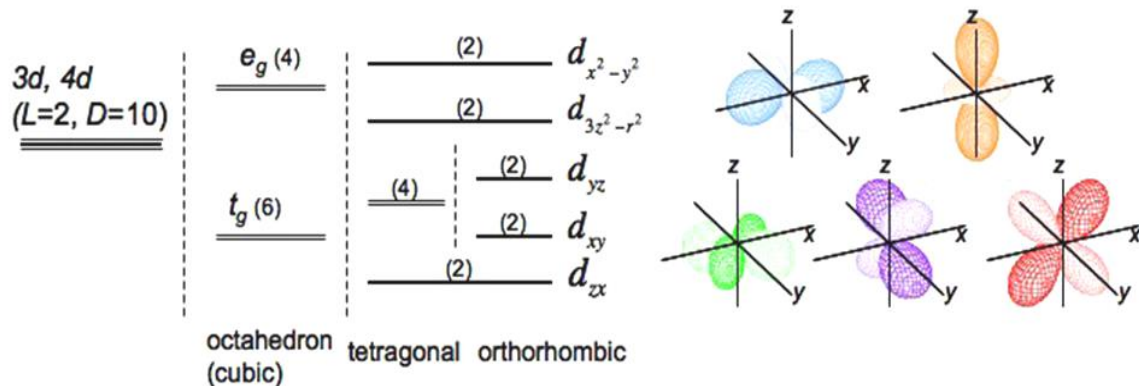


Fig.2.12.  $d$ -electron band splitting by crystal fields and their orbitals.<sup>83,84</sup>

### 2.2.5. Thermodynamic model of SMT in VO<sub>2</sub>

The change in Gibbs free energy associated with phase transition can be derived as  $\Delta G_r = \frac{\Delta T_r}{\Delta S_0}$ , where  $\Delta T_r$  is the deviation from the equilibrium transition temperature and  $\Delta S_0$  is the change in entropy between the two phases.<sup>51</sup> On the basis of the nucleation model, the critical size of a stable nucleus is derived as  $r_c = \frac{2\gamma}{\Delta T_r \Delta S_0}$ , where  $\gamma$  is the interfacial energy. It is known that tetragonal to monoclinic phase transformation in VO<sub>2</sub> is reversible and ultrafast ( $\sim 10^2$  femtoseconds). To model the phase transition, it is envisaged that a single coordinated atomic jump can accomplish monoclinic to tetragonal and reverse structural phase transformation. Using these concepts, the phase transition velocity is derived as  $V = \lambda v_D \left( \frac{\Delta T_r \Delta S_0}{k T_r} \right) \times \exp\left(-\frac{\Phi}{kT}\right)$ . In this equation,  $\lambda$  is jump distance,  $v_D$  is Debye frequency, and  $\Phi$  is the activation barrier. The activation barrier is about  $kT_r$ , where  $k$  is the Boltzmann constant and  $T_r$  is the transition temperature. Assuming  $\lambda = \sim 1 \text{ \AA}$ ,  $v_D = \sim 10^{12} \text{ sec}^{-1}$ , and  $\Phi = \sim kT_r$ , transformation velocity is estimated to be about 40 m.sec.<sup>-1</sup>. The application dictates the desired microstructure. For instance, for sensor applications, a large  $\Delta T$  and  $\Delta A$ , and a negligible  $\Delta H$  are required; thus, epitaxial films are preferred. The key considerations are related to the control of overall defect content and characteristics of the grain boundaries.<sup>51</sup> Using time-resolved, near-edge X-ray absorption measurements of the SMT, Cavalleri et al. estimated the monoclinic to tetragonal and reverse transformation velocities in thin films, which were found to be in complete agreement with this model. Based upon this model,  $\Delta T$ ,  $\Delta A$ , and  $\Delta H$  were predicted for different microstructures as follows:<sup>51</sup>

#### *2.2.5.1. Single-crystal films*

For high quality films with large grains separated by low angle ( $<1^\circ$ ) boundaries, the model predicts sharp transition (small  $\Delta T$ ) with a large amplitude ( $\Delta A$ ) and negligible hysteresis (very small  $\Delta H$ ). However, for poor quality films, i.e. small grains with high defect content, but still separated by low angle boundaries, the model predicts larger transition width without much hysteresis. The transition width can be controlled by defect content, and hysteresis width can be minimized by having low angle boundaries. This is the most suitable microstructure for sensor applications.<sup>51</sup>

#### *2.2.5.2. Textured polycrystalline films*

In the case of films with small angle boundaries, the SMT behavior would be similar to that of the high quality films with large grains separated by low angle boundaries, but with a finite  $\Delta T$ , and  $\Delta H$  will increase with the misorientation of small angle boundaries. For large angle boundary textured films, as the boundary misorientation increases,  $\Delta H$  will continue to increase.<sup>51</sup>

#### *2.2.5.3. Random polycrystalline films*

Films with small grains and large angle random boundaries will exhibit larger  $\Delta T$  and  $\Delta H$  with a smaller  $\Delta A$ . For the films having large grains, as the grain size increases, the  $\Delta T$  decreases as the bulk defect density decreases; however,  $\Delta H$  will stay constant or even increase with increasing grain boundary misorientation. This microstructure

will be suitable for memory device applications. Random polycrystalline films usually form onto amorphous substrates or nucleate from an amorphous phase.<sup>51</sup>

#### 2.2.5.4. Amorphous films

We can predict the properties of amorphous films by the equation:  $\Delta T_r = \frac{2\gamma}{r_c \Delta S_0}$ . In amorphous films,  $\gamma$ ,  $r_c$ , and  $\Delta S_0$  all tend to zero making  $\Delta T_r$  or hysteresis approach to zero. Thus, for those devices where reliability is critical, amorphous films can be used, even though it means sacrificing sensitivity and efficiency. In the case of amorphous films, the SMT is predicted to be large with a minimum of hysteresis, i.e. large  $\Delta T$  and very small  $\Delta H$ . The amplitude of transition will be smaller due to higher defect content. The absence of grain boundaries in amorphous films reduces  $\Delta H$  because the propagation of transition phase boundary upon heating and cooling remains symmetric. This transition in amorphous films is of second order and is less of a structural nature; that is, pairing of V atoms, unit cell doubling, and charge ordering are of less relevance. Amorphous characteristics emphasize the importance of Coulomb effects as the electrons diffuse more slowly and interact more strongly.<sup>51</sup>

### 2.3. Thin film epitaxy

Epitaxy represents an important concept observed in thin films and has its roots in two ancient Greek words: *επι* (*epi*-placed or resting upon) and *ταξιξ* (*taxis*-arrangement). In the context of thin films, epitaxy refers to the growth of an extended

single-crystalline film onto a crystalline substrate. The actual word epitaxy was introduced into the literature by the French mineralogist L. Royer in 1928, even though it was probably observed in alkali halide crystal over a century ago.<sup>93,94</sup> There are two large categories for epitaxy, namely homoepitaxy and heteroepitaxy. In the former, the film and the substrate are the same material. Epitaxial silicon films deposited on silicon wafers using vapor-phase epitaxy (VPE) is the most common example of homoepitaxy. In this case, the lattice parameters of the film and the substrate are the same, i.e. no misfit strain exists and there are no missing interfacial bonds. In the latter, the film and the substrates are different materials. In the heteroepitaxies, properties of the film mainly depend on the mismatch between the film and substrate lattice parameters, the difference in the film and substrate chemistry, and the difference in the thermal expansion coefficient of the film and the substrate. It is heteroepitaxy which is technologically of utmost importance, since it allows the growth of novel materials and devices in the form of epitaxial thin films on commonly available substrate systems. For example, compound semiconductor heteroepitaxial film structures have application in optoelectronic devices such as light-emitting diodes and lasers. Thin film growth in heteroepitaxial systems can occur via the formation of a coherently strained lattice.<sup>94-96</sup>

### **2.3.1. Sources of strains**

There are three primary sources of strains during the growth of thin film heterostructures: lattice misfit, thermal misfit, and dopant/impurity and defect related strains. These strains are additive during thin film growth process such that at the

growth temperature the lattice relaxation is determined by the total of lattice, thermal and microstructural defect strains.<sup>104</sup>

#### *2.3.1.1. Lattice misfit strains*

The lattice misfit strain arises when spacing of lattice planes, aligning across the film/substrate interface in a particular orientation, do not match. This mismatch is manifested in terms of the lattice strain. The strain is relaxed by dislocations which represent either an extra or a missing plane, depending upon compressive or tensile strain in the film. Hence, lattice planes play a dominant role during thin film growth and the lattice misfit is more correctly described by the planar misfit as the planes are aligned across the film/substrate interface.<sup>104</sup> Due to the mismatch in lattice constants, the epilayer grows pseudomorphically;<sup>95-97</sup> that is, it assumes the crystalline lattice of the substrate; as such, the epilayer becomes strained. With increase in thickness the strain energy in the system keeps increasing. Finally, dislocations or missing half planes are formed to relieve the built-in strain in the system. Because the film and the substrate materials are different in heteroepitaxy, the properties of heteroepitaxial films are influenced by the crystallographic properties of the substrate and the film, difference in film and substrate chemistry, and the difference in film and substrate thermal expansion coefficients.<sup>95</sup> The lattice misfit between substrate and film is the key parameter which controls growth, morphology, and the properties of the film. The lattice misfit is defined as:  $\epsilon = \frac{a_f}{a_s} - 1$ , where  $a_f$  and  $a_s$  are lattice parameters of the film and the substrate.

### *2.3.1.2. Thermal misfit strains*

Thermal misfit strain arises due to differences in thermal expansion coefficients of the film and the substrate. If the coefficient of thermal expansion of the film ( $\alpha_f$ ) is greater than that of the substrate ( $\alpha_s$ ), the film will have tensile stress after cooling down from the growth temperature. On the other hand, if  $\alpha_f < \alpha_s$ , the film will be under compression and the substrate under tension. Thermal misfit strain  $\epsilon_T$  in the film plane is given by  $\epsilon_T = (\alpha_s - \alpha_f)\Delta T$ , where  $\Delta T$  is the difference between the growth and the room temperatures and is negative during cooling down and positive during heating.<sup>104</sup> Corresponding thermal stress  $\sigma_T$  in the film is given by  $\sigma_T = 2(\alpha_s - \alpha_f)\Delta T \times \mu_f \frac{1+vf}{1-vf}$  where  $\mu_f$  and  $vf$  are the shear modulus and the Poisson's ratio of the film. Usually, small strains such as thermal strains are difficult to relax because of large critical thicknesses associated with them. This problem gets amplified in strongly bonded oxide and nitride materials, where dislocation nucleation and propagation steps are difficult. Strains accumulate with thickness and large unrelaxed tensile strains ( $\alpha_f > \alpha_s$ ) can lead to cracking and delamination above a certain thickness, where accumulated stress can exceed the fracture stress. Residual compressive stresses can be managed easier.<sup>104</sup>

### *2.3.1.3. Microstructural and defect related strains*

These strains are associated with grown-in dislocations, point defects (vacancies and interstitials), and their clusters. For doped and alloyed materials, dopant distribution and lattice relaxation around dopants will lead to additional misfit strains. It is well known that boron in silicon leads to tensile stress due to its smaller size than

the host material; on other hand, Ge and Sb in Si result in compressive stress. This strain is quite sensitive to processing variables and growth kinetics which determine lattice location, clustering, and annealing of defects. In certain cases, particularly in oxides and nitrides, the planar/lattice misfit can be accommodated by the presence of defects without generating misfit dislocations. The defect strains are also related to chemical strains and stabilization of pseudomorphic metastable phases.<sup>104</sup>

### **2.3.2. Lattice matching epitaxy**

The strains across the interface can be relaxed via two different mechanisms, namely lattice matching epitaxy and domain matching epitaxy. The former is discussed here and the latter is discussed in section 2.3.3. In lattice matching epitaxy (LME), one-to-one matching of the lattice parameters of the film and substrate takes place at the interface. In other words, unit cells of the films and the substrate match with one another. This matching of lattice parameters takes place by means of strain in the films and up to some extent in the substrate as the films initially grow pseudomorphically. The pseudomorphic growth of the film continues until a critical thickness is reached. At this point, strain energy becomes large enough to trigger the nucleation of dislocation to relax the strain. These dislocations are nucleated at the film surface and must glide to the interface to relieve the misfit stain in the film. The mechanism behind lattice matching epitaxy is presented in Fig.2.13 where the crystalline lattice of the film and the substrate before growth, after pseudomorphic or coherent growth below the critical

thickness, and formation of dislocation or missing half planes beyond the critical thickness are schematically illustrated.

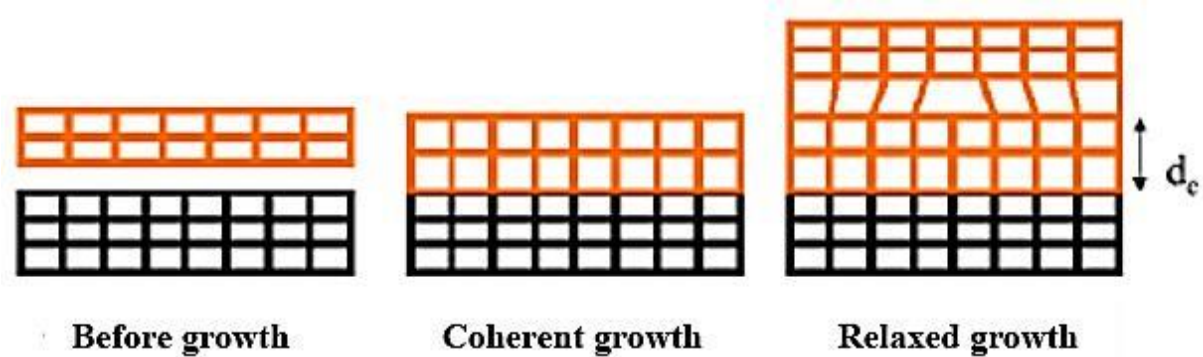


Fig.2.13. Schematic illustration of lattice matching epitaxy.<sup>98</sup>

The critical thickness is denoted as  $d_c$  in this figure. The critical thickness at which dislocation nucleation occurs is directly related to the misfit. In low misfit systems the critical thickness for dislocation nucleation may be quite large and dislocation nucleation and, therefore, strain relaxation may not be possible. Meanwhile, the obstacles to the glide of dislocations often gives rise a high threading dislocation density in the films, which is detrimental to the device properties. The reason behind this suggestion is that these dislocations act as charge carrier trap or recombination centers.<sup>95-97</sup> The critical thickness is the thickness at which the misfit strain energy stored in the system exceeds the energy of misfit dislocations; as a consequence, the system prefers to accommodate dislocations to minimize the free energy. It is worth mentioning that the stored strain energy is proportional with the thickness of the film. For the thicknesses below the critical thickness, the strain energy is smaller than the

energy of misfit dislocations; therefore, the misfit dislocations are not generated and, hence, the system remains under strain.

### 2.3.3. Domain matching epitaxy

Conventional lattice matching epitaxy during thin film growth is possible as long as the lattice misfit between the film and the substrate is less than 7-8%. Beyond this misfit, it was expected that the films grow only as textures or largely polycrystalline. However, the epitaxial growth was also observed in large misfit systems where the misfit strain is far beyond 7-8% regime. Since the strain across the film/substrate interface is relaxed by dislocations which are essentially an extra plane or a missing plane, the epitaxial growth in large misfit systems can be explained by considering the matching of lattice planes in the concept domain matching epitaxy (DME). In the domain matching epitaxy, we consider the matching of lattice planes which could be in different directions of the film/substrate interface. This is in contrast to the lattice matching epitaxy where one-to-one matching of lattice constants occurs. Strain relaxation by the misfit dislocations is schematically explained in Fig.2.14.<sup>95</sup> An important feature of the domain matching epitaxy is that most of the misfit strain is relaxed quickly within a couple of monolayers so that the misfit strain and dislocations can be engineered and confined near the interface. In large misfit systems, the critical thickness is very small; hence, the dislocations nucleate in first couple of monolayers to relieve the strain making it possible for the rest of the film to grow free of lattice strains. It is important to note that at misfit strains larger than 8%, the critical thickness is less

than a monolayer. The atomic steps formed within the second monolayer provide nucleation sites for the dislocations. At the initial steps of the growth, there are a lot of steps onto the surface of the film making the nucleation of the misfit dislocations easy. The dislocations have to propagate only a monolayer to reach the film/substrate interface. In contrast, in low misfit systems, the dislocations nucleate only after the critical thickness is reached and must, then, glide across the critical thickness to the interface. This process results in the formation of half loops that are composed of two threading segments and a straight segment along the interface.<sup>95,99-101</sup> The burgers vector and planes of the misfit dislocation are governed by the active slip systems and glide planes are determined by the crystal structure of the film. It is worth mentioning that thermal and defect stains still exist. In domain matching epitaxy, misfit is accommodated by matching of integral multiples of lattice planes, and there is an extra half plane corresponding to each domain, as shown in Fig.2.14. If the misfit falls in between the perfect matching ratios of planes, then the size of the domain can vary in a systematic way to accommodate the additional misfit.<sup>95</sup>

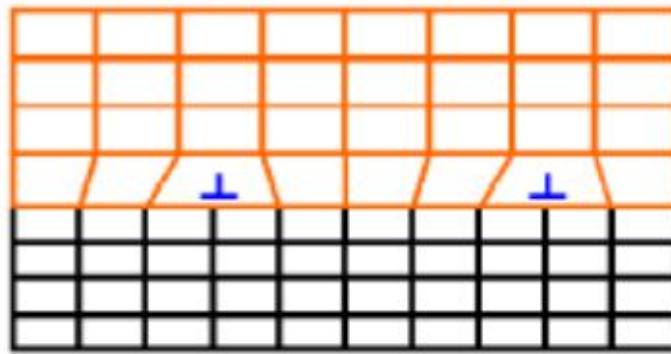


Fig.2.14. Schematic illustration of domain matching epitaxy.<sup>98</sup>

The interface structure and the nature of dislocations in the ZnO/sapphire heterostructure are depicted in Fig.2.15. The epitaxial relationship between the ZnO thin film and the sapphire substrate was established as  $(0001)_{\text{ZnO}}|| (0001)_{\text{sapphire}}$  and  $[2\bar{1}\bar{1}0]_{\text{ZnO}}|| [1\bar{1}00]_{\text{sapphire}}$ . In other words, ZnO(10\bar{1}1) planes rotate by 30° with respect to sapphire(01\bar{1}2) planes. In this system, the misfit strain was calculated to be about 15.44%. To accommodate such a large strain, 5/6 and 7/6 domains should alternate across the film/substrate interface.<sup>102</sup> Fig.2.16 displays the *h*-GaN/sapphire interface demonstrating matching of integral multiples of lattice planes. As is seen, there is one dislocation contained in each domain. This figure shows alternating of 6/7 and 7/8 film/substrate planes matching across the interface, which is in agreement with the paradigm of domain matching epitaxy for the formation of single-crystal films on substrates with large lattice misfits. According to the DME paradigm, for a complete relaxation of misfit strain, three 6/7 domains should alternate with one 7/8 domain.<sup>103</sup>

In summary, dislocations are involved in thin film relaxation and detailed TEM studies clearly established that nucleation of dislocations at the free surface and propagation of these dislocations to the interface are critical steps in the relaxation process of thin films.<sup>95,99,104-106</sup> The dislocations represent largely either missing planes under compressive stress, where planar spacing of the film is larger than that of the substrate, or extra planes under tensile stress. In either case, thin film relaxation involves matching of atomic columns. However, if the film and substrate orientations remain the same, which is often the case for small misfit systems, then, lattice matching will occur. The important point to remember is that lattice matching results as a

consequence of matching of the planes. It should be also pointed out that in cases where Burgers vectors of dislocations match with lattice vectors, lattice and planar matching will be indistinguishable.<sup>95</sup>

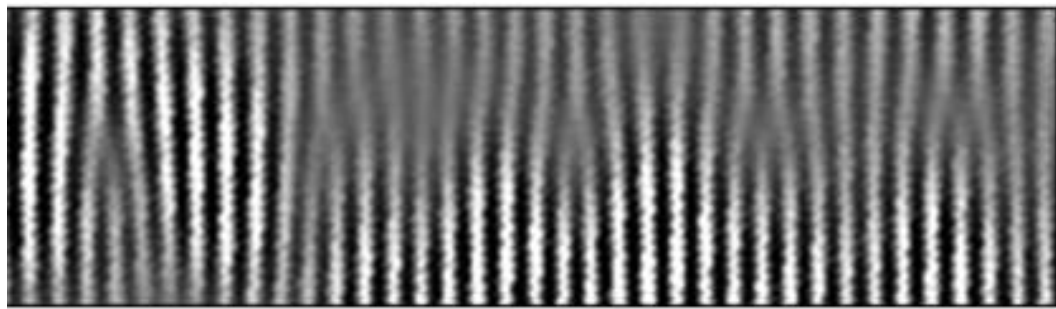


Fig.2.15. High-resolution TEM cross-section image obtained from ZnO/sapphire interface.<sup>102</sup>

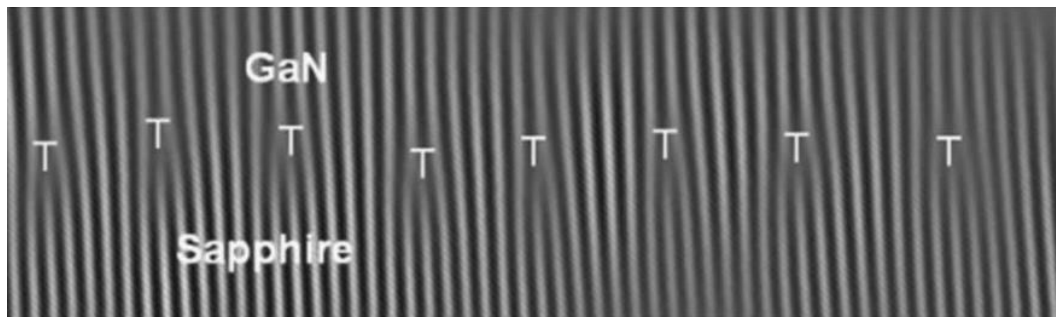


Fig.2.16. High-resolution TEM cross-section image of GaN epilayer grown on sapphire substrate.<sup>103</sup>

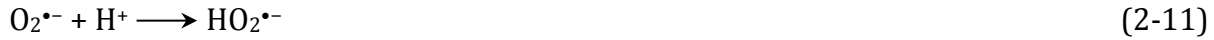
## 2.4. Photocatalytic reactions

Photocatalysis is a special kind of catalysis where the material is activated by light. The following mechanism for degradation of environmental pollutants over a semiconductor photocatalyst (SP) has been proposed. First, the semiconductor is illuminated. The wavelength of the light should be shorter than that of the

semiconductor absorption edge; the light energy should be higher than the band gap energy of semiconductor. The electrons and holes are generated:<sup>107,108</sup>



Afterward, the photo-generated electron-hole pairs chemically react with the adsorbed water and oxygen molecules as below:



These processes are schematically depicted in Fig.2.17. The  $OH^{\cdot}$  and  $O_2^{\cdot-}$  radicals, generated through the above reactions, are very active and have a high oxidizing power. These radicals can attack the pollutant molecules and decompose them to nonhazardous species. They can also attack the bacteria cells and kill them.<sup>108,109</sup>

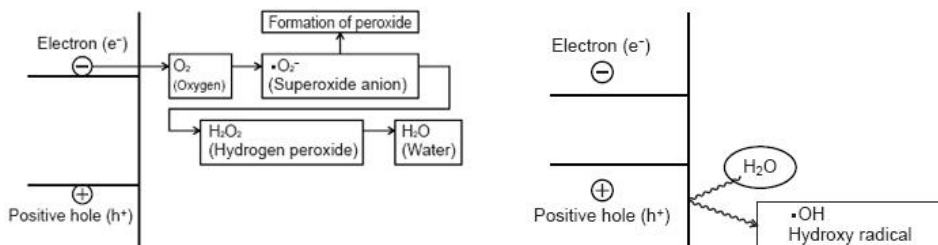


Fig.2.17. Schematic illustration of the photocatalytic reactions.

## References

1. A. Fujishima, X. Zhang, and D.A. Tryk, *Surf. Sci. Rep.* 63, 515 (2008).
2. X. Hou and K.L. Choy, *Mater. Sci. Eng. C* 25, 669 (2005).
3. C.S. Enache, J. Schoonman, and R. Krol, *Appl. Surf. Sci.* 252, 6342 (2006).
4. A. Fujishima and X. Zhang, *C. R. Chimie* 9, 750 (2006).
5. H. Zhang and J.F. Banfield, *J. Phys. Chem. B* 104, 3481 (2000).
6. M.R. Ranade, A. Navrotsky, H.Z. Zhang, J.F. Banfield, S.H. Elder, A. Zaban, P.H. Borse, S.K. Kulkarni, G.S. Doran, and H.J. Whitfield, *Proc. Nat. Acad. Sci.* 99, 6476 (2002).
7. M.S. Nahar, J. Zhang, K. Hasegawa, S. Kagaya, and S. Kuroda, *Mater. Sci. Semicond. Process.* 12, 168 (2009).
8. G.B. Song, J.K. Liang, F.S. Liu, T.J. Peng, and G.H. Rao, *Thin Solid Films* 491, 110 (2005).
9. A. Fahmi, C. Minot, B. Silvi, and M. Causa, *Phys. Rev. B: Condens. Matter.* 47, 11717 (1993).
10. S. Qiu and S.J. Kalita, *Mater. Sci. Eng. A* 435-436, 327 (2006).
11. R. Roy and W.B. White, *J. Cryst. Growth* 13/14, 78 (1972).
12. N. Sbai, J. Perriere, W. Seiler, and E. Millon, *Surf. Sci.* 601, 5649 (2007).
13. T. Bak, J. Nowotny, N.J. Sucher, and E. Wachsman, *J. Phys. Chem. C* 115, 15711 (2011).
14. D. Yoo, I. Kim, S. Kim, C. Hahn, C. Lee, and S. Cho, *Appl. Surf. Sci.* 253, 3888 (2007).
15. Y.Q. Hou, D.M. Zhuang, G. Zhang, M. Zhao, and M.S. Wu, *Appl. Surf. Sci.* 218, 97 (2003).
16. M.R. Bayati, F. Golestani-Fard, and A.Z. Moshfegh, *Appl. Catal. A* 382, 322 (2010).

17. M.R. Bayati, A.Z. Moshfegh, and F. Golestani-Fard, *Electrochim. Acta* 55, 3093 (2010).
18. R. Vinu and G. Madras, *J. Indian Inst. Sci.* 90, 189 (2010).
19. S.D. Burnside, V. Shklover, C. Barbe, P. Comte, F. Arendse, K. Brooks, and M. Gratzel, *Chem. Mater.* 10, 2419 (1998).
20. R. Hengerer, B. Bolliger, M. Erbudak, and M. Gratzel, *Surf. Sci.* 460, 162 (2000).
21. Y. Liang, S. Gan, S.A. Chambers, and E.I. Altman, *Phys. Rev. B* 63, 235402 (2001).
22. N. Ruzycki, G.S. Herman, L.A. Boatner, and U. Diebold, *Surf. Sci.* 529, L239 (2003).
23. B. Xi, L.K. Verma, J. Li, C.S. Bhatia, A.J. Danner, H. Yang, and H.C. Zeng, *ACS Appl. Mater. Interfaces* 4, 1093 (2012).
24. M.N. Chong, B. Jin, H. Zhu, and C. Saint, *J. Photochem. Photobiol. A: Chem.* 14, 1 (2010).
25. Q. Gu, J. Long, Y. Zhou, R. Yuan, H. Lin, and X. Wang, *J. Catal.* 289, 88 (2012).
26. S. Yuan, R. Mao, Y. Li, Q. Zhang, and H. Wang, *Electrochim. Acta* 60, 347 (2012).
27. K. Zhu, Q. Wang, J.H. Kim, A.A. Pesaran, and A.J. Frank, *J. Phys. Chem. C* 116, 11895 (2012).
28. W. Guo, C. Xu, X. Wang, S. Wang, C. Pan, C. Lin, and Z.L. Wang, *J. Am. Chem. Soc.* 134, 4437 (2012).
29. P. Murugan, R.V. Belosludov, H. Mizuseki, T. Nishimatsu, T. Fukumura, M. Kawasaki, and Y. Kawazoe, *J. Appl. Phys.* 99, 08M105 (2006).
30. A.Y. Ahmed, T. Oekermann, P. Lindner, and D. Bahnemann, *Phys. Chem. Chem. Phys.* 14, 2774 (2012).
31. C. Lu and Z. Chen, *Sens. Actuators B* 140, 109 (2009).

32. K.T. Lin and J.M. Wu, JPN. J. Appl. Phys. 43, 232 (2004).
33. M. Ramamoorthy, D. Vanderbilt, and R.D. King-Smith, Phys. Rev. B 49, 16721 (1994).
34. S. Na-Phattalung, M.F. Smith, K. Kim, M.H. Du, and S.H. Wei, Phys. Rev. B 73, 125205 (2006).
35. E. Cho, S. Han, H.S. Ahn, K.R. Lee, S.K. Kim, and C.S. Hwang, Phys. Rev. B: Condens. Matter 73, 193202 (2006).
36. E. Finazzi, C.D. Valentin, and G. Pacchioni, J. Phys. Chem. C 113, 3382 (2009).
37. T. Bak, J. Nowotny, M. Rekas, and C.C. Sorrell, J. Phys. Chem. Solids 64, 1057 (2003).
38. E.G. Seebauer and M.C. Kratzer, Charged Semiconductor Defects Structure, Thermodynamics and Diffusion, London: Springer (2009).
39. D.K. Lee, J.I. Jeon, M.H. Kim, W. Choi, and H.I. Yoo, J. Solid State Chem. 178, 185 (2005).
40. J.B. Moser, R.N. Blumenthal, and D.H. Whitmore, J. Am. Ceram. Soc. 48, 384 (1965).
41. P. Kofstad, J. Phys. Chem. Solids 23, 1579 (1962).
42. F.A. Kroger, The Chemistry of Imperfect Crystals, North Holland: Amsterdam (1974).
43. M.K. Nowotny, T. Bak, and J. Nowotny, J. Phys. Chem. B 110, 16270 (2006).
44. M.K. Nowotny, L.R. Sheppard, T. Bak, and J. Nowotny, J. Phys. Chem. C 112, 5275 (2008).
45. T. Bak, J. Nowotny, M. Rekas, and C.C. Sorrell, J. Phys. Chem. Solids 64, 1057 (2003).
46. D.C. Cronemeyer, Phys. Rev. 113, 1222 (1959).
47. A.K. Ghosh, F.G. Wakim, and R.R. Addiss, Phys. Rev. 184, 979 (1969).

48. F.M. Hossain, G.E. Murch, L.R. Sheppard, and J. Nowotny, *Adv. Appl. Ceram.* 106, 95 (2007).
49. M. Imada, A. Fujimori, and Y. Tokura, *Rev. Mod. Phys.* 70, 1039 (1998).
50. F.J. Morin, *Phys. Rev. Lett.* 3, 34 (1959).
51. J. Narayan and V.M. Bhosle, *J. Appl. Phys.* 100, 103524 (2006).
52. D. Ruzmetov and S. Ramanathan, *Thin Film Metal Oxides: Fundamentals and Applications in Electronics and Energy*, New York: Springer (2010).
53. W. Burkhardt, T. Christmann, S. Franke, W. Kriegseis, D. Meister, B. K. Meyer, W. Niessner, D. Schalch, and A. Scharmann, *Thin Solid Films* 402, 226 (2002).
54. F. Beteille and J. Livage, *J. Sol Gel Sci. Tec.* 13, 915 (1998).
55. P. Jin and S. Tanemura, *Jpn. J. Appl. Phys., Part 1* 34, 2459 (1995).
56. C.N. Berglund and A. Jayaraman, *Phys. Rev.* 185, 1034 (1969).
57. A. Cavalleri, T. Dekorsy, H.H.W. Chong, J.C. Kieffer, and R.W. Schoenlein, *Phys. Rev. B* 70, 161102 (2004).
58. H. Zhan, V. Astley, M. Hvasta, J.A. Deibel, and D.M. Mittleman, *Appl. Phys. Lett.* 91, 162110 (2007).
59. G. Stefanovich, A. Pergament, and D. Stefanovich, *J. Phys.: Condens. Matter* 12, 8837 (2000).
60. V.S. Vikhnin, S. Lysenko, A. Rua, F. Fernandez, and H. Liu, *Solid State Comm.* 137, 615 (2006).
61. J. Nag and R.F. Haglund, *J. Phys. C: Condens. Matter* 20, 264016 (2008).
62. R. Lopez, L. C. Feldman, and R.F. Haglund, *Phys. Rev. Lett.* 93, 177403 (2004).

63. R. Lopez, T.E. Haynes, L.A. Boatner, L.C. Feldman, and R.F. Haglund, Phys. Rev. B 65, 224113 (2002).
64. C.H. Griffith and H. K. Easwood, J. Appl. Phys. 45, 2201 (1974).
65. J. Macchesn and H. Guggenhe, J. Phys. Chem. Solids 30, 225 (1969).
66. A. Gupta, R. Singhal, J. Narayan, and D.K. Avasthi, J. Mater. Res. 26, 2901 (2011).
67. J.W. Byon, M.B. Kim, M.H. Kim, S.Y. Kim, S.H. Lee, B.C. Lee, and J.M. Baik, J. Phys. Chem. C 116, 226 (2012).
68. R.T. Kivaisi and M. Samiji, Sol. Energy Mater. Sol. Cells 57, 141 (1999).
69. B.J. Kim, Y.W. Lee, B.G. Chae, S.J. Yun, S.Y. Oh, H.T. Kim, and Y. S. Lim, Appl. Phys. Lett. 90, 023515 (2007).
70. R.T.R. Kumar, B. Karunagaran, D. Mangalaraj, S.K. Narayandass, P. Manoravi, M. Joseph, and V. Gopal, Sens. Actuators A: Phys. 107, 62 (2003).
71. B. Hu, Y. Ding, W. Chen, D. Kulkarni, Y. Shen, L.V. Tsukruk, and Z.L. Wang, Adv. Mater. 22, 5134 (2010).
72. Y. Zhang, Y. Huang, J. Zhang, W. Wu, F. Niu, Y. Zhong, X. Liu, X. Liu, and C. Huang, Mater. Res. Bull. 47, 1978 (2012).
73. Y. Zhang, M. Fan, X. Liu, G. Xie, H. Li, C. Huang, Solid State Commun. 152, 253 (2012).
74. S.H. Chen, H. Ma, X.J. Yi, T. Xiong, H.C. Wang, and C.J. Ke, Sens. Actuators A: Phys. 115, 28 (2004).
75. R.H. Walden, IEEE Trans. Electron Devices ED17, 603 (1970).
76. M. Soltani, M. Chaker, E. Haddad, R. Kruzelecky, and J. Margot, J. Vac. Sci. Technol. A 25, 971 (2007).

77. R.K. Karn, M. Misra, O.N. Srivastava, Int. J. Hydrogen Energy 25, 407 (2000).
78. K. Kato, P.K. Song, H. Odaka, Y. Shigesato, Jpn. J. Appl. Phys. 42, 6523 (2003).
79. W.R. Roach, Appl. Phys. Lett. 19, 453 (1971).
80. J.S. Chivian, M.W. Scott, W.E. Case, and N.J. Krasutsky, IEEE J. Quantum Electron. 21, 383 (1985).
81. V. Eyert, Ann. Phys. (Leipzig) 11, 650 (2002).
82. Crystallography Open Database Information Card 9009089.
83. J.B. Goodenough, J. Solid State Chem. 3, 490 (1971).
84. J. Nag, Ph.D. dissertation, University of Tennessee Nashville (2011).
85. J.D. Budai, A. Tselev, J.Z. Tischler, E. Strelcov, A. Kolmakov, W.J. Liu, A. Gupta, and J. Narayan, Acta Mater. 61, 2751 (2013).
86. M. Ghedira, H. Vincent, M. Marezio, and J.C. Launay, J. Solid State Chem. 22, 423 (1977).
87. M. Ghedira, J. Chenavas, and M. Marezio, J. Phys. C: Solid State Phys. 10, L309 (1977).
88. J.P. Pouget, H. Launois, T.M. Rice, P. Dernier, A. Gossard, G. Villeneuve, and P. Hagenmuller, Phys. Rev. B 10, 1801 (1974).
89. A. Zylbersztein and N.F. Mott, Phys. Rev. B 11, 4383 (1975).
90. S. Biermann, A. Poteryaev, A.I. Lichtenstein, and A. Georges, Phys. Rev. Lett. 94, 026404 (2005).
91. A. Cavalleri, M. Rini, H.H.W. Chong, S. Fourmaux, T.E. Glover, P.A. Heimann, J.C. Kieffer, and R.W. Schoenlein, Phys. Rev. Lett. 95, 067405 (2005).

92. S. Shin, S. Suga, M. Taniguchi, M. Fujisawa, H. Kanzaki, A. Fiujimori, H. Daimon, Y. Ueda, K. Kosuge, and S. Kachi, Phys. Rev. B 41, 4993 (1990).
93. L. Royer, Bull. Soc. Fr. Mineral. 51, 7 (1928).
94. M. Ohring, The Materials Science of Thin Films, Boston: Academic Press (1992).
95. J. Narayan and B.C. Larson, J. Appl. Phys. 93, 27 (2003).
96. J.W. Mathews, J. Vac. Sci. Technol. 12, 126 (1975).
97. J.W. Mathews and A.E. Blakeslee, J. Cryst. Growth 27, 118 (1974).
98. G. Trichy, Ph.D. dissertation, North Carolina State University (2008).
99. J. Narayan and S. Sharan, Mater. Sci. Eng. B10, 261 (1991).
100. F.K. LeGoues, M.C. Reuter, J. Tersoff, M. Hammer, and R.M. Tromb, Phys. Rev. Lett. 73, 300 (1994).
101. J. Narayan, P. Tiwari, X. Chen, J. Singh, R. Chowdhury, and A.T. Zheleva, Appl. Phys. Lett. 61, 1290 (1992).
102. P. Pant, J.D. Budai, R. Aggarwal, R.J. Narayan, and J. Narayan, J. Phys. D: Appl. Phys. 42, 105409 (2009).
103. J. Narayan, P. Pant, A. Chugh, H. Choi, and J.C. Fan, J. Appl. Phys. 99, 054313 (2006).
104. J. Narayan, Acta Mater. 61, 2703 (2013).
105. S. Sharan and J. Narayan, J. Appl. Phys. 66, 2376 (1989).
106. K. Jagannadham and J. Narayan, J. Mat. Sci. Eng. A 113, 65 (1989).
107. A. Fujishima and K. Honda, Nature 238, 37 (1972).
108. G.A. Somorjai, Introduction to Surface Science and Catalysis, New York: Wiley (1994).

109. C. Guillard, D. Debayle, A. Gagnaire, H. Jaffrezic, and J.M. Herrmann, Mater. Res. Bull. 39, 1445 (2004).

## Chapter 3

# Experimental Techniques

### 3.1. Substrates and buffer layers

#### 3.1.1. Silicon

One of the substrates used in this study was single-side polished Si(100) wafers. Silicon is a group VI elemental semiconductor. As shown in Fig.3.1, crystalline silicon has a diamond structure with a lattice constant of 5.43072 Å. The diamond structure can be thought of as the union of two superimposed face centered cubic crystal lattices where one is displaced by a quarter of the length of the unit cell in the [100], [010], and [001] directions. Each silicon atom has four valence electrons that it shares to form tetrahedral covalent bonds with its neighbors. The thermal expansion coefficient and band gap of silicon are about  $2.6 \times 10^{-6} \text{ K}^{-1}$  and 1.12 eV at room temperature, respectively. Most of the commercial electronic devices are currently based on silicon. Both *n*-type and *p*-type silicon substrates with different doping concentration are available. Owing to the natural abundance and large scale industrial use, silicon substrates are widely and cheaply available. Hence the integration of new functional materials with silicon substrate offers unique technological advantage. Silicon substrates are available in large sizes (up to 400 mm diameter). One of the biggest challenges in integration of epitaxial films with silicon is the tendency of silicon to

readily form an oxide ( $\text{SiO}_x$ ) layer which is amorphous and prevents epitaxial or even textured growth.<sup>1,2</sup>

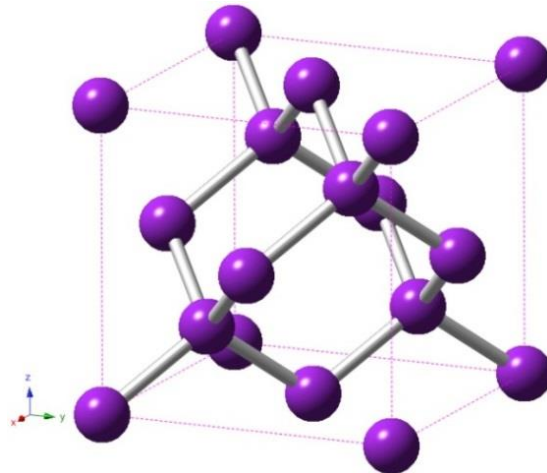


Fig.3.1. Diamond cubic lattice of silicon.

### 3.1.2. Sapphire (Aluminum oxide)

In the present work, in addition to the silicon substrates, sapphire substrates with varying crystallographic orientations were used for thin film deposition as well. Sapphire ( $\text{Al}_2\text{O}_3$ ) is an ionic solid and has a rhombohedral/hexagonal crystalline structure which belongs to the space group of  $\text{R}\bar{3}\text{C}$ . The lattice structure of the hexagonal unit cell consists of close packed planes of oxygen, alternating with a hexagonal array of aluminum planes. The aluminum planes are in hexagonal close packed arrangement, with one third of the sites vacant. The vacant sites produce the  $2/3$  stoichiometric ratio of Al/O in sapphire. The aluminum planes are arranged with the aluminum vacancies ordered with a three-fold symmetry axis along the [0001] direction. The lattice constants of  $\text{Al}_2\text{O}_3$  hexagonal unit cell are  $a=4.7587 \text{ \AA}$  and

$c=12.9929 \text{ \AA}^3$  Sapphire is an insulator with a band gap of about 9 eV at room temperature. The thermal expansion coefficients of sapphire are  $6.2 \times 10^{-6}$  and  $7.07 \times 10^{-6} \text{ K}^{-1}$  along its  $a$ -axis and  $c$ -axis, respectively. Due to its stability up to  $\sim 1100^\circ\text{C}$ , transparency, hexagonal symmetry, ease of handling, and simple pre-growth cleaning, sapphire has been one of the most commonly used substrates for the thin films growth and device fabrication. There are four common face terminations of sapphire, namely  $c$ -plane ( $0006$ ),  $r$ -plane ( $1\bar{1}02$ ),  $m$ -plane ( $1\bar{1}00$ ), and  $a$ -plane ( $2\bar{1}\bar{1}0$ ). The lattice structures and important crystallographic planes of sapphire are depicted in Fig.3.2.<sup>4,5</sup>

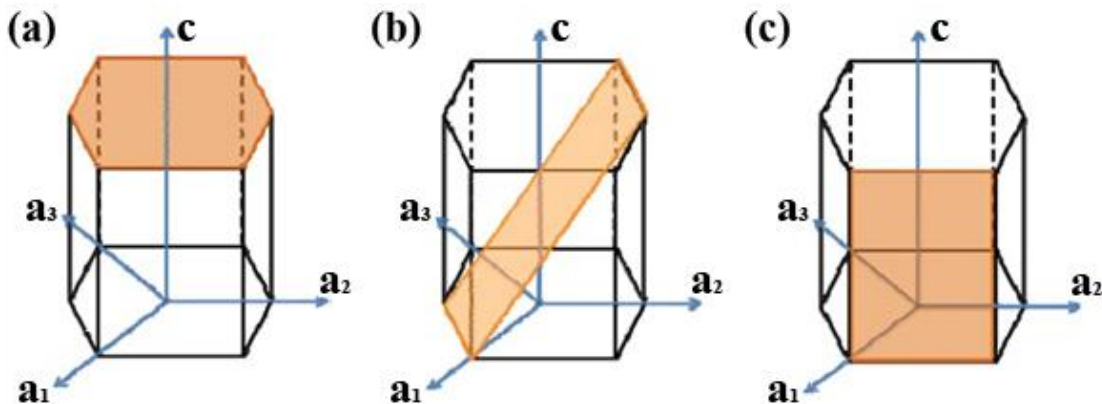


Fig.3.2. Delineation of several crystallographic planes of sapphire:

(a)  $c$ -plane, (b)  $r$ -plane, and (c)  $m$ -plane.

### 3.1.3. Yttria-stabilized zirconia

Direct growth of epilayers on silicon is a technological challenge owing to the formation of the native amorphous  $\text{SiO}_x$  layer leading to growth of polycrystalline and textured thin films. Yttria-stabilized zirconia (YSZ) buffer was used to efficiently destroy and remove the  $\text{SiO}_x$  layer from the silicon substrates prior to the thin film

deposition. YSZ is an attractive buffer layer for the subsequent growth of numerous oxide materials on non-oxide substrates. It has excellent chemical stability on silicon. The thermal expansion coefficient of YSZ is about  $11.4 \times 10^{-6}$  K<sup>-1</sup>. YSZ has a high dielectric constant and large band gap of about 25 and 7.8 eV, respectively. Basically, pure zirconia ( $\text{ZrO}_2$ ) has a monoclinic lattice (Fig.3.3a), but the tetragonal and cubic phases of zirconia can be stabilized at room temperature through combining with other oxides.<sup>6,7</sup>

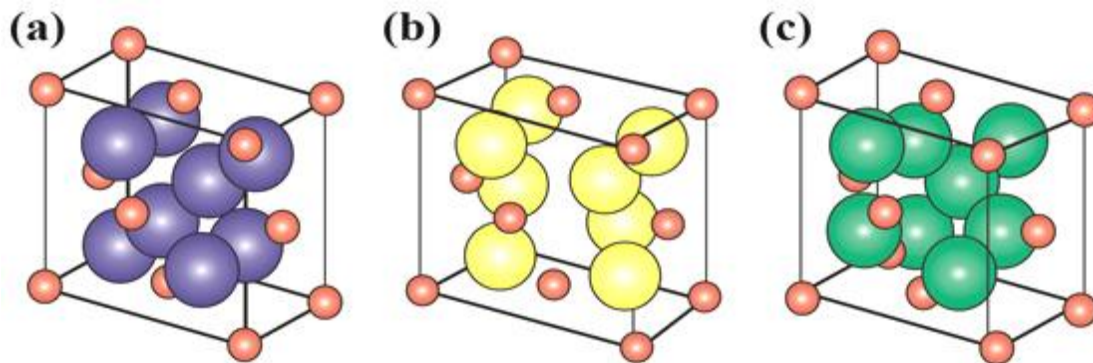


Fig.3.3. Crystal structure of zirconia: (a) monoclinic, (b) tetragonal, and (c) cubic structures.<sup>7</sup>

Different oxides, such as yttrium oxide ( $\text{Y}_2\text{O}_3$ ), calcium oxide ( $\text{CaO}$ ), or magnesium oxide ( $\text{MgO}$ ), can be added to zirconia as a stabilizer. For instance, the tetragonal state would be stabilized at room temperature by doping with 3 to 5 mol.% of yttria. Lattice parameters of tetragonal YSZ which belongs to the  $\text{P}4_2/\text{nmc}$  space group are  $a=3.6067$  Å and  $c=5.1758$  Å (for 3 mol.% yttria-doped  $\text{ZrO}_2$ ). A unit cell of tetragonal YSZ is shown in Fig.3.3b. Yttria content of 8 mol.% or higher makes cubic phase of zirconia stable at room temperature. Cubic YSZ has a fluorite-type structure with the space group  $\text{Fm}\bar{3}\text{m}$ .

Its lattice parameter is 5.1289 Å (for 15 mol.% yttria-doped ZrO<sub>2</sub>). A unit cell of the cubic YSZ is displayed in Fig.3.3c.<sup>6,7</sup>

### 3.2. Thin film growth

Pulsed laser deposition (PLD) was employed to grow thin film heterostructures in this project. It was first realized in 1965 and was first used for VO<sub>2</sub> deposition by Borek et al. in 1993.<sup>8</sup> PLD is a versatile non-equilibrium technique for thin film growth which is based on physical vapor deposition. It is a comparatively recent inclusion in the world of thin film deposition and is especially suited for oxide growth. This technique involves the use of a high-powered laser beam to vaporize the target material to be deposited. This phenomenon is frequently referred to as laser ablation. The ablated material is ejected in a direction normal to the target surface in the form of a plume and is deposited as a film onto a substrate facing the target. This process can occur in ultrahigh vacuum or in the presence of a background gas such as oxygen which is commonly used when depositing oxides. Laser-assisted growth was first demonstrated by Smith et al.<sup>9</sup> in 1965 using a high power ruby laser. In 1983, Cheung et al.<sup>10</sup> successfully synthesized epitaxial Hg<sub>0.7</sub>Cd<sub>0.3</sub>Te/CdTe and CdTe/GaAs using PLD. Later in the decade, in 1987, Dijkkamp et al.<sup>11</sup> and Narayan et al.<sup>12</sup> demonstrated the growth of YBa<sub>2</sub>Cu<sub>3</sub>O<sub>7</sub> superconducting thin films on sapphire. Since then, PLD has been widely used to synthesize a variety of high quality thin films of metals, oxides, and nitrides. Recently, PLD has probably become the most popular technique for the deposition of VO<sub>2</sub> thin films.<sup>7,13-17</sup> Fig.3.4 displays the schematic of a typical PLD configuration which

simply consists of three main components, namely the laser, the vacuum chamber, and the optic system controlling the laser beam. Various lasers have been used for pulsed laser deposition of thin films, namely ruby, CO<sub>2</sub>, Nd:YAG, and excimer lasers. The latter one is the most widely used due to the fact that these lasers can deliver high energy densities by high energy photons. During PLD, the laser is directed into the vacuum chamber and focused onto the target by a set of lenses and mirrors. The vacuum chamber houses the target holder, the substrate holder, and the gauges. The focused laser beam interacts with the target surface creating a luminous plasma plume. The ejected species comprising the plume consists of high-energy atoms, electrons, molecules, free radicals and sometimes clusters, particulates and molten globules.<sup>18</sup> These species form the film onto a substrate facing the target (Fig.3.4).

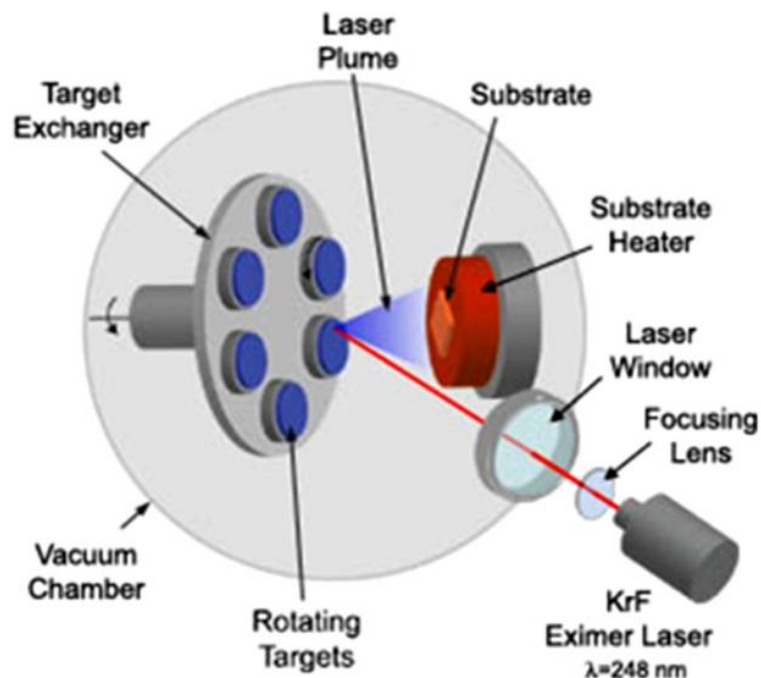


Fig.3.4. Schematic illustration of a typical PLD chamber.

### **3.2.1. Advantages and disadvantages of PLD**

Several advantages associate with PLD make it a powerful and outstanding thin film deposition technique compared to other methods. Most advantages arise owing to the high energy of the ablated species which can be as high as 10 to 100 eV (i.e. about  $10^2\text{-}10^3$  kT). For the sake of comparison, the energy of the ejected species in thermal or electron evaporation techniques is about 0.1 eV at 1200 K. Following are other positive aspects of the PLD technique:

1. The high energy of the plume makes PLD a highly non-equilibrium processing technique by which complex metastable phases can be formed which would otherwise be difficult to form by equilibrium synthesizing routes.<sup>19,20</sup>
2. In case of a multi-component system, such as YBCO<sup>11</sup>, the high energy of the plume leads to reproducing the stoichiometry of the target in the film. The forward directed nature of the plume in PLD is responsible for preserving the stoichiometry. Due to the high energy density of the laser, the material removal from the target is very fast such that vapor pressures of the individual components do not play a role.<sup>19,20</sup>
3. The high energy of the plume reduces processing temperatures. In other words, high quality films can be deposited at lower temperatures.<sup>19,20</sup> For instance, epitaxial TiN can be grown on Si(100) at temperatures below 600 °C by PLD.<sup>21</sup> However, CVD growth of TiN requires temperatures as high as about 1000 °C.<sup>22</sup>
4. Multi-layered thin film heterostructures can be easily synthesized by using PLD. The target carousel can be suitably manipulated to hold multiple targets. This enables us to deposit multi-layered films without breaking the vacuum.<sup>19,20</sup>

5. Conceptually, any material can be ablated to form a thin film as long as it has a large enough absorption coefficient for the laser used.<sup>18</sup>

6. Depending on the repetition rate of the laser beam, the deposition rate of the film can be tuned. In fact, in PLD, the number of nucleation sites can be controlled such that they are much higher than those formed in MBE or sputter deposition. By controlling the impingement rate and the nucleation site density, the surface roughness of the film can be manipulated.<sup>18-20</sup>

7. It is important to realize that in the PLD system, the sputtering agent, namely the laser beam, is placed externally. Therefore, there is no need to inject any sputtering agent or other precursors to the deposition chamber unlike what should be done in chemical vapor deposition, atomic layer deposition, magnetron sputtering, and some other techniques. The vacuum chamber in itself is devoid of filaments and other sources of contamination, thereby resulting in a clean processing environment.<sup>18</sup>

8. The interaction between the laser and gas species in the vacuum chamber is minimal. This means that the dynamic range of deposition pressures can be high, resulting in less stringent vacuum requirements. Meanwhile, the spatial confinement of laser-solid interaction and the subsequent plume render PLD a clean process. The deposited films are thus relatively contamination free.<sup>18</sup>

On the other hand, PLD suffers from some disadvantages. The area of deposited material obtained by PLD is relatively small (typically 1 cm × 1 cm). In the case of large substrates, uniformity in film thickness is observed due to the forward directed nature of the plume.<sup>18</sup> Deposition on larger substrates and uniformity of film thickness can be

achieved to some extent by rastering the laser beam over a large target and/or rotation and translation of the substrate.<sup>23</sup> The other important drawback of PLD is the formation of chunks during ablation, which are detrimental to the quality of the film. Chunks are nothing but large (few microns) particulates or globules of molten material. These undesirable chunks are formed due to improper ablation that involves various mechanisms such as subsurface boiling, expulsion of the liquid layer by shock wave recoil, and exfoliation. By careful manipulation of the laser parameters, the size and number of chunks can be minimized to some extent. Chunk control is also possible by increasing the absorption coefficient and thermal conductivity of the target material. A compact target with better cohesion of the grains reduces the emission of chunks.<sup>18-20,24</sup>

### **3.2.2. Physics of the laser-solid interaction**

Even though the PLD system in itself is easy to build and operate, the underlying physics involving the laser-solid interaction is quite complex. At energy densities above the threshold for vaporization the laser solid interaction has been analyzed and modeled by Singh et al.<sup>19,20</sup> Depending upon the interaction of the laser with the target material, they divided the laser ablation process into three important regimes:

#### *3.2.2.1. Laser-solid interaction*

Interaction of the laser beam with the bulk target results in evaporation of the surface layers. This regime can be also termed as the evaporation regime. When the laser beam strikes the target, the electromagnetic energy is used to excite free electrons

in the target material. The thermal energy generated by the electron-phonon coupling, then, evaporates the target material. It is important to realize that the reaction time for this process to occur is on the order of picoseconds.<sup>18-29</sup> In order to have better laser-solid coupling, the target must be suitably prepared. A target with high roughness, low reflectivity ( $R$ ), and high absorption coefficient ( $\alpha_t$ ) allows for efficient laser-solid coupling and, thus, provides low threshold energy for vaporization. Depending on the laser wavelength and the porosity and surface roughness of the target, typical values of threshold energy vary from 0.11 to 0.40 J.cm<sup>-2</sup>.<sup>20</sup> It is important to notice that the energy deposited by the laser beam comprises, the energy required to evaporate the target material, conduction heat loss in the target, and energy loss due to laser absorption by the expanding plasma. Using these concepts of energy balance, the thickness of the target for which evaporation ( $\Delta X_t$ ) takes place can be calculated through the following equation:<sup>19,20</sup>

$$\Delta X_t = (1 - R)(E - E_{th}) / (\Delta H + C_v \Delta T) \quad (3-1)$$

Where  $R$  is the reflectivity,  $E_{th}$  is the threshold energy,  $\Delta H$  is the latent heat,  $C_v$  is the volume heat capacity, and  $\Delta T$  is the maximum rise in temperature. It is important to realize that this equation is valid when the thermal diffusion length  $(2Dt)^{1/2}$  is larger than the light penetration depth ( $L = \alpha_t^{-1}$ ). Here,  $D$  is the thermal diffusion constant and  $t$  is the pulse duration of the laser. This validation is true for most metallic and semiconducting targets. However, for low thermal diffusivity materials (non-metallic

targets), where  $(2Dt)^{1/2}$  is smaller than  $\alpha_t^{-1}$ , a second regime is prevailing. Here, thermal diffusivity does not play an important role and evaporation depth mainly depends on the attenuation distance of the laser beam.<sup>18-20</sup>

### *3.2.2.2. Plasma formation and initial isothermal expansion*

The interaction of the laser beam with the evaporated material leads to the formation of a high temperature isothermal expanding plasma. This regime prevails when the target starts to evaporate and continues until the end of the pulse. The laser interaction with the target material yields surface temperatures in the range of 2000-3200 K. This results in the emission of positive ions and electrons from the free surface. Generally, the ablation of the target is accompanied by the formation of a plasma extending normal to the target surface which contains charged and neutral species of atoms and molecules. The plasma also interacts with the incoming laser; this produces temperatures higher than the vaporization temperature in the plasma. The absorption of laser energy by the plasma occurs due to electron-ion collisions. This absorption primarily occurs by an inverse Bremsstrahlung process that involves absorption of a photon by a free electron.<sup>19,20</sup> The absorption coefficient ( $\alpha_p$ ) of the plasma is given as:

$$\alpha_p = 3.69 \times 10^8 (Z^3 n_i^2 / T^{1/2} v^3) [1 - \exp(-\frac{hv}{kT})] \quad (3-2)$$

Where, Z is the average charge,  $n_i$  is the ion density, T is the temperature of the plasma, h is Planks constant, K is the Boltzmann constant, and v is the free energy of the

laser light. Since the absorption coefficient ( $\alpha_p$ ) is proportional to  $n_i^2$ , the laser light is heavily absorbed close to the target surface where the density of the ionized species is high. In comparison, the leading edge of the plume is associated with high expansion velocities and low electron and ion densities. Hence, the outer edge of the plasma is transparent to the laser beam. The  $[1 - \exp(-\frac{hv}{kT})]$  term represents the losses due to stimulated emission depending upon the plasma temperature and laser wavelength. A variety of processes such as impact ionization, photo ionization, thermal ionization, and electronic ionization affect the extent of ionization of the laser generated species. Fig.3.5 schematically illustrates the different regimes present during the laser-solid interaction.<sup>19,20</sup>

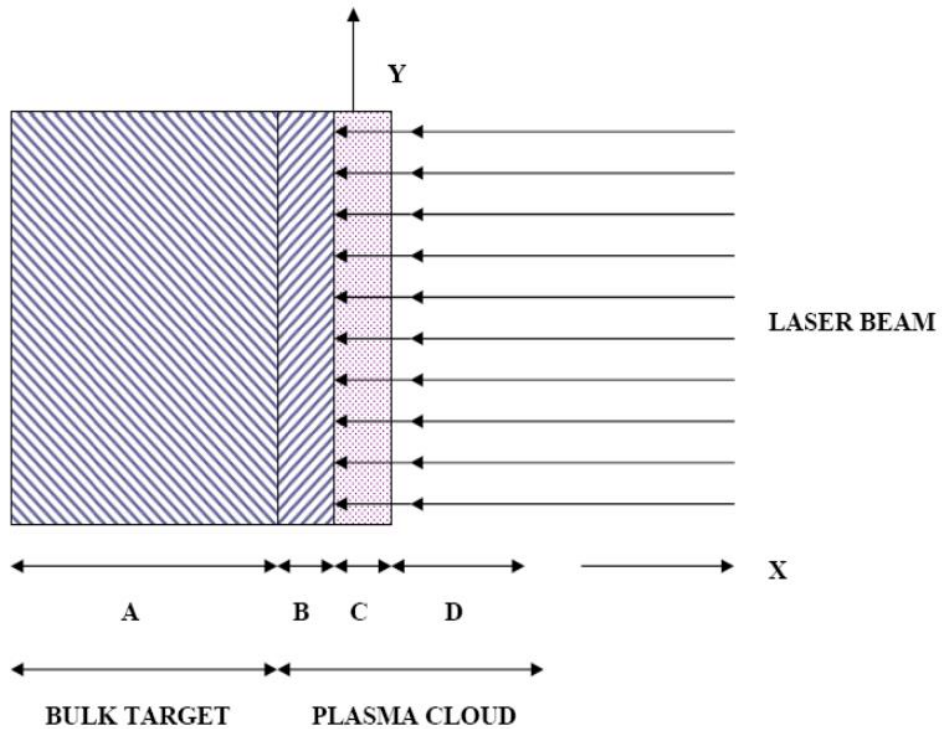


Fig.3.5. Different regimes during laser irradiation of the target.<sup>19,25</sup>

In this figure, region “A” represents the unaffected zone of the bulk target, region “B” shows the evaporated section of the target material, region “C” shows the zone where the plasma absorbs the laser heavily. In this region, evaporated particles are continuously injected into the plasma. Finally, region “D” represents the rapidly expanding plasma which is transparent to the laser. In the region, near the target surface, a dynamic self-regulating equilibrium exists between the plasma absorption coefficient and the rapid transfer of thermal energy into kinetic energy due to injection of evaporated particles of the target into the plume. These mechanisms govern the isothermal temperature attained by the plasma near the target surface.<sup>19,20,25</sup>

### *3.2.2.3. Adiabatic expansion of the plasma*

The anisotropic three-dimensional adiabatic expansion of the plume gives rise to the characteristic forward directed nature of the deposition. It is worth noticing that this regime starts right after the termination of the laser pulse. After the plasma formation and isothermal regime, the plasma plume expands adiabatically into the vacuum. It is important to realize that, in this regime, there is no injection of particles from the target into the plume and also the laser is no longer being absorbed by the plume. In this regime, the expanding plasma is associated with very high velocities arising from the thermal energy being converted to the kinetic energy. The loss in thermal energy leads to a drop in temperature determined by a balance between cooling due to expansion and energy gain due to recombination of ions in the plasma. Fig.3.6 shows a schematic of the developing shape of the plume in adiabatic regime. As

is observed in Fig.3.6, the initial dimensions of the plasma are larger in the transverse directions, i.e. along the Y and Z directions. In the longitudinal X-direction the expansion is minimal. It is also important to note that the plasma is elliptically shaped with y-axis being the major axis. During the adiabatic expansion regime, the longitudinal x-dimension expands rapidly resulting in the characteristic PLD plume. The plasma pressure drops rapidly until most of the thermal energy is converted to kinetic energy. Then, the plume has no more energy for expansion and the plasma elongates in the shorter dimension. Eventually, an elliptical shape is retained but with the z-dimension being the major axis.<sup>19,20</sup>

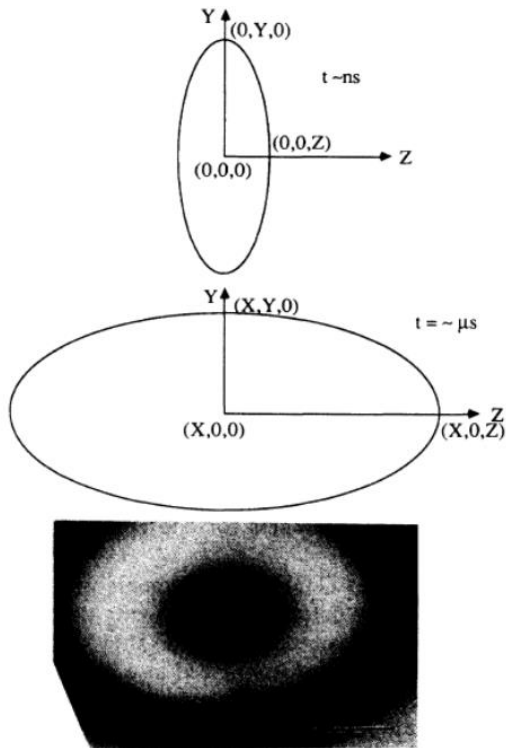


Fig.3.6. (a) The initial elliptical shape of the plasma after the laser pulse is terminated, (b) Final shape of the plasma when it hits the substrate, and (c) Shape of a YBCO film deposited on a Si substrate.<sup>20</sup>

### 3.2.3. Lasers used for PLD

The term LASER stands for light amplification by stimulated emission of radiation. A laser emits coherent light with a well-defined wavelength in a narrow low divergent beam. The most important lasers used for PLD are the Nd:YAG<sup>19,20</sup> and the excimer laser.<sup>26-29</sup> Nd:YAG is a solid state neodymium doped yttrium aluminum garnet laser. The fundamental frequency for this laser is 1064 nm. These lasers can be doubled, tripled, or quadrupled to produce 532, 355, and 262 nm wavelengths. The more popular laser used for PLD is the excimer laser which uses a combination of an inert gas and a reactive gas. Typically the inert gases used are Argon, Krypton, and Xenon. The reactive gases frequently used are fluorine and chlorine. The excimer lasers are pulsed and operate in the ultraviolet range. They operate with pulse duration in the nanosecond regime and repetition rates up to 100 Hz. They can have output energy as high as 1 J/pulse. Various excimer lasers and their wavelengths are listed in Tab.3.1.

Tab.3.1. Operating wavelengths of several excimer lasers.

Excimer Laser	KrF	ArF	KrCl	F <sub>2</sub>	Cl <sub>2</sub>	XeCl	KeF
Wavelength (nm)	248	193	222	157	259	308	351

The term excimer is a short form of excited dimer. The excited state is formed from the inert gas that forms temporarily bound molecules either with themselves or the halide. The excited state is usually induced by an electric discharge. The excited state then gives up its energy via stimulated emission to form the dissociated ground

state molecules. This happens very rapidly within a picoseconds period resulting in a population inversion between the excited and ground state molecules. The reactions forming a KrF excimer laser are as following:<sup>25</sup>



In this study, a Lambda Physik KrF excimer laser (LPX200) with a wavelength of 248 nm and pulse duration of 25 ns was employed to ablate the high purity targets for thin film depositions and laser annealing of the samples as well.

### **3.3. Characterization techniques**

In order to study characteristics and properties of the PLD grown heterostructures, various characterization techniques were used which are briefly described in the following:

#### **3.3.1. Crystalline structure**

X-ray diffraction (XRD) was employed to determine the crystalline structure and in-plane and out-of-plane orientations of the heterostructures. The XRD technique is based on the diffraction governed by the Bragg's law ( $n\lambda=2dsin(\theta)$ ). The diffraction takes place providing that this law is satisfied.<sup>30</sup> When an X-ray beam is incident on a crystal, it interacts with the parallel plane of atoms either constructively or

destructively depending on the path difference. Bragg's law is satisfied when the waves interfere constructively. In the present work,  $\theta$ - $2\theta$  scans were performed using a Rigaku SmartLab diffractometer with Cu-K $\alpha$  radiation at a wavelength of 0.154 nm. This machine was employed to determine the phase structure and the out-of-plane orientation of the films. However, this measurement does not provide any information on the epitaxial growth and the in-plane crystallographic alignment across the interfaces.

The in-plane orientation and the epitaxial relationship, in this project, were accessed by  $\varphi$ -scan XRD done by a Philips X'Pert diffractometer having a Cu-K $\alpha$  X-ray source. In addition to rotation along the  $\theta$ -axis, in four-circle diffractometers, the sample can be tilted with respect to the incident beam ( $\psi$ -axis) and rotated by 360° around the surface normal ( $\varphi$ -axis). Using this geometry, the in-plane epitaxial details can be established by scanning along the  $\varphi$ -axis. In order to perform  $\varphi$ -scan, an appropriate crystallographic plane inclined to the growth plane needs to be selected. The  $2\theta$  angle is set at the corresponding Bragg angle of the selected plane. Then, the sample is tilted along the  $\psi$ -axis by an angle equal to the crystallographic angle between the growth plane and the plane selected for the  $\varphi$ -scan. The diffraction intensity is then recorded as a function of the sample rotation along the  $\varphi$ -axis. If the film is epitaxial, the  $\varphi$ -scan exhibits sharp peaks at certain  $\varphi$ -angles. On the other hand, if the in-plane orientation of the film is random, no appreciable variation in the diffraction intensity is observed in the  $\varphi$ -scan XRD.

The  $\theta$ ,  $\varphi$ , and  $\psi$  axes are seen in the schematic in Fig.3.7.

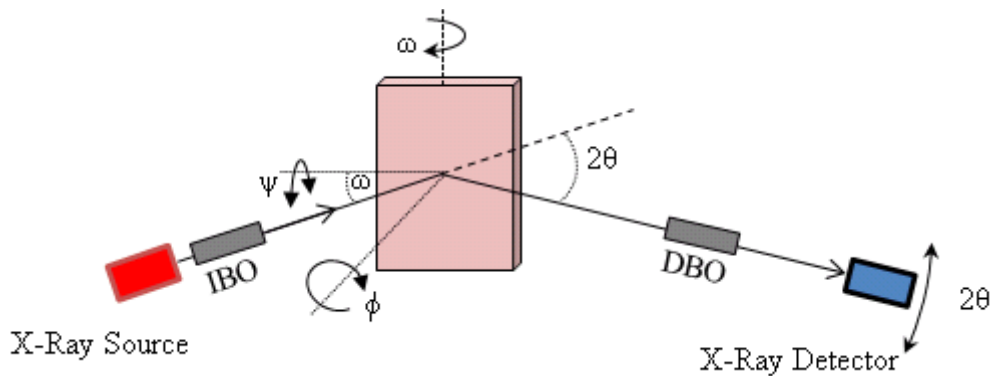


Fig.3.7. A schematic diagram showing  $\theta$ ,  $\varphi$ , and  $\psi$  axes

### 3.3.2. Stoichiometry

X-ray photoelectron spectroscopy (XPS) is a powerful quantitative spectroscopic technique to determine the chemical composition and stoichiometry of the surface and the depths smaller than 10 nm. It can detect all elements with concentrations higher than 0.1 – 1 % except hydrogen and helium. The chemical or oxidation state of one or more of the elements in the sample can be assessed by this technique. In XPS, X-Ray irradiation of a material under ultra-high vacuum (UHV) leads to the emission of electrons from the core orbitals of the surface elements present in the top 10 nm of the material to be analyzed. The binding energy of the emitted photoelectron can be determined from the following equation:

$$hv = KE + BE + \Phi_s \quad (3-5)$$

where,  $hv$  is the energy of the incident radiation,  $KE$  is the kinetic energy of the photoelectron as measured by the instrument,  $BE$  is the binding energy of the orbital

from which the electron is ejected, and  $\Phi_s$  is the work function of the instrument. The binding energy of the electrons reflects the local environment of the specific surface elements from which they are ejected. Thus, any shift observed in the peak position can be correlated with a change in the oxidation state. The number of electrons reflects the proportion of the specific elements at the surface and in the near surface regions. To count the number of electrons at each KE value, with the minimum error, XPS must be performed under UHV conditions. The emitted photoelectrons are energy separated and detected by a complex energy analyzer. In this research, a PHOIBOS 150 analyzer with a resolution better than 1 eV was employed. The photoelectrons passing through the energy analyzer are deflected by the electrostatic field and leave the analyzer at a specific position depending on its energy. XPS analysis was carried out by a SPEC X-ray photoelectron spectrometer using Mg/Al K $\alpha$  X-ray source. The obtained data were interpreted by using the SDP ver.4.1 software where the C(1s) core level binding energy was set at 285.0 eV, as the reference point.

### 3.3.3. Microstructure

In this dissertation, microstructural details including atomic arrangement across the interfaces, crystalline defects, and grain structure were studied by transmission electron microscopy (TEM) which utilizes electrons to image materials. Owing to very small de-Broglie wavelength of electrons ( $\lambda = 0.0251 \text{ \AA}$  at the acceleration voltage of 200 keV), resolutions of the order of 1  $\text{\AA}$  can be achieved making the imaging with atomic resolution possible.<sup>32</sup> In TEM images the contrast arises because of the

scattering of the incident electron beam as it passes through the sample. The electron wave can change both its amplitude and its phase as it traverses the specimen and both types of change can give rise to image contrast. Thus, a fundamental distinction we make in the TEM is between amplitude contrast and phase contrast. In many situations both types of contrast may contribute to the image. However, TEM operating conditions are often selected in a way that one type of contrast dominates. Two types of amplitude contrast are possible: mass-thickness contrast and diffraction contrast. Mass-thickness contrast occurs due to the incoherent elastic scattering of electrons. This type of contrast is important when imaging non-crystalline samples. Diffraction contrast occurs due to the coherent elastic scattering at Bragg angles. In TEM, there are two fundamental systems: the illumination system controlling the electron source (intensity) and the imaging system collecting the electrons scattered and transmitted from the sample. Depending on the operation mode, the electrons collected by the imaging system can either form a selected area diffraction pattern (SAED) or an image. In diffraction mode, the electrons which form the SAED pattern are elastically scattered by the sample. Thus, if the atomic arrangement in the sample is periodic, the diffraction pattern consists of well-defined spots; whereas, in case of polycrystalline sample with less atomic order, the diffraction results in diffused spots, arcs, or even rings. The corresponding alignment of the electron beam in the imaging and the diffraction modes is shown in Fig.3.8. In this study, SAED patterns were acquired to establish the epitaxial details and confirm the information obtained from the X-ray diffractometry. Besides, high resolution TEM (HRTEM) imaging was also conducted which is based on phase

contrast and relies on the difference in phase among the electron waves scattered through a thin sample. In HRTEM the objective astigmatism has to be minimized to achieve atomic resolution. The other main requirement for a HRTEM is a highly coherent and monochromatic electron beam. The interpretation of contrast in HRTEM images is not easy, since it is sensitive to many factors. The appearance of the image varies with small changes in the thickness, orientation, or scattering factor of the specimen, and variations in the focus or astigmatism of the objective lens.

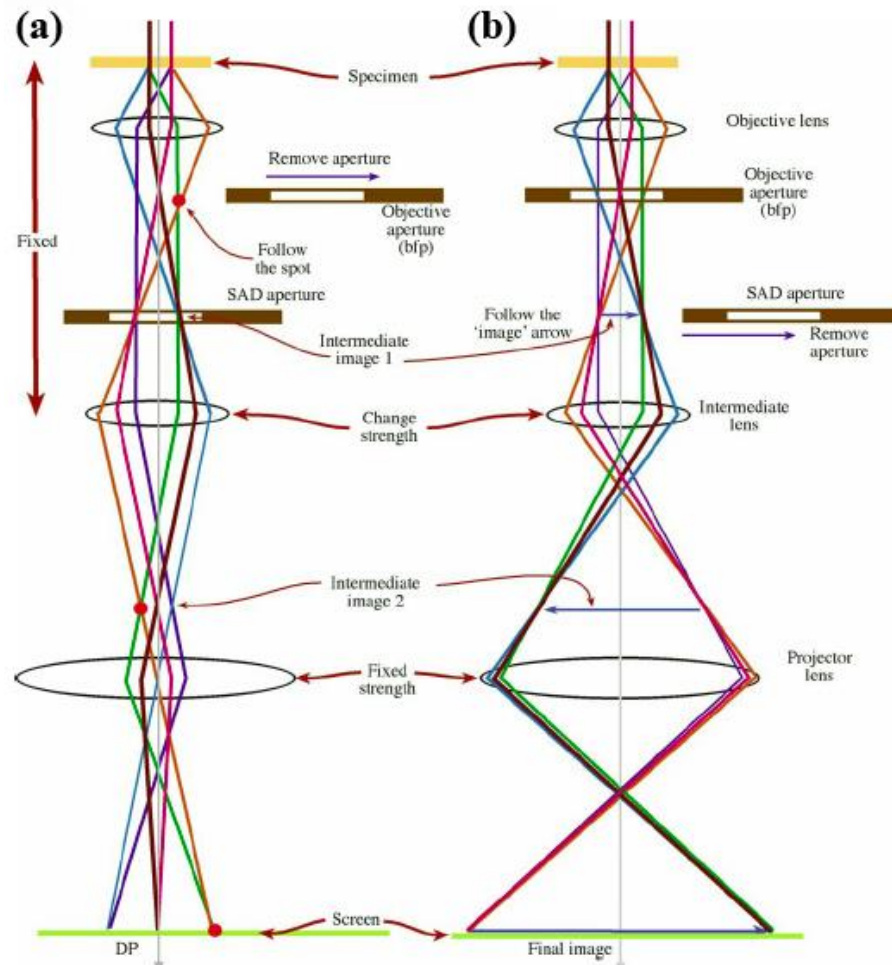


Fig.3.8. Two operation modes of the TEM imaging system: (a) diffraction mode and (b) image mode.<sup>32</sup>

In the present study, a JEOL 2010F microscope, which was equipped with a field emission gun providing a highly coherent electron beam and operated at 200 kV, was used for detailed microstructural evaluations. This microscope can also be operated in STEM, STEM-Z contrast, and EELS spectroscopy modes. In addition, an aberration corrected Ultra STEM 200 operated at 200 kV was used to investigate the atomic and crystallographic arrangements across the interfaces. The aberration corrector improved the spatial resolution of the microscope to 0.78 Å; therefore, direct imaging of the interface atomic structure was permitted.

The electron transparent samples were prepared by mechanical polishing, wedging, and ion milling. In some cases a FEI Quant 3D FEG focused ion beam instrument was used to fabricate the TEM samples.

### **3.3.4. Morphology**

Atomic force microscopy (AFM) was employed for morphological studies in this project. AFM has the advantage of imaging almost any type of surfaces, including polymers, ceramics, composites, glass, and biological samples. Today, most AFMs combine a laser beam deflection system, AFM tips, and cantilevers. A laser is reflected from the back of the reflective AFM lever and onto a position-sensitive detector. Since typical tip radius is from a few to tens of nanometers, resolutions of the order of fractions of nanometer or even Armstrong can be reached.<sup>33</sup> A schematic of the AFM system is shown in Fig.3.9. When the tip is brought into proximity of a sample surface, forces between the tip and the sample lead to a deflection of the cantilever according to

Hooke's law. Depending on the situation, forces which are measured in AFM include mechanical contact force, Van-der Waals forces, capillary forces, chemical bonding, and electrostatic forces. In this dissertation, a Caliber atomic force microscope (Veeco Inc.) was used to study the surface morphology of the samples.

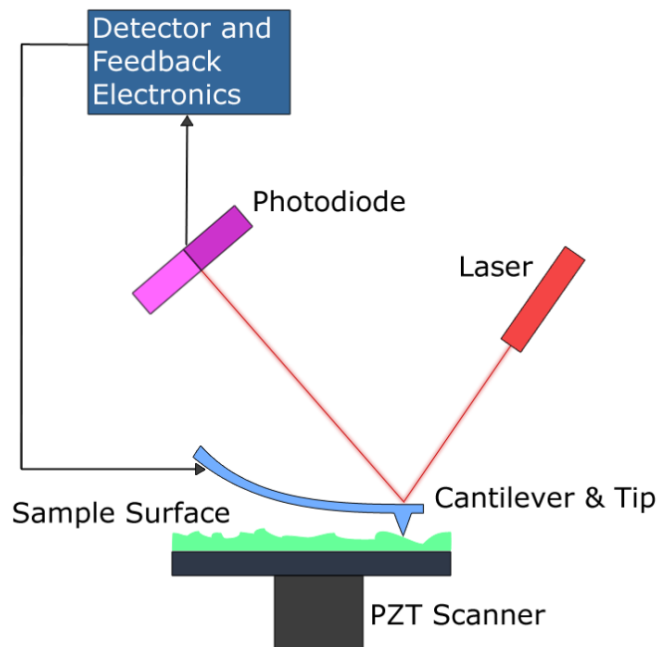


Fig.3.9. Schematic illustration of the optic system and mechanical parts of AFM.<sup>34</sup>

### 3.3.5. Optical characteristics

#### 3.3.5.1. UV-Vis spectroscopy

Transmission spectra were collected employing a Hitachi U-3010 UV-Vis dual-beam spectrometer, in the present work. As a light beam strikes a substance, reflection, transmission, and absorption of the light occur simultaneously. Absorption takes place

through excitation of the electrons from lower energy levels to the higher energy levels at a specific frequency or wavelength of the incident beam. Thus, the intensity of the absorption varies as a function of frequency, and a measurement of this variation makes the absorption spectrum. Absorption and transmission spectra represent equivalent information; in other words, one can be calculated from the other through a mathematical transformation as below:

$$A = -\log(T) \quad (3-6)$$

where A and T are absorption and transmission values, respectively. Based on this equation, a transmission spectrum has its maximum intensities at wavelengths where the absorption is weakest. An absorption spectrum has its maximum intensities at wavelengths where the absorption is strongest.

### *3.3.5.2. Photoluminescence spectroscopy*

Photoluminescence refers to light emission that occurs when a sample is excited with an external source of light. When irradiated with light of suitable wavelength, electrons in the sample are excited to higher energy levels. The radiative transition of the excited electron from the higher energy levels to lower energy levels gives rise to luminescence. To record the PL spectrum, the sample is illuminated with a specific wavelength of light and the variation of luminescence intensity is measured as function of the luminescence wavelength. Under the PLE mode, the intensity of a specific

luminescence wavelength is recorded as a function of wavelength of the illuminating light. The PL spectrum contains information about radiative energy levels within the band structure of the sample. The PLE spectrum gives the information about the energy transformation among the energy levels in the sample. The PL measurements in the present study were carried out at room temperature using a Hitachi F2500 fluorescence spectrophotometer where a Xe lamp was used as the excitation source. A diffraction grating on the incident beam side was used to select the desired wavelength for the excitation beam. In this spectrophotometer, the excitation wavelength can be varied from 220 nm to 800 nm. The light emitted by the sample goes to a photomultiplier through another diffraction grating where it is recorded by a computer.<sup>35,36</sup>

### 3.3.6. Electrical properties

Four-point probe technique has been the preferred method to measure electrical resistivity of both bulk and thin film samples, because it is simple and, more importantly, measurement errors including the probe resistance, the spreading resistance under each probe, and the contact resistance between the probes and the specimen material are eliminated. Fig.3.10 schematically illustrates the basic configuration of this technique. In this method, a current is passed through the two outer probes and the voltage drop between two inner probes is measured.<sup>37</sup> By adopting this configuration, the two contact resistances ( $R_c$ ) and two spreading resistances ( $R_{sp}$ ) can be eliminated from the analysis, as mentioned above; therefore,

the sheet resistance ( $R_s$ ) is derived from the slope of the I-V curve. Then, the resistivity ( $\rho$ ) can be obtained simply by multiplying  $R_s$  by thickness, namely  $\rho = R_s \times t$ . In the present study, the ohmic contacts to the  $TiO_2$  and  $VO_2$  thin films were made using gold wires attached to the film by freshly cleaved indium pads. The measurements were performed using a self-made labview program employing a Keithley 2400 sourcemeter. The samples were cooled by a closed cycle helium cryostat and warmed by a resistive heater.

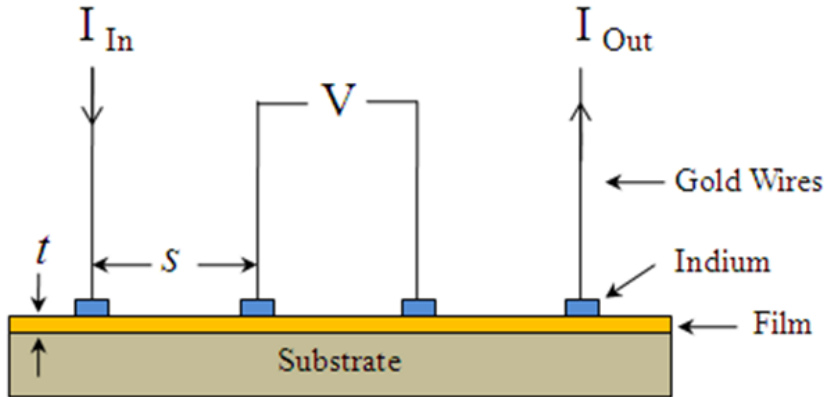


Fig.3.10. Delineation of a typical four point probe resistivity measurement setup.

### 3.3.7. Photochemical activity

#### 3.3.7.1. Photocatalytic properties

Photocatalytic activity of the layers was evaluated by measuring the degradation rate of aqueous 4-chlorophenol (4CP) solution at room temperature. 50 milliliters of the 4CP solution ( $2 \times 10^{-4}$  M) and a  $1\text{ cm} \times 1\text{ cm}$  sample, as a photocatalyst, were placed in a beaker. A UV lamp ( $\lambda = 365$  nm) was used to excite the samples during

photocatalytic experiments. Prior to UV irradiation, in each experiment, the solution and the catalyst were left in the dark for 30 minutes (considered as a reference point) until adsorption/desorption equilibrium was reached. The solution was then irradiated by UV light. A UV-Vis spectrophotometer (Hitachi, U3010) was used to measure the change in concentration, based on the Beer-Lambert equation<sup>38</sup> stating  $A = \epsilon \times b \times C$  where A,  $\epsilon$ , b, and C are absorptance of the solution, molar absorptivity, path length, and solution concentration, respectively. A fixed quantity of the solution was removed every 20 minutes to measure the absorption and concentration at a wavelength of 230 nm.

### 3.3.7.2. Wetting properties

The hydrophilicity/hydrophobicity characteristics of the heterostructures were examined in ambient atmosphere by evaluating the behavior of deionized water droplets on the surface of the samples using optical photographs. A droplet of water was placed onto the surface using a fine tip syringe and, then, the contact angle was measured by screening photos using a zoom lens and a CCD camera.

## References

1. W.C. O'Mara, R.B. Herring, and L.P. Hunt, *Handbook of Semiconductor Silicon Technology*, Park Ridge, New Jersey: Noyes Publications (1990).
2. O.U. Hanaizumi and K.M. Miura, *Silicon Science and Advanced Micro-Device Engineering II*, Trans. Tech. Publications (2012).
3. R.H. French, *J. Am. Ceram. Soc.* 73, 447 (1990).

4. M. Lucht, M. Lerche, H.C. Wille, V. Shvydko, H.D. Ruter, E. Gerdau, and P. Becker, *J. Appl. Cryst.* **36**, 1075 (2003).
5. M.L. Kronberg, *Acta Mater.* **5**, 507 (1957).
6. J.R. Kelly and I. Denry, *Dent. Mater.* **24**, 289 (2008).
7. R.H.J. Hannink, P.M. Kelly, and B.C. Muddle, *J. Am. Ceram. Soc.* **83**, 461 (2000).
8. M. Borek, F. Qian, V. Nagabushnam, and R.K. Singh, *Appl. Phys. Lett.* **63**, 3288 (1993).
9. H.M. Smith and A.F. Turner, *Appl. Opt.* **4**, 147 (1965).
10. J.T. Cheung and T. Magee, *J. Vac. Sci. Technol. A* **1**, 1604 (1983).
11. D. Dijkkamp, T. Venkatesan, X.D. Wu, S. A. Shaheen, N. Jisrawi, Y.H. MinLee, W.L. Mclean, and M. Croft, *Appl. Phys. Lett.* **51**, 619 (1987).
12. J. Narayan, N. Biunno, R. Singh, O.W. Holland, and O. Auciello, *Appl. Phys. Lett.* **51**, 1845 (1987).
13. T.H. Yang, S. Nori, S. Mal, and J. Narayan, *Acta Mater.* **59**, 6362 (2011).
14. J. Li and J. Dho, *J. Crys. Growth* **312**, 3287 (2010).
15. K. Nagashima, T. Yanagida, H. Tanaka, and T. Kawai, *J. Appl. Phys.* **101**, 026103 (2007).
16. H. Zhou, M. F. Chisholm, T.H. Yang, S.J. Pennycook, and J. Narayan, *J. Appl. Phys.* **110**, 073515 (2011).
17. T.H. Yang, R. Aggarwal, A. Gupta, H. Zhou, R.J. Narayan, and J. Narayan, *J. Appl. Phys.* **107**, 053514 (2010).
18. D.B. Chrisey and G.K. Hubler, *Pulsed Laser Deposition of Thin Films*, New York: Wiley-Interscience (1994).

19. R.K. Singh and J. Narayan, Phys. Rev. B 41, 8843 (1990).
20. R.K. Singh, O.W. Holland, and J. Narayan, J. Appl. Phys. 68, 233 (1990).
21. J. Narayan, P. Tiwari, X. Chen, J. Singh, R. Chowdhury, and T. Zheleva, Appl. Phys. Lett. 61, 1290 (1992).
22. P. Ding and W.K. Yuan, Chem. Eng. Sci. 49, 2153 (1994).
23. J.A. Greer and M.D.J. Tabat, Vac. Sci. Technol. A 13, 1157 (1995).
24. R.K. Singh, D. Bhattacharya, and J. Narayan, Appl. Phys. Lett. 57 2022 (1990).
25. T. Dutta, Ph.D. dissertation, North Carolina State University (2011).
26. E.W. Chase, P. Barboux, J.M. Tarascon, and B. Wilkens, Appl. Phys. Lett. 52, 754 (1988).
27. J.J. Kingston, F.C. Wellstood, P. Lerch, A.H. Miklich, and J. Clarke, Appl. Phys. Lett. 56, 189 (1990).
28. S. Mal, T.H. Yang, P. Gupta, J.T. Prater, and J. Narayan, Acta Mater. 59 2526 (2011).
29. S. Mal, T.H. Yang, C. Jin, S. Nori, J. Narayan, J.T. Prater, Scripta Mater. 65, 1061 (2011).
30. B.D. Cullity, Elements of X-Ray Diffraction, Addison-Wesley Publishing Co. Inc. (1982).
31. A. Gupta, Ph.D. dissertation, North Carolina State University (2011).
32. D.B. Williams and C.B. Carter, Transmission Electron Microscopy, New York: Plenum Press (1996).
33. S.H. Cohen and M.L. Lightbody, Atomic Force Microscopy/Scanning Tunneling Microscopy, New York: Kluwer Academic/Plenum Publishers (1999).
34. <http://www.nisenet.org>

35. C.F. Klingshirn, *Semiconductor Optics*, Springer-Verlag (1997).
36. R. Aggarwal, Ph.D. dissertation, North Carolina State University (2010).
37. D.K. Schroder, *Semiconductor Material and Device Characterization*, New York: Wiley-Interscience Publication (1998).
38. J.M. Schurr, *Chem. Phys.* 15, 1 (1976).

## **Chapter 4**

# **Control of Structure and Properties of Epitaxial TiO<sub>2</sub>/c-Sapphire Thin Film Heterostructures**

We have investigated the formation of the rutile and the anatase phases of TiO<sub>2</sub>, with emphasis on the epitaxial growth characteristics, and defect content as a function of laser and substrate variables. XRD studies revealed that the rutile phase is more stable at higher substrate temperatures and lower oxygen pressures; in contrast, decreasing the temperature and increasing the oxygen pressure gave rise to formation of anatase. Epitaxial rutile films with a (200) orientation were obtained at 450 °C using the pressure of  $5 \times 10^{-4}$  Torr and laser energy of 3.5-4.0 J.cm<sup>-2</sup>. The epitaxial relationship, determined by  $2\theta$  and  $\varphi$  scan of X-ray diffraction and confirmed by STEM and TEM, was shown to be rutile(100)||sapphire(0001), rutile[001]||sapphire[10̄10], and rutile[010]||sapphire[1̄210]. An atomically sharp interface between the rutile epitaxial film and the sapphire substrate was observed. The films exhibited a transmittance of 75-90% over the visible region. The absorption edge was observed to shift toward longer wavelengths at higher deposition temperatures or lower pressures. XPS and PL results showed that concentration of lattice point defects, namely oxygen vacancies and

titanium interstitials, increased at lower oxygen pressures. Formation of nanostructured films with a surface roughness of 1.5-13.1 nm was confirmed by AFM investigations.

#### **4.1. Introduction**

Titanium dioxide ( $\text{TiO}_2$ ) is a wide-band-gap semiconductor with versatile applications such as photocatalysis,<sup>1-4</sup> photovoltaics,<sup>5-7</sup> anti-bacterial applications,<sup>8,9</sup> hydrophilic surfaces and anti-fogging mirrors,<sup>10-12</sup> gas sensors,<sup>13-15</sup> bio-devices,<sup>16,17</sup> microelectronic devices,<sup>18-20</sup> and pigments.<sup>21,22</sup> As often described,  $\text{TiO}_2$  crystallizes in three different polymorphs: rutile (tetragonal,  $a=b=0.45933$  nm and  $c=0.29592$  nm), anatase (tetragonal,  $a=b=0.37852$  nm and  $c=0.95139$  nm), and brookite (orthorhombic,  $a=0.54558$  nm;  $b=0.91819$  nm, and  $c=0.51429$  nm). However, only anatase and rutile play a significant role in determining or providing the applications of titania. Anatase and brookite are metastable states of  $\text{TiO}_2$  which transform to rutile upon heating at high temperatures indicating that rutile is the most stable state.<sup>23-25</sup> Pure titania is n-type semiconductor with indirect band gaps of 3.2 eV for anatase, and 3.0 eV for rutile between the full oxygen 2p valence band and titanium 3d states at the bottom of the conduction band.<sup>26-29</sup> In addition, rutile possesses a superior light scattering property<sup>30,31</sup> being beneficial for effective light harvesting. Meanwhile, in the electronics industry, rutile is the most frequently used polymorph, because it exhibits a higher dielectric constant, as compared to the anatase, which is a desirable property in applications such as capacitors and temperature-compensating condensers.<sup>32</sup>

Fabrication of DRAM capacitors with an equivalent oxide thickness (EOT) lower than 0.5 nm requires oxide materials with a dielectric constant ( $k$ ) of at least 50.<sup>33</sup> One of the oxides that fulfills this condition is  $\text{TiO}_2$ , but only in the rutile phase which has a high dielectric constant ( $k$ ) reported to be  $\sim 90$  and as high as  $\sim 170$ , depending on crystallographic orientation.<sup>34</sup>

Another interesting application of titania is related to the photolysis of water on  $\text{TiO}_2$  electrodes with no external bias where the idea is that the surface defect states play a role in the decomposition of water into hydrogen and oxygen.<sup>24,35</sup> As characteristics of defects on the titania surface change from one crystallographic plane to another, it is necessary to grow epitaxial  $\text{TiO}_2$  films with known defect characteristics to investigate the role of defects for different properties. Furthermore, epitaxial growth enables us to fabricate devices with controllable properties, since lattice orientation of  $\text{TiO}_2$  thin films determines the efficiency and performance of advanced devices. Phase structure, orientation, defect content, and morphology of titania determine its performance; hence, it is critical to control the structure of  $\text{TiO}_2$  films. Fabrication of high-quality  $\text{TiO}_2$  films has attracted much interest from the viewpoints of basic materials science, properties, and applications.

In this chapter, we report control of microstructure from poly to textured to single-crystal films as a function of substrate and laser deposition variables. Special emphasis is placed on epitaxial growth and control of growth orientation of  $\text{TiO}_2$  on sapphire(0001) by the paradigm of domain matching epitaxy (DME) where integral multiples of planes match across the film-substrate interface. We are able to control the

defect content in epitaxial films by changing laser deposition and substrate variables and study the details of defect-property correlations. We optimized the growth conditions (energy density, temperature, and oxygen pressure) such that we can obtain a pure rutile epitaxial film at low temperatures (e.g. 450 °C). Decreasing the processing temperature is critical for device fabrication, particularly for nano-sized devices where thermal budget plays a much more important role in determining the phase structure, morphology, defect texture, and, consequently, performance of the device.

## 4.2. Experimental

TiO<sub>2</sub> thin films were deposited on single crystal sapphire(0001) substrates using PLD technique. The substrates were initially cleaned through a multi-step procedure including degreasing in hot acetone for 15 min., ultrasonic cleaning in acetone for 5 min. followed by ultrasonic cleaning in methanol for 5 min. The cleaned substrates were fully dried by nitrogen gun before being loaded into the deposition chamber. A Lambda Physik (LPX200) KrF excimer laser ( $\lambda = 248$  nm,  $\tau = 25$  ns) was employed to ablate the TiO<sub>2</sub> target which was being rotated during the deposition to provide a uniform ablation and avoid pitting on the target surface. Frequency and the target-substrate distance were maintained as 10 Hz and 4.5 cm, respectively during the film deposition. Different laser energies of 1.5-2.0, 2.5-3.0, 3.5-4.0, and 4.5-5.0 J.cm<sup>-2</sup> were used. The chamber was evacuated to a base pressure of  $\sim 1 \times 10^{-6}$  Torr and, then, oxygen partial pressure was controlled by leaking oxygen into the chamber. A series of thin films were deposited for 20 min. at various substrate temperatures (RT, 150, 250, 450, and 550 °C)

under different oxygen partial pressures ranging from  $5 \times 10^{-6}$  to  $5 \times 10^0$  Torr with  $10^{+2}$  intervals. The layers were subjected to thermal annealing for 1 h, after deposition inside the PLD chamber, at temperature and pressure similar to those of deposition.

The crystalline structure and out-of-plane orientation of the  $\text{TiO}_2$  films were investigated by  $2\theta$  XRD-scanning using a Rigaku X-ray diffractometer with Cu-K $\alpha$  radiation ( $\lambda=0.154$  nm). A Philips X'Pert Pro X-ray diffractometer was employed for  $\varphi$ -scanning to determine in-plane orientation of  $\text{TiO}_2$  films. A Nion UltraSTEM 200 operated at 200 kV and a JEOL-2010 TEM were used to study the atomic and crystallographic arrangements at the interfaces and to confirm the epitaxial growth of the layers. To determine surface chemical composition and stoichiometry of the layers, X-ray photoelectron spectroscopy (XPS) was performed employing a Riber instrument with an Mg-K $\alpha$  X-ray source. The samples were sputtered by  $\text{Ar}^+$  bombardment for 5 min. prior to acquiring data to remove any probable surface contamination. Morphology of the layers was studied by a Veeco AFM. Optical properties of the films were studied by a U-3010 Hitachi UV-Vis spectrophotometer. The room temperature photoluminescence (PL) spectra of the samples were recorded with a fluorescence spectrophotometer (Hitachi, F-2500) using an excitation wavelength of 300 nm.

### **4.3. Results and discussion**

#### **4.3.1. Microstructure**

The results from XRD measurement on phase structure of the  $\text{TiO}_2$  films grown at different substrate temperatures are depicted in Fig.4.1. Oxygen partial pressure and

laser energy were kept constant at  $5 \times 10^{-2}$  Torr and 1.5-2.0 J.cm $^{-2}$ , respectively for all these samples. As is seen, the layers grown at 150 and 250 °C have an amorphous structure. The formation of anatase phase dominantly occurs at 450 °C and the rutile phase forms at 550 °C. That is, the intensity of the rutile(200) peak increases with the substrate temperature, while decreasing the intensity of the anatase (004) and (112) peaks. Reason of this behavior is that anatase is a metastable phase and it transforms into rutile, which is the thermodynamically favored phase of titania and is stable at higher temperatures.

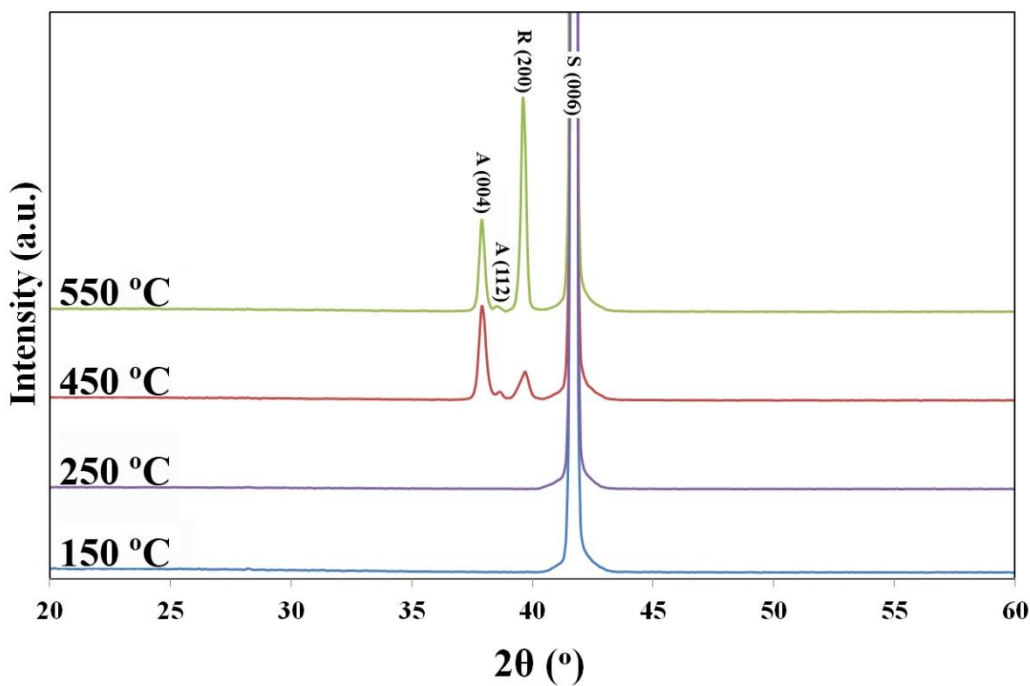


Fig.4.1. XRD patterns of the TiO<sub>2</sub> layers grown at different temperatures.

Although phase transformation between the anatase and rutile phases takes place at about 800-900 °C in vacuum,<sup>36,37</sup> it is interesting to note that the rutile phase has

formed at lower temperatures in our experiments. The reduction in transformation temperature is attributed to non-equilibrium nature of pulsed laser deposition where the ablated species arriving the substrate have an energy of  $nKT$  ( $n \sim 10^2\text{-}10^3$ )<sup>38</sup> and can transfer their extra kinetic energy to the growing layer once they strike the substrate and provide favorable energetic conditions for the aforementioned phase transformation even at lower temperatures than the equilibrium temperature. To measure the thickness of the films, the samples were masked during deposition and their thickness was determined by a Tencor Alpha Step stylus profilometer. The thickness of the layers was the same about 250 nm for all of the growth temperatures.

Effect of the oxygen partial pressure on phase structure of the layers fabricated at temperatures of 450 and 550 °C is shown in Fig.4.2a and Fig.4.2b, respectively.

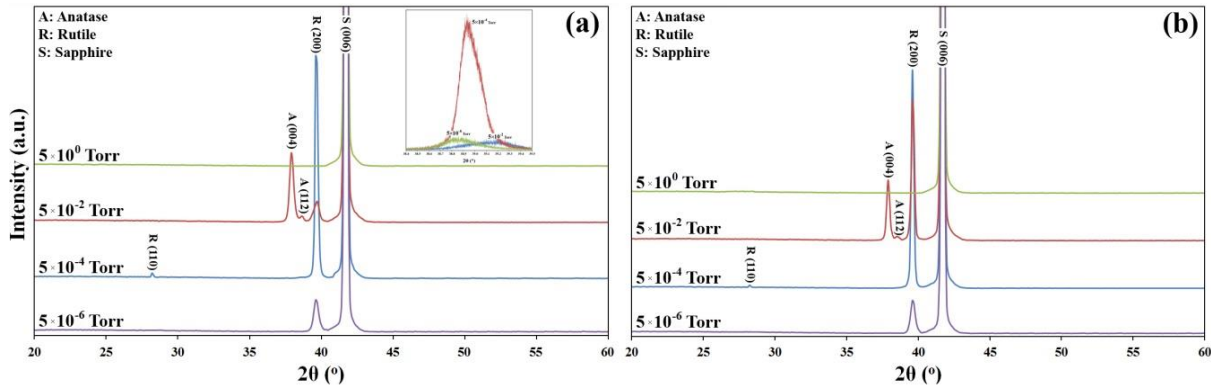


Fig.4.2. XRD patterns of the  $\text{TiO}_2$  layers grown under different pressures at: (a) 450 and (b) 550 °C.

It is suggested that the crystallinity of titania layers gets worse at very high pressures, i.e.  $5 \times 10^0$  Torr.<sup>39</sup> The laser-ablated species from the  $\text{TiO}_2$  target encounter and collide with the  $\text{O}_2$  molecules under very high oxygen pressures giving rise to

reduction of their kinetic energy and thermalization of plasma. Indeed, under high pressures, the plasma from the target is prevented from reaching the surface of the substrate and lack of mobility of the species results in a poor crystallinity.<sup>40</sup> Taking into account the relationship between mobility of the species on the substrate and their kinetic energy,<sup>39</sup> it is concluded that the ablated species under high ambient pressures do not have enough mobility when they arrive at the substrate and, hence, cannot diffuse to find equilibrium positions during crystallization. One can see that rutile is the predominant phase at lower ambient pressures; in contrast, increasing the pressure results in the formation of anatase phase. Such controllability over volume fraction of the rutile and the anatase phases seems remarkable. In fact, the Ti-O bond length in rutile is longer than that in anatase<sup>41</sup> meaning that the Ti-O bond energy in rutile is smaller than in anatase and, thus, the formation of Ti-O bond in the rutile structure is more energetically favored. The packing factors for rutile and anatase unit cells are 0.486 and 0.445, respectively. High energy species, produced under lower pressures, can diffuse across the substrate surface easily to find and occupy the energetically most favored equilibrium sites to occupy them when imping on the substrate; as a result, a single phase rutile film is obtained. In contrast, the less dense and metastable state, anatase, can form when the adatoms do not have enough energy to diffuse on the surface. Typically, the rutile phase does not form under high oxygen pressures. As is seen in the inset of Fig.4.2a, increasing the pressure results in a peak shift toward higher diffraction angles which are closer to the diffraction angle of bulk TiO<sub>2</sub>. This indicates that the intrinsic residual strain, which has originated due to structural

defects, is less in the films grown under higher pressures. There are six different kinds of point defects envisaged in the  $\text{TiO}_2$  structure, namely titanium interstitial ( $\text{Ti}_i$ ), titanium vacancy ( $\text{V}_{\text{Ti}}$ ), oxygen interstitial ( $\text{O}_i$ ), oxygen vacancy ( $\text{V}_0$ ), and two anti-site defects,  $\text{Ti}_0$  and  $\text{O}_{\text{Ti}}$ . Each of these defects has specific formation energies ( $\Delta H$ ) under titanium and oxygen rich growth conditions. Theoretical estimation of formation energies of anti-site and titanium vacancy defects are too high; as a result, they form merely under extreme conditions. However, formation energies of  $\text{Ti}_i$  and  $\text{V}_0$  defects are about 2-3 eV under Ti-rich (low oxygen partial pressure) growth condition,<sup>42</sup> so these defects form easily in  $\text{TiO}_2$  and may convert to each other via reaction 2-1. As it was explained back in the section 2.1.3, formation of  $\text{V}_0$  is more favored than  $\text{Ti}_i$  and oxygen vacancies are important native point defects in the reduced rutile.<sup>42</sup> According to the inset of Fig.4.2a, the low intensity and large FWHM (Full Width at Half-Maximum) of the rutile peak in the film grown under  $5 \times 10^{-6}$  Torr reveals a poor crystallinity, since using such a low oxygen pressure results in formation of point defects and, hence, decreasing the structure factor that, in turn, decreases the peak intensity.

Regarding the intensity and FWHM of the rutile(002) peak, the oxygen pressure of  $5 \times 10^{-4}$  Torr was selected for our next sets of experiments. In addition, a temperature of 450 °C was also selected as the optimum substrate temperature. Fig.4.3 shows the XRD patterns of the layers fabricated at different laser energies. These results indicate that the growing film assumes a [100] orientation and other crystallographic directions disappear when higher energies are used. As shown in inset of Fig.4.3, the rutile(200) peak shifts toward smaller  $2\theta$  values when the laser energy increases.

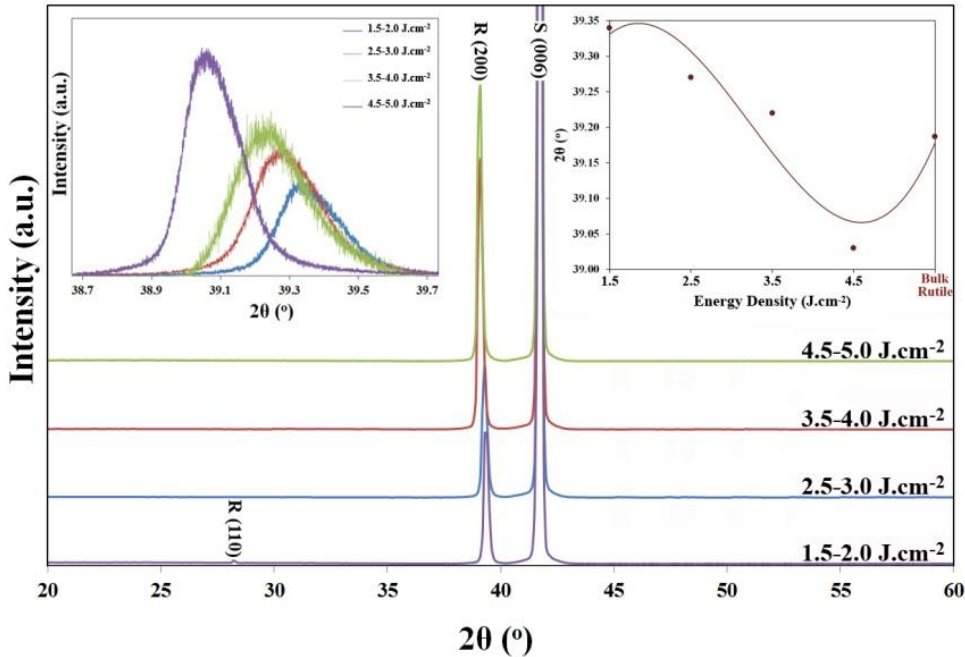


Fig.4.3. Effect of the laser energy on phase structure of the  $\text{TiO}_2$  layers grown at  $450^\circ\text{C}$  under oxygen pressure of  $5 \times 10^{-4}$  Torr.

#### 4.3.2. Epitaxial relationship and the DME details

To confirm the epitaxial growth and determine the in-plane alignment of the  $[200]$  oriented rutile- $\text{TiO}_2$  films on the sapphire(0001) substrate, we performed XRD  $\varphi$ -scans where the number of planes of a particular family with the same angle with the film surface is represented by number of the peaks. Fig.4.4 shows  $\varphi$ -scans of the  $(01\bar{1}2)$  reflection ( $2\theta=25.58^\circ$ ,  $\psi=57.70^\circ$ ) for the sapphire substrate and the  $(110)$  reflection ( $2\theta=27.44^\circ$ ,  $\psi=45.00^\circ$ ) of the rutile film. Due to the threefold symmetry of the sapphire(0001) substrate, three  $(01\bar{1}2)$  reflection peaks with  $120^\circ$  intervals are observed. It is also seen from Fig.4.4 that 6 strong symmetrical peaks appear with an azimuthal interval of  $60^\circ$  for the  $(110)$  family of planes of rutile. As schematically

illustrated in Fig.4.5, the rutile film consists of three twin domains rotated by  $120^\circ$ . This is due to the three-fold symmetry in the pseudo-hexagonal structure of the (0001) sapphire substrate, which is not present in the (100) tetragonal rutile structure.<sup>43</sup>

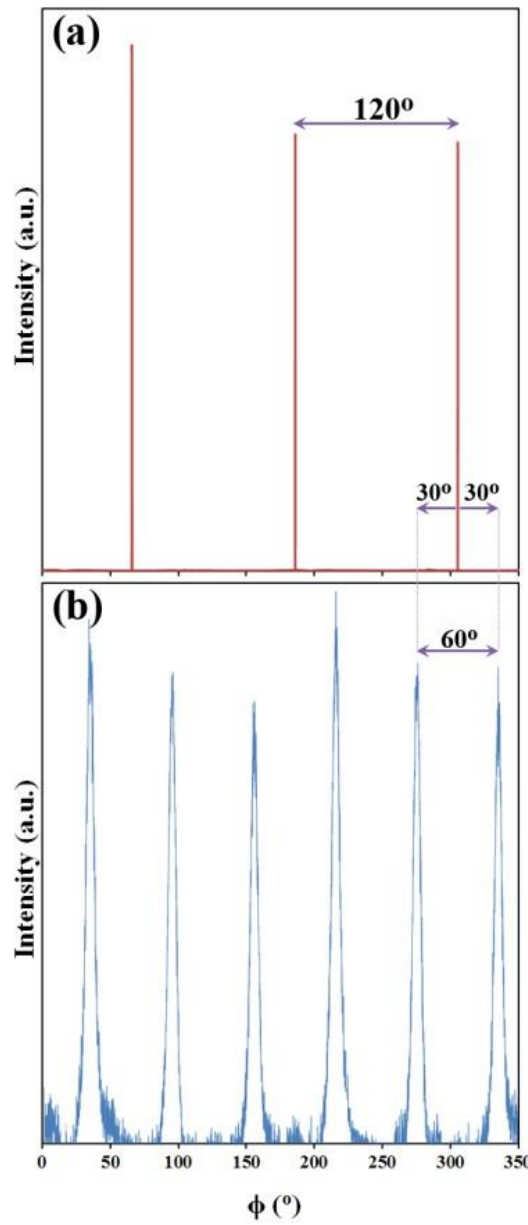


Fig.4.4. XRD  $\varphi$ -scan of the  $\text{TiO}_2$  film grown at  $450^\circ\text{C}$  under  $5 \times 10^{-4}$  Torr oxygen pressure with energy density of  $3.5\text{-}4.0 \text{ J.cm}^{-2}$ : (a) Sapph(0112) and (b) Rutile(110) reflections.

Formation of the twin domain structure becomes understandable if one puts a plane of twofold symmetry on a threefold-symmetry surface. In this case, three variants rotated by  $120^\circ$  (or  $60^\circ$  if considering an  $180^\circ$  rotation of the twofold crystal) on the surface is seen. Thus, formation of the threefold twin domain structure in the epitaxial rutile  $\text{TiO}_2$  film is due to the nucleation and growth of the three variants on the sapphire(0001) substrate.<sup>43</sup>

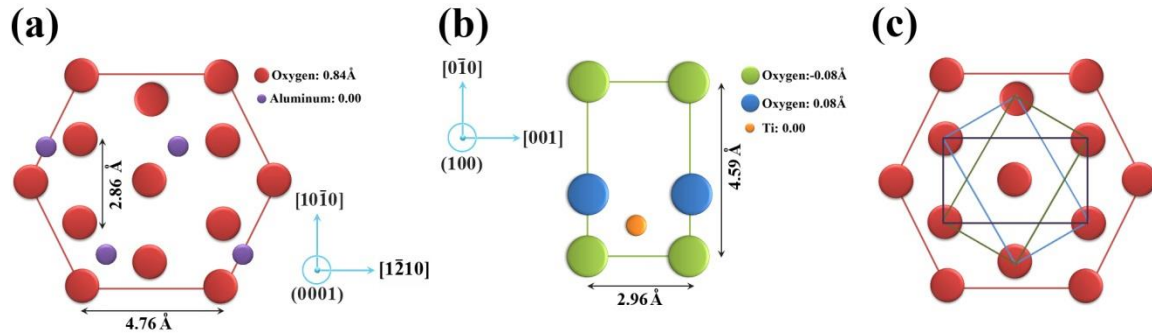


Fig.4.5. Schematic drawing of: (a) sapphire(0001) plane, (b) rutile(001) plane, and (c) epitaxial relationship of rutile(200) on *c*-sapphire.

According to Fig.4.5, the epitaxial relationship between the rutile  $\text{TiO}_2$  films and the sapphire(0001) substrate is established as rutile(100)||sapphire(0001), rutile[001]||sapphire[10\bar{1}0], and rutile[010]||sapphire[1\bar{2}10]. Here it should be noted that a [010] direction of  $\text{TiO}_2$  can be parallel to any of the three equivalent [10\bar{1}0] directions of *c*-sapphire. Consequently, there are three twin variants in  $\text{TiO}_2$  film, with a twin boundary angle of  $60^\circ$ . Nucleation of  $\text{TiO}_2$  in any of these in-plane orientations is equally likely, as these three different orientations of  $\text{TiO}_2$  are energetically equivalent. Fig.4.6a shows TEM cross section image of the rutile/sapphire sample prepared at 450

$^{\circ}\text{C}$  under  $5 \times 10^{-4}$  Torr where formation of a columnar structure, as a result of the in-plane  $60^{\circ}$  rotation, is evident.

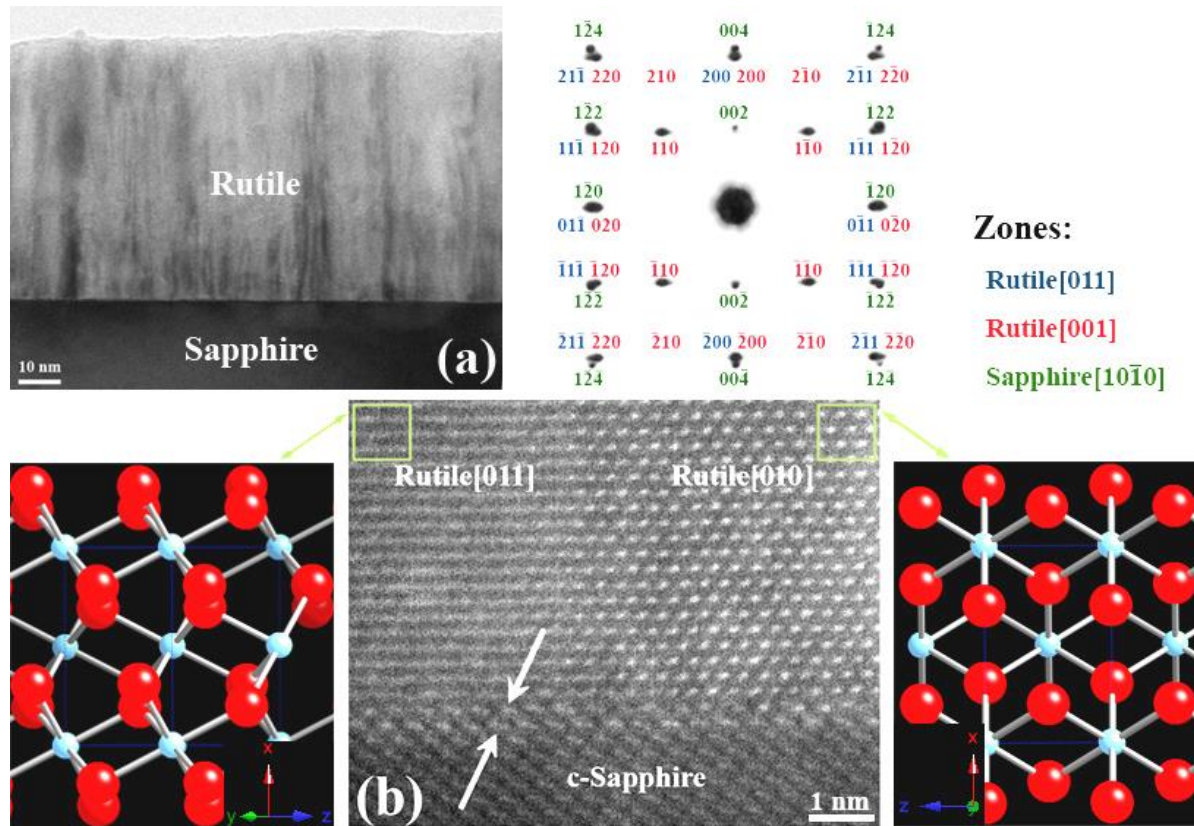


Fig.4.6. (a) Cross section TEM image of the rutile  $\text{TiO}_2$  film on sapphire substrate and the indexed TEM-SAED pattern, and (b) High resolution STEM image of 2 adjacent rutile grains with two different in-plane orientations. Formation of  $\text{Ti}_2\text{O}_3$  inter layer is shown by arrows.

The columnar grain structure indicates that the threefold mosaic structure was initiated on the substrate surface via the nucleation of the three variants. Meanwhile, the spotty feature of the SAED pattern, taken from the interface between 2 adjacent rutile grains and the sapphire substrate (rutile [011] and [001] and sapphire[ $10\bar{1}0$ ] zones), confirms formation of an epitaxial film. The indexed SAED pattern is consistent

with the schematic illustration shown in Fig.4.5 and further ascertains the proposed epitaxial relationship. The in-plane rotation of the grains is observed in Fig.4.6b where formation of atomically sharp interfaces between the grains and the substrate is notable. This image shows 2 adjacent grains with [001] and [011] in-plane orientations aligned with sapphire  $[10\bar{1}0]$  direction that is consistent with the schematic illustration in Fig.4.5. It was already found by our group that an oxygen deficient intermediate layer grows on the sapphire substrate before formation of the top layer when deposition is carried out under low pressures, namely  $10^{-6}$ - $10^{-5}$  Torr.<sup>44</sup> Here, in the  $\text{TiO}_2$  system, the rutile film initially grows pseudomorphically on the sapphire substrate as  $\text{Ti}_2\text{O}_3$  that has a rhombohedral structure (In Bulk:  $a=b=5.15 \text{ \AA}$ ,  $c=13.61 \text{ \AA}$ ,  $\gamma=120^\circ$ ) and is isostructural with sapphire ( $a=b=4.76 \text{ \AA}$ ,  $c=12.99 \text{ \AA}$ ,  $\gamma=120^\circ$ );<sup>45,46</sup> however, after a few monolayers, rutile starts growing tetragonally on the  $\text{Ti}_2\text{O}_3$ /sapphire(0001) platform, as shown in Fig.4.6b. The possible atomic arrangement at the  $\text{TiO}_2/\text{Ti}_2\text{O}_3$  interface is schematically illustrated in Fig.4.7. The matching of lattice parameters produces strain in the film that is relaxed by formation of misfit dislocations at the film/substrate interface. According to Fig.4.7, lattice misfits at the rutile/ $\text{Ti}_2\text{O}_3$  interface are calculated as  $\varepsilon_b=+3.57\%$   $\varepsilon_c=+28.15\%$  where  $\varepsilon_b$  and  $\varepsilon_c$  are the lattice misfits along b and c directions of the  $\text{TiO}_2$  film. According to the domain matching epitaxy (DME) paradigm,<sup>47</sup> the misfit along b-axis is accommodated by matching of 28 planes of the film with 27 planes of the substrate with a frequency factor of zero. Meanwhile, the misfit strain along the c-direction of rutile is relaxed when 4/3 and 3/2 domains alternate with a relative frequency of 0.55.

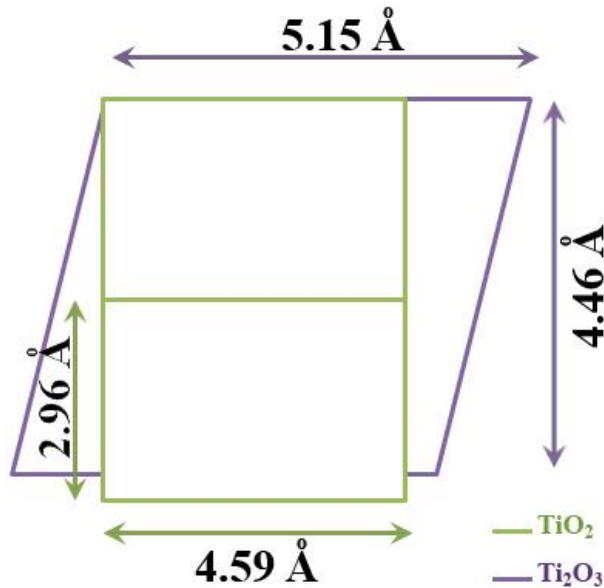


Fig.4.7. Schematic illustration of crystallographic orientation at the  $\text{TiO}_2/\text{Ti}_2\text{O}_3$  interface.

#### 4.3.3. Morphology

AFM images of the films deposited at  $450^\circ\text{C}$  under different oxygen pressures are exhibited in Fig.4.8 where formation of nanostructured films is evident. A non-uniform surface is obtained at high oxygen partial pressure, i.e.  $5 \times 10^0$  Torr. The surface roughness of the samples was determined as 13.1, 11.8, 8.1, and 1.5 nm for the ambient pressures of  $5 \times 10^0$ ,  $5 \times 10^{-2}$ ,  $5 \times 10^{-4}$ , and  $5 \times 10^{-6}$  Torr. As explained earlier, the adatoms have relatively low energy and mobility on the substrate when deposition is performed under high pressures. Consequently, they are quickly quenched and sit wherever they arrive in the substrate. As a result, surface diffusion to form a smooth surface is not appreciable. In contrast, as the oxygen pressure decreases, the kinetic energy of the species increases. Under such circumstances, their mobility is high enough to diffuse on the substrate surface and form a smooth surface.

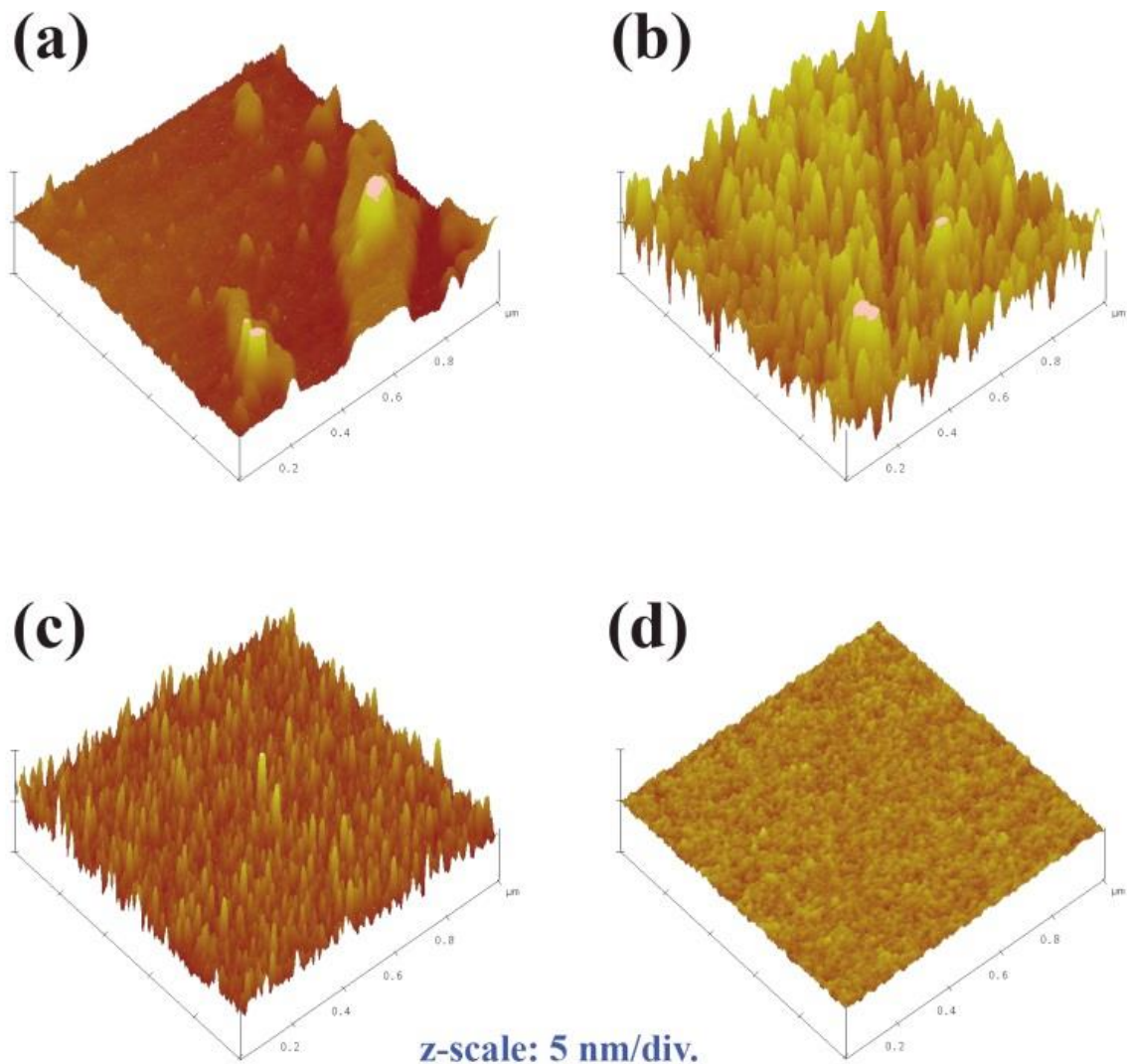


Fig.4.8. Surface morphology of the  $\text{TiO}_2$  films grown at 450  $^{\circ}\text{C}$  under various oxygen pressures:  
 (a)  $5 \times 10^0$ , (b)  $5 \times 10^{-2}$ , (c)  $5 \times 10^{-4}$ , and (d)  $5 \times 10^{-6}$  Torr.

The effect of laser energy on the surface morphology of the samples, fabricated at 450  $^{\circ}\text{C}$  and  $5 \times 10^{-4}$  Torr, is depicted in Fig.4.9. The surface roughness of the samples was measured as 8.1, 7.9, 6.3, and 2.1 nm for the laser energies of 1.5-2.0, 2.5-3.0, 3.5-4.0, and 4.5-5.0  $\text{J.cm}^{-2}$ . Thickness of the layers was respectively measured as 170, 275, 335, and 450 nm for the laser energies of 1.5-2.0, 2.5-3.0, 3.5-4.0, and 4.5-5.0  $\text{J.cm}^{-2}$ .

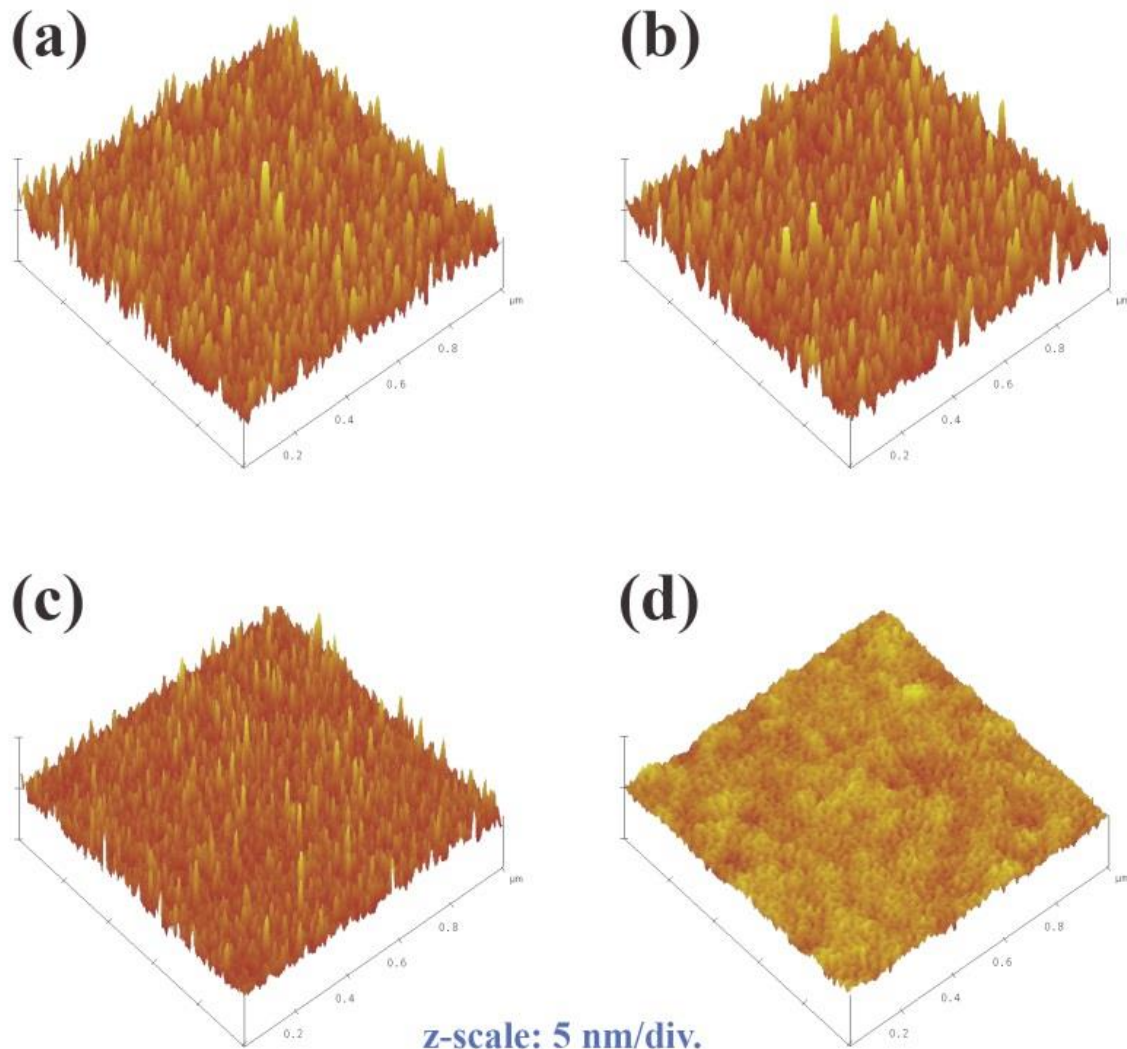


Fig.4.9. Surface morphology of the  $\text{TiO}_2$  films grown at  $450^\circ\text{C}$  and  $5 \times 10^{-4}$  Torr with applying different laser energies: (a) 1.5-2.0, (b) 2.5-3.0, (c) 3.5-4.0, and (d) 4.5-5.0  $\text{J.cm}^{-2}$ .

#### 4.3.4. Stoichiometry

To study stoichiometry as well as defects content of the layers, XPS technique was employed. Fig.4.10 shows O(1s) core level binding energies for the  $\text{TiO}_2$  layers grown under various pressures which have been deconvoluted into 4 distinct peaks using the Gaussian function. Peak A, located at a binding energy of  $\sim 531.7$  eV, corresponds to the

$O^{2-}$  ions in oxygen deficient regions (in  $Ti_2O_3$  compound). To preserve the charge neutrality of the crystal, two  $Ti^{4+}$  cations must convert to two  $Ti^{3+}$  cations when an oxygen vacancy forms. The electron charge density in the region of a  $V_O$  is reduced which results in less screening of the  $O^{2-}(1s)$  electrons from the nuclei.<sup>48</sup> Hence, peak A can represent the  $V_O$  defects and its intensity is associated with the concentration of oxygen vacancies ( $V_O$ ). Peak B, with a binding energy of 530.2 eV, is assigned to the oxygen ions in the crystalline lattice of  $TiO_2$ . Peaks C and D, which respectively have binding energies of 528.2 and 527.1 eV, may represent oxygen atoms in contact with  $Ti_i^{3+}$  and  $Ti_i^{4+}$  defects. The  $Ti_i$  neutral atom donates three or four electrons to the host crystal and transforms to  $Ti^{3+}$  or  $Ti^{4+}$  ions.<sup>51</sup> The released electrons are captured by  $Ti^{4+}$  lattice cations. Therefore, lattice  $Ti^{2+}$  and  $Ti^{3+}$  cations, represented by peaks C and D, form. Portion of all these peaks for different oxygen pressures are listed in Tab.4.1.

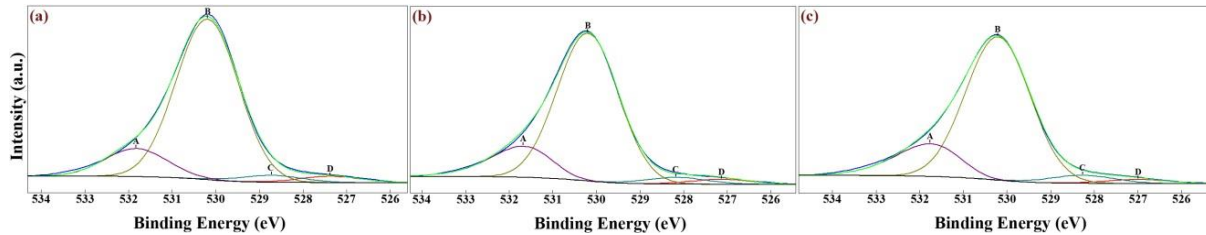


Fig.4.10. XPS O(1s) core level binding energies in the  $TiO_2$  films grown under oxygen pressures of: (a)  $5 \times 10^{-2}$ , (b)  $5 \times 10^{-4}$ , and (c)  $5 \times 10^{-6}$  Torr.

Results reveal that the amount of the lattice disorder, which is represented by peaks A, C and D in O(1s) core level, increases as oxygen pressure decreases. A small peak shift is also observed for these peaks due to variation of defect concentrations.

Regarding the reactions 2-2 to 2-7 and as it was discussed in section 2.1.3, it can be suggested that lowering the oxygen partial pressure results in an increase in concentration of point defects. Meanwhile, concentration of  $Ti_i$  defects increases more rapidly with decreasing oxygen pressure.

Tab.4.1. Portion of the XPS peaks for different oxygen pressures.

XPS peak \ O <sub>2</sub> pressure		5×10 <sup>-2</sup> Torr	5×10 <sup>-4</sup> Torr	5×10 <sup>-6</sup> Torr
		Portion (%)		
O(1s)	A	14.2	16.5	17.7
	B	79.8	77.0	74.7
	C	3.2	3.5	4.3
	D	2.8	3.0	3.3

O(1s) core level binding energies of the layers at different laser energies at substrate temperature of 450 °C under ambient pressure of 5×10<sup>-4</sup> Torr are depicted in Fig.4.11. It is reminded that peaks A, C, and D were assigned to the disordered titania and peak B was attributed to the perfect titania. Portion of peak B was calculated as 78.1, 81.0, and 78.5% for the laser energies of 2.5-3.0, 3.5-4.0, 4.5-5.0 J.cm<sup>-2</sup>. These results and those presented in Tab.4.1 (laser energy of 1.5-2.0 J.cm<sup>-2</sup>) reveal that using medium energies, namely 3.5-4.0 J.cm<sup>-2</sup>, gives rise to formation of crystalline structures with fewer defects. At very low laser energies, i.e. 3.5-4.0 J.cm<sup>-2</sup>, the adatoms are not mobile enough to diffuse to proper lattice positions. On the other hand, more defective films grow when much higher energies, i.e. 4.5-5.0 J.cm<sup>-2</sup>, are applied, since a massive flux of the ablated particles from the target form and, hence, the deposition rate is raised. At higher deposition rates, films with higher defect contents are grown.

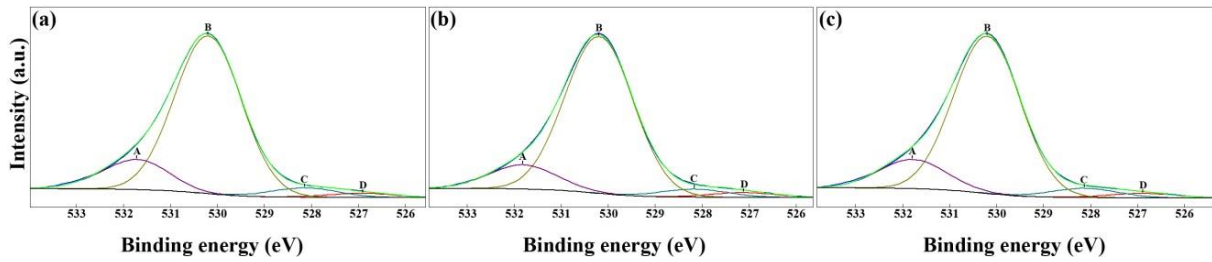


Fig.4.11. XPS O(1s) core level binding energies in the TiO<sub>2</sub> films grown under oxygen pressure of  $5 \times 10^{-4}$  at 450 °C with laser energies of: (a) 2.5-3.0, (b) 3.5-4.0, and (c) 4.5-5.0 J.cm<sup>-2</sup>.

#### 4.3.5. Optical properties

Fig.4.12 shows the transmittance spectra of the titania layers grown at various substrate temperatures. The sharp fall in transmittance below 400 nm is due to the onset of fundamental absorption of TiO<sub>2</sub>.

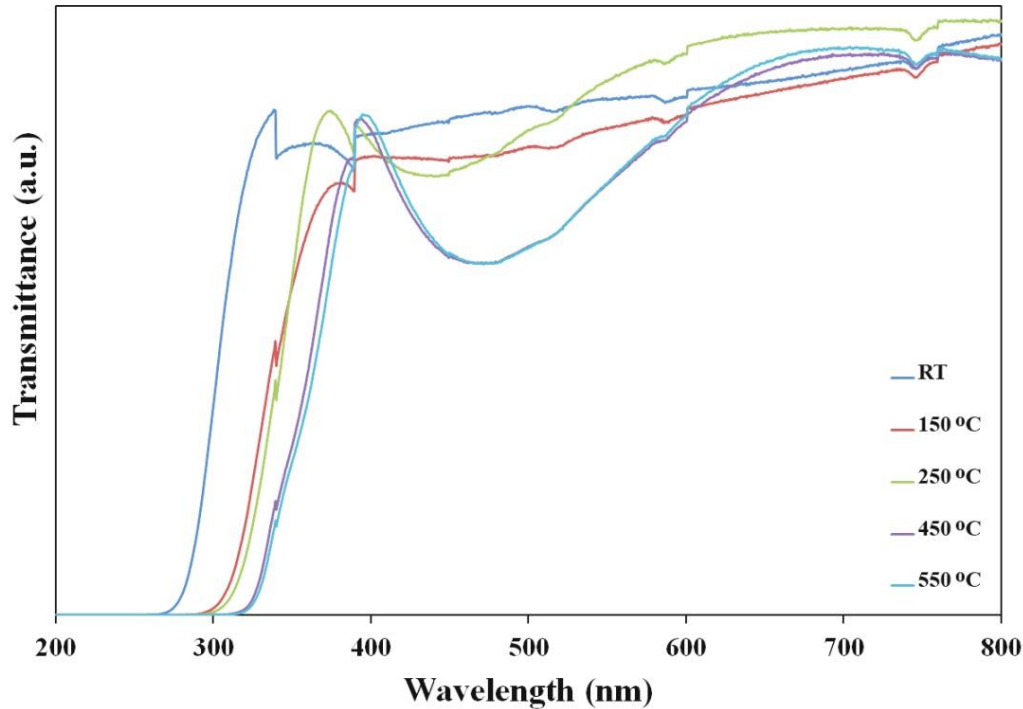


Fig.4.12. Transmittance spectra of the layers grown at different substrate temperatures.

As is seen, this edge shifts toward longer wavelengths when the deposition temperature increases. Reason of this behavior can be found in the band gap difference between the rutile and the anatase phases. The anatase phase has a band gap energy of around 3.2 eV, while that of the rutile phase is about 3.0 eV,<sup>24</sup> so increasing the rutile fraction results in decreasing band gap energy of the deposited film. Transmittance spectra of the films fabricated at 450 °C under various oxygen pressures are displayed in Fig.4.13.

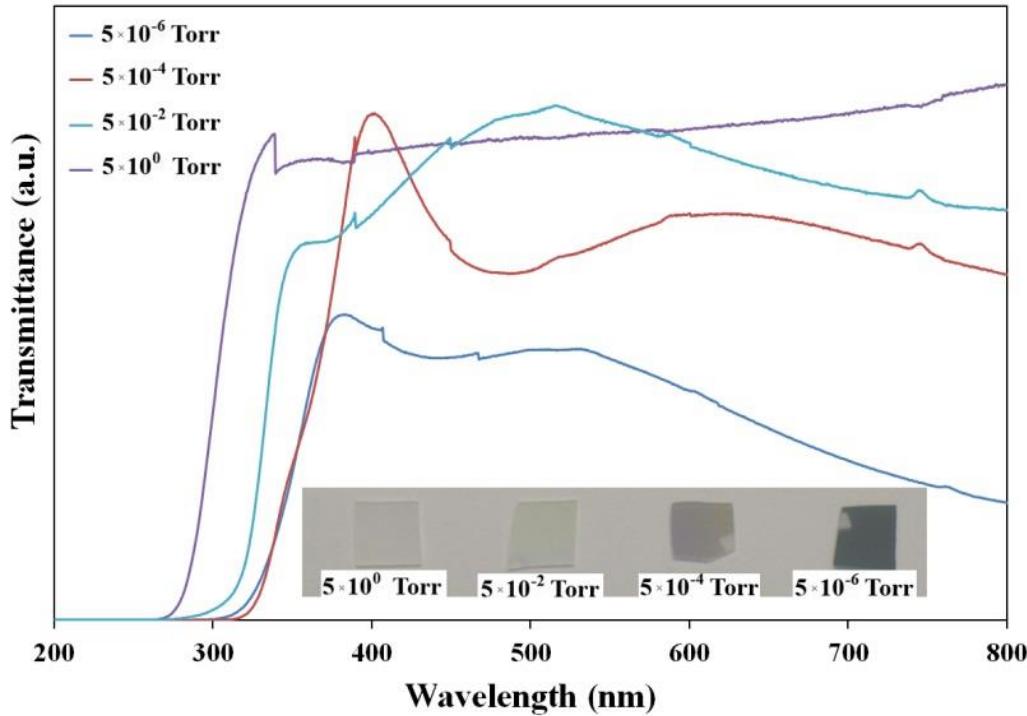


Fig.4.13. Transmittance spectra of the layers grown under various oxygen pressures.

As is seen in inset of this figure, lowering the pressure give rise to growth of films with a darker (dark blue) color. Films grown under higher pressures show a very high

transmittance ( $\sim$ 75-90%) in the visible region, while transmittance of the film fabricated at  $5 \times 10^{-6}$  Torr is less than 45% asserting growth of a film with a high defect concentration. Sharper transmittance edge indicates a reduction of point defects in the films as well<sup>48</sup>. It can be also observed that the absorption edge shifts toward longer wavelengths at lower oxygen pressures. The reason for this behavior is formation of more anatase phase under higher pressures which has a wider band gap than the rutile phase, as elucidated earlier. Hence, the optical results are in a good agreement with the XRD results (Fig.4.1 and Fig.4.2).

To further shed light on the defect structure of the samples, photoluminescence (PL) spectroscopy technique was employed as well. Fig.4.14 shows the emission PL spectra of the rutile films grown under different pressures at 450 °C. The excitation wavelength of 300 nm was used for all samples. Meanwhile, all emissions having wavelengths shorter than 420 nm were eliminated by a filter to highlight the peaks from the energy levels of defects. The wide emission peak located at wavelength of about 450 nm is attributed to the defect levels, e.g. oxygen vacancy. Any change in the PL intensities can be related to the recombination rate between the photogenerated electrons and holes.<sup>54,55</sup>

Since the trap levels play a positive role in reducing the recombination, low PL intensity is ascribed to a lower recombination rate, and, hence, a higher defect concentration. Therefore, it is again confirmed that decreasing the oxygen pressure results in the formation of more point defects.

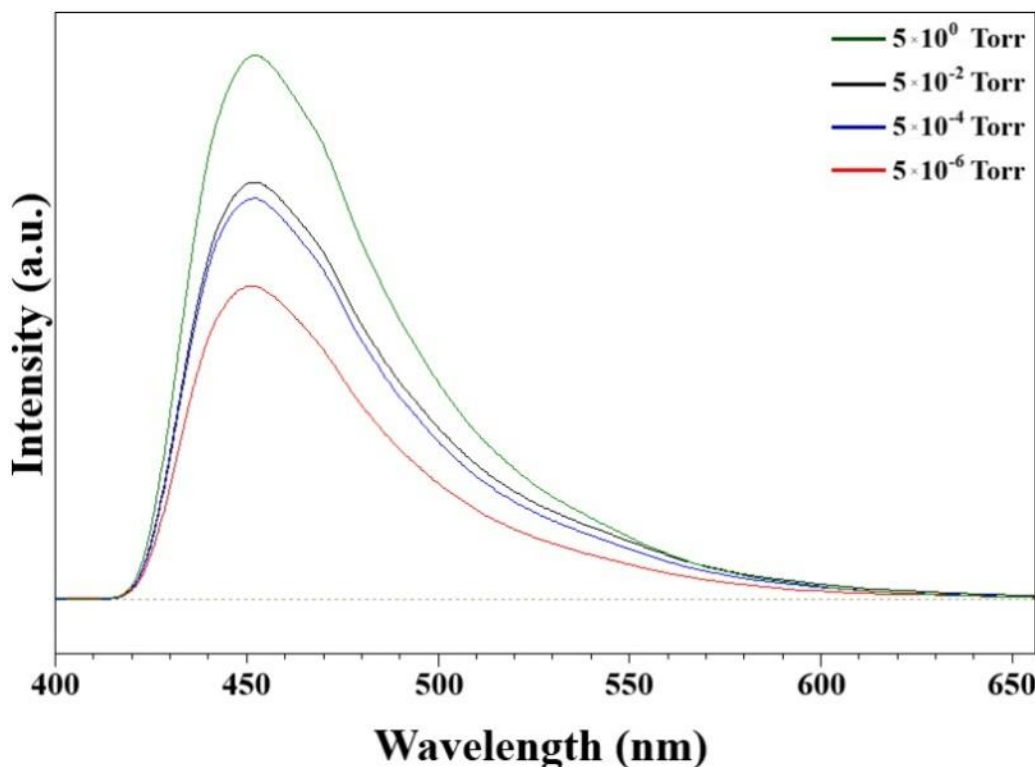


Fig.4.14. Room temperature PL spectra of the  $\text{TiO}_2$  films grown at 450  $^{\circ}\text{C}$  under various pressures.

#### 4.4. Conclusions

Rutile thin films with a (200) orientation on sapphire(0001) substrate were grown epitaxially via PLD method. It was found that the rutile phase forms at elevated temperatures and low ambient pressures; meanwhile, increasing the laser energy gave rise to film growth along [200] orientation and elimination of any other crystallographic orientations. The epitaxial relationship between the substrate and the rutile film was established as rutile(100)||sapphire(0001), rutile[001]||sapphire[10 $\bar{1}$ 0], and rutile[010]||sapphire[1 $\bar{2}$ 10]. UV-Vis spectrophotometry, PL, and XPS investigations showed that concentration of lattice point defects, namely oxygen vacancies and

titanium interstitials, increases at lower oxygen pressures. Films with smoother surfaces were obtained at higher laser energies and lower oxygen pressures.

## References

1. M.R. Bayati, A.Z. Moshfegh, and F. Golestani-Fard, *J. Appl. Catal. A* 389, 60 (2010).
2. M.R. Bayati, F. Golestani-Fard, and A.Z. Moshfegh, *Electrochim. Acta* 55, 3093 (2010).
3. M.R. Bayati, F. Golestani-Fard, and A.Z. Moshfegh, *J. Appl. Catal. A* 382, 322 (2010).
4. M.R. Bayati, F. Golestani-Fard, A.Z. Moshfegh, and R. Molaei, *Mater. Res. Bull.* 46, 531 (2011).
5. H. Park, W.R. Kim, H.T. Jeong, J.J. Lee, H.G. Kim, and W.Y. Choi, *Sol. Energy Mater. Sol. Cells* 95, 184 (2011).
6. J. Yu, Q. Li, and Z. Shu, *Electrochim. Acta* 56, 6293 (2011).
7. G.J. Yang, C.J. Li, S.Q. Fan, and J.C. Gao, *Surf. Coat. Technol.* 205, 3205 (2011).
8. C. Karunakaran, G. Abiramasundari, P. Gomathisankar, G. Manikandan, and V. Anandi, *Mater. Res. Bull.* 46, 1586 (2011).
9. B.S. Necula, I. Apachitei, F.D. Tichelaar, L.E. Fratila-Apachitei, and J. Duszczyk, *Acta Biomater.* 7, 2751 (2011).
10. M.R. Bayati and R. Molaei, *J. Phys. D: Appl. Phys.* 43, 505304 (2010).
11. K.X. Zhang, W. Wang, J.L. Hou, J.H. Zhao, Y. Zhang, and Y.C. Fang, *Vacuum* 85, 990 (2011).
12. M.R. Bayati, R. Molaei, and F. Golestani-Fard, *Colloid. Surf. A* 373, 51 (2011).
13. J. Moon, J. Park, S.J. Lee, T. Zyung, and I.D. Kim, *Sens. Actuators B* 149, 301 (2010).

14. S. Lin, D. Li, J. Wu, X. Li, and S.A. Akbar, *Sens. Actuators B* 156, 505 (2011).
15. C. Han, D. Hong, S. Han, J. Gwak, and K. Singh, *Sens. Actuators B* 125, 224 (2007).
16. A.A. Ashkarran, S.M. Aghigh, M. kavianipour, and N.J. Farahani, *Curr. Appl. Phys.* 11, 1048 (2011).
17. R. Khan and M. Dhayal, *Electrochem. Commun.* 10, 492 (2008).
18. K. Fröhlich, B. Hudec, J. Aarik, A. Tarre, D. Machajdík, A. Kasikov, K. Hušeková, and Š. Gaži, *Microelectron. Eng.* 88, 1525 (2011).
19. B. Hudec, K. Hušeková, A. Tarre, J.H. Han, S. Han, A. Rosová, W. Lee, A. Kasikov, S.J. Song, J. Aarik, C.S. Hwang, and K. Fröhlich, *Microelectron. Eng.* 88, 1514 (2011).
20. M. Popovici, M.S. Kim, K. Tomida, J. Swerts, H. Tielens, A. Moussa, O. Richard, H. Bender, A. Franquet, T. Conard, L. Altimime, S.V. Elshocht, and J.A. Kittl, *Microelectron. Eng.* 88, 1517 (2011).
21. B.B. Topuz, G. Gündüz, B. Mavis, and Ü. Çolak, *Dyes Pigm.* 90, 123 (2011).
22. M.R. Mahmoudian, W.J. Basirun, Y. Alias, and M. Ebadi, *Appl. Surf. Sci.* 257, 8317 (2011).
23. M.R. Bayati, A.Z. Moshfegh, and F. Golestani-Fard, *Mater. Lett.* 64, 2215 (2010).
24. A. Fujishima, X. Zhang, and D.A. Tryk, *Surf. Sci. Rep.* 63, 515 (2008).
25. N. Sbai, J. Perriere, W. Seiler, and E. Millon, *Surf. Sci.* 601, 5649 (2007).
26. J.F. Banfield, D.R. Veblen, and D.J. Smith, *Am. Mineral.* 76, 343 (1991).
27. C.T. Dervos, E. Thirios, J. Novacovich, P. Vassiliou, and P. Skafidas, *Mater. Lett.* 58, 1502 (2004).
28. G. Madras, B.J. McCoy, and A. Navrotsky, *J. Am. Ceram. Soc.* 90, 250 (2007).

29. D.H. Lindsley, Oxide Minerals: Petrologic and Magnetic Significance, *Rev. Mineral.* 25, 69 (1991).
30. J.C. Auger, B. Stout, R.G. Barrera, and F. Curiel, *J. Quant. Spectrosc. Radiative Transfer* 70, 675 (2001).
31. M. Cernea, M. Secu, C.E. Secu, M. Baibarac, and B.S. Vasile, *J. Nanopart. Res.* 13, 77 (2011).
32. M. Andersson, A. Kiselev, L. Osterlund, and A.E.C. Palmqvist, *J. Phys. Chem. C* 111, 6789 (2007).
33. S.K. Kim, S.W. Lee, J.H. Han, B. Lee, S. Han, and C.S. Hwang, *Adv. Funct. Mater.* 20, 2989 (2010).
34. U. Diebold, *Surf. Sci. Rep.* 48, 53 (2003).
35. A. Fujishima and K. Honda, *Nature* 238, 37 (1972).
36. D. Yoo, I. Kim, S. Kim, C. Hahn, C. Lee, and S. Cho, *Appl. Surf. Sci.* 253, 3888 (2007).
37. Y.Q. Hou, D.M. Zhuang, G. Zhang, M. Zhao, and M.S. Wu, *Appl. Surf. Sci.* 218, 97 (2003).
38. R.K. Singh and J. Narayan, *Phys. Rev. B* 41, 8843 (1990).
39. D.G. Syarif, A. Miyashita, T. Yamaki, T. Sumita, Y. Choi, and H. Itoh, *Appl. Surf. Sci.* 193, 287 (2002).
40. H. Long, G. Yang, A. Chen, Y. Li, and P. Lu, *Thin Solid Films* 517, 745 (2008).
41. S.D. Mo and W.Y. Ching, *Phys. Rev. B* 51, 13023 (1995).
42. S. Na-Phattalung, M.F. Smith, K. Kim, M.H. Du, and S.H. Wei, *Phys. Rev. B* 73, 125205.1 (2006).

43. S.W. Chan, *J. Phys. Chem. Solids* 55, 1137 (1994).
44. H. Zhou, M.F. Chisholm, T.H. Yang, S.J. Pennycook, and J. Narayan, *J. Appl. Phys.* 110, 073515.1 (2011).
45. J.J. Cappom, M. Marezio, J. Dumas, and C. Schienker, *Solid State Commun.* 20, 893 (1976).
46. M.A. Afifi, M.M. Abdel-Aziz, I.S. Yahia, M. Fadel, and L.A. Wahab, *J. Alloys Compnd.* 455, 92 (2008).
47. J. Narayan and B. C. Larson, *J. Appl. Phys.* 93, 278 (2003).
48. S. Mal, S. Nori, C.M. Jin, J. Narayan, S. Nellutla, A.I. Smirnov, and J.T. Prater, *J. Appl. Phys.* 108, 073510 (2010).
49. E. Finazzi, C.D. Valentin, and G. Pacchioni, *J. Phys. Chem. C* 113, 3382 (2009).
50. F.A. Kroger, *The Chemistry of Imperfect Crystals*, North Holland: Amsterdam, (1974).
51. M.K. Nowotny, T. Bak, and J. Nowotny, *J. Phys. Chem. B* 110, 16270 (2006).
52. M.K. Nowotny, L.R. Sheppard, T. Bak, and J. Nowotny, *J. Phys. Chem. C* 112, 5275 (2008).
53. T. Bak, J. Nowotny, M. Rekas, and C.C. Sorrell, *J. Phys. Chem. Solids* 64, 1057 (2003).
54. K.V. Baiju, A. Zachariah, S. Shukla, S. Biju, M.L.P. Reddy, and K.G.K. Warrier, *Catal. Lett.* 130, 130 (2009).
55. Y. Cong, J. Zhang, F. Chen, and M. Anpo, *J. Phys. Chem. C* 111, 6976 (2007).

## **Chapter 5**

# **Structure-Property Correlation in Epitaxial Rutile Films Grown on Sapphire(0001) Substrates by Pulsed Laser Deposition**

We have investigated the influence of the deposition variables on photocatalytic properties of epitaxial rutile films. Despite a large lattice misfit strain, rutile(100) epitaxial layers were grown on sapphire(0001) by domain matching epitaxy paradigm. Using  $\varphi$ -scan XRD and cross section TEM, the epitaxial growth was confirmed. Based on the XRD patterns, increasing the repetition rate introduced tensile stress along the film normal direction, which may arise as a result of trapped defects. Formation of such defects was studied by UV-Vis, PL, and XPS techniques. AFM studies showed that the film roughness increases with the repetition rate. Finally, photocatalytic performance of the layers was investigated through measuring the decomposition rate of 4-chlorophenol on the films surface. The films grown at higher frequencies revealed higher photocatalytic efficiency. The observed improvement of the photochemical properties was mainly related to the formation of point defects which enhance the charge separation.

## 5.1. Introduction

Owing to the technologically favorable characteristics, namely large refractive index,<sup>1</sup> high dielectric constant,<sup>2</sup> high photochemical activity,<sup>3</sup> high thermal<sup>4</sup> and photochemical stability,<sup>5</sup> titanium dioxide ( $\text{TiO}_2$ ) has been widely used in different applications in the past. Titania is known to exist primarily in three different crystal structures, i.e. rutile (tetragonal), anatase (tetragonal), and brookite (orthorhombic). The equilibrium phase is rutile which is stable at almost all temperatures. The metastable anatase phase, which is stable at low temperatures, transforms to rutile upon heating. Anatase is a low-temperature, metastable crystal and shows good photocatalytic properties.<sup>6</sup> It has been widely studied as a material for photocatalysis,<sup>7,8</sup> while other properties of anatase are less known than those of rutile. Brookite exists only in some extreme conditions, so it is not considered useful for practical applications. Other structures (e.g. Magneli phases, corundum sesquioxide, and so on) also exist under extreme conditions with no practical application.<sup>9</sup>

$\text{TiO}_2$  thin films have been grown by chemical vapor deposition,<sup>10</sup> physical vapor deposition,<sup>11</sup> sol gel,<sup>12</sup> micro arc oxidation,<sup>13</sup> hydrothermal,<sup>14</sup> pulsed laser deposition<sup>15</sup> methods. Among these methods, pulsed laser deposition (PLD) has emerged as a promising technique for the fabrication of nanostructures of complex multicomponent materials because of its non-equilibrium characteristics and the ability to control the dimensions and the crystalline phase of nanodeposits by varying the laser parameters and the deposition conditions. This technique is also suitable for depositing oxide films at relatively low temperatures.<sup>16-18</sup> PLD is extensively used in the deposition of complex

materials, especially multicomponent oxides,<sup>19,20</sup> nitrides,<sup>21</sup> polymers,<sup>22</sup> carbides,<sup>23</sup> etc. The quality of the films depends on various parameters like laser wavelength, energy, fluence, ambient pressure of the gas, substrate, target-substrate distance, and thermo-physical properties of the target material which include density, mass, absorption coefficient, etc. The optimization of these parameters to obtain high quality films for a desired application is, therefore, a critical part of PLD.

Even though numerous studies have focused on photocatalytic applications of anatase and anatase/rutile mixture,<sup>24-26</sup> only a few have been dedicated to the photocatalytic property of pure rutile which can be used as a visible-light-responsive material, due to its 3.0 eV band gap. Here, we focus on structure-property correlation of epitaxial rutile films grown on c-sapphire substrates. Previous studies did not address control of phase purity, defect, and epitaxial growth and their role on photocatalytic properties of rutile films. In this study, we deposited epitaxial rutile TiO<sub>2</sub> thin films by pulsed laser deposition (PLD) technique at various repetition rates (frequencies). We show that more defective films, grown at higher repetition rates, have higher photocatalytic efficiency; whereas, films grown at lower frequencies contained less defects with reduced photocatalytic activity.

## 5.2. Experimental

TiO<sub>2</sub> thin films were deposited on single crystal *c*-sapphire (Al<sub>2</sub>O<sub>3</sub>) substrates by PLD method. The substrates were initially cleaned through a multi-step procedure including boiling in hot acetone for 15 min., ultrasonic cleaning in acetone for 5 min.

followed by ultrasonic cleaning in methanol for 5 min. both at room temperature. The cleaned substrates were fully dried by nitrogen gun and, then, loaded into the deposition chamber where the target-substrate distance was 4.5 cm. The chamber was evacuated to a base pressure of  $\sim 1 \times 10^{-6}$  Torr before injecting oxygen into the chamber to control the ambient pressure. A KrF excimer laser ( $\lambda=248$  nm,  $\tau=25$  ns) was employed to ablate the TiO<sub>2</sub> target which was being rotated during the deposition in order to provide a uniform ablation and avoid pitting on the target surface. Laser fluence, oxygen pressure, deposition time, and substrate temperature were the same for all samples as 3.5-4.5 J.cm<sup>-2</sup>,  $5 \times 10^{-4}$  Torr, 20 min., and 450 °C, respectively. Different repetition rates of 1, 10, 20, and 30 Hz were applied in order to study the effect of this parameter on the properties of the layers. Immediately after deposition, the layers were thermally annealed inside the PLD chamber for 60 min. at 450 °C under oxygen pressure of  $5 \times 10^{-4}$  Torr.

The crystalline structure of the TiO<sub>2</sub> films was investigated by  $\theta$ -2 $\theta$  scanning using a Rigaku X-ray diffractometer with Cu-K $\alpha$  radiation ( $\lambda=0.154$  nm). The  $\theta$ -2 $\theta$  scans provide out-of-plane orientation and lattice spacing for film planes parallel to the substrate. A Philips X-Pert Pro X-ray diffractometer was employed for  $\varphi$ -scanning XRD to determine in-plane orientation of TiO<sub>2</sub> films. In order to determine surface chemical composition and stoichiometry of the layers, X-ray photoelectron spectroscopy (XPS) was performed employing a Riber instrument with an Mg-K $\alpha$  X-ray source. The samples were sputtered by Ar<sup>+</sup> bombardment for 5 minutes prior to acquiring data in order to remove any probable surface contamination. Interpretation of the XPS results was

performed using SDP ver.4.1 software. Morphology of the layers was studied by a Veeco AFM as well and the obtained results were interpreted by nanoscope ver. 5.12r3 software. Optical properties of the films were studied by a U-3010 Hitachi UV-Vis spectrophotometer. The room temperature photoluminescence (PL) spectra of the samples were recorded with a fluorescence spectrophotometer (Hitachi, F-2500) where the excitation wavelength of 300 nm was used for all samples. Meanwhile, all emissions having wavelengths shorter than 420 nm were eliminated by a filter in order to highlight the peaks due to defect energy levels. The samples were masked during deposition, and their thickness was determined by a Tencor Alpha Step stylus profilometer. A JEOL-2000 FX TEM was also used to perform diffraction and imaging studies in cross section to confirm the epitaxial growth of the TiO<sub>2</sub> layers. Finally, photocatalytic activity of the TiO<sub>2</sub> layers was evaluated by measuring the degradation rate of aqueous 4-chlorophenol solution at room temperature, as it was explained in chapter 3.

### **5.3. Results and discussion**

#### **5.3.1. Phase structure**

Fig.5.1 shows XRD phase structure of the layers grown at different repetition rates where rutile(200) and sapphire(006) characteristic peaks are labeled by R and S letters, respectively. The patterns reveal that highly textured layers have been deposited. As is seen, the intensity of the rutile peak increases with the frequency. The reason for this behavior is likely the deposition rate which increases with the repetition rate. As a

result, thicker layers grow when higher repetition rates are applied. Thickness of the layers was measured as 418, 430, 690, and 990 nm for the repetition rates of 1, 10, 20, and 30 Hz, respectively. Meanwhile, high resolution  $\theta$ - $2\theta$  scanning was performed to determine the exact diffraction angle of the rutile(200) peak whose results are provided in the inset of Fig.5.1.

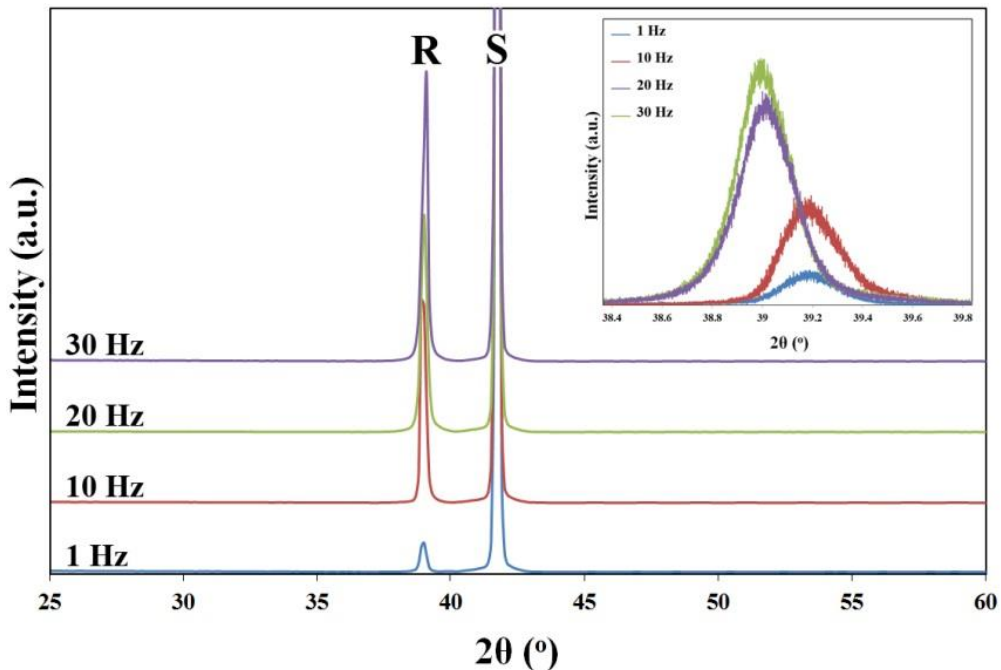


Fig.5.1. Effect of the repetition rate on phase structure of the rutile films.

It is observed that the rutile peak shifts toward smaller  $2\theta$  values than the diffraction angle of the bulk rutile(200) peak ( $2\theta=39.187^\circ$ ) with increasing repetition rate. This phenomenon indicates introduction of tensile stain along the direction perpendicular to the substrate surface which presumably arises from introduction of defects into the rutile crystalline lattice. At higher repetition rates, namely 30 Hz, flux of

the ablated species approaching the substrate is so high and, therefore, they do not have enough time to diffuse to equilibrium positions on the substrate surface. This enhanced non-equilibrium condition gives rise to formation of a defect-rich film. Considering the XRD peak shift toward smaller diffraction angle, it may be concluded that increasing the repetition rate leads to formation of high concentration of oxygen vacancies. Full Width at Half Maximum (FWHM) of the rutile(200) peaks were determined ranging from 0.20 to 0.29 for different repetition rates.

### 5.3.2. Optical properties

Photoluminescence (PL) spectroscopy technique was also employed to study defect content in the films and the results are shown in Fig.5.2.

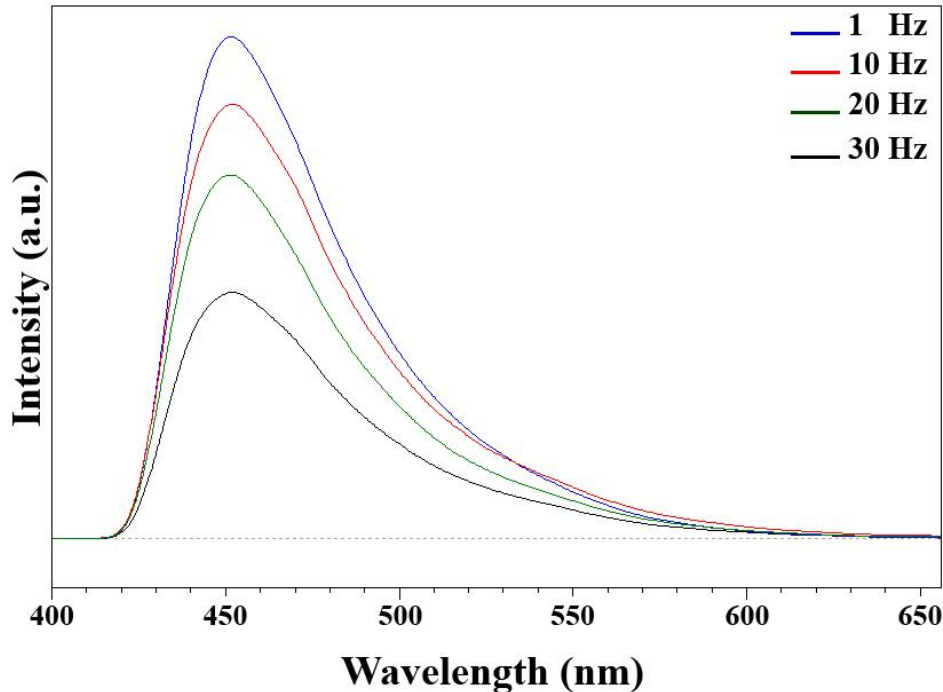


Fig.5.2. Room temperature PL spectra of the rutile films grown at different frequencies.

The wide emission peak located at wavelength of about 450 nm is attributed to the oxygen vacancy levels.<sup>27,28</sup> Any change in the PL intensities can be related to the recombination rate between the photogenerated electrons and holes.<sup>28,29</sup> Since the trap levels play a positive role in reducing the recombination, low PL intensity is ascribed to a lower recombination rate, and, hence, higher defect concentrations. Therefore, it is further ascertained that more oxygen vacancies form when the films are deposited at higher frequencies or repetition rates. UV-Vis transmittance spectra of the rutile films deposited at different repetition rates are shown in Fig.5.3.

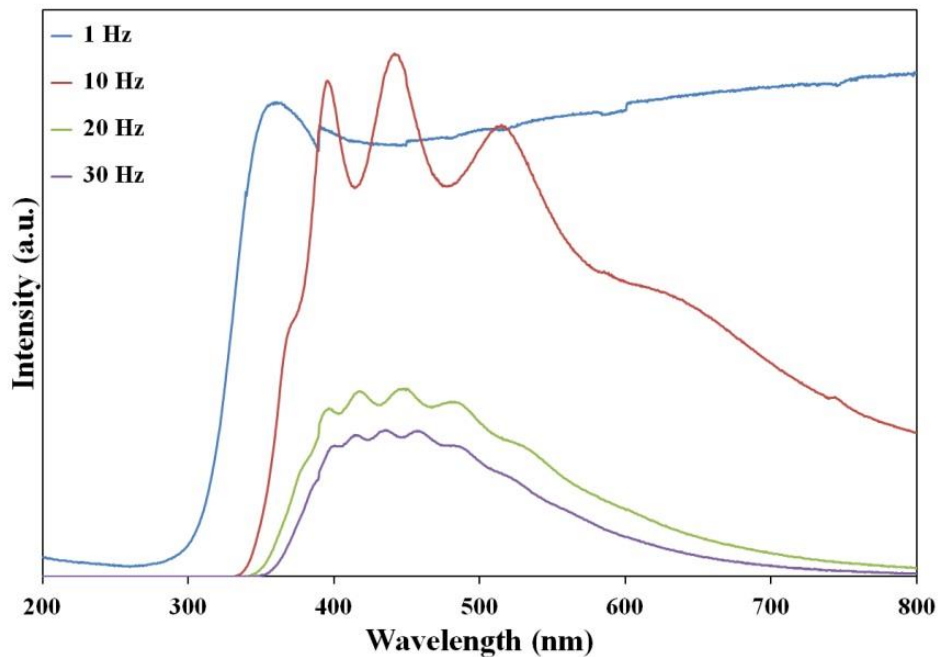


Fig.5.3. Transmittance spectra of the rutile films grown at different frequencies.

It was found that visible transmittance of the layers decreases with the repetition rate, which indicates creation of more structural defects at higher repetition rates. This

suggestion is further confirmed by the sharper absorption edge of the layers grown at lower repetition rates, i.e. 1 and 10 Hz, which reveals less defect concentration in these films. Another reason for lower transmittance within the visible region might be the thickness of the films which increases with the repetition rate, as explained before. The oscillations in the spectra are caused by light interference at the film/substrate interface and are attenuated when the grown films get thicker. These oscillations appear when a transparent thin film of a material having a high refractive index ( $n=2.6$  for rutile) is deposited on a substrate with a lower refractive index ( $n=1.7$  for sapphire).

### 5.3.3. Stoichiometry

XPS technique was employed to study stoichiometry as well as defect content of the layers and the results are shown in Fig.5.4. As is observed, the O(1s) core level binding energy has been fitted by 4 distinct peaks. Peak A, located at a binding energy of around 531.8 eV, corresponds to the  $O^{2-}$  ions in oxygen deficient regions and its intensity is associated with the concentration of oxygen vacancies ( $V_O$ ). Peak B, having a binding energy of 530.2 eV, belongs to the oxygen ions in the crystalline lattice of perfect  $TiO_2$ . Peaks C and D, with binding energies of 528.1 and 527.2 eV, may represent oxygen atoms in contact with  $Ti_i^{3+}$  and  $Ti_i^{4+}$  defects.<sup>30</sup> When a titanium interstitial cation locates in rutile crystalline lattice, it attracts the electron cloud between neighboring Ti and O atoms resulting in decrease of the energy of the neighboring Ti-O bond. In conclusion, peaks A, C and D in O(1s) core level reflect defects content in the grown rutile films. A small peak shift is also observed for these peaks whose reason can be

variation of defect concentration. Results reveal that more defects form in the crystalline lattice when higher repetition rates are applied, as discussed earlier in section 5.3.1.

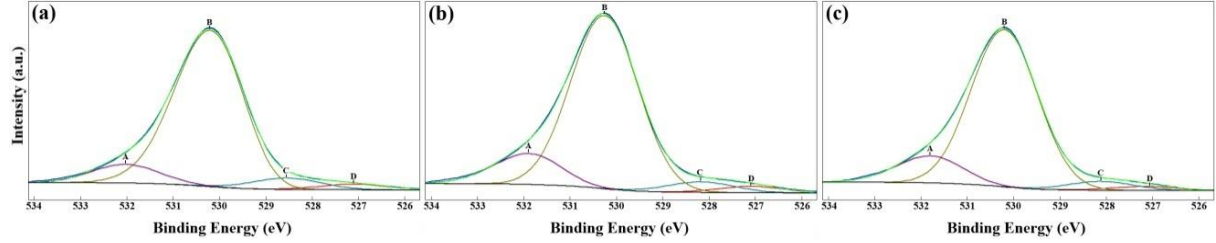


Fig.5.4. O(1s) XPS core level binding energy in the rutile films grown at different frequencies: (a) 1, (b) 20, and (c) 30 Hz.

#### 5.3.4. Epitaxial relationship

The  $\varphi$ -scan XRD was employed to confirm the epitaxial growth and determine the in-plane alignment of the (200) oriented rutile  $\text{TiO}_2$  films on the *c*-sapphire substrate (Fig.5.5). To acquire these patterns,  $(01\bar{1}2)$  plane of substrate ( $2\theta=25.58^\circ$ ,  $\psi=57.70^\circ$ ) and  $(110)$  plane of rutile ( $2\theta=27.44^\circ$ ,  $\psi=45.00^\circ$ ) were selected as the reflection planes and the epitaxial relationship was established as out-of-plane alignment: rutile(100)||sapphire(001); in-of-plane alignment: rutile[001]||sapphire[10\bar{1}0] and rutile[010]||sapphire[1\bar{2}10]. Three  $(01\bar{1}2)$  reflection intense peaks with a  $120^\circ$  interval originate from the threefold symmetry of the sapphire substrate. Considering 6 symmetrical peaks of rutile film having intervals of  $60^\circ$ , it is demonstrated that the film consists of three domains rotated by  $120^\circ$ . In other words, the orientation of the rutile film grown on the *c*-sapphire is affected by three fold symmetry of the *c*- $\text{Al}_2\text{O}_3$ .

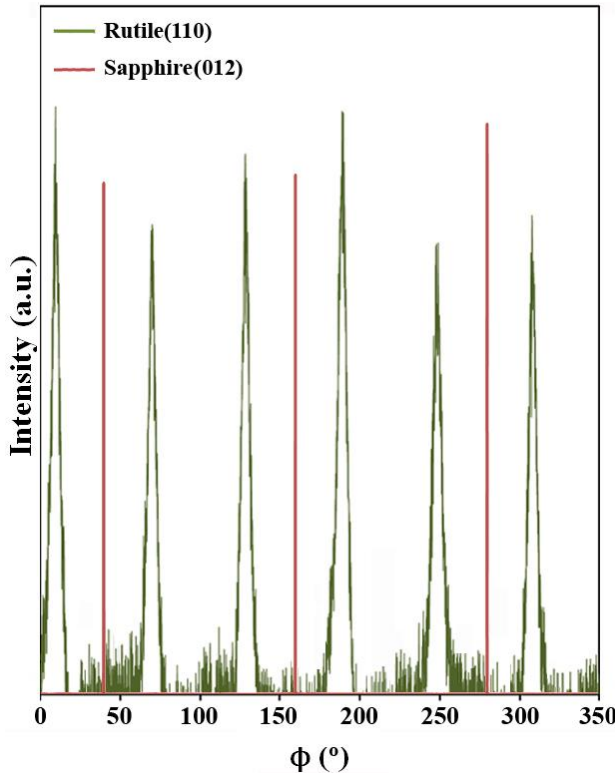


Fig.5.5. XRD  $\varphi$ -scan of the rutile(110) and sapphire(0112) reflection planes.

Fig.5.6 shows TEM cross section BF-image of the rutile/sapphire sample prepared at repetition rate of 1 Hz where formation of columnar structure is evident. The columnar grain structure indicates that the threefold mosaic structure was initiated on the substrate surface via the nucleation of the three variants. The epitaxial growth as well as the proposed epitaxial relationship was confirmed by TEM-SAD pattern, depicted in the inset of Fig.5.6. Indexing of this pattern shows that the diffraction spots are from the [001] zone axis of the rutile film and the [1010] zone axis of sapphire. Hence, it can be concluded that the rutile layer is single crystalline and grows epitaxially on a *c*-sapphire substrate with the proposed orientation relationship which is schematically illustrated in Fig.5.7.

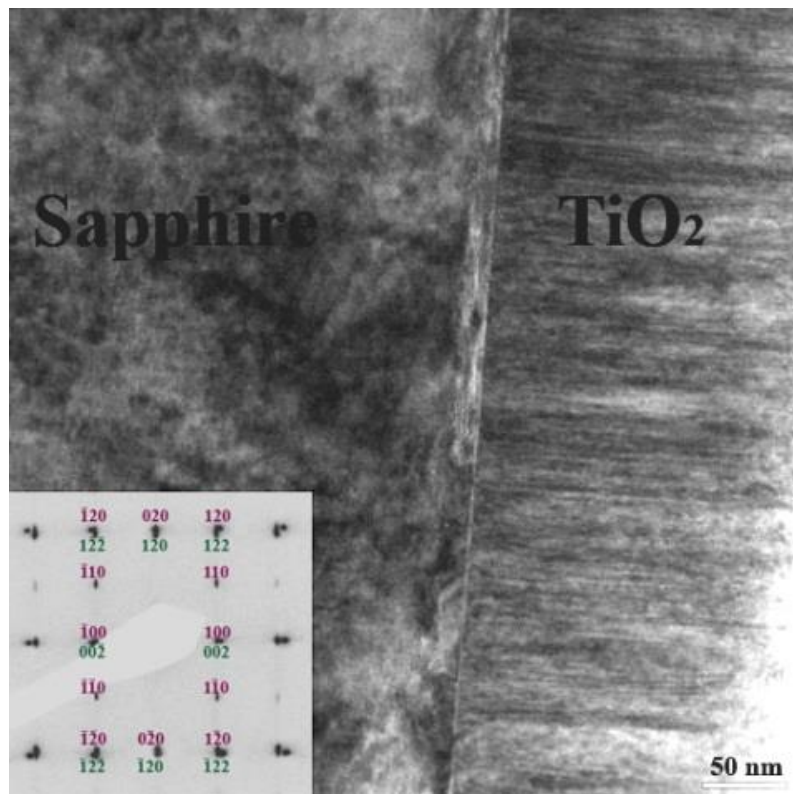


Fig.5.6. TEM bright field image and indexed SAED pattern of the film/substrate interface (Rutile[001] and Sapphire[10̄10] zones, film: red, substrate: green).

The rutile(110) and sapphire(01̄12) reflection planes, used for  $\varphi$ -scan XRD, are also shown in green in this figure. Lattice misfits at the film/substrate interface are calculated as follows:

$$\varepsilon_b = 1 - (4.59/4.76) = +3.57\% \quad (5-1)$$

$$\varepsilon_c = 1 - (2.96/4.12) = +28.15\% \quad (5-2)$$

where  $\varepsilon_b$  and  $\varepsilon_c$  are the lattice misfits along b and c directions of the film. According to the domain matching epitaxy (DME) paradigm,<sup>31</sup> these misfits are

accommodated by matching of integral multiples of lattice planes. Along the  $b$ -axis, 28 planes of the film match with 27 planes of the substrate with a frequency factor of  $\alpha = 0$  to fully relax the misfit strain. Such a frequency factor shows that there is perfect 28/27 integral multiple matching with one dislocation every 27 planes. Meanwhile, the misfit strain along the  $c$ -direction of rutile is relaxed when 4/3 and 3/2 domains alternate with a relative frequency of 0.55.

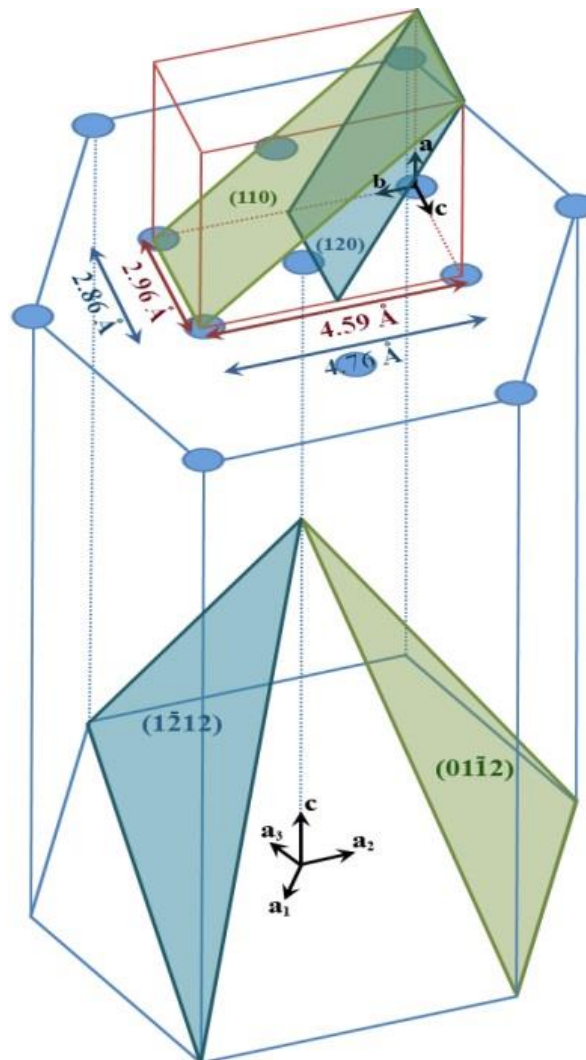


Fig.5.7. Schematic illustration of plausible growth mechanism of rutile  $\text{TiO}_2$  on  $c$ -sapphire.

### 5.3.5. Morphology

AFM surface morphology of the rutile films is shown in Fig.5.8 where formation of nanostructured films is obvious. Surface roughness of the layers was determined as 0.9, 2.1, 7.3, and 8.5 nm for repetition rates of 1, 10, 20, and 30 Hz. At low frequencies, the deposition rate is low and the ablated species have enough time to diffuse across the substrate surface and find appropriate surface positions and create a smooth surface. In contrast, when high frequencies, i.e. 20 and 30 Hz, are applied, the adatoms do not have enough time to locate on proper surface sites with the lowest free energy.

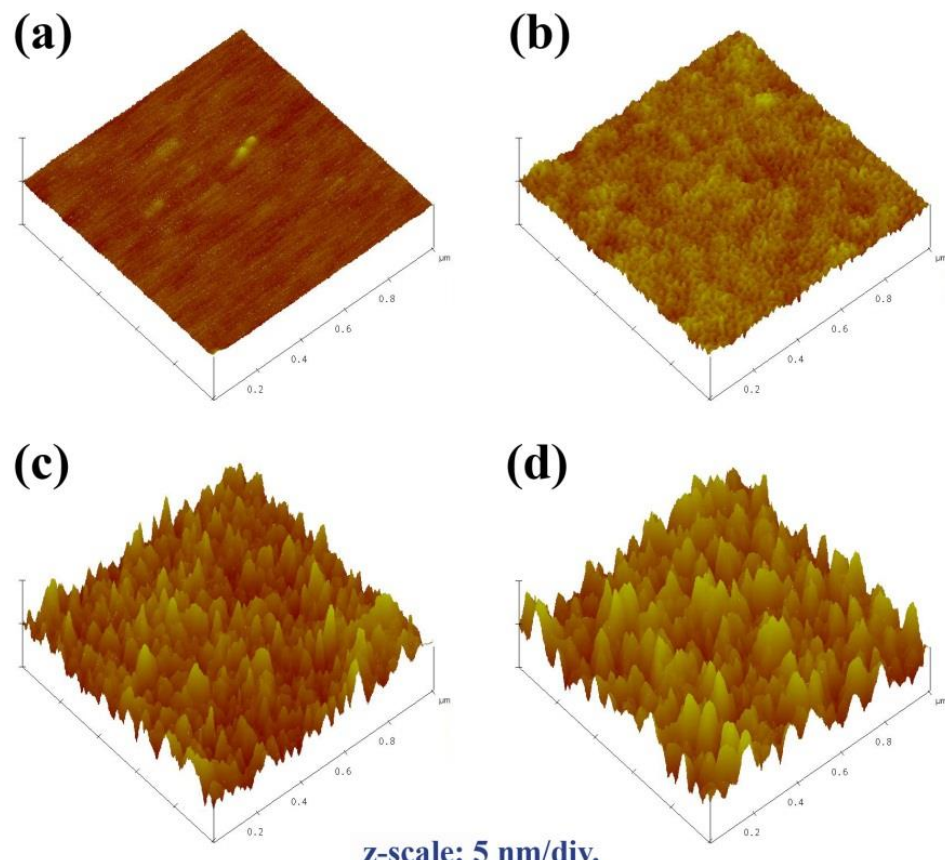


Fig.5.8. AFM surface morphology of the  $\text{TiO}_2$  films grown at frequencies of: (a) 1, (b) 10, (c) 20, and (d) 30 Hz.

### 5.3.6. Photocatalytic activity

Results of photocatalytic experiments are shown in Fig.5.9. Results show that the concentration of 4CP decreases with illumination time; that is, 4CP is photocatalytically decomposed by the UV-activated  $\text{TiO}_2$  films.

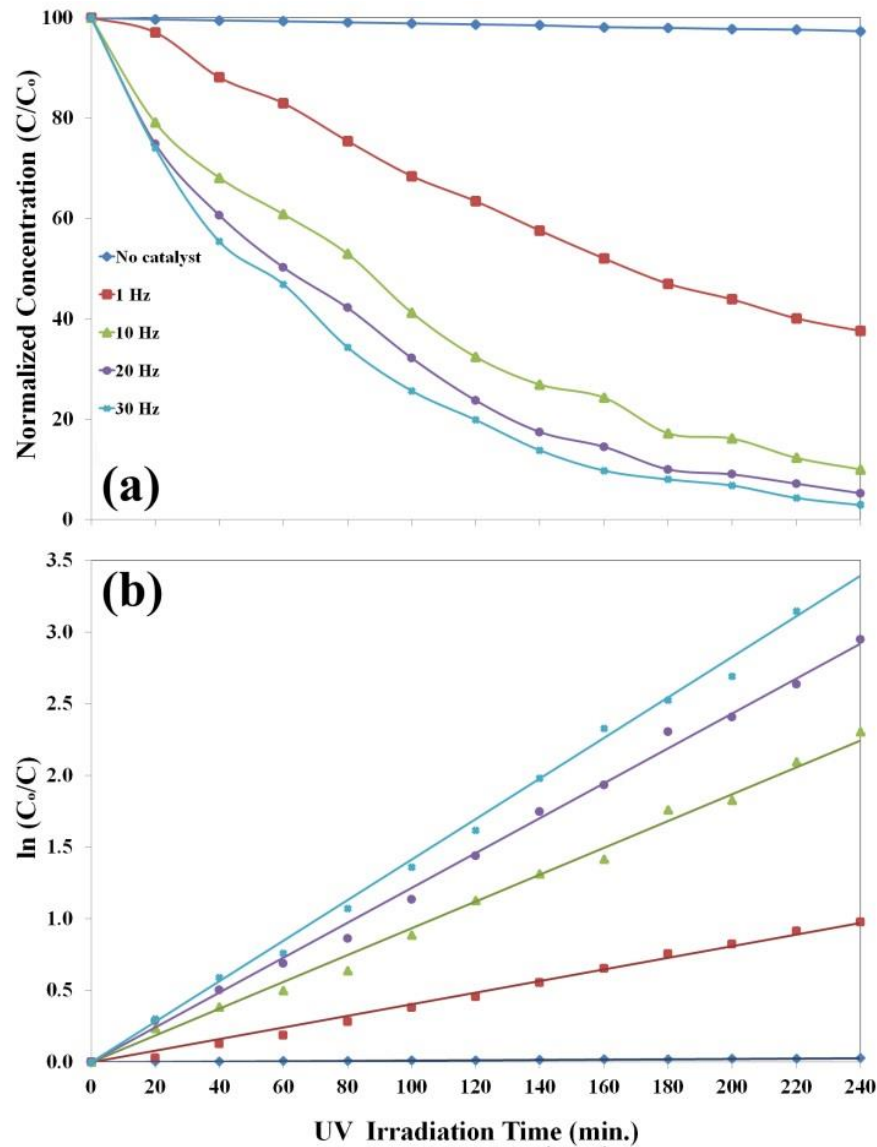


Fig.5.9. Photocatalytic activity of the rutile  $\text{TiO}_2$  thin films: (a) normalized concentration of 4CP and (b)  $\ln(C_0/C)$  at different UV-irradiation times.

It should be noted that the curve “No catalyst” belongs to the experiment where no sample was used as catalyst and only the 4CP solution was irradiated by the UV light. This experiment was considered as the reference point. In order to quantitatively compare the photocatalytic activity of the layers, the photocatalytic reaction rate constants ( $k$ ) should have been calculated. Since photocatalytic decomposition of 4CP solution agrees with pseudo-first-order kinetics, the constant ( $k$ ) can be calculated by the equation  $\ln(C/C_0) = -kt$  (where  $C_0$  is the initial concentration of 4CP at  $t=0$  and  $C$  represents the concentration of 4CP at later times  $t$ ). The quantity  $\ln(C_0/C)$  versus irradiation time was plotted for different repetition rates. Straight lines, whose slopes represent  $k$ , indicate that the degradation of 4CP is a first order reaction. The reactions rate values (listed in Tab.5.1) show that the photocatalytic activity increases with repetition rate.

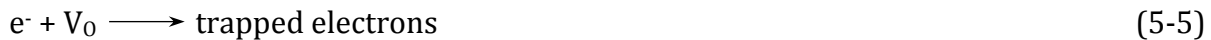
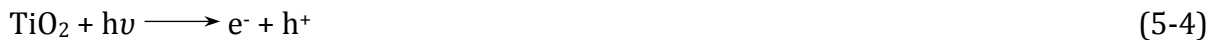
Tab.5.1. Photocatalytic reaction rate constants ( $k$ ) as a function of the frequency.

Frequency (Hz)	1	10	20	30
$k$ (min. <sup>-1</sup> )	0.00431	0.00952	0.01210	0.01440

$k$  for “No catalyst” experiment = 0.000109 min.<sup>-1</sup>

Two reasons can be proposed for this behavior. Firstly, the effective surface area of the grown catalysts, where photocatalytic reactions take place, increases at higher repetition rates, as is seen in Fig.5.9. Secondly, it was already shown that films with higher defect content grow when higher repetition rates are applied. The structural defects, namely  $V_0$ , trap photogenerated electrons and, consequently, lead to enhanced

charge separation so that positive holes, which are prerequisite for photocatalytic decomposition of 4CP, can participate in reactions without recombination. According to the literature<sup>32</sup> and our results, the following reactions are put forward for photocatalytic degradation of 4CP over defected rutile TiO<sub>2</sub> catalysts:



#### 5.4. Conclusions

The rutile epitaxial layers with a (200) orientation were grown on *c*-cut sapphire substrate employing PLD technique. The rutile(200) characteristic peak was observed to shift toward smaller 2θ values as the repetition rate increased. The reason for such a behavior was assumed to be developing a tensile stress along out-of-plane direction due to formation of oxygen vacancies. The films grown at higher repetition rates revealed a rougher surface which was suitable for photocatalytic application. These rutile films grown at higher repetition rates exhibited higher photocatalytic efficiency and could decompose about 97% of 4CP after 240 min. under UV-irradiation. Since the TiO<sub>2</sub> films present a (200) surface, the observed photocatalytic activity is attributed to (200) surface morphology and defect structure.

## References

1. Y. Yamada, H. Uyama, T. Murata, and H. Nozoye, Vacuum 66, 347 (2002).
2. G. Liu, W. Jian, H. Jin, Z. Shi, and G. Qiao, Script. Mater. 65, 588 (2011).
3. F. Dong, H. Wang, Z. Wu, and J. Qiu, J. Colloid Interface Sci. 343, 200 (2010).
4. Y. Li, X. Sun, H. Li, S. Wang, and Y. Wei, Powder Technol. 194, 149 (2009).
5. D. Li, H. Huang, X. Chen, Z. Chen, W. Li, D. Ye, and X. Fu, J. Solid State Chem. 180, 2630 (2007).
6. A. Fujishim, X. Zhang, and D.A. Tryk, Surf. Sci. Rep. 63, 515 (2008).
7. F.G. Gassim, A.N. Alkhateeb, and F.H. Hussein, Desalin. 209, 342 (2007).
8. L.H. Kao, T.C. Hsu, and K.K. Cheng, J. Colloid Interface Sci. 341 (2010) 359-365.
9. R. Roy and W.B. White, J. Cryst. Growth 14, 78 (1972).
10. H. Xie, L. Zhu, L. Wang, S. Chen, D. Yang, L. Yang, G. Gao, and H. Yuan, Particuology 9, 75 (2011).
11. P. Singh and D. Kaur, Physica B: Condensed Matter. 405, 1258 (2010).
12. N. Zhao, M. Yao, F. Li, and F. Lou, J. Solid State Chem. 184, 2770 (2011).
13. M.R. Bayati, A.Z. Moshfegh, and F. Golestani, Electrochim. Acta 55, 3093 (2010).
14. Y. Huang, G. Xie, S. Chen, and S. Gao, J. Solid State Chem. 184, 502 (2011).
15. G. Socol, Y. Gnatyuk, N. Stefan, N. Smirnova, V. Djokić, C. Sutan, V. Malinovschi, A. Stanculescu, O. Korduban, and I.N. Mihailescu, Thin Solid Films 518, 4648 (2010).
16. D.B. Chrisey and G.K. Huber (Eds.), Pulsed Laser Deposition of Thin Films, New York: Wiley, (1994).
17. R.K. Singh and J. Narayan, Phys. Rev. B 41, 8843 (1990).

18. R. Eason (Ed.), Pulsed laser deposition of thin films: Applications-led growth of functional materials, New York: Wiley, (2006).
19. W. Wei, S. Nori, C. Jin, J. Narayan, R.J. Narayan, D. Ponarin, and A. Smirnov, Mater. Sci. Eng. B 171, 90 (2010).
20. S. Mal, T.H. Yang, P. Gupta, J.T. Prater, and J. Narayan, Acta Mater. 59, 2526 (2011).
21. F. Tian and E.F. Chor, Thin Solid Films 518, e121 (2010).
22. R. Cristescu, C. Popescu, A. Popescu, S. Grigorescu, I.N. Mihailescu, D. Mihaiescu, S.D. Gittard, R.J. Narayan, I. Stamatin, and D.B. Chrisey, Appl. Surf. Sci. 255, 9873 (2009).
23. R. Teghil, A. De Bonis, A. Galasso, P. Villani, A. Santagata, D. Ferro, and S.M. Barinov, Appl. Surf. Sci. 255, 5220 (2009).
24. M.R. Bayati, F. Golestani-Fard, and A.Z. Moshfegh, Mater. Chem. Phys. 120, 582 (2010).
25. M.R. Bayati, F. Golestani-Fard, A.Z. Moshfegh, and R. Molaei, Mater. Chem. Phys. 128, 427 (2011).
26. M.R. Bayati, R. Molaei, A. Kajbafvala, S. Zanganeh, H.R. Zargar, and K. Janghorban, Electrochim. Acta 55, 5786 (2010).
27. Q. Xiao, L. Ouyang, L. Gao, and W. Jiang, Mater. Chem. Phys. 124, 1210 (2010).
28. Y. Cong, J. Zhang, F. Chen, and M. Anpo, J. Phys. Chem. C. 111, 6976 (2007).
29. K.V. Baiju, A. Zachariah, S. Shukla, S. Biju, M.L.P. Reddy, and K.G.K. Warrier, Catal. Lett. 130, 130 (2009).
30. B. Liu, X. Zhao, Q. Zhao, X. He, and J. Feng, J. Electron. Spectrosc. Relat. Phenom. 148, 158 (2005).

31. J. Narayan and B.C. Larson, *J. Appl. Phys.* 93, 278 (2003).
32. Y. Cheng, H. Sun, W. Jin, and N. Xu, *Chem. Eng. J.* 128, 127 (2007).

## **Chapter 6**

# **Domain Epitaxy in $\text{TiO}_2/\alpha\text{-Al}_2\text{O}_3$ Thin Film Heterostructures with $\text{Ti}_2\text{O}_3$ Transition Layer**

Rutile  $\text{TiO}_2$  films were grown epitaxially on  $\alpha$ -alumina (sapphire(0001)) substrates and characterized by X-ray diffraction and scanning transmission electron microscopy. It was revealed that the rutile film initially grows pseudomorphically on sapphire as  $\text{Ti}_2\text{O}_3$  and, after a few monolayers, it grows tetragonally on the  $\text{Ti}_2\text{O}_3$ /sapphire platform. Formation of the  $\text{Ti}_2\text{O}_3$  transient layer was attributed to the symmetry mismatch between the tetragonal structure of  $\text{TiO}_2$  and the hexagonal structure of alumina. The separation between the  $\frac{1}{2}[10\bar{1}](101)$  misfit dislocations was dictated by  $\text{Ti}_2\text{O}_3$  and was determined to be  $9.7\text{\AA}$  which is consistent with  $4/3$  and  $3/2$  alternating domains across the film/substrate interface.

### **6.1. Introduction**

Titanium dioxide ( $\text{TiO}_2$ ) is one of the most important semiconductor materials which has been widely used in a wide range of applications. It primarily crystallizes in three different phases, i.e. rutile (tetragonal), anatase (tetragonal), and brookite

(orthorhombic), among which the rutile state is the most stable one. It has a tetragonal lattice with  $P4_2/mnm$  space group and lattice parameters of  $a=b=4.5933$  and  $c=2.9592$  Å.<sup>1</sup> The band gap and refractive index in bulk are about 3.0 eV and 2.9, respectively.<sup>2,3</sup> These unique characteristics as well as its high thermal stability make rutile a promising candidate for many applications such as solar cells,<sup>4</sup> superomniphobicity,<sup>5</sup> photonic crystals,<sup>6</sup> capacitors,<sup>7</sup> ferroelectrics,<sup>8</sup> magnetism,<sup>9</sup> photocatalysis,<sup>10,11</sup> sensors,<sup>12</sup> photoconductors,<sup>13</sup> photodetectors,<sup>14</sup> and so on. Its strong oxidizing power is valuable for hydrogen generation. In addition to the aforementioned promising properties, rutile is biologically and chemically inert, cost-effective, and stable against photo-corrosion and chemical corrosion.<sup>14,15</sup>

Epitaxial growth of  $TiO_2$  thin films on the sapphire substrate (Rhombohedral with the  $R\bar{3}c$  space group,  $a=4.7587$  and  $c=12.9929$  Å,  $\gamma=120^\circ$ ) is important from technological point of view, since it leads to integration of functionalities with improved and novel smart device structures. It is also interesting from a scientific viewpoint, because a tetragonal lattice is juxtaposed with a hexagonal lattice in the rutile/sapphire heterostructures. As a consequence, the atomic arrangement across the film/substrate interface and the transition from the 3-fold hexagonal symmetry to the 2-fold tetragonal symmetry are surmised to play a critical role in controlling the properties of the  $TiO_2$ /sapphire heterostructures.

Although the epitaxial rutile/sapphire(0001) heterostructures have been grown<sup>9,16-18</sup> by different techniques, there is no detailed study on the nature of the interfaces in this system. In the present chapter, the  $TiO_2$  thin films are epitaxially

grown on the sapphire substrates by pulsed deposition technique where high quality films are obtained by optimizing the laser and substrate variables.<sup>19,20</sup> The atomic and the crystallographic arrangements across the film/substrate interface as well as the boundaries between the rutile adjacent grains are investigated using X-ray diffractometry ( $\theta$ - $2\theta$  and  $\varphi$  scan) and aberration-corrected scanning transmission electron microscopy. It is revealed that a  $\text{Ti}_2\text{O}_3$  transient layer with a rhombohedral structure forms initially onto the sapphire substrate which serves as a template for epitaxial growth of tetragonal rutile  $\text{TiO}_2$ . The separation of misfit dislocations is dictated by the lattice relaxation at the  $\text{TiO}_2/\text{Ti}_2\text{O}_3$  interface.

## 6.2. Experimental

$\text{TiO}_2$  thin films were grown on single crystal sapphire(001) substrates by pulsed laser deposition technique. A Lambda Physik (LPX200) KrF excimer laser ( $\lambda = 248 \text{ nm}$ ,  $\tau = 25 \text{ ns}$ ) was employed to ablate the  $\text{TiO}_2$  target which was being rotated during the deposition to provide a uniform ablation. Prior to the film deposition, the substrates were cleaned by degreasing in hot acetone for 15 min., ultrasonic cleaning in acetone for 5 min. followed by ultrasonic cleaning in methanol for 5 min. at room temperature. Finally, the substrates were fully dried by nitrogen gun and loaded into the deposition chamber immediately. Laser energy density, repetition rate, and the target-substrate distance used for deposition were as follows:  $3.5\text{-}4.0 \text{ J.cm}^{-2}$ , 10 Hz, and 4.5 cm. The chamber was evacuated to a base pressure of  $\sim 1\times 10^{-6}$  Torr and, then, oxygen partial pressure was increased to  $5\times 10^{-4}$  Torr for deposition. Meanwhile, the films were

deposited at 450 °C. The layers were subjected to thermal annealing for 1 hour, immediately after deposition inside the PLD chamber, at 450 °C under the pressure of  $5 \times 10^{-4}$  Torr.

The in-plane and out-of-plane orientations of the rutile TiO<sub>2</sub> films were determined by  $\varphi$  and 2θ-θ scans of XRD using a Philips X'Pert Pro X-ray diffractometer and a Rigaku X-ray diffractometer, respectively. An aberration corrected UltraSTEM 200 operated at 200 kV was used to investigate the atomic and crystallographic arrangements across the interfaces and to confirm the epitaxial growth of the layers. The aberration corrector improved the spatial resolution of the microscope to 0.78 Å; therefore, direct imaging of the interface atomic structure was permitted.<sup>21</sup>

### 6.3. Results and discussion

Fig.6.1a shows the θ-2θ X-ray diffraction pattern of the rutile TiO<sub>2</sub> thin film grown on the sapphire(001) substrate. The pattern reveals formation of a highly textured or epitaxial layer along the *a*-axis of rutile. Hence, the out of plane alignment of the rutile film is expressed as (100)<sub>rutile</sub>||(0001)<sub>sapphire</sub>. In addition, Fig.6.1b depicts the  $\varphi$ -scan pattern performed on (110) reflection of rutile ( $2\theta=27.44^\circ$ ,  $\psi=45.00^\circ$ ) and (01 $\bar{1}$ 2) reflection of sapphire ( $2\theta=25.58^\circ$ ,  $\psi=57.70^\circ$ ) where 3 symmetrical peaks appear with azimuthal intervals of  $60^\circ$  and a  $30^\circ$  angular separation from the sapphire peak. As schematically illustrated in Fig.6.1c, the rutile film consists of three domains rotated by  $120^\circ$ . The reason behind this particular arrangement is that a tetragonal unit cell with a 2-fold symmetry matches with a hexagonal unit cell with a 3-fold symmetry in the

$\text{TiO}_2/\text{Al}_2\text{O}_3$  system. It is worth noting that the [010] direction of rutile can orient with any of the three equivalent  $[10\bar{1}0]$  directions of c-sapphire. Consequently, there are three equal domain variants in the  $\text{TiO}_2$  film, with a boundary angle of  $60^\circ$ .

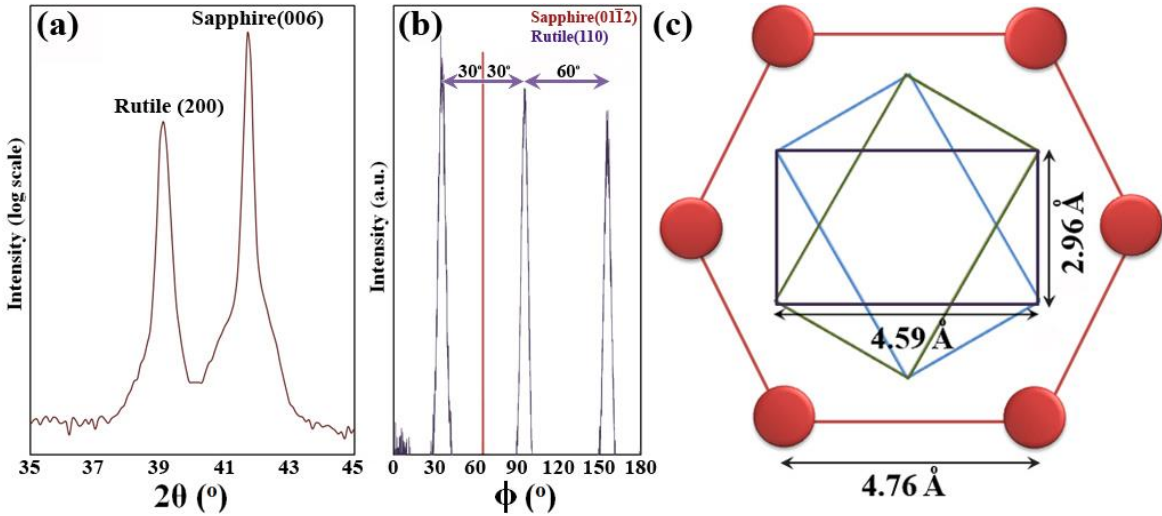


Fig.6.1. (a)  $\theta$ - $2\theta$  pattern of the rutile/sapphire heterostructure, (b)  $\varphi$ -scan XRD performed on rutile(110) and sapphire(0112) reflections, and (c) Schematic illustration of crystallographic arrangement across the film/sapphire interface.

Nucleation of  $\text{TiO}_2$  in any of these in-plane orientations is equally likely, as these three different orientations of  $\text{TiO}_2$  are energetically equivalent. The in-plane epitaxial relationship across the rutile/sapphire interface is determined as rutile[001]||sapphire[1010] and rutile[010]||sapphire[1210]. Fig.6.2 shows STEM cross section HAADF-image of the rutile/sapphire heterostructure acquired from the  $[10\bar{1}0]$  direction (Fig.6.2a) and  $[1\bar{2}10]$  direction (Fig.6.2b and Fig.6.2c) of sapphire. Formation of a highly epitaxial film is confirmed. Meanwhile, the in-plane rotation of the grains,

discussed earlier, is evident. In this image, adjacent grains of rutile with [001] and [011] in-plane orientations are observed whose interface is atomically sharp and crystallographically continuous; in other words, the adjacent grains are connected to each other by twin boundaries.

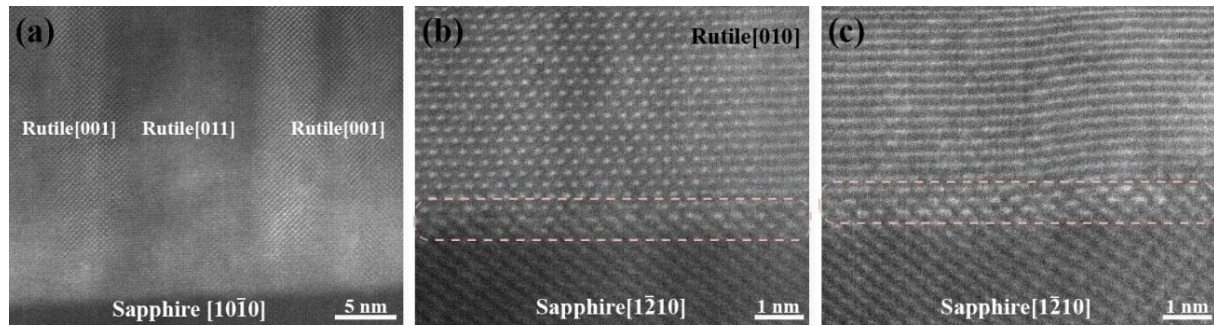


Fig.6.2. High angle angular dark field STEM cross section images from:  
 (a) sapphire[ $10\bar{1}0$ ], (b) and (c) sapphire[ $\bar{1}\bar{2}10$ ] direction.

Based on our previous experience<sup>22</sup> and as highlighted by the dashed squares in the images taken from the [ $\bar{1}\bar{2}10$ ] direction of sapphire, a transient region at the film/substrate interface has formed where the lattice seems to be the same as that of sapphire, but with heavier Ti atoms locating at the Al positions. The lattice in these regions is identified as that of  $Ti_2O_3$  with a rhombohedral crystalline structure (In bulk:  $a=b=5.15 \text{ \AA}$ ,  $c=13.61 \text{ \AA}$ ,  $\gamma=120^\circ$ ) which is isostructural with alumina.<sup>23,24</sup> Therefore, formation of  $TiO_2/Ti_2O_3/Al_2O_3$  structure is confirmed. The rutile film initially grows pseudomorphically on the c-sapphire substrate as  $Ti_2O_3$  and, after a few monolayers, it starts growing tetragonally on the  $Ti_2O_3/c$ -sapphire platform. The  $Ti_2O_3$  interfacial region was also observed in the images acquired from the [ $10\bar{1}0$ ] zone (data are not

shown here). Formation of the  $\text{Ti}_2\text{O}_3$  transient layer is related to the pseudomorphic growth or the templating effect from the substrate, because it preserves the crystal structure of the sapphire substrate.<sup>22</sup> In this region, the film has a chemical composition near to that of  $\text{Ti}_2\text{O}_3$ , but a crystallographic structure analogous to that of the sapphire substrate. Thus, it can be suggested that the crystalline structure as well as the chemical composition gradually changes from  $\text{Al}_2\text{O}_3$  to  $\text{TiO}_2$  along the  $\text{Ti}_2\text{O}_3$  transient region.

Considering Fig.6.1c, the atomic arrangement at the  $\text{TiO}_2/\text{Ti}_2\text{O}_3$  interface was as illustrated in Fig.6.3. The matching of lattice parameters produces strain in the film and to some extent in the substrate. The pseudomorphic growth of the film continues until a “critical thickness” is reached where the strain energy becomes large enough to trigger the nucleation of misfit dislocations.<sup>25</sup> These dislocations nucleate at the film surface and glide to the interface to relieve the misfit strains.

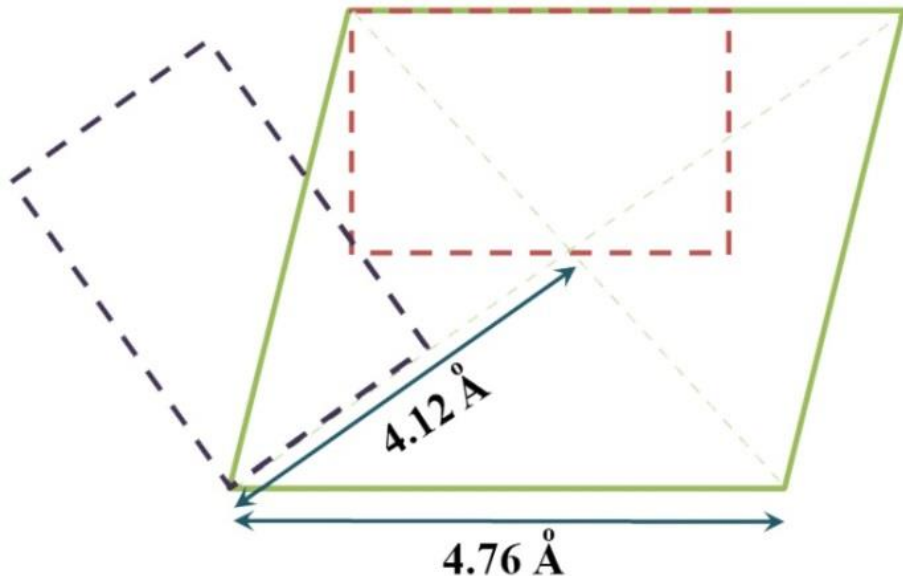


Fig.6.3. Schematic illustration of crystallographic arrangement across the  $\text{TiO}_2/\text{Ti}_2\text{O}_3$  interface.

According to Fig.6.3, the lattice misfits across the  $\text{TiO}_2/\text{Ti}_2\text{O}_3$  interface are determined as  $\varepsilon_b=+3.57\%$   $\varepsilon_c=+28.15\%$  where  $\varepsilon_b$  and  $\varepsilon_c$  are the lattice misfits along the b and c directions of the rutile film. It should be noted that the lattice parameters of  $\text{Al}_2\text{O}_3$ , shown in Fig.6.1c, were considered in all of the calculations, since the  $\text{Ti}_2\text{O}_3$  layers assumes the crystalline lattice of sapphire. According to the domain matching epitaxy (DME) paradigm,<sup>25</sup> the misfit along *b*-direction is accommodated by matching of 28 planes of the film with 27 planes of the substrate. Meanwhile, the misfit strain along the *c*-axis of rutile is relaxed when 4/3 and 3/2 domains alternate with a relative frequency of 0.55. Arrangement of misfit dislocations at the  $\text{TiO}_2/\text{Ti}_2\text{O}_3$  interface is observed in Fig.6.4 where alternation of 4/3 and 3/2 domains is evident.

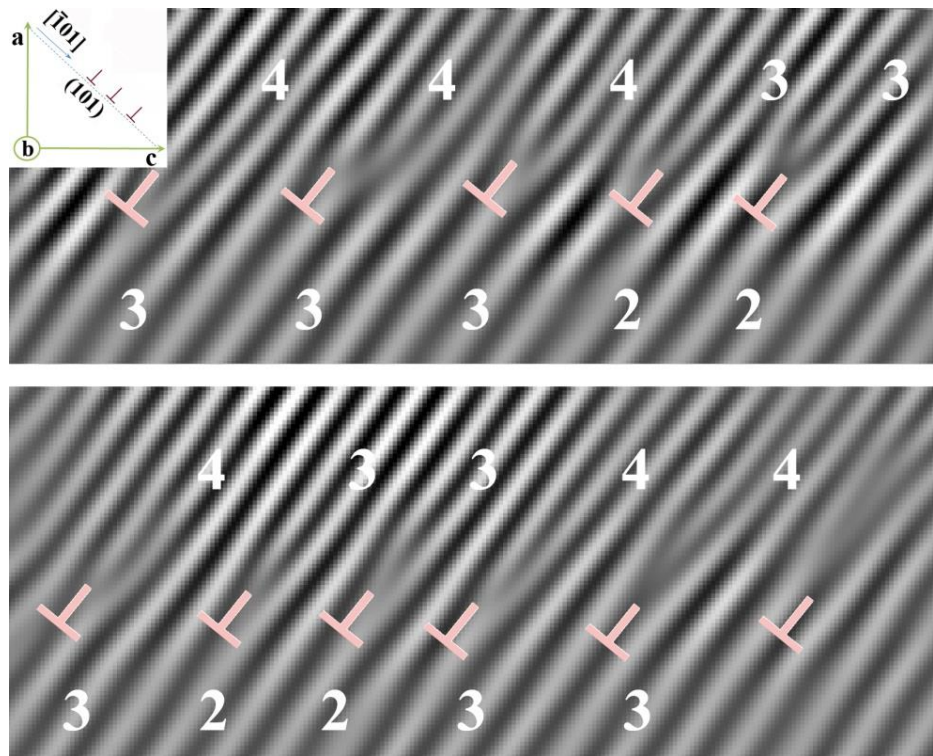


Fig.6.4. Arrangement of the misfit dislocations across the  $\text{TiO}_2/\text{Ti}_2\text{O}_3$  interface.

The  $\frac{1}{2}<\bar{1}01>\{101\}$  dislocations are the most probable dislocations in the rutile  $\text{TiO}_2$ .<sup>26</sup> According to the schematic shown in Fig.6.4, the  $90^\circ$  misfit dislocations forms at the film surface and glide along the  $[10\bar{1}]$  direction on the  $(101)$  planes to reach the film/substrate interface to relax the misfit strain. The length of the Burger's vector ( $b$ ) of these dislocations was determined as  $2.731 \text{ \AA}$ . Considering a  $28.15\%$  misfit strain along the  $c$ -axis of the rutile film, the separation between the misfit dislocations would be about  $2.731/0.2815=9.7 \text{ \AA}$ . As the lattice parameter of rutile  $\text{TiO}_2$  is  $2.96 \text{ \AA}$  along its  $c$ -direction,<sup>1</sup> each  $3.28$  planes of rutile accommodate one dislocation. Consequently, the misfit dislocations should appear every  $3$  or  $4$  planes of the rutile film which is in excellent agreement with the details of the DME paradigm.

## 6.4. Conclusions

Rutile/sapphire(001) epitaxial heterostructures were grown by PLD technique and characterized by  $\theta$ - $2\theta$  and  $\varphi$  scans of X-ray diffraction and STEM Z-contrast imaging. The epitaxial relationship was explained as  $(100)_{\text{rutile}}|| (0001)_{\text{sapphire}}$ ,  $[001]_{\text{rutile}}|| [10\bar{1}0]_{\text{sapphire}}$ , and  $[010]_{\text{rutile}}|| [1\bar{2}10]_{\text{sapphire}}$ . No interfacial reaction was observed across the film/substrate interface. The twin boundaries between the  $\text{TiO}_2$  grains were also atomically sharp. It was found that a  $\text{Ti}_2\text{O}_3$  transient layer forms on the sapphire substrate to match the tetragonal symmetry of the rutile film with the hexagonal symmetry of the sapphire substrate. After a couple of monolayers, the rutile film grows on the  $\text{Ti}_2\text{O}_3/\text{sapphire}$  platform. Finally, the separation between the

$\frac{1}{2}[10\bar{1}](101)$  dislocations across the film/substrate interface was determined as 9.7 Å which was in a good agreement with alternation of 4/3 and 3/2 domains.

## References

1. N. Sbai, J. Perriere, W. Seiler, and E. Millon, *Surf. Sci.* 601, 5649 (2007).
2. J.K. Yao, H.L. Huang, J.Y. Ma, Y.X. Jin, Y.A. Zhao, J.D. Shao, H.B. He, K. Yi, Z.X. Fan, F. Zhang, and Z.Y. Wu, *Surf. Eng.* 25, 257 (2009).
3. Fujishima, X. Zhang, and D.A. Tryk, *Surf. Sci. Rep.* 63, 515 (2008).
4. V. Saxena, P. Veerender, A.K. Chauhan, P. Jha, D.K. Aswal, and S.K. Gupta, *Appl. Phys. Lett.* 100, 133303 (2012).
5. H. Kim, K. Noh, C. Choi, J. Khamwannah, D. Villwock, and S. Jin, *Langmuir*, 27, 10191 (2011)
6. H.S. Shim, J. Lim, C.G. Shin, S.J. Jeon, M.G. Han, and J.K. Lee, *Appl. Phys. Lett.* 100, 063113 (2012).
7. J.C. Woo, Y.S. Chun, Y.H. Joo, and C.I. Kim, *Appl. Phys. Lett.* 100, 081101 (2012).
8. Y. Liu, L. Ni, Z. Ren, G. Xu, C. Song, and G. Han, *J. Phys. C: Condens. Matter.* 21, 275901 (2009).
9. P.H. Nemec, C. Kadlec, F. Kadlec, P. Kuzel, R. Yahiaoui, U.C. Chung, C. Elissalde, M. Maglione, and P. Mounaix, *Appl. Phys. Lett.* 100, 061117 (2012).
10. M.R. Bayati, Sh. Joshi, R. Molaei, R.J. Narayan, and J. Narayan, *J. Solid State Chem.* 187, 231 (2012).

11. A. Lu, Y. Li, S. Jin, H. Ding, C. Zeng, X. Wang, and C. Wang, Energy Fuels 24, 1184 (2010).
12. A. Lu, and Z. Chen, Sens. Actuators B 140, 109 (2009).
13. R.S. Chen, C.A. Chen, H.Y. Tsai, W.C. Wang, and Y.S. Huang, Appl. Phys. Lett. 100, 123108 (2012).
14. W.J. Lee and M.H. Hon, Appl. Phys. Lett. 99, 251102 (2011)
15. M.R. Hoffmann, S.T. Martin, W. Choi, and D.W. Bahnemann, Chem. Rev. 95, 69 (1995).
16. P.A. Morris Hotsenpiller, A. Roshko, J.B. Lowekamp, and G.S. Rohrer, J. Cryst. Growth 174, 424 (1997).
17. D.R. Burgess, P.A. Morris Hotsenpiller, T.J. Anderson, and J.L. Hohman, J. Cryst. Growth 166, 763 (1996).
18. S. Chen, M.G. Mason, H.J. Gysling, G.R. Paz-Pujalt, T.N. Blanton, T. Castro, K.M. Chen, C.P. Fictorie, W.L. Gladfelter, A. Franciosi, P.I. Cohen, and J.F. Evans, J. Vac. Sci. Technol. A 11, 2419 (1993).
19. B.C. Riggs, A.D. Dias, N.R. Schiele, R. Cristescu, Y. Huang, D.T. Corr, D.B. Chrisey, MRS Bull. 36, 1043 (2011).
20. C.F. Koch, S. Johnson, D. Kumar, M. Jelinek, D.B. Chrisey, A. Doraiswamy, C. Jin, R.J. Narayan, and I.N. Mihailescu, Mater. Sci. Eng. C 27, 484 (2007).
21. H. Zhou, M.F. Chisholm, P. Pant, H.J. Chang, J. Gazquez, S.J. Pennycook, and J. Narayan, Appl. Phys. Lett. 97, 121914 (2010).

22. H. Zhou, M.F. Chisholm, T.H. Yang, S.J. Pennycook, and J. Narayan, *J. Appl. Phys.* 110, 073515 (2011).
23. M.A. Afifi, M.M. Abdel-Aziz, I.S. Yahia, M. Fadel, and L.A. Wahab, *J. Alloys Compnd.* 455, 92 (2008).
24. J.J. Cappom, M. Marezio, J. Dumas, and C. Schienker, *Solid State Commun.* 20, 893 (1976).
25. J. Narayan and B. C. Larson, *J. Appl. Phys.* 93, 278 (2003).
26. Y. Motohashi, M.G. Blanchi, E. Vicario, G. Fontain, and S. Otake, *Phys. Stat. Sol. A* 64, 355 (1979).

## **Chapter 7**

# **Defect Mediated Photocatalytic Decomposition of 4-chlorophenol on Epitaxial Rutile Thin Films under Visible and UV Illuminations**

We show that pure rutile  $\text{TiO}_2$  can be photo-responsive even under low energy visible light after annealing in vacuum where we envisage the point defects, i.e. oxygen vacancies and titanium interstitials, serve an important role. In this study, single crystal rutile films were grown by pulsed laser deposition technique and, then, vacuum annealed under different oxygen pressures to introduce defects into their lattice. The 4-chlorophenol was selected as a model material and decomposed by the annealed  $\text{TiO}_2$  films where maximum photocatalytic reaction rate constants were determined as 0.0107 and  $0.0072 \text{ min}^{-1}$  under UV and visible illuminations. Epitaxial growth along the [200] direction was confirmed by  $\varphi$ -scan and  $2\theta$ -scan XRD and the in-plane alignment between the rutile film and *c*-sapphire substrate was explained as  $[010](100)_{\text{rutile}} \parallel [1\bar{2}10](0001)_{\text{sapphire}}$ . Formation of atomically sharp interfaces and the epitaxial growth were ascertained by annular dark field STEM imaging. Based on the

XPS, UV-Vis and PL spectroscopy results, it was found that the defect concentration increased after annealing under lower pressures, e.g.  $5 \times 10^{-6}$  Torr. In contrast, more perfect crystals were obtained when the films were annealed under high oxygen pressures, namely  $5 \times 10^{+1}$  Torr. Morphology of the films was also investigated employing AFM technique. It was observed that increasing the annealing pressure results in formation of larger grains. It was also found that electrical resistivity of the rutile films increased by about three orders of magnitude when annealing pressure increased from  $5 \times 10^{-4}$  to  $5 \times 10^{+1}$  Torr.

## 7.1. Introduction

Chlorinated phenolic compounds are characterized by high toxicity even at relatively low concentrations and persistency in both water and soils. They are usually released to the environment by pulp and paper manufacturers, oil refining activities, and textile industries. Particularly, 4-chlorophenol (4CP) can originate from the chlorination processes of phenol containing wastewater or from the breakdown of pesticides and chlorinated aromatic compounds. Moreover, it is an intermediate by-product in the production of 2,4-dichlorophenol and 4-chlorophenol-o-cresol. The latter can be oxidized by chemical, photochemical, and microbiological processes. Photocatalytic decomposition of 4CP has been considered as a promising technique where the toxic material is mineralized to harmless products of CO<sub>2</sub> and H<sub>2</sub>O. During this processes, the 4CP molecules are degraded mainly by the attack of •OH radicals.<sup>1-3</sup>

Among many kinds of photocatalyst materials, titanium dioxide ( $\text{TiO}_2$ ) has been widely studied and has attracted considerable attention during the last decade, since it has superior physical and chemical properties. To enhance the photocatalytic efficiency, it is necessary to understand the principles of the photocatalytic reactions. In such reactions, first, the semiconductor is illuminated by light whose energy should be larger than the band gap energy of semiconductor ( $h\nu \geq E_g$ ). Then, electrons are excited from the valence band to the conduction band and, hence, holes are generated on the valance band. This process leads to generation of electron-hole pairs which are prerequisite for photocatalytic applications:<sup>4,5</sup>



Afterward, the photo-generated electron-hole pairs chemically react with the adsorbed water and oxygen molecules to create high energy  $\text{OH}\cdot$  and  $\text{O}_2\cdot^-$  radicals:



The  $\text{OH}\cdot$  and  $\text{O}_2\cdot^-$  radicals, generated through the above reactions, are extremely energetic and active. As strong oxidizing and reducing agents, they have impressive

chemical activities which can decompose both organic and inorganic molecules efficiently. Regarding the aforementioned mechanism, generation and separation of e<sup>-</sup> h<sup>+</sup> pairs are the critical steps of any photocatalytic reaction. Since the band gap energy of TiO<sub>2</sub> is 3.0-3.2 eV, only the ultraviolet part of the solar radiation (about 4% of the total solar energy reaching the Earth's surface) can excite TiO<sub>2</sub> to generate e<sup>-</sup>-h<sup>+</sup> pairs. This, to some extents, limits practical applications of TiO<sub>2</sub>. At this point, several studies have been carried out to enhance the catalytic efficiency under visible light and different solutions have been proposed such as doping and combining titania with metallic elements, non-metallic elements, and other semiconductors.<sup>6-11</sup> Another way, which has not been investigated thoroughly, is based on introduction of point defects to the crystalline lattice of TiO<sub>2</sub>. Such defects might alter the energy bands of semiconductor by introducing defect energy levels within the band gap resulting in band gap narrowing. There are six different kinds of point defects in TiO<sub>2</sub> structure, namely titanium interstitial (Ti<sub>i</sub>), titanium vacancy (V<sub>Ti</sub>), oxygen interstitial (O<sub>i</sub>), oxygen vacancy (V<sub>O</sub>), and two anti-site defects: Ti<sub>O</sub> and O<sub>Ti</sub>. Each of these defects has specific formation energy ( $\Delta H$ ) under titanium and oxygen rich growth conditions. Theoretical estimations of formation energies of anti-site and titanium vacancy defects are too high. They form only under extreme conditions due to the large cation-anion size mismatch and strong iconicity of the material. However, formation energies of Ti<sub>i</sub> and V<sub>O</sub> defects are about 2-3 eV under Ti-rich (low oxygen partial pressure) growth condition. As a result, V<sub>O</sub> and Ti<sub>i</sub> defects are the most probable structural defects of TiO<sub>2</sub>.<sup>12</sup> From the kinetics viewpoint, formation of V<sub>O</sub> is more favored than Ti<sub>i</sub>. Both V<sub>O</sub> and Ti<sub>i</sub> defects

introduce energy levels inside the band gap of titania and play a significant role in increasing absorbance in the visible region. It is worth mentioning that  $\text{Ti}_i$  defect has two different types:  $\text{Ti}_i^{4+}$  and  $\text{Ti}_i^{3+}$ . The fingerprint of the formation of  $\text{Ti}^{3+}$  ions is an energy band edge at about 2 eV above the valence band maxima and about 1 eV below the conduction band minima.<sup>13</sup> The defects, no matter whether they are located at the surface or at the interface, are considered to act as functional electron traps to reduce the recombination of electrons and holes, resulting in a promoted photoactivity of  $\text{TiO}_2$  films.<sup>14</sup> Oxygen vacancies can form defect centers serving as electron traps and, thus, promote charge transfer.<sup>15</sup> As a consequence, defects can decrease the recombination rate of  $e^-$ - $h^+$  pairs resulting in the improvement in photocatalytic activity.

It is well known that the competition among the recombination, trapping, and transfer of photogenerated electron-hole pairs determines the overall photocatalytic efficiency. To achieve a high photocatalytic efficiency in  $\text{TiO}_2$  films, the  $e^-$ - $h^+$  pairs should be effectively extracted to the surface without recombination. Inasmuch as grain boundaries can scatter or trap the photogenerated electrons and holes and act as charge recombination center, reducing grain boundaries and growing single crystal films lead to formation of highly photoactive  $\text{TiO}_2$  films.

In this chapter, we report growth and characterization of single crystal rutile films on *c*-sapphire. We will show that the defect content as well as photocatalytic performance of the films can be aptly tuned by changing the annealing pressure. It will be also shown that the pure rutile films, annealed under low pressures, are responsive under visible light where we envisage that point defects play a major role.

## 7.2. Experimental

Epitaxial rutile TiO<sub>2</sub> films were deposited on single crystal *c*-cut sapphire (Al<sub>2</sub>O<sub>3</sub>) substrates by PLD technique. Prior to deposition, the substrates were cleaned through a multi-step procedure including degreasing in hot acetone for 15 min., ultrasonic cleaning in acetone for 5 min. followed by ultrasonic cleaning in methanol for 5 min. Finally, the cleaned substrates were fully dried by a nitrogen gun and loaded to the PLD chamber. A Lambda Physik (LPX200) KrF excimer laser ( $\lambda = 248$  nm,  $\tau = 25$  ns) was employed to ablate the TiO<sub>2</sub> target. The target was being rotated during the deposition to provide a uniform ablation and avoid any pitting on its surface. Before injecting oxygen into the chamber, the chamber was evacuated to a background pressure of  $\sim 1 \times 10^{-6}$  Torr. Laser energy, shot frequency, oxygen pressure, growth time, and substrate temperature were the same for all samples:  $\sim 3.5$  J.cm<sup>-2</sup>, 10 Hz,  $5 \times 10^{-4}$  Torr, 20 min., and 450 °C, respectively. Immediately after deposition, the layers were subjected to vacuum annealing inside the PLD chamber for 1 hr at 450 °C under different pressures of  $5 \times 10^{-6}$  to  $5 \times 10^{-1}$  Torr with  $10^{-1}$  intervals.

The crystalline structure of the TiO<sub>2</sub> films was investigated by  $2\theta$  XRD-scanning using a Rigaku X-ray diffractometer with Cu-K $\alpha$  radiation ( $\lambda=0.154$  nm). A Philips X'Pert Pro X-ray diffractometer was also employed for  $\varphi$ -scanning to determine in-plane and out of plane orientations of TiO<sub>2</sub> films. Morphology of the layers was studied by a Veeco AFM as well and the results were interpreted by nanoscope ver. 5.12r3 software. Optical properties of the films were studied by a U-3010 Hitachi UV-Vis spectrophotometer. The room temperature photoluminescence (PL) spectra of the

samples were recorded with a fluorescence spectrophotometer (Hitachi, F-2500) using an excitation wavelength of 300 nm. Annular dark-field scanning transmission electron microscopy (ADF-STEM) imaging with a Nion UltraSTEM 200 operated at 200 kV was used to confirm the epitaxial growth of the layers. To determine surface chemical composition and stoichiometry of the layers, X-ray photoelectron spectroscopy (XPS) was performed employing a Riber instrument with an Mg-K $\alpha$  X-ray source. The samples were sputtered by Ar $^+$  bombardment for 5 min. prior to acquiring data to remove any probable surface contamination. Interpretation of the XPS results was performed using the SDP ver.4.1 software. Electrical properties of the films were studied using a self-made labview program employing a Keithley 2400 sourcemeter. The measurements were done in a temperature range of 242-342 K. The samples were cooled using a closed cycle helium cryostat.

The procedure of measuring the photocatalytic activity of the layers was explained in chapter 3.

### **7.3. Results and discussion**

#### **7.3.1. Phase structure**

Fig.7.1 shows XRD patterns of the rutile TiO<sub>2</sub> films annealed under different pressures where formation of epitaxial or highly textured films is evident. It was found that the rutile(200) characteristic peak gets more intense at higher annealing pressures. Simultaneously, full width at half-maximum (FWHM) decreases when the grown films were annealed under higher pressures. In other words, layers with more

favorable crystallinity and better quality were obtained after annealing under higher pressures.

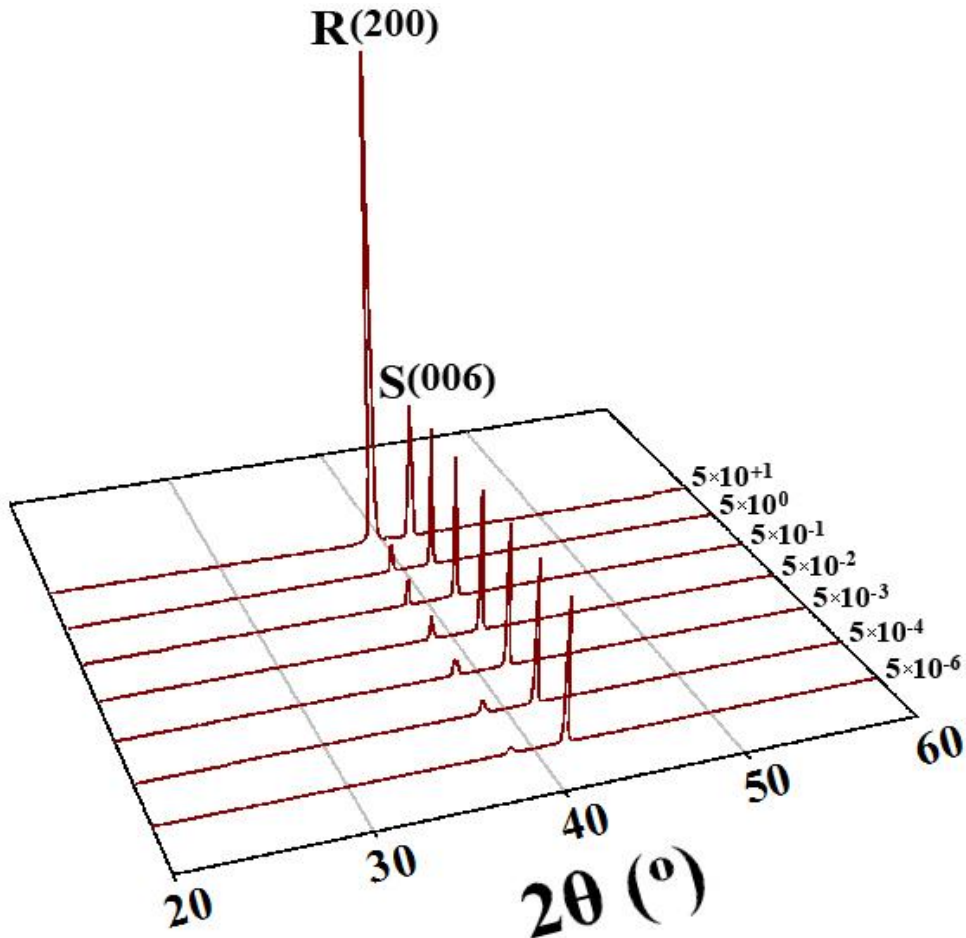


Fig.7.1.  $\theta$ - $2\theta$  XRD patterns of the rutile films annealed under various pressures.

As it was discussed earlier in chapter 2, oxygen vacancies ( $V_O$ ) and titanium interstitials ( $Ti_{ii}$ ) are two most important intrinsic defects in  $TiO_2$ . According to the equations 2-2 through 2-7, it can be concluded that oxygen pressure plays an important role in the formation or removal of these point defects in  $TiO_2$  crystalline structure. It

can be also suggested that annealing the films under higher oxygen partial pressures results in decreasing concentration of point defects in the grown samples. As a consequence, rutile films with better quality were obtained at higher annealing pressures, i.e.  $5 \times 10^{+1}$  Torr. The structure factor increases when point defects are removed leading to appearance of more intense and sharper XRD peaks. High resolution XRD was also carried out to determine the exact  $2\theta$  values of rutile (200) peak results of which are presented in Fig.7.2.

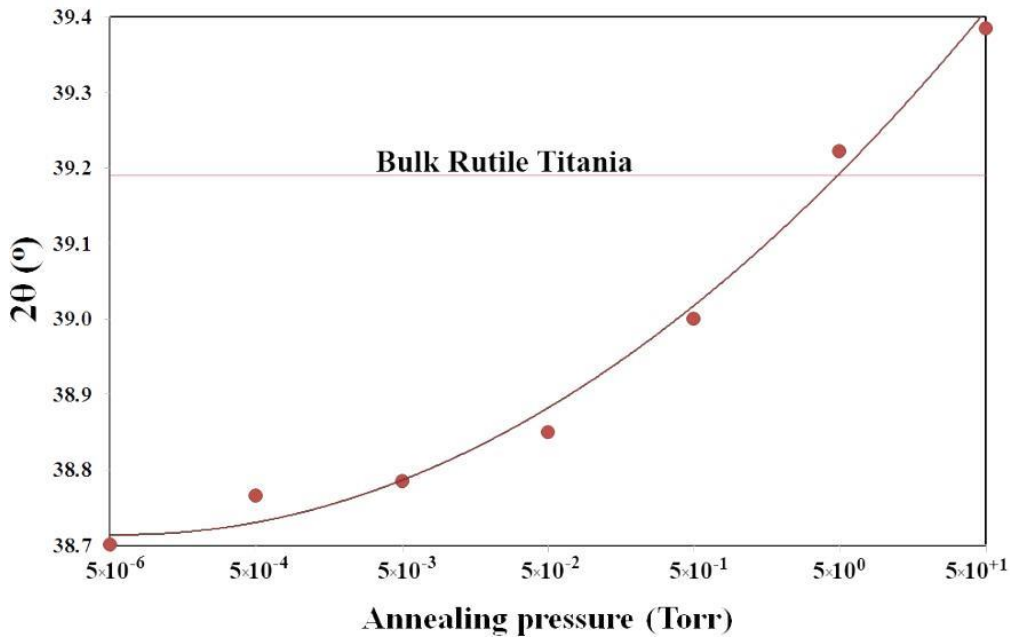


Fig.7.2. Diffraction angle ( $2\theta$ ) of the rutile(200) peak as a function of the annealing pressure.

As is seen, the rutile(200) peak shifts toward smaller  $2\theta$  values when the layers were annealed under lower pressures. This peak shift can be assigned to formation of more defects which results in changing the *d*-spacing between the planes.

### 7.3.2. Optical properties

Room temperature PL spectra of the rutile films are depicted in Fig.7.3. It is noteworthy that all emissions having wavelengths shorter than 420 nm were eliminated by a filter to highlight the peaks from the energy levels of defects. The wide emission peak at the wavelength of  $\sim$ 450 nm is attributed to the oxygen vacancy energy levels. PL intensities can be related to the recombination rate between the photogenerated electrons and holes. Since the charge carriers are trapped by defects, low PL intensity reveals a lower recombination rate and, thus, a higher defect concentration. Taking the PL results into closer consideration, it is suggested that annealing the rutile films under higher oxygen pressures leads to removing the point defects or decreasing their concentration.

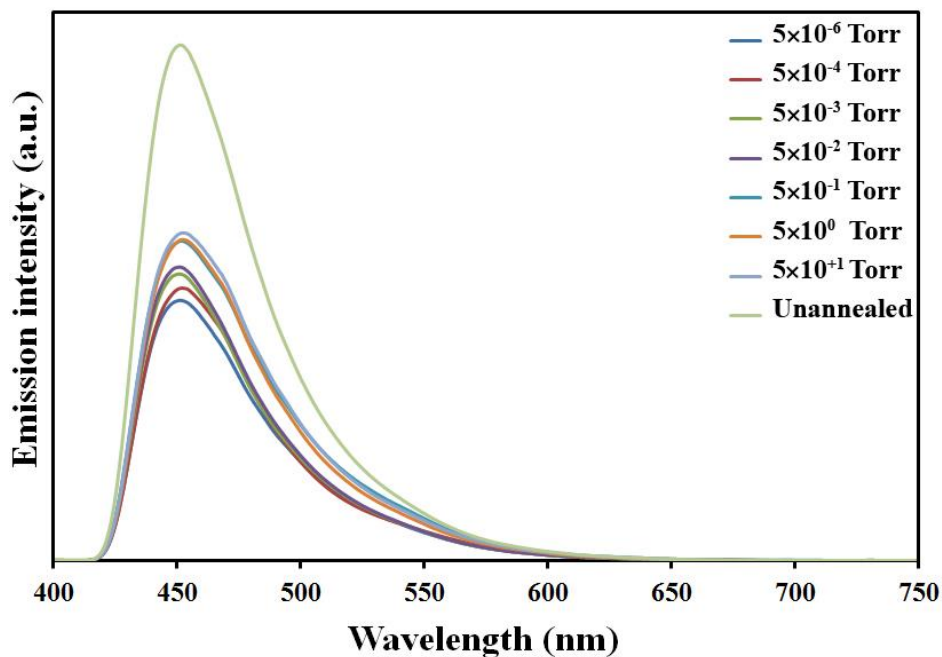


Fig.7.3. Influence of the annealing pressure on the room temperature PL spectra of the rutile films.

UV-Vis spectroscopy was employed to study the influence of vacuum annealing on optical properties of the films and the results are shown in Fig.7.4.

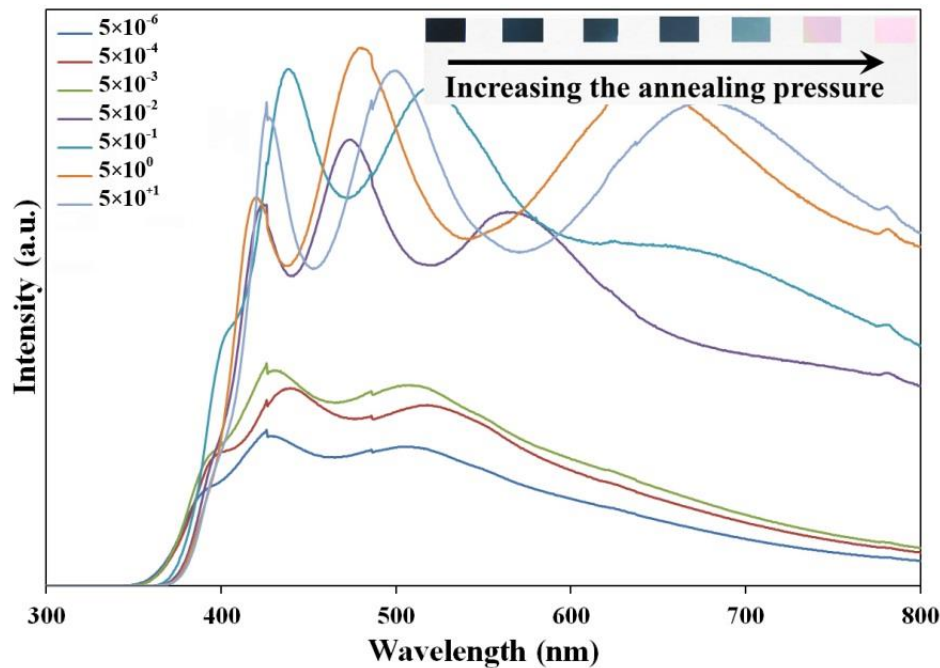


Fig.7.4. Transmittance spectra of the layers annealed under various oxygen pressures.

The films annealed under higher pressures are more transparent and their transmittance is about 85% which further confirms the formation of higher quality films after high oxygen pressure annealing. However, according to the equations 10-12, the concentration of point defects increases at lower pressures. This phenomenon results in decreasing the transmittance, since these defects act as scattering centers for the incoming photons. Moreover, the films annealed under higher pressures exhibit a sharper absorbance edge which confirms lower defect content in these layers. It is also important to note that transmittance spectra of the rutile films annealed at lower

pressures have an absorbance edge at  $\sim$ 425 nm. That is, these films have a narrower band gap. We attribute this band gap narrowing to the introduction of  $Ti_i$  defects. The formation of  $Ti^{3+}$  cations gives rise to the formation of a band edge in between the conduction and valence bands of titania. This energy level locates about 2 eV above the valence band maximum and about 1 eV below the bottom of the conduction band. As is shown in the inset of Fig.7.4, the samples annealed at low pressures assume a bluish color whose intensity is a measure of the level of reduction and is assigned to d-d transitions.<sup>13</sup>

### 7.3.3. Stoichiometry

The above studies on defect characteristics in the layers were completed by XPS. Fig.7.5a to Fig.7.5c show O(1s) core level binding energies for the rutile films annealed under various pressures. Meanwhile, the O(1s) core level of the un-annealed layer is depicted in Fig.7.5d, as a reference. As is seen, the XPS peaks have been deconvoluted into distinct peaks using the Gaussian function. Peak A with a binding energy of  $\sim$ 531.8 eV corresponds to the  $O^{2-}$  ions in oxygen deficient regions and its fraction scales with the concentration of oxygen vacancies ( $V_0$ ). When an oxygen vacancy forms, the nearby Ti atoms relax outward, so the neighboring Ti-O bonds are shortened resulting in an increased bonding energy. As a consequence of the formation of a  $V_0$  defect, two  $Ti^{4+}$  ions must convert to  $Ti^{3+}$  ions to preserve the charge neutrality. In other words,  $Ti^{4+}$  ions trap two electrons that are generated when a  $V_0$  defect forms (eq.7). Indeed, peak A is assigned to the oxygen deficient regions and can be attributed to the  $V_0$  defects.

Peak B, located at binding energy of 530.2 eV, is assigned to the oxygen ions in the crystalline lattice of perfect  $\text{TiO}_2$ . Peaks C and D, which respectively have binding energies of about 528.0 and 526.9 eV, may represent oxygen atoms in contact with  $\text{Ti}_{\text{i}}^{3+}$  and  $\text{Ti}_{\text{i}}^{4+}$  defects. When a titanium interstitial resides in the rutile lattice, it attracts the electron cloud between neighboring Ti and O atoms, leading to a decrease in energy of neighboring Ti-O bonds. A small peak shift is also observed for all these peaks due to variation of defect concentrations. Taking the peak portions into consideration (Tab.7.1), it can be suggested that the amount of lattice disorder, which is represented by peaks A, C, and D, increases when the films are annealed under lower oxygen pressures.

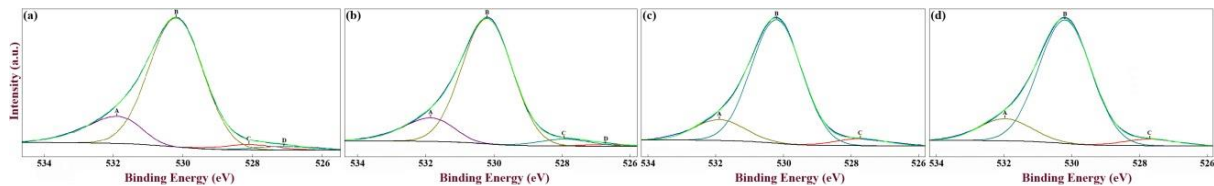


Fig.7.5. XPS O(1s) core level binding energies in the  $\text{TiO}_2$  films annealed under pressures of:  
 (a)  $5 \times 10^{-6}$ , (b)  $5 \times 10^{-3}$ , (c)  $5 \times 10^{+1}$  Torr, and (d) un-annealed sample.

It is worth pointing out that peaks C and D are merged together in Fig.7.5c and Fig.7.5d, since the concentration of the  $\text{Ti}_{\text{i}}^{3+}$  and  $\text{Ti}_{\text{i}}^{4+}$  defects in the un-annealed sample as well as the sample annealed under pressure of  $5 \times 10^{+1}$  Torr is not that much different making it difficult to allocate distinct peaks to these defects. Because lowering the annealing pressure results in an increasing concentration of point defects, peak B shrinks when the films are annealed under lower ambient pressures.

Tab.7.1. Portion of the XPS peaks for different oxygen pressures.

pressure \ XPS peak	Un-Annealed	$5 \times 10^{-1}$ Torr	$5 \times 10^{-3}$ Torr	$5 \times 10^{-6}$ Torr	
		Portion (%)			
O(1s)	A	14.6	13.8	15.3	17.0
	B	79.9	81.4	79.3	77.4
	C	4.5	4.8	4.4	3.3
	D	---	---	1.0	2.3

### 7.3.4. Morphology

Surface morphology of the rutile films is depicted in Fig.7.6. It is seen that the surface roughness increases when the oxygen pressure. The surface roughness increases when the annealing oxygen pressure increases from  $5 \times 10^{-6}$  to  $5 \times 10^{-1}$  Torr.

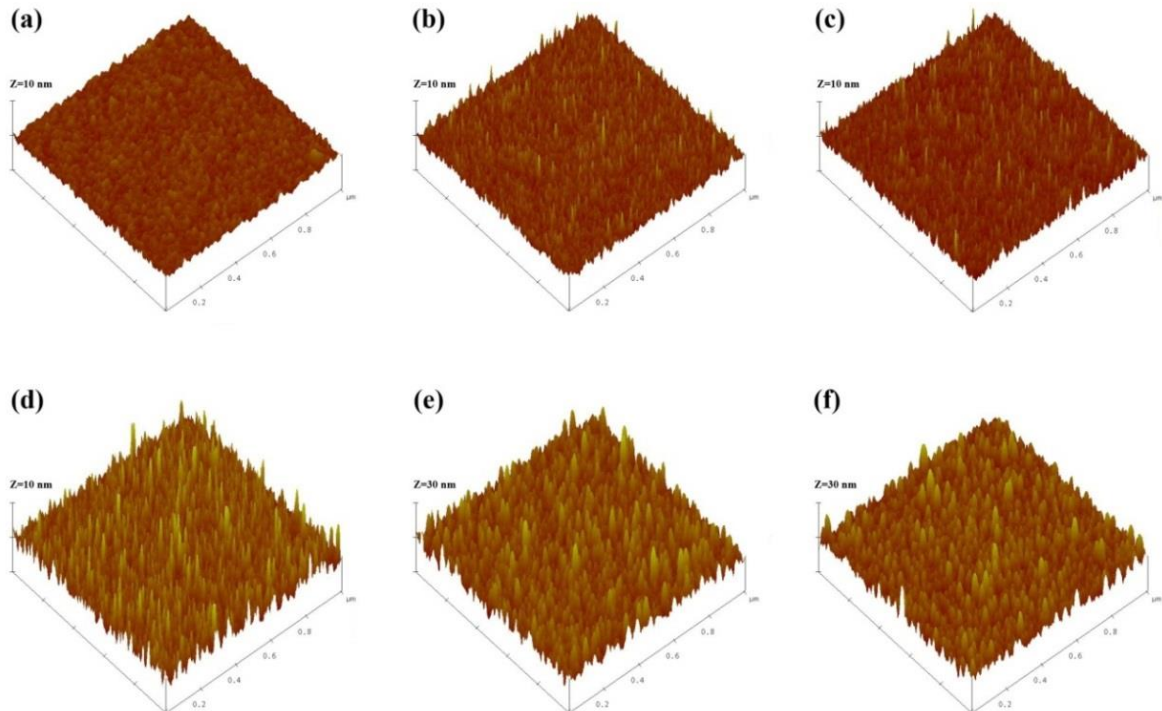


Fig.7.6. The effect of annealing pressure on AFM surface morphology of the  $\text{TiO}_2$  films:

(a)  $5 \times 10^{-6}$ , (b)  $5 \times 10^{-4}$ , (c)  $5 \times 10^{-3}$ , (d)  $5 \times 10^{-2}$ , (e)  $5 \times 10^0$ , and (f)  $5 \times 10^{-1}$  Torr.

We already saw that most of the structural defects were removed after annealing under high oxygen pressures, namely  $5 \times 10^{+1}$  Torr. Since the defects tend to accumulate around grain boundaries, the grain boundaries are to some extent confined by them and cannot migrate freely. That is, their migration needs a higher energy. However, after annealing under higher pressures and, hence, reducing the defect content, grain boundaries can migrate more simply, so larger grains form.

We will show in the future that the grown films are single crystal and the grain boundaries are small angle grain boundaries. That is, the adjacent grains are crystallographically twin boundaries and, so quite low in energy.

### 7.3.5. Thin film epitaxy

To confirm the growth of single crystal rutile films, XRD  $\varphi$ -scanning was carried out on the  $(01\bar{1}2)$  reflection plane ( $2\theta=25.58^\circ$ ,  $\psi=57.70^\circ$ ) of the sapphire substrate and the  $(110)$  reflection plane ( $2\theta=27.44^\circ$ ,  $\psi=45.00^\circ$ ) of the rutile film (Fig.7.7). Due to the threefold symmetry of the sapphire(0001) substrate having a hexagonal lattice, three  $(01\bar{1}2)$  reflection peaks with  $120^\circ$  intervals were observed. In addition, 6 strong symmetrical peaks appear with angular intervals of  $60^\circ$  for  $(110)$  family of planes of the film. This indicates that three different grain orientations are present in the rutile film which is due to the three-fold symmetry in the pseudo-hexagonal structure of the (0001) sapphire substrate. Thus, formation of the threefold mosaic structure in the epitaxial  $(200)$   $TiO_2$  rutile film was due to the nucleation and growth of the three variants on the sapphire(0001) substrate.<sup>21</sup> As it was already shown in the previous

chapters, the epitaxial relationship was established as rutile(100)||sapphire(0001), rutile[001]||sapphire[10 $\bar{1}$ 0], and rutile[010]||sapphire[1 $\bar{2}$ 10].<sup>22</sup> Since the films grew epitaxially, grain boundaries present in the films have low angle which show lower scattering effect against electron-hole pairs.<sup>23</sup> The proposed epitaxial relationship, columnar growth, and the in-plane 60° rotation are further confirmed by the high resolution ADF-STEM imaging as shown in Fig.7.8a and Fig.7.8b where formation of atomically sharp interface between film and substrate is also observed. In-plane rotation of the rutile grains is also evident.

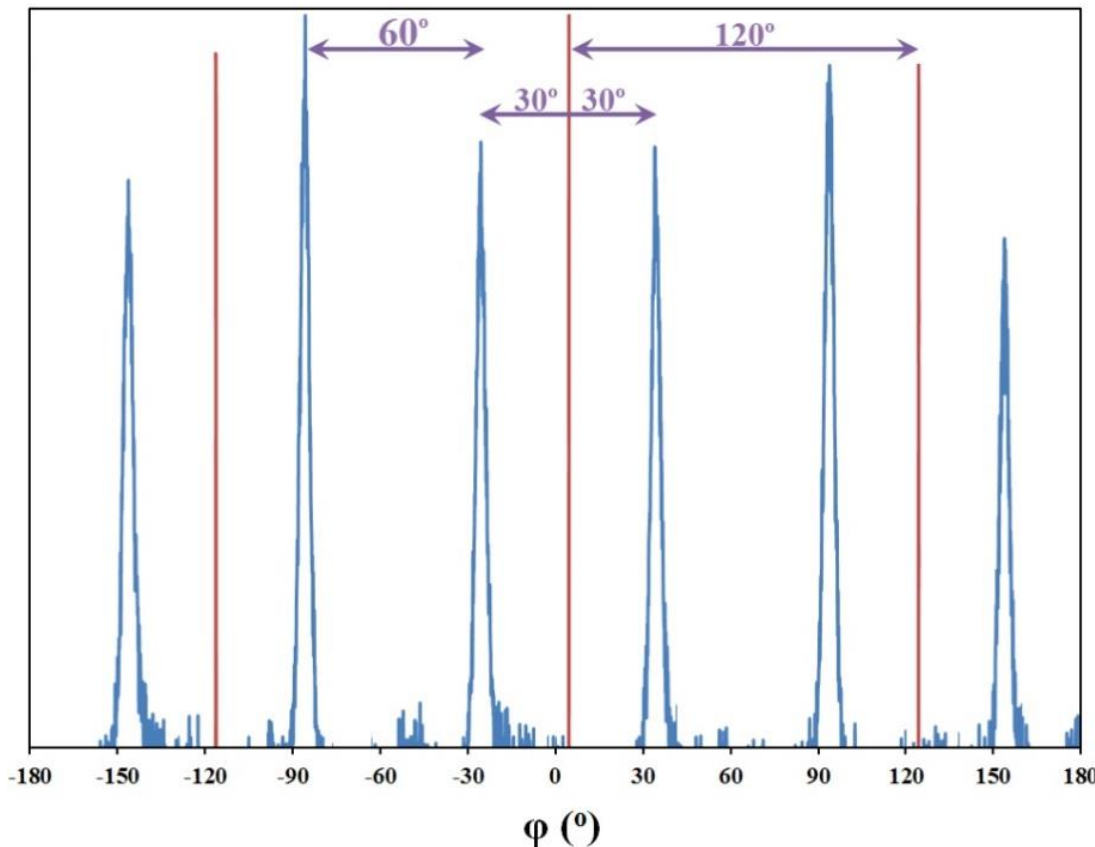


Fig.7.7.  $\varphi$ -scan XRD pattern of the rutile  $\text{TiO}_2$  sample on *c*-cut sapphire  
(Sapphire(011̄2) reflection: red and Rutile(110) reflection: blue)

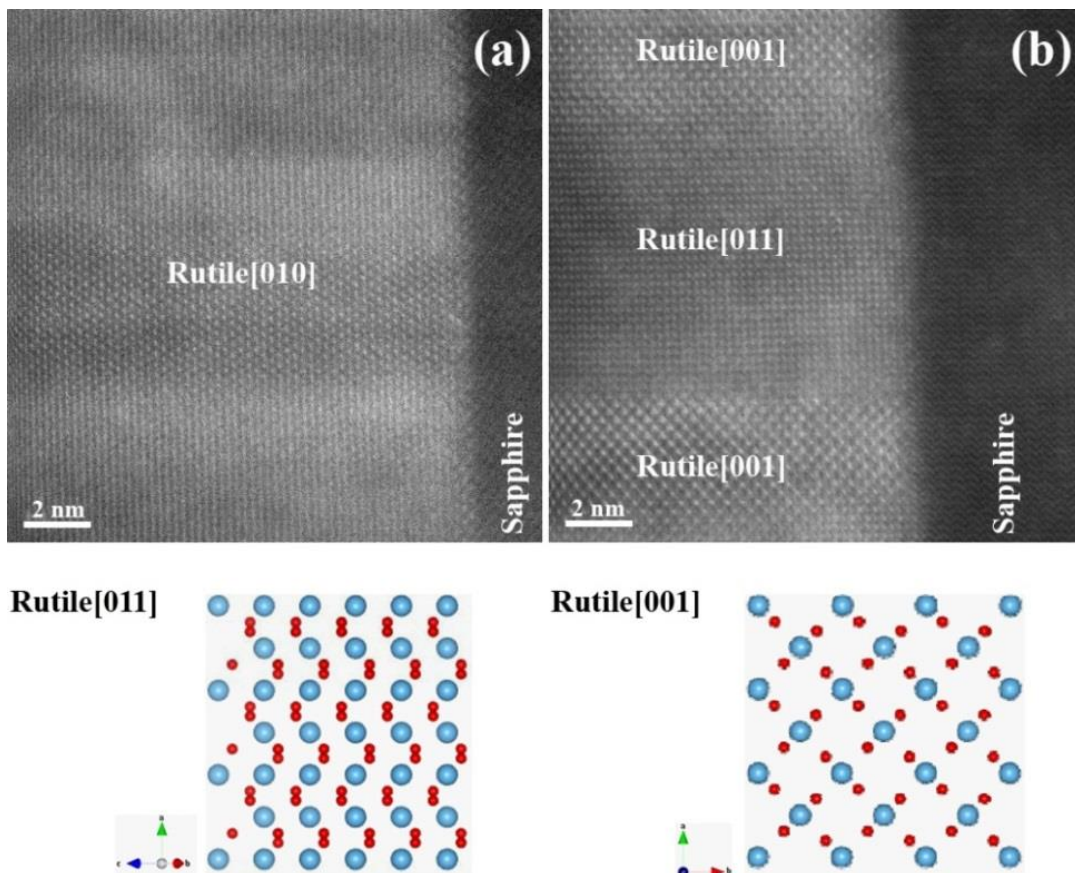


Fig.7.8. A high resolution ADF-STEM image showing: (a)  $[1\bar{2}10]$  and (b)  $[10\bar{1}0]$  zones of *c*-sapphire.

Epitaxial films are expected to exhibit significantly higher photocatalytic efficiencies, because charge carriers have higher mobility and can diffuse to the surface of the catalyst without scattering to participate in the catalytic reactions (equations 7-1 to 7-6), as discussed earlier.

### 7.3.6. Photocatalytic activity

Results of photocatalytic experiments under ultraviolet light are shown in Fig.7.9. As is seen in the inset of this figure, concentration of 4CP decreases with illumination

time showing that 4CP is being decomposed. It should be noted that the curve “No catalyst” corresponds to the experiment where no sample was used as catalyst and only the 4CP solution was irradiated by the UV light. Since no appreciable concentration change is seen in this experiment, it can be deduced that in other experiments, which were performed using a catalyst, 4CP was degraded by photo-activated rutile films.

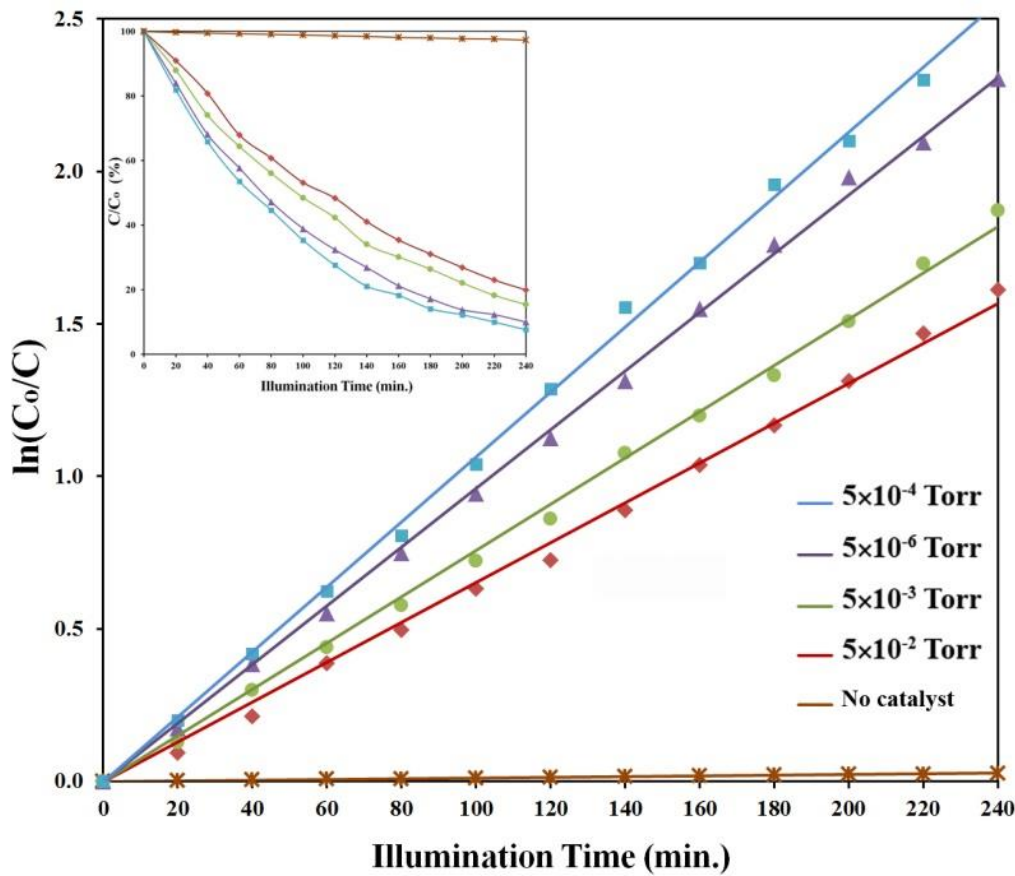


Fig.7.9. Photocatalytic activity of the rutile  $\text{TiO}_2$  films under ultraviolet illumination.

To quantitatively compare the photocatalytic activity of the layers, the photocatalytic reaction rate constants ( $k$ ) should be calculated. Since photocatalytic

decomposition of 4CP solution agrees with pseudo-first-order kinetics, the constant ( $k$ ) can be calculated by the equation  $\ln(C/C_0) = -kt$  (where  $C_0$  is the initial concentration of 4CP at  $t=0$  and  $C$  represents the concentration of 4CP at later times  $t$ ). The quantity  $\ln(C_0/C)$  versus irradiation time was plotted for all samples. Straight lines, whose slopes represent  $k$ , indicate that the degradation of 4CP is a first-order reaction. The reaction rate constants (listed in Tab.7.2) show that the photocatalytic activity increases when the catalysts were annealed under lower pressures, namely  $5 \times 10^{-4}$  Torr. It was already shown that defect content increases at lower annealing pressures. The structural defects, namely  $V_0$ , trap photogenerated electrons and, consequently, enhance charge separation so that positive holes which are prerequisite for photocatalytic decomposition of 4CP can participate in reactions without any recombination. Furthermore, oxygen vacancies at the  $TiO_2$  surface promote the adsorption of molecules. However, the sample annealed under pressure of  $5 \times 10^{-6}$  Torr displays an apparently abnormal behavior, as its photocatalytic efficiency is lower than for the sample annealed under  $5 \times 10^{-4}$  Torr. The reason may be formation of deep level point defects. The energy level of defects is influenced by their concentration; that is, the environment around the defects can affect the energy band edge of defects. As it was already shown, the concentration of defects is raised by low-pressure-annealing leading to formation of deep level defects acting as recombination centers. The efficiency of a photocatalytic process is determined by two factors: the absorption capacity of the semiconductor, which dictates the initial number of carriers, and the time required for the carrier to reach the surface and participate in the photocatalytic reactions. Electron-

hole recombination is an important competing process, since it decreases the carrier mobility and prevents them from reaching to the surface. We think the charge recombination at the deep level defects is responsible for diminishing the photocatalytic efficiency. Meanwhile, the film annealed under the pressure of  $5 \times 10^{-6}$  Torr, had a smoother surface (Fig.6) and, hence, smaller surface area where photocatalytic reactions happen resulting in a lower photocatalytic efficiency. According to the literature<sup>24</sup> and our results, the following reactions are put forward for photocatalytic degradation of 4CP over defected rutile TiO<sub>2</sub> catalyst:



Reaction 7-10 is schematically illustrated in Fig.7.10.

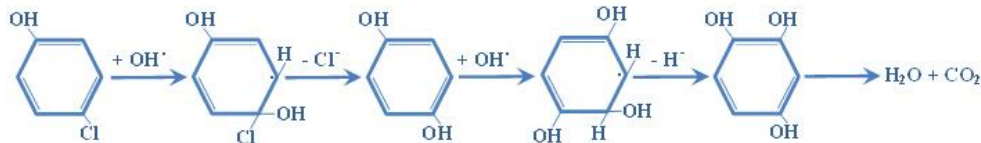


Fig.7.10. Schematic illustration of photo-degradation of 4-chlorophenol on TiO<sub>2</sub> films.

Photocatalytic performance of the rutile films under visible light was also investigated. The results are shown in Fig.7.11. Corresponding photocatalytic reaction

rate constants are listed in Tab.7.2. In these experiments, the short wavelengths ( $\lambda < 420$  nm) were cut off by a UV-filter. As is observed, the layers are photoactive even under low energy visible irradiation.

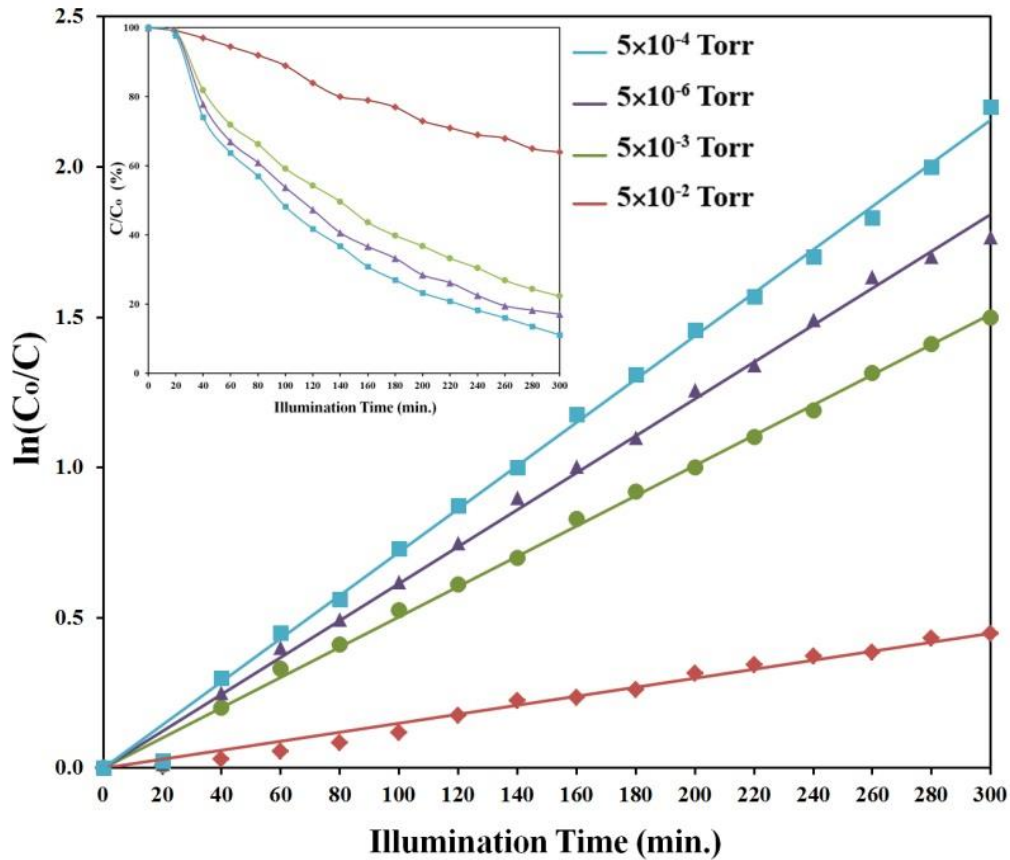


Fig.7.11. Photocatalytic activity of the rutile  $\text{TiO}_2$  films under visible illumination.

As discussed earlier, the films annealed under low oxygen pressures had a narrow band gap and, therefore, they are photo-responsive under visible light. The reason behind this behavior is that the  $\text{Ti}_i$  atom spontaneously donates three electrons to the surrounding lattice  $\text{Ti}$  ions and forms a  $\text{Ti}^{3+}$  ion with a single electron localized on a 3d

shell. In addition, the formation of each  $V_0$  defect results in formation of two  $Ti^{3+}$  in the lattice, as explained earlier. The presence of both lattice and interstitial  $Ti^{3+}$  ions leads to creation of new energy states (about 1-1.5 eV below the conduction band) within the  $TiO_2$  band gap.

Tab.7.2. Photocatalytic reaction rate constants ( $min^{-1}$ ) as a function of the annealing pressure.

	Annealing pressure	No	$5 \times 10^{-2}$	$5 \times 10^{-3}$	$5 \times 10^{-4}$	$5 \times 10^{-6}$
	Illumination	Catalyst	Torr	Torr	Torr	Torr
Ultraviolet		0.00011	0.00667	0.00774	0.01070	0.00973
Visible			0.00151	0.00507	0.00728	0.00616

We proposed that lower photocatalytic efficiency of the film annealed at  $5 \times 10^{-6}$  Torr originated from its lower carrier mobility. To further confirm this conjecture, electrical properties of the layers were investigated. Variation of the electrical resistivity of the annealed rutile  $TiO_2$  films with temperature for different oxygen pressures is displayed in Fig.7.12 where a strong dependence of resistivity on oxygen pressure is apparently observed. It is seen that the resistivity increases by about three orders of magnitude as the oxygen pressure increases from  $5 \times 10^{-6}$  to  $5 \times 10^{-1}$  Torr. As discussed earlier, increased oxygen diffusion at high oxygen pressures decreases the concentration of oxygen vacancies and titanium interstitials and, thus, suppressing the carrier concentration and conductivity. It is also seen that the electrical resistivity increases when the annealing pressure decreases from  $5 \times 10^{-4}$  to  $5 \times 10^{-6}$  Torr. Indeed, the film annealed under the pressure of  $5 \times 10^{-6}$  Torr exhibited lower photocatalytic

efficiency and electrical conductivity as compared to the film annealed under  $5 \times 10^{-4}$  Torr. The reason behind this behavior is that carrier mobility is determined by different scattering mechanisms, including scattering by grain boundaries and intrinsic defects. As already deduced, the concentration of defects increases significantly at very low pressures, e.g.  $5 \times 10^{-6}$  Torr leading to appreciable scattering and trapping phenomena that, in turn, increase the resistivity.

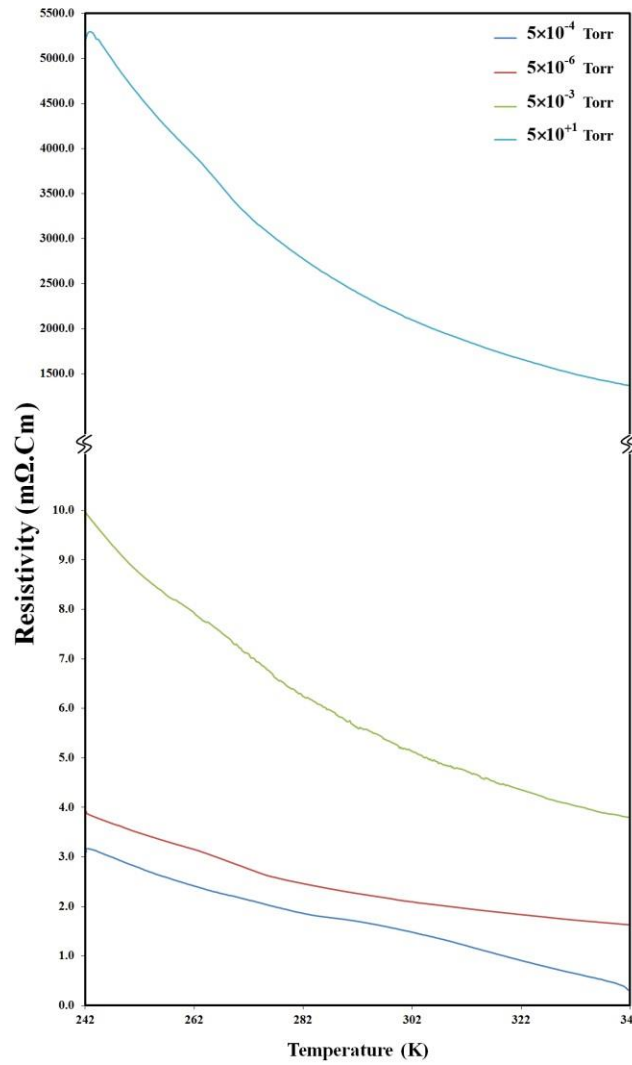


Fig.7.12. Dependence of the electrical resistivity on the annealing pressure.

## **7.4. Conclusions**

Visible-light-responsive rutile TiO<sub>2</sub> films were developed by PLD process followed by vacuum annealing where it is envisaged that the point defects play a crucial role by introducing mid-band energy levels. The layers were single crystalline and the epitaxial relationship between the film and the substrate was shown to be (100)<sub>R</sub>|||(0001)<sub>S</sub>, rutile[001]<sub>R</sub>|||[10̄10]<sub>S</sub>, and [010]<sub>R</sub>|||[1̄210]<sub>S</sub>. Epitaxial growth and formation of atomically sharp interface between the rutile film and the substrate were confirmed by STEM as well. The maximum photocatalytic reaction rate constant for degradation of 4-chlorophenol was determined as 0.0107 and 0.0072 min.<sup>-1</sup> under UV and visible illuminations, respectively. It was also shown that electrical resistivity increased by three orders of magnitude when the annealing pressure was increased from 5×10<sup>-4</sup> to 5×10<sup>+1</sup> Torr. Thus, the photocatalytic activity of titania films can be tuned by controlling the annealing pressure, hence, enabling a variety of environmental remediation processes.

## **References**

1. Y. Du, Q.S. Fu, Y. Li, and Y. Su, J. Hazard. Mater. 186, 491 (2011).
2. Y. Cheng, H. Sun, W. Jin, and N. Xu, Chem. Eng. J. 128, 127 (2007).
3. M. Blanco and L. Pizzio, Appl. Catal. A 405, 69 (2011).
4. G.A. Somorjai, Introduction to Surface Science and Catalysis, New York: Wiley (1994).
5. W. Zhao, L. Feng, R. Yang, J. Zheng, and X. Li, Appl. Catal. B 103, 181 (2011).

6. M. Palacio, P.I. Villabrille, G.P. Romanelli, P.G. Vázquez, and C.V. Cáceres, *Appl. Catal. A* 417-418, 273 (2012).
7. P. Wang, P. Yap, and T. Lim, *Appl. Catal. A* 399, 252 (2011).
8. M.R. Bayati, A.Z. Moshfegh, and F. Golestani-Fard, *Appl. Catal. A* 389, 60 (2010).
9. H.Y. Chang, S.P. Wang, J.R. Chang, H.S. Sheu, and S.G. Shyu, *Appl. Catal. B* 111-112, 476 (2012).
10. M.R. Bayati, F. Golestani-Fard, and A.Z. Moshfegh, *Appl. Catal. A* 382, 322 (2010).
11. M.R. Bayati, A.Z. Moshfegh, and F. Golestani-Fard, *Electrochim. Acta* 55, 3093 (2010).
12. S. Na-Phattalung, M.F. Smith, K. Kim, M.H. Du, and S.H. Wei, *Phys. Rev. B* 73, 125205.1 (2006).
13. E. Finazzi, C.D. Valentin, and G. Pacchioni, *J. Phys. Chem. C* 113, 3382 (2009).
14. J. Zhuang, W. Dai, Q. Tian, Z. Li, L. Xie, J. Wang, and P. Liu, *Langmuir* 26, 9686 (2010).
15. S. A. Campbell, D.C. Gilmer, X.C. Wang, M.T. Hsieh, H.S. Kim, W.L. Gladfelter, and J. Yan, *IEEE Trans. Electron Devices* 44, 104 (1997).
16. F.A. Kroger, *The Chemistry of Imperfect Crystals*; North Holland: Amsterdam, (1974).
17. M.K. Nowotny, T. Bak, and J. Nowotny, *J. Phys. Chem. B* 110, 16270 (2006).
18. M.K. Nowotny, L.R. Sheppard, T. Bak, and J. Nowotny, *J. Phys. Chem. C* 112, 5275 (2008).
19. T. Bak, J. Nowotny, M. Rekas, and C.C. Sorrell, *J. Phys. Chem. Solids* 64, 1057 (2003).
20. I.N. Martyanov, T. Berger, O. Diwald, S. Rodrigues, and K.J. Klabunde, *J. Photochem. Photobiol A: Chem.* 212, 135 (2010).

21. S.W. Chan, J. Phys. Chem. Solids 55, 1137 (1994).
22. M.R. Bayati, Sh. Joshi, R. Molaei, R.J. Narayan, and J. Narayan, J. Solid State Chem. 187, 231 (2012).
23. H.S. Jung, J.K. Lee, J. Lee, B.S. Kang, Q. Jia, M. Nastasi, J.H. Noh, C.M. Cho, and S.H. Yoon, Langmuir 24, 2695 (2008).
24. Y. Cheng, H. Sun, W. Jin, and N. Xu, Chem. Eng. J. 128, 127 (2007).

## **Chapter 8**

# **Phase Tuning, Thin Film Epitaxy, and Properties of YSZ-Buffered TiO<sub>2</sub> on Si(001) Substrate**

We have studied systematically the influence of pulsed laser deposition variables on microstructure and properties of TiO<sub>2</sub> epitaxial thin films where integration with Si(100) substrates was achieved by cubic yttria-stabilized-zirconia (c-YSZ) buffer layer. Details of crystallographic and atomic arrangements across the interfaces are discussed in the light of domain matching epitaxy paradigm. Single crystalline rutile films were obtained at higher substrate temperatures and lower oxygen pressures; whereas, the growth of epitaxial anatase films was promoted by decreasing the temperature and increasing the oxygen pressure. We showed that crystallographic structure of the TiO<sub>2</sub> films is determined mainly by the termination structure of the c-YSZ layer and the bonding characteristics across the TiO<sub>2</sub>/c-YSZ interface. Using  $2\theta$  and  $\varphi$  scans of XRD, the epitaxial relationship between Si(100) substrate and the zirconia buffer layer was shown to be cube-on-cube. Furthermore, the epitaxial relationships at the rutile(100)/zirconia(001) and the anatase(001)/zirconia(001) interfaces were established as  $[0\bar{1}1](100)_{\text{rutile}}||[010](001)_{\text{YSZ}}$  and  $[110](001)_{\text{anatase}}||[100](001)_{\text{YSZ}}$ .

respectively. The proposed crystallographic arrangements as well as the epitaxial growth were confirmed by high resolution TEM diffraction and imaging. XPS and XRD studies showed less defect content and improved crystallinity in the films grown at higher temperatures. AFM results revealed that the finest domain size and the smoothest surface were obtained at intermediate deposition temperatures. Based on the four-point electrical measurements, the heterostructures deposited at 500 °C were more conductive than those grown at 300 and 700 °C. Photocatalytic activity of the films were studied through decomposition of 4-chlorophenol under UV-illumination. The maximum photocatalytic reaction rate constants were determined as 0.0124 and 0.0087 min.<sup>-1</sup> for the anatase and the rutile films grown at 500 °C.

## 8.1. Introduction

Rutile TiO<sub>2</sub> (r-TiO<sub>2</sub>) and anatase TiO<sub>2</sub> (a-TiO<sub>2</sub>) as the two most important states of titania with different characteristics can provide numerous applications in a broad variety of applications. While r-TiO<sub>2</sub> is the thermodynamically favored phase at elevated temperatures, a-TiO<sub>2</sub> is a metastable phase at temperatures below 800-900 °C and it transforms into r-TiO<sub>2</sub> upon heating above this temperature in vacuum.<sup>1-3</sup> Rutile has a tetragonal lattice with P4<sub>2</sub>/mnm space group and lattice parameters of a=b=4.5933 and c=2.9592 Å.<sup>4</sup> It has a band gap of 3.0 eV and a refractive index of about 2.9.<sup>1,5</sup> These properties along with its high thermal stability make r-TiO<sub>2</sub> a promising candidate for many applications such as dye-sensitized solar cells,<sup>6</sup> photonic crystals,<sup>7</sup> anti-bacterial agents,<sup>5</sup> magnetism,<sup>8</sup> ferroelectrics,<sup>9</sup> spintronics,<sup>10</sup> photocatalysis,<sup>11,12</sup>

sensors,<sup>13</sup> and microelectronics.<sup>14</sup> Similar to r-TiO<sub>2</sub>, a-TiO<sub>2</sub> also has a tetragonal lattice, but with different parameters of  $a=b=3.7852$  and  $c=9.5139$  Å and I4<sub>1</sub>/amd space group.<sup>4</sup> Its band gap is about 3.2 eV which is larger than that of rutile.<sup>1</sup> In addition, the refractive index of anatase is about 2.49.<sup>5</sup> Even though a-TiO<sub>2</sub> exhibits attractive properties as well, its relatively low thermal stability limits its applications to low temperatures. However, it is one of the most important known photocatalyst materials able to efficiently decompose almost any kind of environmental pollutants due to the position of its valance and conductance bands.<sup>1,15-18</sup> The a-TiO<sub>2</sub> is used in anti-fogging and self-cleaning surfaces,<sup>19</sup> anti-bacteria agents,<sup>20</sup> hydrogen production,<sup>21</sup> gas and chemical sensors,<sup>22</sup> Li-ion batteries,<sup>23</sup> and magnetic devices.<sup>24,25</sup>

Epitaxial growth of TiO<sub>2</sub> on silicon can lead to integration of functionalities with improved and novel smart device structures. However, direct growth of TiO<sub>2</sub> on silicon is a technological challenge owing to the formation of the native amorphous SiO<sub>x</sub> layer leading to growth of polycrystalline and textured thin films. To grow single crystal layers, therefore, the amorphous surface oxide layer on silicon has to be removed before thin film deposition. So far, deposition of intermediate buffer layers has been introduced as the simplest way to destroy the silicon surface oxide layer. Titanium nitride,<sup>26</sup> cubic zirconia,<sup>27</sup> yttria,<sup>28</sup> and tetragonal zirconia<sup>29</sup> are some examples of the buffers utilized to integrate thin films with silicon epitaxially.

Since the anatase and the rutile states of titania have different physical and chemical characteristics, it is important to tune the phase structure of TiO<sub>2</sub> thin films to achieve the desired properties for the specific application. In this chapter, TiO<sub>2</sub> thin

films were epitaxially grown on the silicon substrates by pulsed deposition technique where high quality films were obtained by optimizing the laser and substrate variables.<sup>30,31</sup> Precise control over phase and microstructure of TiO<sub>2</sub> thin films from pure anatase to pure rutile is reported by controlling laser and substrate variables. Special emphasis is placed on the epitaxial growth of the anatase and rutile TiO<sub>2</sub> films on Si(100) substrate using a cubic yttria-stabilized-zirconia (c-YSZ) buffer layer and modeling the interfaces. The electrical and photocatalytic properties of the heterostructures are also investigated and a correlation between the properties and the microstructure is established.

## 8.2. Experimental

TiO<sub>2</sub>/YSZ heterostructures were grown epitaxially on Si(100) substrates by pulsed laser deposition (PLD). A Lambda Physik (LPX200) KrF excimer laser ( $\lambda = 248$  nm,  $\tau = 25$  ns) was employed to ablate the high purity TiO<sub>2</sub> and c-YSZ targets (8-12% Y<sub>2</sub>O<sub>3</sub> doped-ZrO<sub>2</sub>) which were rotated during the deposition to provide a uniform ablation and avoid pitting on the target surfaces. The Si(100) substrates were cleaned through a multi-step procedure including degreasing in hot acetone for 10 min., ultrasonic cleaning in acetone for 5 min. followed by ultrasonic cleaning in methanol for 5 min. The cleaned substrates were fully dried by a nitrogen gun and, immediately, loaded into the PLD chamber. The chamber was evacuated to a base pressure of  $\sim 1 \times 10^{-6}$  Torr before injecting oxygen into the chamber. Cubic YSZ buffer layers were deposited at 700°C, energy density of 3-3.5 J.cm<sup>-2</sup>, and repetition rate of 5 Hz. To effectively destroy

the native oxide layer on the silicon substrates, the c-YSZ films were deposited for 1000 pulses under vacuum followed by 2000 pulses under the oxygen partial pressure of  $5 \times 10^{-4}$  Torr. Subsequently, TiO<sub>2</sub> thin films were deposited on the c-YSZ buffer layers at different substrate temperatures (300, 500, and 700 °C) and various oxygen partial pressures ( $5 \times 10^{-6}$ ,  $5 \times 10^{-4}$ , and  $5 \times 10^{-2}$  Torr). The energy density, repetition rate, and number of pulses were kept constant at 3-3.5 J.cm<sup>-2</sup>, 5 Hz, and 6000 for all TiO<sub>2</sub> films. Eventually, the samples were cooled down to room temperature inside the PLD chamber under the oxygen partial pressure of 1 Torr.

The out-of-plane orientation of the TiO<sub>2</sub> films were investigated by θ-2θ-scan of XRD using a Rigaku diffractometer with a Cu-Kα radiation ( $\lambda=0.154$  nm). A Philips X'Pert Pro diffractometer was also employed for φ-scan XRD to determine the in-plane orientation of the films. We also used a JEOL 2010F transmission electron microscope, operated at 200 KV, with a point-to-point resolution of 1.8 Å to study the atomic and crystallographic arrangements at the interfaces and to confirm the epitaxial growth where a Gatan imaging filtering system was used for high resolution imaging. The electron transparent samples were prepared through a multistep procedure including polishing, dimpling, and ion-milling. A SPECS XPS with an Mg-Kα excitation of 1254 eV and a PHOIBIS 150 hemispherical analyzer was employed to study the stoichiometry of the films. The XPS results were interpreted by the SDP ver.4.1 software where energy calibration was established by referencing to C(1s) binding energy at 285.0 eV. Morphology of the layers was studied by a Veeco AFM as well and the results were interpreted by nanoscope ver. 5.12r3 software. A self-made labview program

employing a Keithley 2400 sourcemeter was used to study the electrical properties of the films. The measurements were done in a temperature range of 225-345 K where the sample was cooled using a closed cycle helium cryostat. Photocatalytic activity of the layers was evaluated as well through the procedure explained in chapter 3.

### **8.3. Results and discussion**

#### **8.3.1. Phase structure**

20-θ XRD patterns of the TiO<sub>2</sub> films grown at different substrate temperatures and oxygen partial pressures are depicted in Fig.8.1. A couple of features of this figure are worth noting. The r-TiO<sub>2</sub> phase tends to form under lower pressures at all temperatures, while appreciable amount of the a-TiO<sub>2</sub> phase only forms under higher oxygen pressures especially at lower temperatures. In other words, no anatase phase formed under the oxygen pressures of  $5 \times 10^{-4}$  and  $5 \times 10^{-6}$  Torr and the rutile phase did not form under the oxygen partial pressure of  $5 \times 10^{-2}$  Torr at low temperatures, particularly at 300 °C. The effect of oxygen pressure on crystallographic characteristics of the oxide thin films grown by PLD technique has been previously reported in the literature.<sup>32,33</sup> The first approach originates from dependence of kinetic energy of the laser ablated species upon the oxygen partial pressure at a certain temperature and laser energy. Interaction between the ablated species and oxygen molecules is not that much appreciable resulting in the high energy adatoms. Hence, the r-TiO<sub>2</sub> phase, which is the energetically favored phase of titania,<sup>34</sup> forms under lower pressures where the adatoms have enough energy for surface diffusion. Also, the change in crystallographic

characteristics of the PLD-grown oxides can be attributed to changes in the surface structure of the substrate or the buffer layer. The surface of the c-YSZ buffer film becomes anion-terminated under higher oxygen pressures and cation-terminated under lower pressures.<sup>32</sup> This phenomenon alters the lattice misfit at the c-YSZ/TiO<sub>2</sub> interface and introduces different misfit strains between the buffer and the top layer.

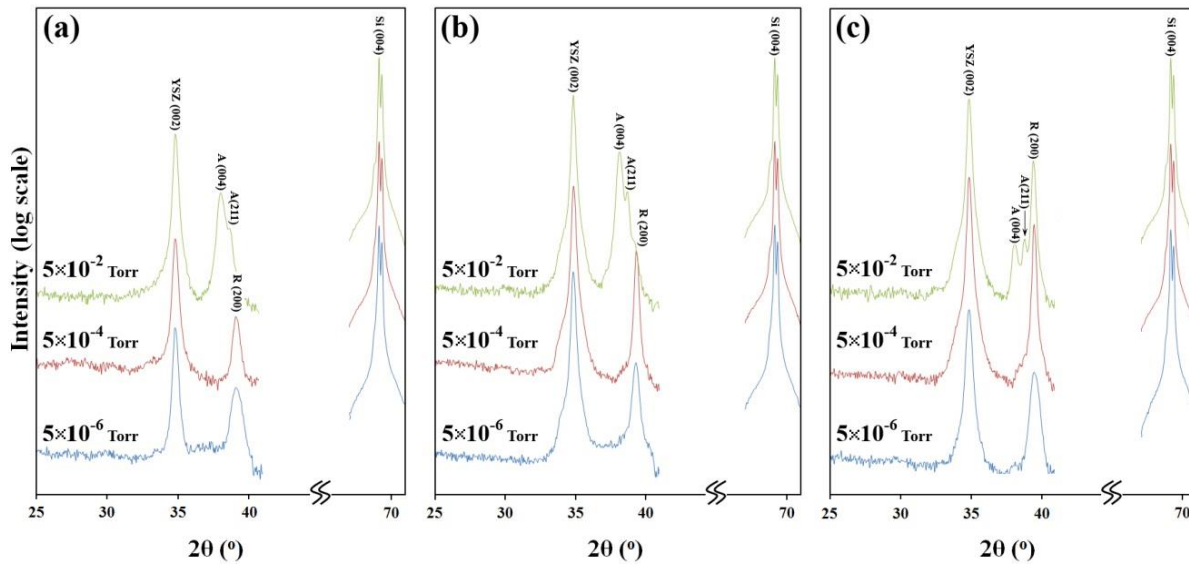


Fig.8.1.  $\theta$ - $2\theta$  XRD patterns of the TiO<sub>2</sub> films deposited on c-YSZ/Si(100) platform under various oxygen pressures at temperatures of: (a) 300, (b) 500, and (c) 700 °C.

In addition, the Zr-terminated surface of c-YSZ is atomically jagged (Fig.8.2a), whereas its O-terminated surface is to some extent smooth at the atomic scale (Fig.8.2b). Consequently, phases with atomically rough surfaces are favored to grow onto the Zr-terminated c-YSZ buffer layer and, in contrast, the formation of phases with atomically smooth surfaces is favored on the O-terminated c-YSZ. Therefore, both the

kinetic energy of the species and the surface chemistry of the c-YSZ layer may control the phase structure of the TiO<sub>2</sub> film.

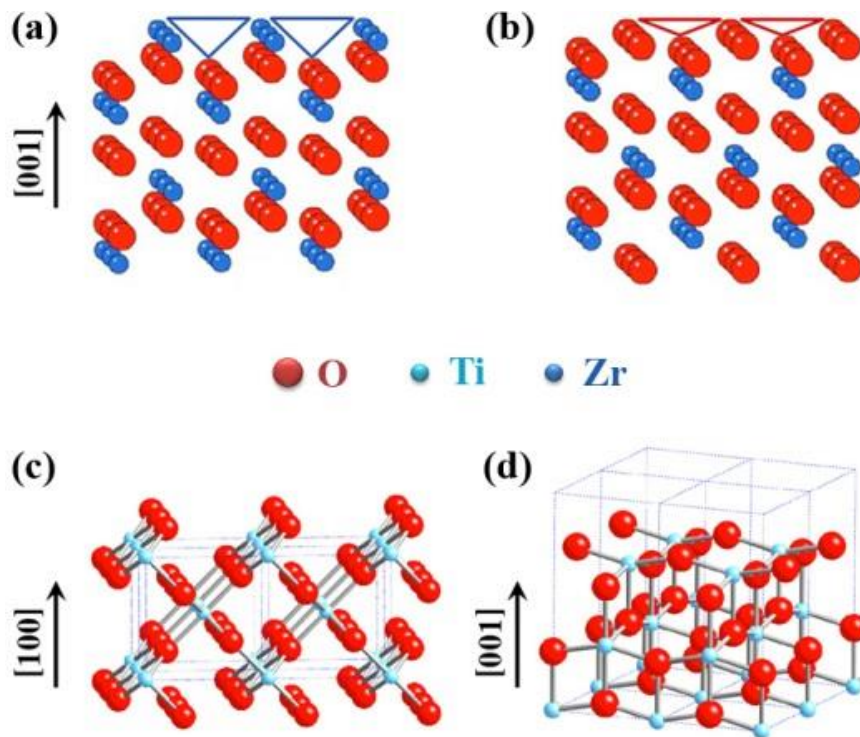


Fig.8.2. Atomic arrangement on: (a) Zr-terminated c-YSZ (200), (b) O-terminated c-YSZ(200), (c) O-terminated r-TiO<sub>2</sub>(200), and (d) Ti-terminated a-TiO<sub>2</sub> planes. Roughness of the Zr- and O-terminated planes of c-YSZ is compared and highlighted by triangles.

To shed more light on the reason behind the dependence of TiO<sub>2</sub> state on the oxygen pressure, two samples were prepared at the substrate temperature of 500 °C, but at varying pressures and number of pulses. For the first sample (sample A), after the deposition of c-YSZ buffer layer, the TiO<sub>2</sub> film was grown under the partial pressure of  $5 \times 10^{-4}$  Torr (where the r-TiO<sub>2</sub> phase is favored) for 500 pulses and, then, the pressure was increased to  $5 \times 10^{-2}$  Torr (where the a-TiO<sub>2</sub> phase is favored) at which the

deposition was continued for 5500 pulses. For the second sample (sample B), the titania top film was grown under the pressure of  $5 \times 10^{-2}$  Torr for 500 pulses and under the pressure of  $5 \times 10^{-4}$  Torr for 5500 pulses, after the deposition of the buffer layer. Since the sample A was mostly grown at the pressure of  $5 \times 10^{-2}$  Torr, its phase structure was expected to be a-TiO<sub>2</sub>, but r-TiO<sub>2</sub> is the dominant phase in this sample, as is seen in Fig.8.3. That is, r-TiO<sub>2</sub> can grow even under high pressures, if the deposition is initially done at low pressures.

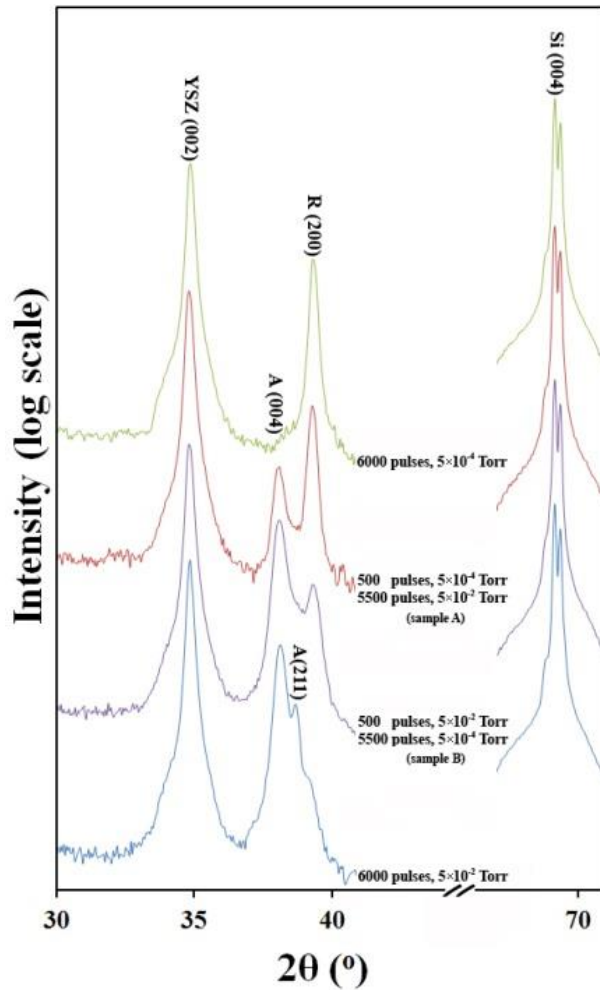


Fig.8.3.  $\theta$ - $2\theta$  XRD data for the TiO<sub>2</sub> thin films grown under varying pressures for different times.

Results indicate that a-TiO<sub>2</sub> grows even at low oxygen pressures, if the oxygen pressure just before the deposition is high, because the sample B mainly consists a-TiO<sub>2</sub>, although it was grown under the pressure of  $5 \times 10^{-4}$  Torr for 18 min., as Fig.8.3 shows. This reveals that initial monolayers act as a template for the subsequent atomic layers. When the oxygen pressure just before the TiO<sub>2</sub> deposition is low, e.g.  $5 \times 10^{-4}$  Torr, the surface of the c-YSZ buffer layer is Zr-terminated, so an O-terminated TiO<sub>2</sub> film is required to bond with the zirconium cations. It is worth reminding that the Zr-terminated c-YSZ film is atomically jagged; consequently, a rough TiO<sub>2</sub> film is favored to grow onto it. Since the O-terminated r-TiO<sub>2</sub> has a rough surface (Fig.8.2c) and the O-terminated a-TiO<sub>2</sub> is atomically smooth (Fig.8.2d), the rutile phase grows under lower oxygen pressures where the c-YSZ is Zr-terminated and jagged. On the other hand, surface of the c-YSZ intermediate layer is O-terminated and atomically smooth (Fig.8.2b), when the oxygen pressure just before the growth of TiO<sub>2</sub> is high, e.g.  $5 \times 10^{-2}$  Torr. Under this condition, a smooth Ti-terminated TiO<sub>2</sub> film is required; thus, first monolayers growing under high pressures is a-TiO<sub>2</sub> having a smooth Ti-terminated surface, as illustrated in Fig.8.2d.

As it is also observed in Fig.8.2, the Ti-terminated surface of the rutile TiO<sub>2</sub> is not smooth in the atomic scale. In summary, crystallographic structure of the first monolayers of TiO<sub>2</sub> is determined by the oxygen partial pressure just before the deposition, rather than the pressure during the deposition. When deposition begins at a low pressure, the rutile phase nucleates and forms a rutile platform. Even though the remaining of the TiO<sub>2</sub> deposition is conducted at a relatively higher pressure (a

condition where a-TiO<sub>2</sub> grows), the rutile TiO<sub>2</sub> continues growing onto the initially formed rutile template. Similarly, an anatase platform forms just at the beginning of the TiO<sub>2</sub> deposition at higher pressures and keeps growing even when the pressure is decreased to  $5 \times 10^{-4}$  Torr. Thus, the phase structure of the TiO<sub>2</sub> films is not controlled by the kinetics of ablated particles.

According to Fig.8.1, intensity of the rutile and YSZ peaks increases with the temperature and their full width at half-maximum (FWHM) decreases; in other words, crystallinity of those phases becomes better at higher substrate temperatures. The samples prepared at higher temperatures, e.g. 700 °C, took a longer time to completely cool down to the room temperature. Because cooling was conducted under an oxygen atmosphere of pressure of 1 Torr, the samples prepared at higher temperatures were oxygen annealed for longer times. As a result, the structural point defects, i.e. vacancies and interstitials, were annealed out in such samples and a more favorable crystallinity was achieved. Our discussions on the effect of the growth temperature on the defect content were further confirmed by XPS analysis. The high resolution O(1s) core level binding energies in the r-TiO<sub>2</sub> films deposited at varying temperatures are shown in Fig.8.4. Peaks A and B with binding energies of about 532.8 and 531.7 eV are attributed to the oxygen in H<sub>2</sub>O and OH compounds attached to the surface defects, namely oxygen vacancies. Oxide free surfaces contacting with the atmosphere are always hydrated, i.e. contain water molecules and hydroxyl groups.<sup>35</sup> Peak C which is located at the binding energy of about 530.2 eV corresponds to the oxygen in the TiO<sub>2</sub> compound. In other words, portion of this peak represents the perfect TiO<sub>2</sub> structure. Finally, peak D at the

binding energy of about 528.7 eV is assigned to the oxygen atoms in contact with the titanium interstitial defects, as explained back in the previous chapters.<sup>11</sup> Therefore, peaks A, B, and D can be assigned to the disorder in the rutile film, while peak C represents the perfection of the TiO<sub>2</sub> structure. The portion of peak C was determined as 74.3, 77.8, and 78.5% for the growth temperatures of 300, 500, and 700 °C. The O/Ti ratio, which reflects the overall stoichiometry of the TiO<sub>2</sub> films, was determined to be 1.62, 1.83, and 1.91 for the growth temperatures of 300, 500, and 700 °C. Thus, the formation of the rutile films with fewer defects occurs at higher temperatures.

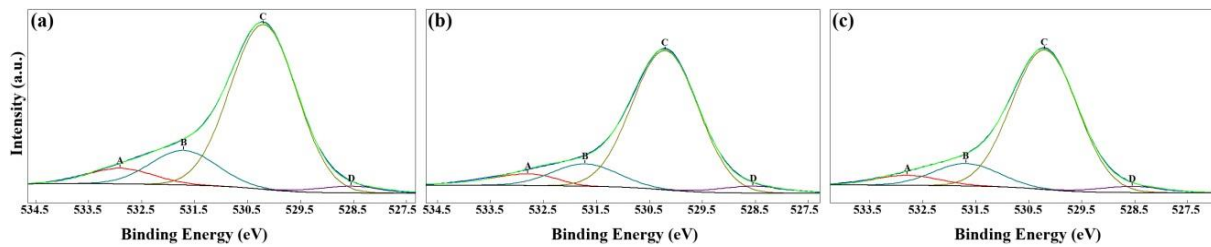


Fig.8.4. High resolution XPS O(1s) core level binding energy of the r-TiO<sub>2</sub> films grown at different temperatures: (a) 300, (b) 500, and (c) 700 °C.

Similar behavior was observed for the a-TiO<sub>2</sub> films as well (data not presented here). It is also seen in Fig.8.1 that the intensity of the anatase peaks decreases at higher deposition temperatures. This behavior arises from the lower stability of the anatase phase at elevated temperatures.<sup>1-3</sup> Even though it was suggested that increasing the substrate temperature leads to formation of films of better crystallinity, it is worth mentioning that the temperature has a different effect at low pressures, e.g.  $5 \times 10^{-6}$  Torr. When such a low pressure is used, the oxygen anions tend to leave the TiO<sub>2</sub> surface at elevated temperatures, e.g. 700 °C; as a consequence, the concentration of the point

defects increases resulting in broad XRD peaks with low intensity. This is the reason behind the large FWHM of the rutile(200) peak of the sample grown at 700 °C under the pressure of  $5 \times 10^{-6}$  Torr. Because the samples grown under the pressure of  $5 \times 10^{-6}$  Torr are so defective, their defects are not annealed out after cooling to the room temperature. Since the defects tend to accumulate along the domain boundaries and pin them, the boundaries cannot migrate freely giving rise to slow grain growth. Thus, the rutile peak of these samples is not as sharp and intense as that of the samples grown under the oxygen pressure of  $5 \times 10^{-4}$  Torr.

### 8.3.2. Epitaxial relationship and the DME details

The details of epitaxial growth and the in-plane alignment of the r-TiO<sub>2</sub> films on the c-YSZ buffer layer were investigated using  $\varphi$ -scanning XRD results of which are presented in Fig.8.5. Eight strong  $\varphi$ -peaks of rutile(110) reflection ( $2\theta=27.44^\circ$  and  $\psi=45.00^\circ$ ) with an angular interval of  $\sim 64.5^\circ$  are due to the 2-fold symmetry about the  $a$ -axis of rutile and four equally probable arrangement of domains on the c-YSZ buffer. It is also seen in Fig.8.5 that the (110)  $\varphi$ -peaks appear with an angular separation of  $32.25^\circ$  from the (202) reflections of YSZ ( $2\theta=50.37^\circ$  and  $\psi=45.00^\circ$ ). The so called four equal orientations are displayed in Fig.8.6 in different colors.

Considering this information, the r-TiO<sub>2</sub>/c-YSZ interface was modeled as schematically illustrated in Fig.8.7 and the epitaxial relationship was established as  $(100)_{\text{rutile}}||(001)_{\text{YSZ}}$ ,  $[0\bar{1}1]_{\text{rutile}}||[010]_{\text{YSZ}}$ , and  $[025]_{\text{rutile}}||[100]_{\text{YSZ}}$ . A detailed TEM study was performed to study the microstructure and verify the epitaxial relationship of the

films whose results are displayed in Fig.8.8. From the low magnification bright field image, the thickness of the c-YSZ and r-TiO<sub>2</sub> layers is determined as ~200 and ~215 nm.

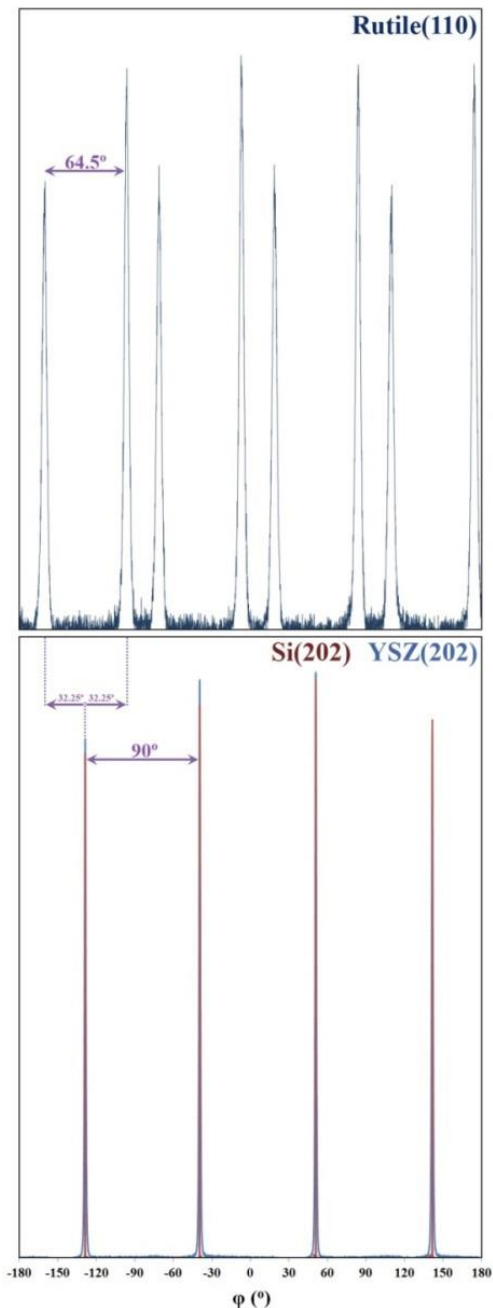


Fig.8.5.  $\varphi$ -scan XRD patterns of the (110)<sub>rutile</sub>, (202)<sub>YSZ</sub>, and (202)<sub>Si</sub> reflections of the heterostructure fabricated at 700 °C under the oxygen pressure of  $5 \times 10^{-4}$  Torr.

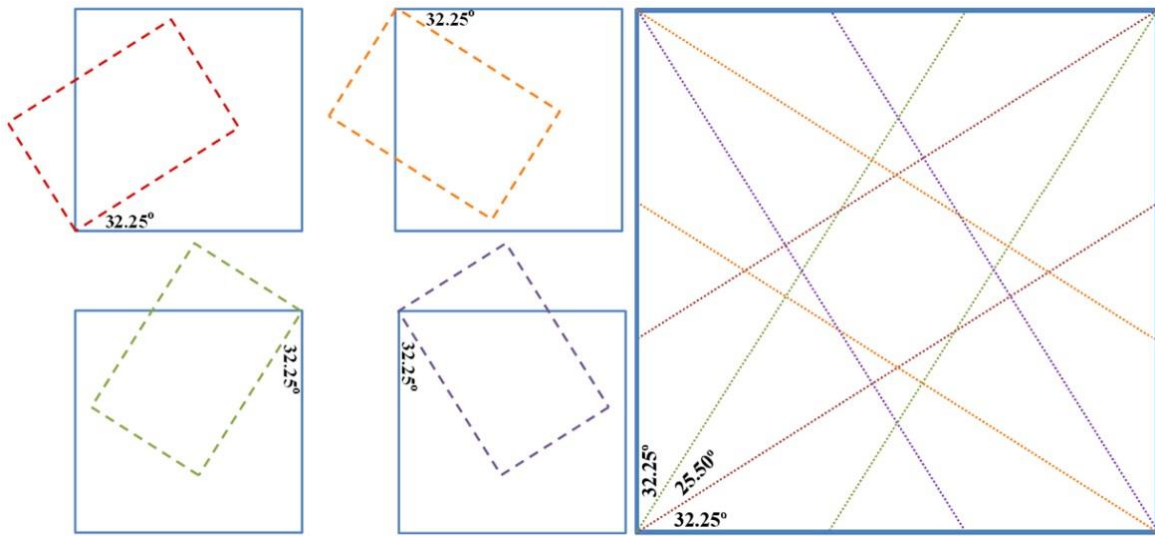


Fig.8.6. Delineation of four equally probable orientations of r-TiO<sub>2</sub> film on c-YSZ layer.

Blue square represents the c-YSZ lattice.

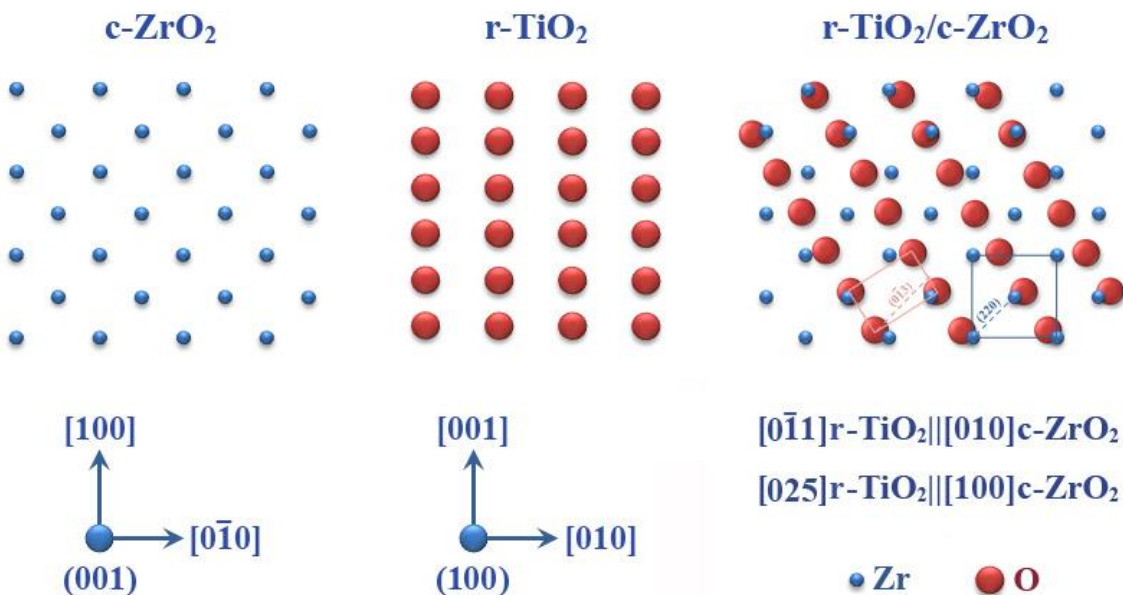


Fig.8.7. Schematic illustration of the atomic arrangement and the epitaxial relationship across the interface between O-terminated r-TiO<sub>2</sub> and Zr-terminated c-YSZ films.

The indexed selected area electron diffraction (SAED) pattern, from a large area cross section, further confirms the proposed epitaxial relationship.

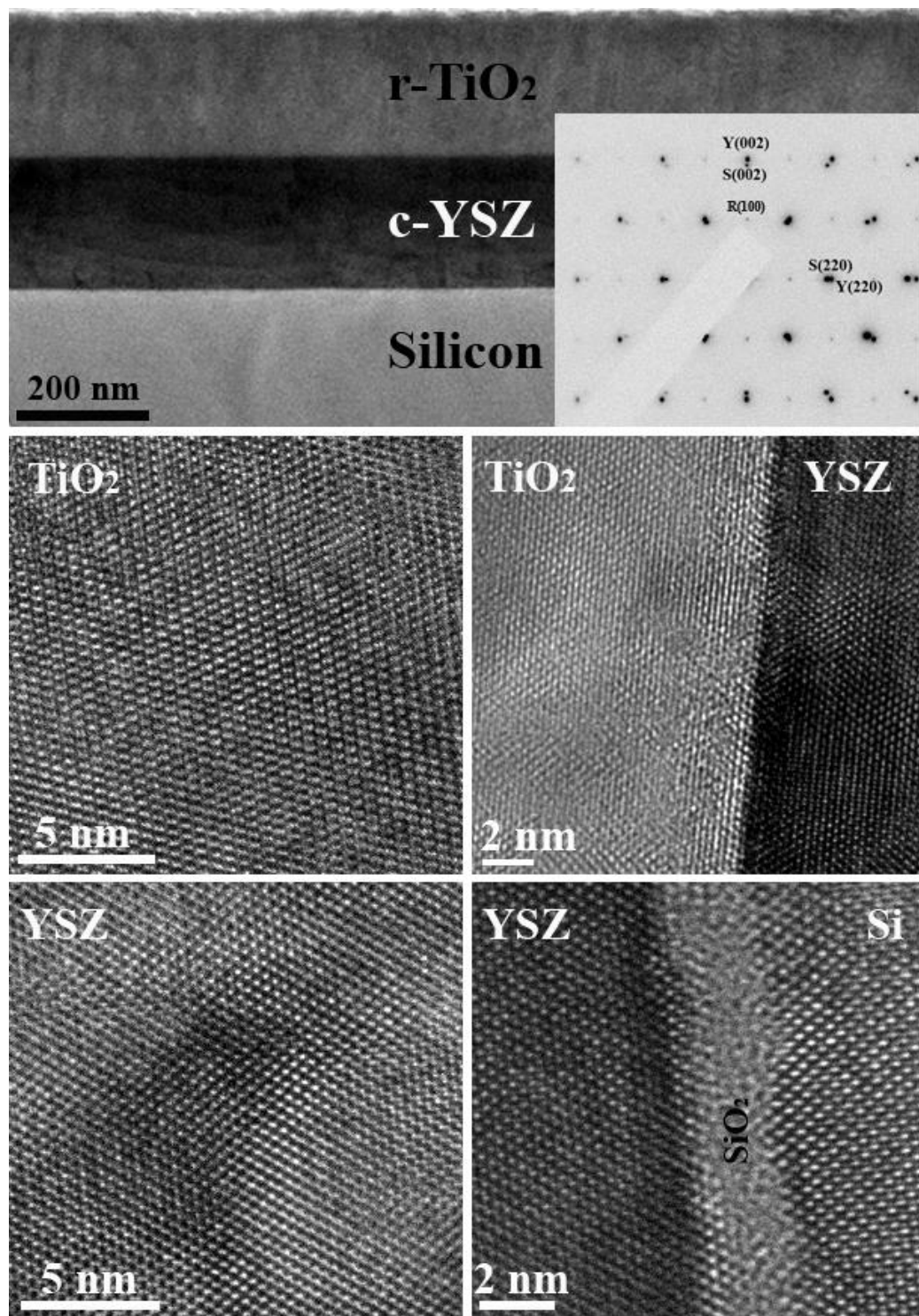


Fig.8.8. TEM low magnification bright field image and the high resolution cross section images of the r- $\text{TiO}_2$ /c-YSZ/Si(001) heterostructure. The indexed SAED pattern shown in the inset of the BF image confirms the proposed epitaxial relationship (Rutile[031], YSZ[110], and Si[110] zones).

The SAED pattern corresponds to  $[031]_{\text{rutile}}$ ,  $[1\bar{1}0]_{\text{YSZ}}$ , and  $[1\bar{1}0]_{\text{Si}}$  zones. As is seen,  $(200)$  planes of rutile align with  $(004)$  planes of c-YSZ and Si. Besides,  $(0\bar{1}3)$  planes of rutile is parallel to the  $(220)$  planes of the c-YSZ and Si. For the sake of simplicity and better understanding, these two planes as well as the unit cells of r-TiO<sub>2</sub> and c-YSZ are schematically shown in Fig.8.7. The detailed high resolution TEM images confirm the highly epitaxial growth of r-TiO<sub>2</sub> film and c-YSZ buffer layer on the silicon substrate. An atomically sharp interface is observed between the rutile film and the YSZ intermediate layer. The spacing between  $(05\bar{2})_{\text{rutile}}$ ,  $(011)_{\text{rutile}}$ , and  $(400)_{\text{YSZ}}$  planes were calculated as about 0.78, 2.49, and 1.28 Å, respectively. Hence, the misfit strains across the r-TiO<sub>2</sub>/c-YSZ interface were determined as  $\varepsilon_1=1-(2\times2.49/5.14)=+3.11\%$  and  $\varepsilon_2=1-(0.78/1.28)=+39.06\%$  where  $\varepsilon_1$  and  $\varepsilon_2$  are the misfits along  $[0\bar{1}1]$  and  $[025]$  directions of r-TiO<sub>2</sub>. The strain in the rutile film is compressive along the both directions. According to the domain matching epitaxy (DME) paradigm,<sup>36</sup> the lattice misfit strain at the r-TiO<sub>2</sub>/c-YSZ interface is accommodated by matching of integral multiples of crystallographic planes. Along direction 1, 32 planes of the r-TiO<sub>2</sub> film match with 31 planes of the c-YSZ film with a frequency factor of  $\alpha=\sim0.1$  to fully relax the misfit strain. That is, the 32/31 and 33/32 domains alternate with the mentioned frequency factor. Besides, the misfit strain along direction 2 is relaxed through matching of 2 planes of the rutile film with 1 planes of the YSZ film or 3 planes of the rutile film with 2 planes of the YSZ film. In this case, the frequency factor would be about 0.56.

The  $\varphi$ -scan XRD was employed to determine the in-plane alignment between the a-TiO<sub>2</sub> film and the c-YSZ buffer layer. The results are presented in Fig.8.9.

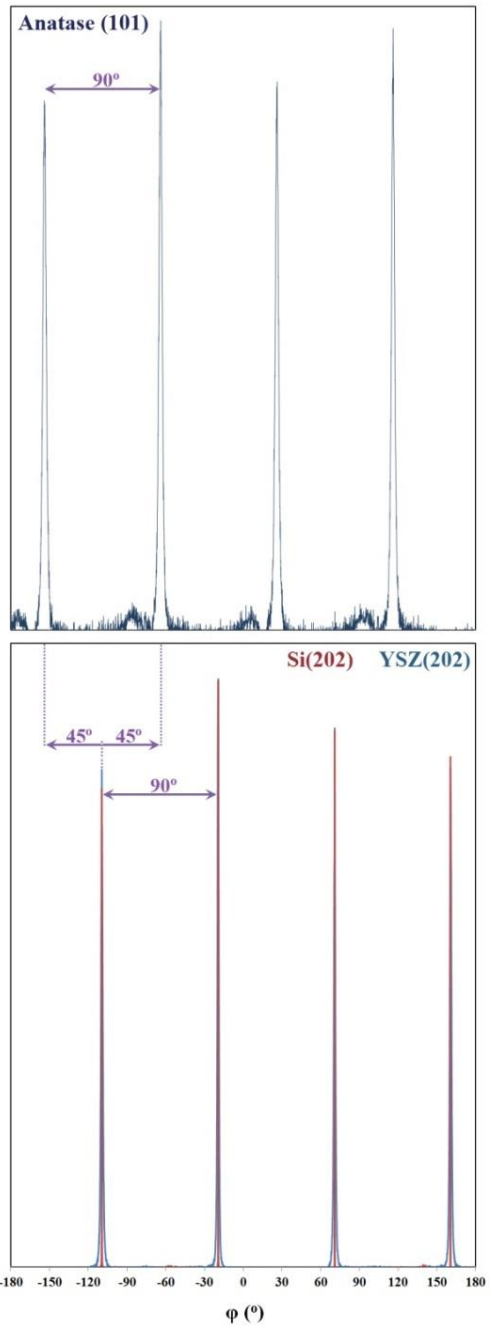


Fig.8.9.  $\varphi$ -scan XRD patterns of the  $(101)_{\text{anatase}}$ ,  $(202)_{\text{YSZ}}$ , and  $(202)_{\text{Si}}$  reflections of the heterostructure fabricated at  $300^\circ\text{C}$  under the oxygen pressure of  $5 \times 10^{-2}$  Torr.

The 4-fold symmetry along [001] directions of a-TiO<sub>2</sub> and c-YSZ results in four strong  $\varphi$ -peaks from (101) reflection of a-TiO<sub>2</sub> ( $2\theta=25.28^\circ$  and  $\psi=68.30^\circ$ ) with a  $90^\circ$

angular separation from each other and a  $45^\circ$  separation from (202) reflection of c-YSZ. The a-TiO<sub>2</sub>/c-YSZ interface was also modeled whose result is shown in Fig.8.10. Taking this model into account, the epitaxial relationship was established as (001)<sub>anatase</sub>||(001)<sub>YSZ</sub>, [110]<sub>anatase</sub>||[100]<sub>YSZ</sub>, and [1 $\bar{1}$ 0]<sub>anatase</sub>||[0 $\bar{1}$ 0]<sub>YSZ</sub>. The inter-planar spacing of (110)<sub>anatase</sub> and (100)<sub>YSZ</sub> planes were calculated as 5.34 and 5.14 Å, respectively. Hence, the misfit strain at the a-TiO<sub>2</sub>/c-YSZ interface was determined as  $\varepsilon=1-(5.34/5.14)=-3.9\%$ . This compressive strain is relaxed when 25/26 and 26/27 domains of the a-TiO<sub>2</sub> and c-YSZ films alternate with a frequency factor of 0.7.

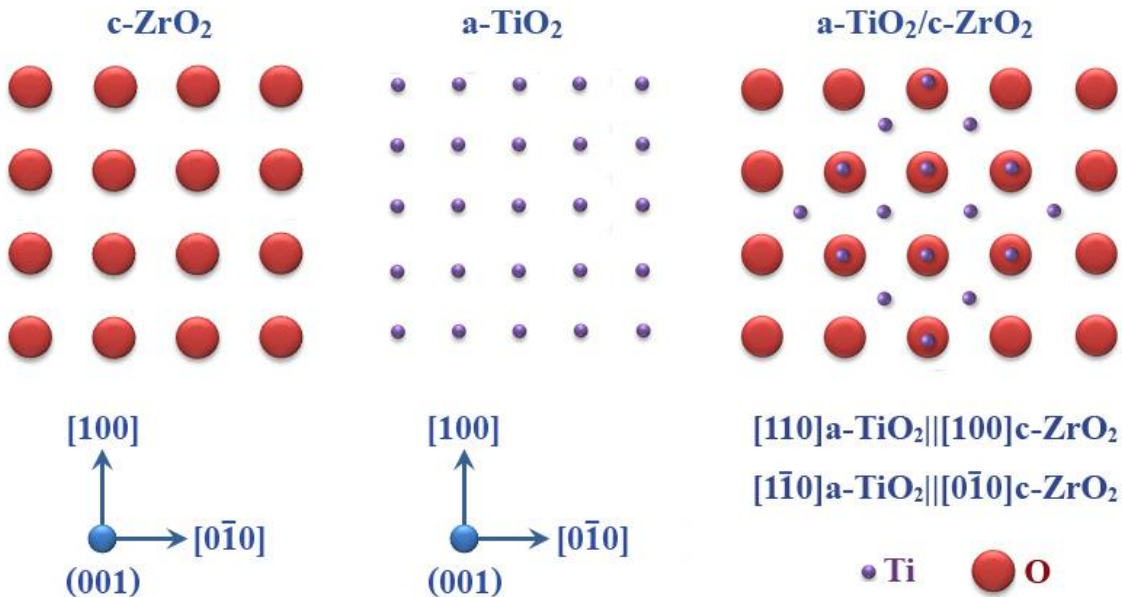


Fig.8.10. Schematic illustration of the atomic arrangement and the epitaxial relationship across the Ti-terminated a-TiO<sub>2</sub> and O-terminated c-YSZ interface.

Considering the low magnification cross section TEM image in Fig.8.11, thickness of the anatase film is determined as about 275 nm. The epitaxial growth of the a-TiO<sub>2</sub>

and the c-YSZ films is evident in the high resolution TEM images shown in this image. To study the epitaxial relationship between the c-YSZ film and the Si (100) substrate,  $\varphi$ -scanning XRD was performed on (202) reflection of c-YSZ and that of Si ( $2\theta=47.04^\circ$  and  $\psi=45.00^\circ$ ) result of which was already shown in both Figs.8.5 and 8.9. The sharp  $\varphi$ -peaks from (202) reflections of c-YSZ and Si at the same azimuthal positions are due to the 4-fold symmetry in both crystals and their lattice parameters. Such patterns confirm the epitaxial cube-on-cube growth of c-YSZ buffer layer on silicon (001). The epitaxial relationship across the c-YSZ/Si(100) interface can be explained as  $(001)_{\text{YSZ}}|| (001)_{\text{Si}}$  and  $[100]_{\text{YSZ}}|| [100]_{\text{Si}}$  which is further confirmed by the indexed SAED pattern in Fig.8.8. The pattern shows that (220) planes as well as (004) planes of YSZ and Si are parallel. Meanwhile, the spots from the YSZ film and the Si substrate are from a same crystallographic zone ( $[1\bar{1}0]$ ).

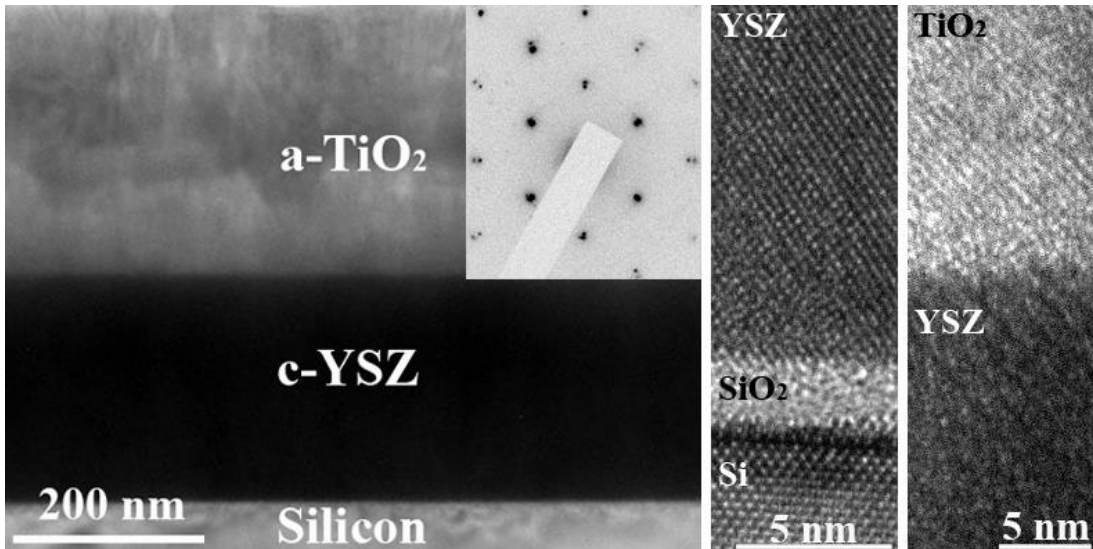


Fig.8.11. TEM low magnification bright field image and the high resolution cross section images of the a-TiO<sub>2</sub>/c-YSZ/Si(001) heterostructure.

The highly epitaxial growth of YSZ film on silicon substrate is also evident in the high resolution TEM images shown in Fig.8.8 and Fig.8.11. It is concluded that c-YSZ provides a promising buffer layer and a template to functionally integrate thin films with silicon substrates. It grows epitaxially on Si(001) surface without removing the native silicon dioxide layer from the surface prior to deposition. It is explained considering the following reaction:<sup>37</sup>



Silicon monoxide (SiO) is quite volatile and evaporates at the deposition temperature. During the initial stages of the deposition where the buffer layer was deposited under vacuum, oxide present on the silicon substrate is destroyed and removed by the above reaction; then, the c-YSZ grows epitaxially on silicon when the oxygen partial pressure is increased to  $5 \times 10^{-4}$  Torr. The very thin  $\text{SiO}_x$  amorphous layer, which is seen in the high resolution TEM images, forms during the growth of the films when oxygen diffuses to the surface of the silicon substrate through the YSZ buffer layer. However, it does not alter the epitaxial growth of the buffer layer, because the buffer layer has been already formed.

### 8.3.3. Morphology

Morphology of the films deposited under the oxygen pressures of  $5 \times 10^{-4}$  and  $5 \times 10^{-2}$  Torr at various temperatures is depicted in Fig.8.12. Results show that the

surface roughness decreases and, then, increases with the deposition temperature. In other words, the samples grown at the intermediate temperature of 500 °C have the smoothest surface.

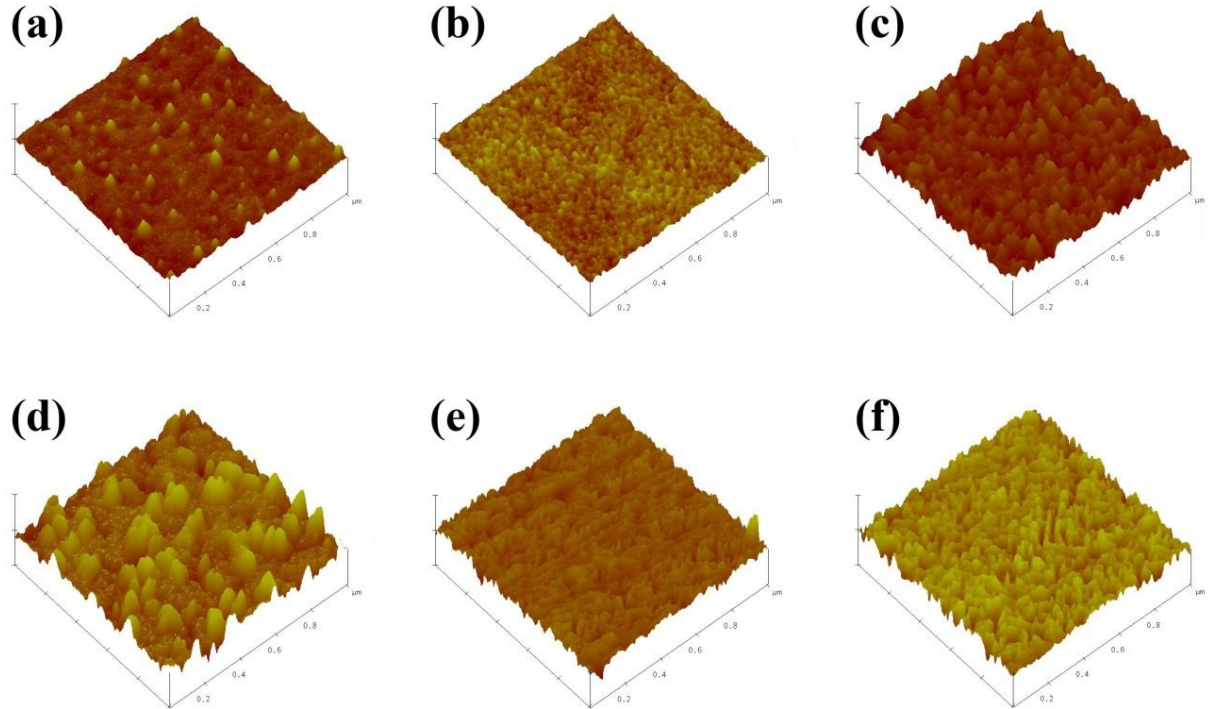


Fig.8.12. Surface morphology of the heterostructures grown under different conditions: (a)  $5 \times 10^{-4}$  Torr and 300 °C, (b)  $5 \times 10^{-4}$  Torr and 500 °C, (c)  $5 \times 10^{-4}$  Torr and 700 °C, (d)  $5 \times 10^{-2}$  Torr and 300 °C, (e)  $5 \times 10^{-2}$  Torr and 500 °C, and (f)  $5 \times 10^{-2}$  Torr and 700 °C. The z-scale in all images is 20 nm.

We propose that the surface roughness is determined by two phenomena: grain growth and mobility of the ablated species across the substrate surface. At lower temperatures, the ablated particles from the target are quenched once they arrive at the substrate and the surface diffusion rate is low. Thus, a rough surface forms at the growth temperature of 300 °C, as shown in Figs.8.12a and 8.12d. This phenomenon

does not prevail at higher temperatures. However, the defect concentration is lower in the samples grown at higher temperatures, as discussed earlier. The point defects tend to accumulate around the domain boundaries and can inhibit boundary motion, so finer domains form at higher defect concentrations. When the defect concentration is low, mobility of the boundaries and, therefore, rate of the grain growth are appreciable; consequently, larger domains and rougher surfaces form at the elevated temperatures (Figs.8.12c and 8.12f). At the intermediate temperature of 500 °C, the surface mobility of the ablated particles is high enough to diffuse and find their equilibrium positions. In addition, the growth rate is not high to form large domains. Therefore, a smooth surface grows at the intermediate temperatures, as depicted in Figs.8.12b and 8.12e. In addition, the films grown at the pressure of  $5 \times 10^{-2}$  Torr have a rougher surface as compared to those deposited under  $5 \times 10^{-4}$  Torr. We attribute this to less point defects in these films and, hence, higher grain growth rate as well as lower kinetic energy of the ablated particles on the substrate surface.

### **8.3.4. Electrical properties**

Resistance-temperature curves of the heterostructures deposited under the pressure of  $5 \times 10^{-4}$  Torr at varying temperatures are delineated in Fig.8.13 where a semiconductor behavior is evident. Results show that the electrical resistance decreases, reaches its minimum value, and, then, increases as the deposition temperature is raised from 300 to 700 °C. This behavior is attributed to two competing

phenomena. As it was already mentioned, the film deposited at 300 °C is more defective where the point defects, namely oxygen vacancies, enhance the electrical conductivity. However, this film has a smaller domain size and, thus, more boundaries which act as scattering centers against the charge carriers. On the other hand, the film deposited at 700 °C has a larger domain size and fewer boundaries leading to a lower scattering effect. However, this film has a lower defect concentration and a more perfect structure, so a lower conductivity. In the case of the film deposited at 500 °C, influences of domain size and the defect concentration are balanced, so the highest conductivity is observed.

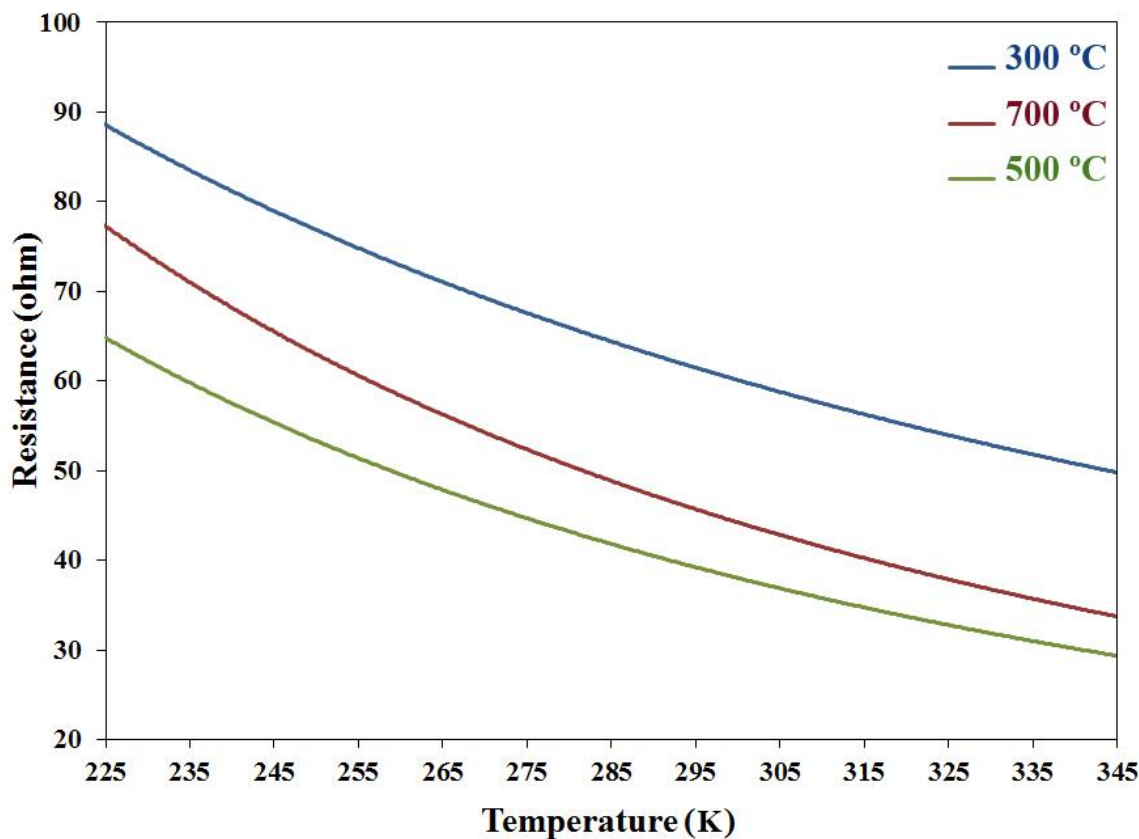


Fig.8.13. Electrical resistance of the TiO<sub>2</sub>/c-YSZ/Si heterostructures fabricated at different temperatures under the oxygen partial pressure of  $5 \times 10^{-4}$  Torr.

### 8.3.5. Photocatalytic properties

Fig.8.14 shows the results of photocatalytic experiments on a-TiO<sub>2</sub>/c-YSZ/Si films grown at 5×10<sup>-2</sup> Torr and r-TiO<sub>2</sub>/c-YSZ/Si films grown at 5×10<sup>-4</sup> Torr at various temperatures. As is seen in the inset, the concentration of 4CP decreases with illumination time showing that 4CP is being decomposed. Photocatalytic decomposition of 4CP solution agrees with pseudo-first-order kinetics, so the reaction constant (k) can be calculated by the equation  $\ln(C_0/C)=kt$  (where C<sub>0</sub> is the initial concentration of 4CP at t=0 and C represents the concentration of 4CP at later times t). The quantity  $\ln(C_0/C)$  versus irradiation time was plotted for all samples. Straight lines, whose slopes represent k, indicate that the degradation of 4CP is a first-order reaction. It should be noted that the curve "No catalyst" corresponds to the experiment where no sample was used as catalyst and only the 4CP solution was irradiated by the UV light. Since no appreciable concentration change is seen in this experiment, it can be deduced that in other experiments, which were performed using a catalyst, 4CP was degraded by photo-activated TiO<sub>2</sub> films. The photocatalytic results (Tab.8.1) are in agreement with the electrical properties discussed back in section 8.3.4. That is, the heterostructures grown at 500 °C have the highest photocatalytic efficiency. We think that the scattering effect of the domain boundaries in the film grown at 300 °C as well as the lower defect concentration in the films deposited at 700 °C is responsible for lower photocatalytic performance of these two heterostructures. Electrons and holes are both prerequisites for photocatalytic reactions which are generated through excitation of electrons from

the valence band to the conduction band of the semiconductor.<sup>14</sup> Moreover, separation of e<sup>-</sup>-h<sup>+</sup> pairs is the key step of any photocatalytic reaction.

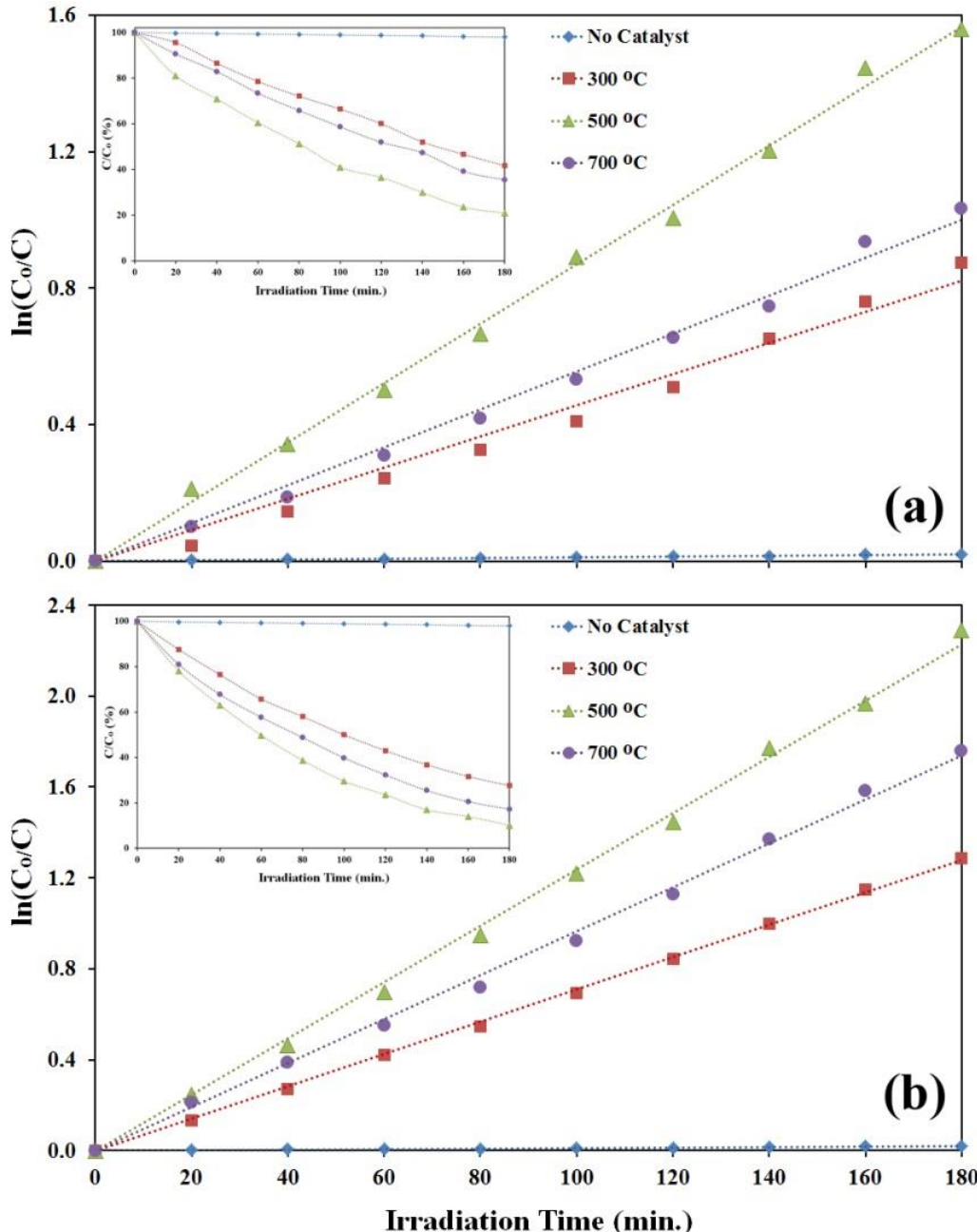


Fig.8.14. Photocatalytic decomposition of 4CP under ultraviolet illumination by:

(a) r-TiO<sub>2</sub>/c-YSZ/Si and (b) a-TiO<sub>2</sub>/c-YSZ/Si heterostructures.

Tab.8.1. Photocatalytic reaction rate constants (min.<sup>-1</sup>) of decomposition of 4CP.

	Growth temperature (°C)	300	500	700
Heterostructure				
a-TiO <sub>2</sub> /c-YSZ/Si		0.0071	0.0124	0.0096
r-TiO <sub>2</sub> /c-YSZ/Si		0.0046	0.0087	0.0056

The defects, such as oxygen vacancies, are considered to act as functional electron traps to reduce the recombination of electrons and holes, resulting in a promoted photoactivity of TiO<sub>2</sub> films.<sup>38,39</sup> However, such defects may also act as charge recombination centers if their concentration exceeds a critical value. The amount of domain boundaries and the defect content are balanced in the heterostructures fabricated at 500 °C enabling them to decompose 4CP at the reaction rate constants of 0.0087 (rutile) and 0.0124 (anatase) min.<sup>-1</sup>. The concentration of defects is raised at lower deposition temperatures leading to formation of deep level defects acting as recombination centers. Electron-hole recombination is an important competing process, since it decreases the carrier mobility and prevents them from reaching to the surface. The recombination of charge carriers at the deep level defects as well as the boundaries is responsible for diminishing the photocatalytic efficiency. The heterostructures grown at 700 °C are more photoactive than those grown at 300 °C; the reason might be its rougher surface and higher surface area, as shown in Fig.8.12.

## 8.4. Conclusions

Effects of substrate temperature and oxygen partial pressure on the formation of r-TiO<sub>2</sub> and a-TiO<sub>2</sub> on Si(001) substrate were investigated where c-YSZ was used as a

buffer layer. It was found that using higher substrate temperatures and low oxygen partial pressures resulted in formation of rutile epitaxial films. On the other hand, anatase epitaxial films were obtained by decreasing the temperature and increasing the oxygen pressure. It was indicated that the oxygen pressure just before the deposition of the TiO<sub>2</sub> film on the c-YSZ buffer layer, rather than that during the deposition, is the key factor determining the crystallographic structure of titania. The epitaxial relationship between silicon substrate and the YSZ buffer layer was established as [100](001)<sub>YSZ</sub>||[100](001)<sub>Si</sub>. The epitaxial relationships at the r-TiO<sub>2</sub>(100)/c-YSZ(001) and a-TiO<sub>2</sub>(001)/c-YSZ(001) interfaces were proposed as [011](100)<sub>rutile</sub>||[010](001)<sub>YSZ</sub> and [110](001)<sub>anatase</sub>||[100](001)<sub>YSZ</sub>, respectively. Less defect content and more favorable crystallinity were confirmed by XPS and XRD studies in the films grown at higher temperatures. The films deposited at 500 °C had the smoothest surface and the highest electrical conductivity. These heterostructures also exhibited the highest photocatalytic efficiency as compared to those deposited at 300 and 700 °C.

## References

1. M.R. Bayati, F. Golestani-Fard, and A.Z. Moshfegh, J. Appl. Catal. A 382, 322 (2010).
2. D. Yoo, I. Kim, S. Kim, C. Hahn, C. Lee, and S. Cho, Appl. Surf. Sci. 253, 3888 (2007).
3. Y.Q. Hou, D.M. Zhuang, G. Zhang, M. Zhao, and M.S. Wu, Appl. Surf. Sci. 218, 97 (2003).
4. N. Sbai, J. Perriere, W. Seiler, and E. Millon, Surf. Sci. 601, 5649 (2007).
5. T. Bak, J. Nowotny, N.J. Sucher, and E. Wachsman, J. Phys. Chem. C 115, 15711 (2011).

6. W. Guo, C. Xu, X. Wang, S. Wang, C. Pan, C. Lin, and Z.L. Wang, *J. Am. Chem. Soc.* 134, 4437 (2012).
7. Y. Li, F. Piret, T. Leonard, and B.L. Su, *J. Colloid Interface Sci.* 348, 43 (2010).
8. X. Wei, R. Skomski, B. Balamurugan, Z.G. Sun, and S. Ducharme, *J. Appl. Phys.* 105, 07C517 (2009).
9. C. Lee, P. Ghosez, and X. Gonze, *Phys. Rev B* 50, 378 (1994).
10. P. Murugan, R.V. Belosludov, H. Mizuseki, T. Nishimatsu, T. Fukumura, M. Kawasaki, and Y. Kawazoe, *Meas. Sci. Technol.* 16, 242 (2005).
11. M.R. Bayati, Sh. Joshi, R. Molaei, R.J. Narayan, and J. Narayan, *J. Solid State Chem.* 187, 231 (2012).
12. D.A. Panayotov, S.P. Burrows, and J.R. Morris, *J. Phys. Chem. C* 116, 6623 (2012).
13. P.R. Ohodnicki, C. Wang, S. Natesakhawat, J.P. Baltrus, and T.D. Brown, *J. Appl. Phys.* 111, 064320 (2012).
14. B. Long, Y. Li, and R. Jha, *IEEE Electron Device Lett.* 33, 706 (2012).
15. A. Fujishima and K. Honda, *Nature* 238, 37 (1972).
16. T.M. Breault and B.M. Bartlett, *J. Phys. Chem. C* 116, 5986 (2012).
17. M.R. Bayati, A.Z. Moshfegh, and F. Golestani-Fard, *Appl. Catal. A* 389, 60 (2010).
18. M.R. Bayati, F. Golestani-Fard, and A.Z. Moshfegh, *Mater. Res. Bul.* 46, 1642 (2011).
19. D. Ollis, *Appl. Catal. B* 99, 478 (2010).
20. G. Fu, P.S. Vary, and C.T. Lin, *J. Phys. Chem. B* 109, 8889 (2005).
21. K.E. DeKrafft, C. Wang, and W. Lin, *Adv. Mater.* 24, 2014 (2012).
22. S. Yuan, R. Mao, Y. Li, Q. Zhang, and H. Wang, *Electrochim. Acta* 60, 347 (2012)

23. M.C. Yang, Y.Y. Lee, B. Xu, K. Powers, and Y.S. Meng, *J. Power Sources* 207, 166 (2012).
24. M.S. Gabor, T. Petrisor, C. Tiusan, M. Hehn, B.S. Vasile, and T. Petrisor, *J. Appl. Phys.* 111, 083917 (2012).
25. B. Santara, B. Pal, and P.K. Giri, *J. Appl. Phys.* 110, 114322 (2011).
26. S. Mal, T.H. Yang, P. Gupta, J.T. Prater, and J. Narayan, *Acta Mater.* 59, 2526 (2011).
27. J. Gao, E.G. Fu, and X.S. Wu, *Surf. Rev. Lett.* 14, 773 (2007).
28. L. Tarnawska, P. Zaumseil, M.A. Schubert, S. Okur, U. Ozgur, H. Morkoc, R. Paszkiewicz, P. Storck, and T. Schroeder, *J. Appl. Phys.* 111, 073509 (2012).
29. A. Gupta, R. Aggarwal, P. Gupta, T. Dutta, R.J. Narayan, and J. Narayan, *Appl. Phys. Lett.* 95, 111915 (2009).
30. B.C. Riggs, A.D. Dias, N.R. Schiele, R. Cristescu, Y. Huang, D.T Corr, and D.B. Chrisey, *MRS Bull.* 36, 1043 (2011).
31. D.B. Chrisey and G.K. Hubler, *Pulsed laser deposition of thin films*, New York: J. Wiley (1994).
32. R. Aggarwal, H. Zhou, C. Jin, J. Narayan, and R.J. Narayan, *J. Appl. Phys.* 107, 113530 (2010).
33. T. Zhao, F. Chen, H. Lu, G. Yang, and Z. Chen, *J. Appl. Phys.* 87, 7442 (2000).
34. S.D. Mo and W.Y. Ching, *Phys. Rev. B* 51, 13023 (1995).
35. A.P. Shpak, A.M. Korduban, M.M. Medvedskij, and V.O. Kandyba, *J. Electron. Spectrosc. Relat. Phenom.* 156–158, 172 (2007).
36. J. Narayan and B.C. Larson, *J. Appl. Phys.* 93, 278 (2003).

37. S.J. Wang, C.K. Ong, L.P. You, and S.Y. Xu, *Semicond. Sci. Technol.* 15, 836 (2000).
38. J. Zhuang, W. Dai, Q. Tian, Z. Li, L. Xie, J. Wang, and P. Liu, *Langmuir* 26, 9686 (2010).
39. S.A. Campbell, D.C. Gilmer, X.C. Wang, M.T. Hsieh, H.S. Kim, W.L. Gladfelter, and J. Yan, *IEEE Trans. Electron Devices* 44, 104 (1997).

## **Chapter 9**

# **Nanosecond Switching in Wetting Properties of TiO<sub>2</sub>/c-YSZ/Si(001) Heterostructures Induced by Laser Irradiation**

We have demonstrated dark hydrophilicity of epitaxial rutile TiO<sub>2</sub> (100) thin films, in which rapid switching from a hydrophobic surface to a hydrophilic surface was achieved using excimer laser irradiation. The TiO<sub>2</sub>/YSZ/Si(001) single crystalline heterostructures were grown by pulsed laser deposition and were subsequently irradiated by a single pulse of a KrF excimer laser at several energies. The wettability of water on the surfaces of the samples was evaluated. The samples were hydrophobic prior to laser annealing and were hydrophilic after laser annealing. Superhydrophilic surfaces were obtained at higher laser energy densities (e.g., 0.32 J.cm<sup>-2</sup>). The stoichiometries of the surface regions of the samples before and after laser annealing were examined using XPS. The results revealed the formation of oxygen vacancies on the surface, which are surmised to be responsible for the observed superhydrophilic behavior. It is envisaged that the concurrent formation of oxygen vacancies and Ti<sup>3+</sup> defects from laser annealing and, therefore, introduction of mid-band states is

responsible for a dark hydrophilicity phenomenon, in which UV illumination is not necessary for excitement of TiO<sub>2</sub>. According to the AFM images, surface smoothening was greater in films that were annealed at higher laser energy densities. The samples exhibited hydrophobic behavior after being placed in ambient atmosphere. The origin of laser induced wetting behavior was qualitatively understood to stem from an increase of point defects near the surface, which lowered the film/water interfacial energy. This type of rapid hydrophobic/hydrophilic switching may be used to facilitate fabrication of electronic and photonic devices with novel properties.

## 9.1. Introduction

The physical and chemical properties of semiconductors such as titanium dioxide (TiO<sub>2</sub>) can be precisely manipulated if the surface phenomena are precisely controlled. Among semiconducting materials, TiO<sub>2</sub> has attracted extensive interest due to its potential use in electronic and photonic devices. TiO<sub>2</sub> has been considered for use in photocatalysts,<sup>1-4</sup> solar cells,<sup>5-7</sup> high-temperature gas sensors,<sup>8</sup> surface-enhanced Raman scattering (SERS) sensors,<sup>9</sup> photonic devices,<sup>10</sup> UV detectors,<sup>11</sup> photoanodes,<sup>12</sup> and other applications. In addition, hydrophilic TiO<sub>2</sub> films have been considered for use as antifogging and self-cleaning surfaces.<sup>13-16</sup>

The commonly accepted mechanism of hydrophilicity in TiO<sub>2</sub> and other semiconductors is based on the generation of e<sup>-</sup>-h<sup>+</sup> pairs at the conduction and valence bands, which are excited by photons with energies higher than the band gap energy. This phenomenon initiates various redox reactions at the semiconductor surface. The

photogenerated electrons and holes are trapped by surface  $\text{Ti}^{4+}$  and  $\text{O}^{2-}$  ions to produce  $\text{Ti}^{3+}$  ions and oxygen vacancies, respectively. As such, creation of photo-induced hydrophilic surfaces involves formation of partially reduced  $\text{TiO}_2$ . This model stipulates that dissociative adsorption of water molecules occurs at the defect sites.<sup>17,18</sup> Even though reduction of  $\text{Ti}^{4+}$  cations to the  $\text{Ti}^{3+}$  state and formation of oxygen vacancies by photon illumination is a well-known mechanism for generation of a hydrophilic surface,<sup>19</sup> we believe that there are other mechanisms (e.g., annealing in vacuum, annealing in a reducing atmosphere, and laser treatment) for introducing point defects on the  $\text{TiO}_2$  surface. In our previous study, we showed that rutile(100) epilayers grown on *c*-sapphire substrates can exhibit photoactive behavior when illuminated by ultraviolet light or visible light after vacuum annealing.<sup>20</sup> The observed photocatalytic behavior was attributed to formation of oxygen vacancies and titanium interstitial defects. In other studies by our group, we demonstrated that the electrical, magnetic, and optical properties of metal oxides can be systematically altered by laser irradiation; in these studies, changes to metal oxide properties were discussed in terms of defects and defect complexes that were created through interaction of energetic photons with the target material.<sup>21-23</sup> It was revealed that oxygen vacancies that are generated by laser treatments play a critical role in altering the properties of the material. Lasers have been employed in variety of applications in the field of semiconductor technology, such as thin film deposition,<sup>24-27</sup> annealing,<sup>21-23,28</sup> and laser machining.<sup>29</sup> Pulsed laser photons are strongly absorbed in the near surface regions of semiconductors when the photon energy exceeds the band gap energy. The absorbed energy is transferred to the

electronic system of the material within less than  $10^{-12}$  of a second; in turn, this energy is transferred to the lattice in less than a nanosecond. Our previous work indicates that novel properties of semiconductor materials can be achieved by laser annealing of materials in a controlled manner.<sup>30-34</sup>

In the previous chapter, thin film epitaxy and phase tuning of titania from rutile to anatase in  $\text{TiO}_2/\text{YSZ}/\text{Si}$  heterostructures were discussed in detail.<sup>35</sup> The motivation behind the present research is developing  $\text{TiO}_2$  surfaces that exhibit switchable wetting behavior. We show that the surface properties, in particular hydrophilicity, of rutile  $\text{TiO}_2$  epitaxial thin films can be manipulated through laser irradiation only; one pulse from the nanosecond KrF excimer laser facilitates switching between hydrophobicity and hydrophilicity. Such a rapid response opens new avenues for use of  $\text{TiO}_2$  in intelligent membranes, sensors, and smart catalysts.

## 9.2. Experimental

We grew cubic yttria-stabilized zirconia (YSZ) buffer layer and rutile  $\text{TiO}_2$  (100) epilayers on Si(001) substrates using pulsed laser deposition. The substrates were initially degreased in hot acetone for 10 minutes; the samples were subsequently ultrasonically cleaned in acetone and methanol each for 5 minutes at room temperature. The cleaned substrates were dried using purified nitrogen and immediately loaded into the deposition chamber. The chamber was evacuated to a background pressure of  $\sim 1 \times 10^{-6}$  Torr using a turbomolecular pump that was backed by a rotary pump. A Lambda Physik (LPX200) KrF excimer laser with a wavelength of 248

nm and pulse duration of 25 ns was employed for ablation of the high purity rutile TiO<sub>2</sub> and YSZ targets and for laser annealing of the samples. The target-substrate distance was maintained at 4.5 cm and the targets were rotated during the depositions. For growth of YSZ and TiO<sub>2</sub> films, the energy density and the repetition rate were maintained at 3.0-3.5 J.cm<sup>-2</sup> and 5 Hz, respectively. The YSZ and rutile films were deposited at 750 °C and 700 °C, respectively. To effectively destroy the native oxide layer of the silicon, the YSZ films were deposited for 1000 pulses under vacuum followed by 1000 pulses under an oxygen partial pressure of 5×10<sup>-4</sup> Torr. By employing a multitarget carousel, the rutile TiO<sub>2</sub> thin films were deposited for 6000 pulses onto the YSZ template layers under an oxygen partial pressures of 5×10<sup>-4</sup> Torr without breaking vacuum. The samples were cooled within the deposition chamber under an oxygen pressure of 1 Torr. Laser annealing was conducted in ambient atmosphere using one pulse of the aforementioned KrF excimer laser; annealing was performed at several energy densities.

Details of characterization techniques were already explained in chapter 3. XRD, XPS, and wettability studies were performed on samples before and after laser annealing for comparison purposes. The phase structure of the samples was assessed by θ-2θ scan diffraction using a Rigaku X-ray diffractometer. Moreover, the in-plane orientation of the films was determined by φ-scan X-ray diffraction using a Panalytical X’Pert PRO MRD HR X-Ray diffractometer. Both diffractometers contained a CuKα X-ray source with  $\lambda= 0.154$  nm. An X-ray photoelectron spectrometer (SPECS) with a MgKα source ( $\lambda=1254$  eV) and a PHOIBIS 150 hemispherical analyzer was employed to

examine the surface stoichiometry of the films. The results were interpreted using Version 4.1 SDP software; the binding energy of the C(1s) peak was set to 285.0 eV as a reference. The morphologies of the samples were examined using a Veeco atomic force microscope and the results were interpreted using Version 5.12r3 Nanoscope software. The wettability properties of the heterostructures were examined in ambient atmosphere by evaluating the behavior of deionized water droplets on the surfaces of the samples using optical photographs. We used a JEOL 2010F transmission electron microscope with a point-to-point resolution of 1.8 Å to study the atomic and crystallographic arrangements at the interfaces and to confirm the epitaxial growth. The microscope was operated at 200 kV.

Wettability characteristics of the as-deposited and laser annealed samples were evaluated at room temperature in air, as explained in chapter 3.

### **9.3. Results and discussion**

#### **9.3.1. Microstructure and thin film epitaxy**

Results of  $\theta$ - $2\theta$  and  $\varphi$  scans X-ray diffraction of the rutile/YSZ/Si(001) heterostructure are displayed in Fig.9.1. In this figure, epitaxial growth of rutile  $\text{TiO}_2$  along its  $a$ -axis on the YSZ(001)/Si(001) platform is evident. The 2-fold symmetry along the  $a$ -axis of rutile and existence of four energetically equal domains on the YSZ(001) plane resulted in appearance of four strong  $\varphi$ -peaks from the rutile(110) reflection with angular intervals of  $64.5^\circ$  and angular separations of  $32.25^\circ$  from the YSZ(202) reflection.<sup>35</sup> Note that the  $\varphi$ -patterns have been presented from  $0^\circ$  to  $180^\circ$ .

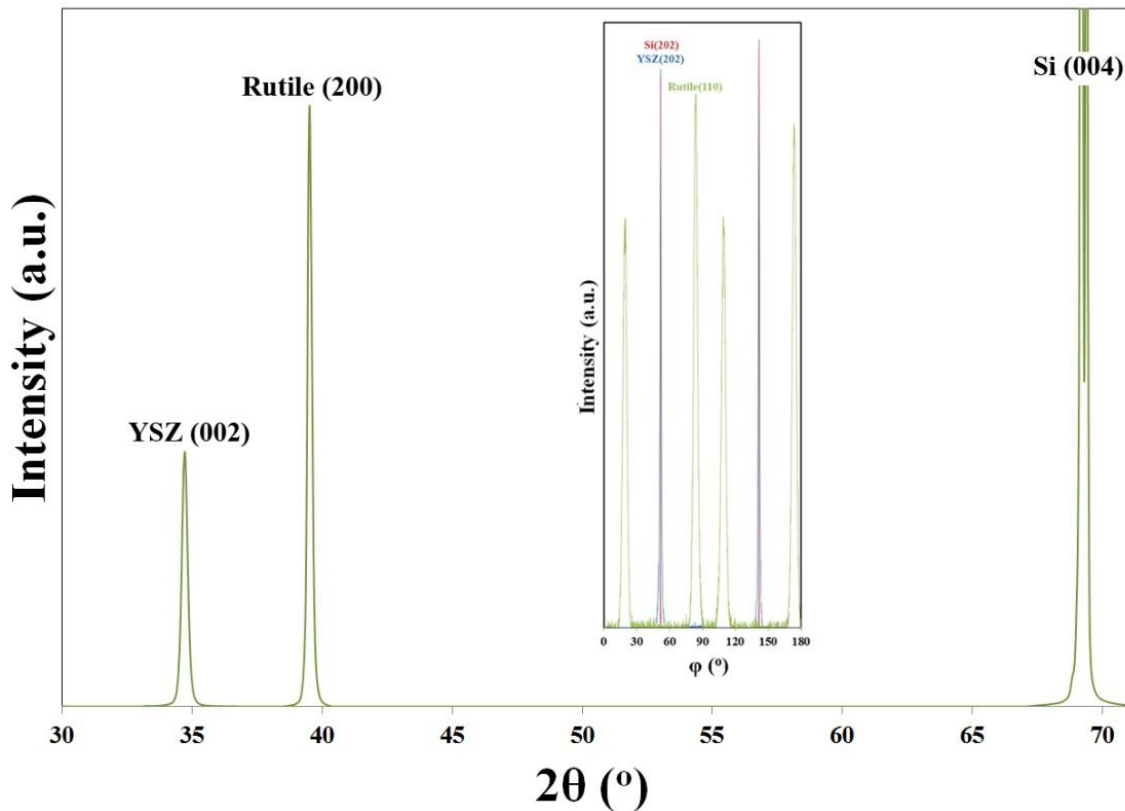


Fig.9.1.  $\theta$ - $2\theta$  and  $\varphi$  patterns obtained from the  $\text{TiO}_2/\text{YSZ}/\text{Si}(001)$  heterostructure.

As schematically illustrated in Fig.9.2, the existence of the so called four equal domains is understood by considering that the  $32.25^\circ$  rotation can take place with respect to each side of the YSZ unit cell along its  $<001>$  axis. As such, four equal crystallographic orientations exist onto the YSZ(001) plane and the rutile unit cells aligns with any of them, leading to formation of four variants that are separated by low energy twin boundaries. Meanwhile, the presence of  $\varphi$ -peaks from Si(202) and YSZ(202) reflections at the same azimuthal angles confirms the epitaxial cube-on-cube growth of the cubic YSZ film on the silicon substrate. Thus, the epitaxial relationship between the YSZ buffer layer and the silicon substrate was determined as

$\{100\}_{\text{YSZ}} \parallel \{100\}_{\text{Si}}$  and  $\langle 100 \rangle_{\text{YSZ}} \parallel \langle 100 \rangle_{\text{Si}}$ . The epitaxial relationship at the rutile/YSZ interface was shown to be  $(100)_{\text{rutile}} \parallel (001)_{\text{YSZ}}$ ,  $[0\bar{1}1]_{\text{rutile}} \parallel [010]_{\text{YSZ}}$ , and  $[025]_{\text{rutile}} \parallel [100]_{\text{YSZ}}$ .

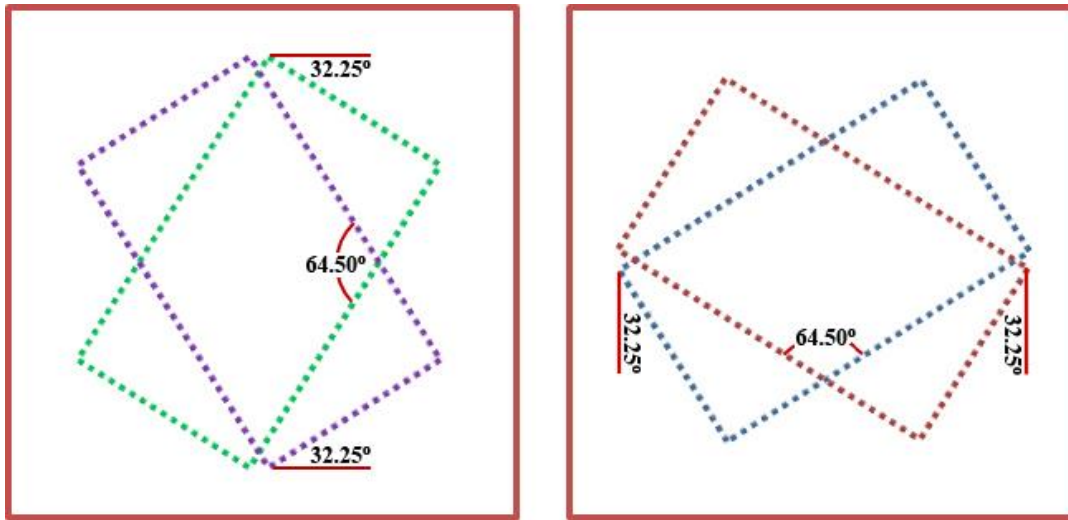


Fig.9.2. Schematic illustration of four equally probable orientations of the rutile film on the YSZ buffer.

Fig.9.3a shows the bright field cross section micrograph of the  $\text{TiO}_2/\text{YSZ/Si}$  heterostructure.<sup>35</sup> The formation of columnar grains in the  $\text{TiO}_2$  film indicates the presence of in-plane rotation, which was discussed earlier. Such a structure is not observed in the YSZ layer due to cube-on-cube growth. The epitaxial growth and the proposed epitaxial relationships are confirmed by the indexed selected area electron diffraction pattern that was acquired from the films and the substrate; this pattern is shown in the inset of Fig.3a. The HRTEM image of the interfaces (Fig.9.3b and Fig.9.3c) shows that the  $\text{TiO}_2/\text{YSZ}$  interface is atomically sharp; no reaction layer at the interfaces was noted.

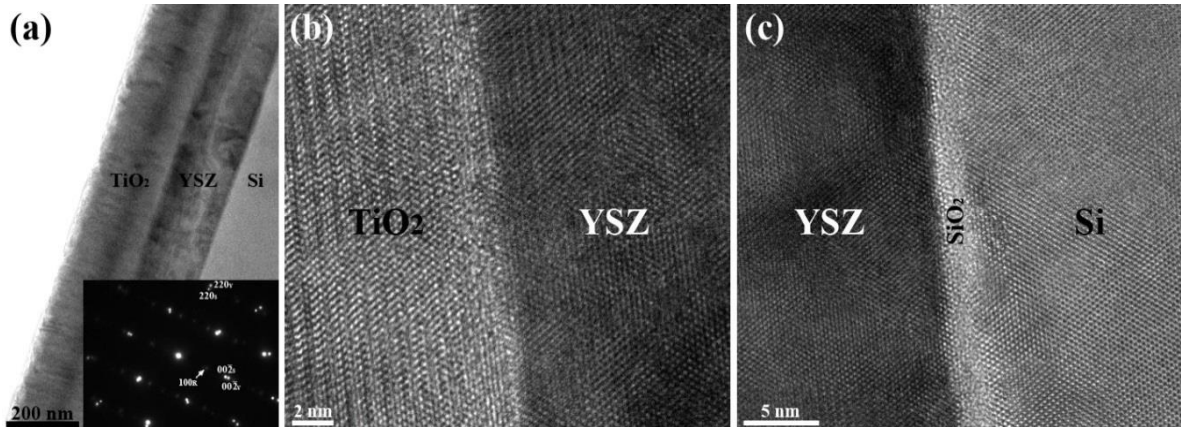


Fig.9.3. (a) Bright field cross section micrograph and the selected area electron diffraction of the  $\text{TiO}_2/\text{YSZ}/\text{Si}(001)$  heterostructure, showing rutile[031], YSZ[1 $\bar{1}$ 0], and Si[1 $\bar{1}$ 0] zones, (b) High resolution image of the rutile/YSZ interface, and (c) High resolution image of YSZ/Si(001) interface.

The  $d$ -spacing values among  $(05\bar{2})_{\text{rutile}}$ ,  $(011)_{\text{rutile}}$ , and  $(400)_{\text{YSZ}}$  planes were calculated to be approximately 0.78 Å, 2.49 Å, and 1.28 Å, respectively. In accordance with the domain matching epitaxy (DME) paradigm,<sup>36</sup> 32 planes of  $\text{TiO}_2$  match with 31 planes of YSZ with a frequency factor of  $\alpha=\sim 0.1$  in order to fully relax the misfit strain along the rutile [0 $\bar{1}$ 1] orientation. The 33/32 and 32/31 matchings are shown in Fig.9.4. The misfit strain along the rutile [025] direction is relaxed through alternation of 2/1 and 3/2 domains; the frequency factor associated with this process is approximately 0.56.

Fig.9.5 shows the  $\theta$ -2 $\theta$  patterns of the rutile/YSZ/Si samples that were laser annealed using several energies. The results confirm that no new phase was formed by laser treatment. In addition, no new out-of-plane orientation was noted. Consequently, it can be deduced that the tetragonal structure of the rutile  $\text{TiO}_2$  films with a [100]-orientation normal to the substrate surface was preserved after the laser treatment. It

was found that the full width at half maximum of the rutile(200) peaks increased with higher laser energy density values. In addition, a small peak shift toward lower  $2\theta$  values was observed at higher energies. These characteristics are attributed to the formation of lattice defects due to the interaction of a high energy laser beam with the material.<sup>22-24</sup> Such defects introduce residual strain to the crystallographic lattice and may alter the inter-planar spacing.

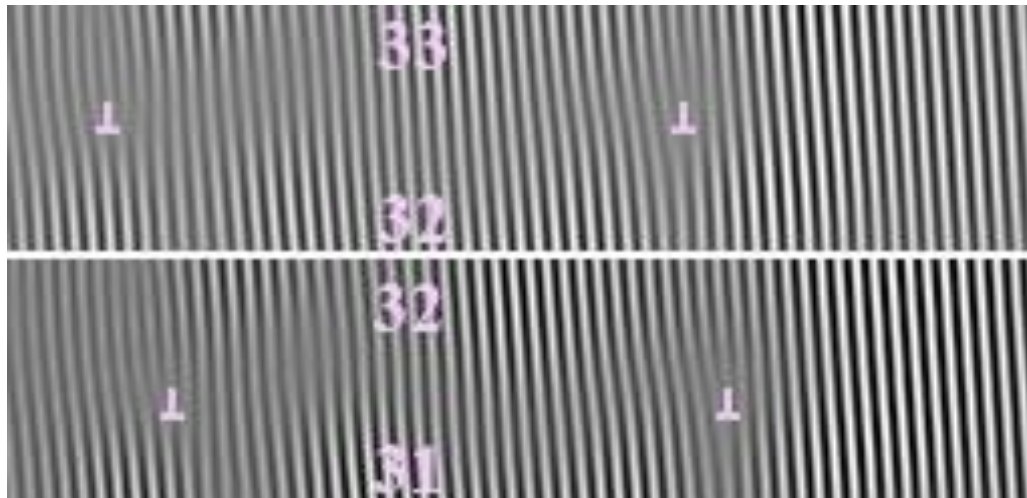


Fig.9.4. Matching of crystallographic planes to relax the misfit strain across the rutile/YSZ interface.

### 9.3.2. Morphology

The effect of laser energy on the surface morphology of annealed  $\text{TiO}_2$  thin films was investigated using atomic force microscopy (Fig.9.6). It is observed that greater surface smoothening occurred when the laser energy was increased; this phenomenon was particularly evident in samples irradiated with energy densities of 0.28 and 0.32  $\text{J.cm}^{-2}$ . Surface smoothing occurs as a result of the evaporation of a very thin surface

layer at higher energy densities.<sup>37</sup> We believe that the low energy laser annealing ( $0.16 \text{ J.cm}^{-2}$ ) only caused heating of a very thin layer, thereby preserving the grain features and surface roughness of the sample.

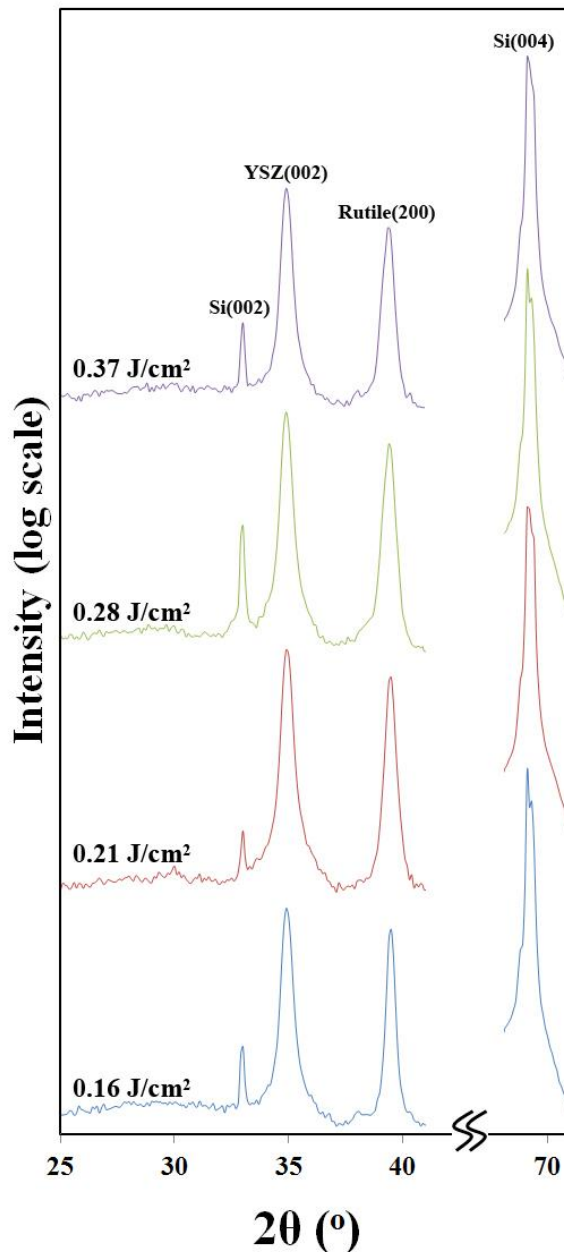


Fig.9.5.  $\theta$ - $2\theta$  XRD patterns of laser annealed samples that were prepared using several laser energies.

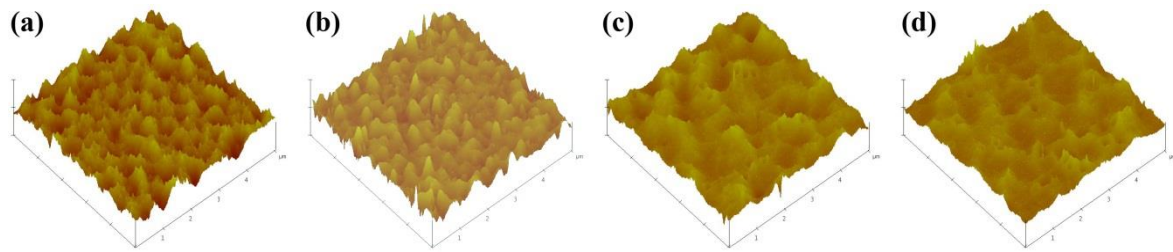


Fig.9.6. Surface morphology of the laser annealed samples. Data for samples annealed at energies of: (a) 0.16, (b) 0.21, (c) 0.28, and (d)  $0.32 \text{ J.cm}^{-2}$  are shown.

The bright field cross-section image obtained from the sample that was annealed with an energy density of  $0.32 \text{ J.cm}^{-2}$  is displayed in Fig.9.7; the laser affected region is clearly seen near the surface of the sample.

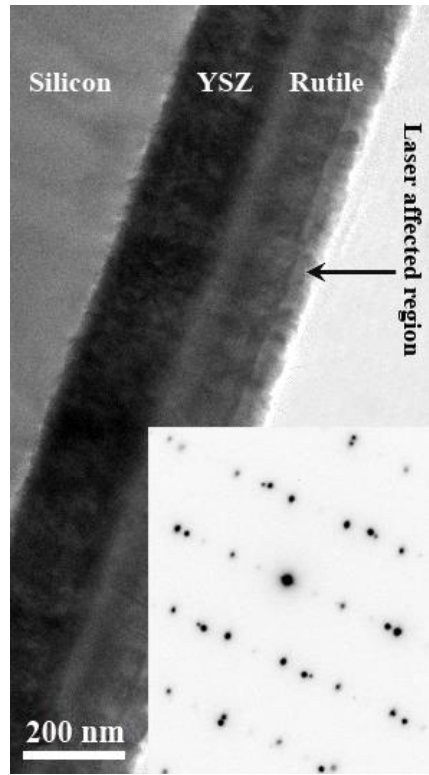


Fig.9.7. Low magnification bright field TEM image obtained from a sample that was laser annealed with an energy density of  $0.32 \text{ J.cm}^{-2}$ .

In nanosecond laser processing, the short thermal diffusion distances and the large dimensions of the laser beam compared to the melt depth limit the thermal gradients parallel to the interface to many orders of magnitude less than the gradients present perpendicular to the interface, thus essentially making it a one-dimensional heat flow problem.<sup>38</sup> The SAED pattern shown in the inset reveals that the epitaxy and initial structure of the rutile thin film has not changed after laser annealing. This images shows that properties of materials can be altered in a precisely controlled way by laser treatment in the near surface regions, while original properties in the bulk are preserved.

### 9.3.3. Stoichiometry

Fig.9.8 depicts the high resolution XPS O(1s) core level binding energy of the as-deposited (un-irradiated) sample. Peaks A and B, which are located at binding energies of approximately 532.8 and 531.7 eV, are assigned to H<sub>2</sub>O and OH compounds that are attached to the surface defects. The surfaces of metal oxides become hydrated in ambient atmosphere; as such, water molecules and hydroxyl groups are almost always present on free surfaces of oxide materials.<sup>39</sup> Hydroxyl groups couple with surface oxygen vacancies; water molecules subsequently interact with these groups by means of hydrogen bonds. Peak C is located at the binding energy of about 530.2 eV; this peak is attributed to oxygen in the Ti-O-Ti bonding. In other words, this peak represents the perfect TiO<sub>2</sub> structure. Peak D with a binding energy of approximately 528.7 eV is indirectly assigned to titanium interstitials. Located in the interstitial sites, these Ti

atoms donate three or four electrons to the host crystal and transform into  $\text{Ti}^{3+}$  or  $\text{Ti}^{4+}$  cations. The released electrons are captured by  $\text{Ti}^{4+}$  lattice cations. Therefore, lattice  $\text{Ti}^{2+}$  and  $\text{Ti}^{3+}$  cations, represented by peak D, form.

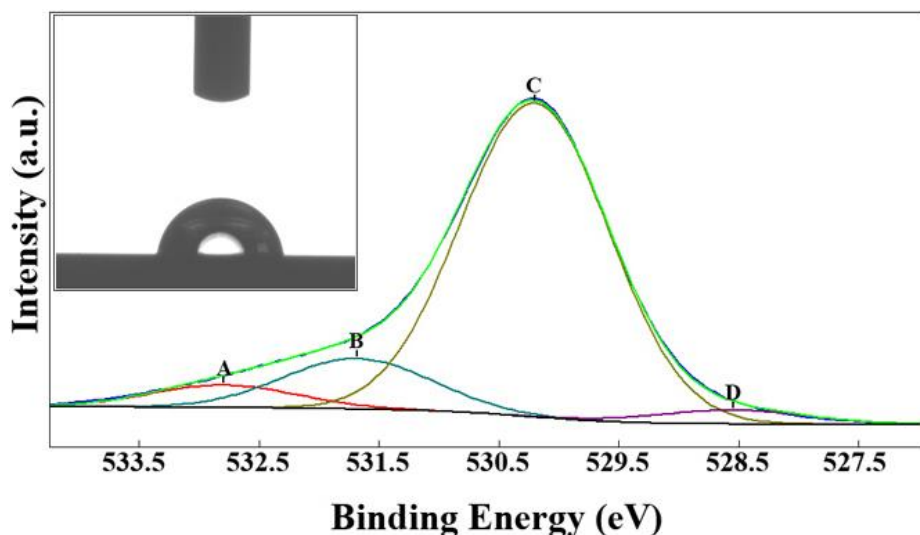


Fig.9.8. XPS high resolution O(1s) core level binding energy for the as-deposited sample.

The result of the wettability study is also shown in the inset.

$\text{TiO}_2$  is an *n*-type semiconductor and its electrical behavior is dictated by the inherent point defects (e.g., oxygen vacancies and titanium interstitials).<sup>40-42</sup> These point defects are always present in  $\text{TiO}_2$  and control its physical and chemical properties. As is shown in the inset of Fig.9.8, the as-deposited sample exhibits a hydrophobic surface. The O(1s) spectra of the laser annealed samples are depicted in Fig.9.9. No new O-bonding was noted; as such, no new compound was formed on the surfaces of the films as well as in the near-surface regions of the films after laser treatment. We already showed that no new phase was formed after laser irradiation in

the bulk as well (Fig.9.5). It is important to note that the portion of peak B, which represented the concentration of oxygen vacancies, increased with higher laser energy density values. The portion of this peak was determined to be 13.4, 14.9, 18.3, and 19.5 % for energy densities of 0.16, 0.21, 0.28, and 0.32 J.cm<sup>-2</sup>, respectively. The concentration of interstitial defects, which was deduced from consideration of peak D, increased with higher laser energy density values. The portion of peak C, which represented the perfect TiO<sub>2</sub> lattice, decreased at higher laser energy density values. This information demonstrates that the defect content in the near surface regions increased with higher laser energy density values.

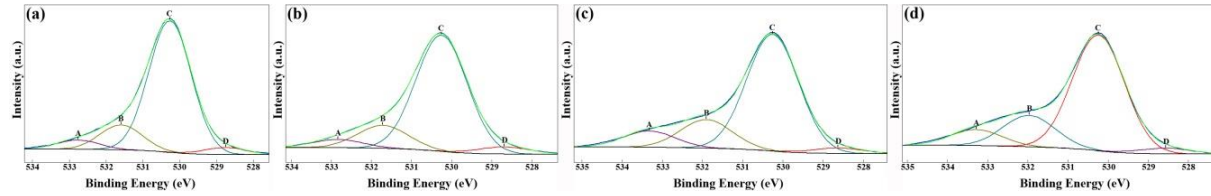


Fig.9.9. XPS high resolution O(1s) core level binding energy for the laser annealed samples. Data are shown for samples annealed at energies of: (a) 0.16, (b) 0.21, (c) 0.28, and (d) 0.32 J.cm<sup>-2</sup>.

### 9.3.4. Wettability characteristics

Results of the wettability test are displayed in Fig.9.10; hydrophilic behavior was observed in the laser annealed samples, particularly in the sample irradiated at an energy density of 0.32 J.cm<sup>-2</sup>. It was found that the hydrophilicity of the samples increased with higher laser energy density values. Based on our previous studies,<sup>21-23</sup> laser irradiation leads to the formation of oxygen vacancies. We have also shown that

concentration of these defects increases when the laser energy or the number of pulses is increased. As discussed in the introduction section, dissociative adsorption of water molecules at oxygen vacancies is the mechanism behind the observed hydrophilicity. Because the concentration of oxygen vacancies increases with the laser energy, a more hydrophilic surface was obtained at higher laser energies.

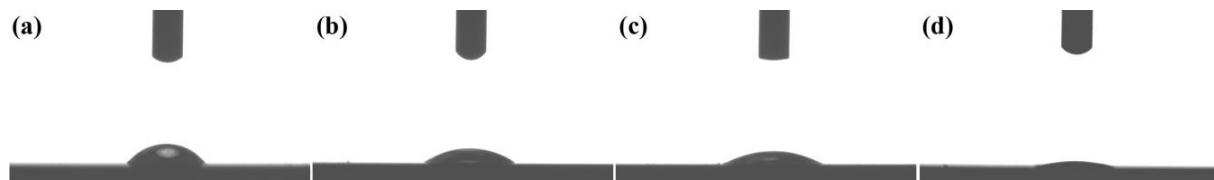


Fig.9.10. Results of the wettability studies for the laser annealed samples. Data are shown for samples annealed at energies of: (a) 0.16, (b) 0.21, (c) 0.28, and (d) 0.32 J.cm<sup>-2</sup>.

When an oxygen vacancy forms, two Ti<sup>4+</sup> cations have to be converted to Ti<sup>3+</sup> to preserve the charge neutrality. In other words, Ti<sup>4+</sup> ions trap two electrons that are generated when an oxygen anion leaves the lattice. Formation of Ti<sup>3+</sup>cations gives rise to a decrease in the band gap energy<sup>41</sup> through introduction of mid-band states. Thus, the samples can get excited and generate e<sup>-</sup>-h<sup>+</sup> pairs without UV irradiation. The process of defective site formation on the TiO<sub>2</sub> surface is explained by the following mechanism:<sup>43,44</sup>





In our experiment, oxygen vacancies, prerequisite for hydrophilicity, form via 2 different mechanisms. First, energy of the laser photons is absorbed by  $\text{TiO}_2$  via photoexcitation of the valence electrons to the conduction band giving rise to the formation of oxygen vacancies, according to the reaction 9-2. Second, temperature of the surface is increased due to the coupling of the high energy laser beam<sup>38</sup> with the surface of the samples leading to reduction of  $\text{TiO}_2$  and, hence, formation of oxygen vacancies. Then a water molecule dissociatively adsorbs on the defect sites. As a result, a new hydroxyl group is produced, which is responsible for the highly hydrophilic surface.<sup>17</sup>

The wettability of water on the surface of the laser annealed samples was measured after 1, 5, 10, and 24 hours. It was found that the samples became hydrophobic after exposure to ambient atmosphere. To shed light on the basis of this behavior, XPS measurements were obtained from the hydrophobic samples after exposure to ambient atmosphere; the results for these samples are shown in Fig.9.11.

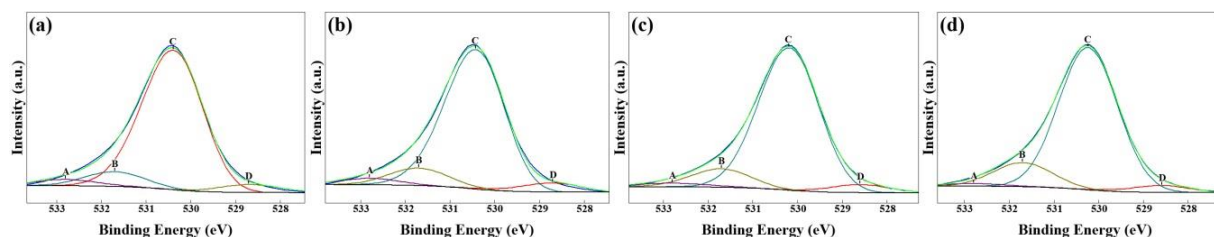


Fig.9.11. XPS O(1s) core level binding energies for the laser annealed samples after 24 hours. Data are shown for samples annealed at energies of: (a) 0.16, (b) 0.21, (c) 0.28, and (d) 0.32  $\text{J}\cdot\text{cm}^{-2}$ .

As can be observed in the figure, a portion of the B peak significantly decreased after exposure to ambient atmosphere. The peak portions were determined to be 6.7, 8.4, 10.1, and 12.6 % for samples processed with energies of 0.16, 0.21, 0.28, and 0.32 J.cm<sup>-2</sup>, respectively. This result shows that surface oxygen vacancies are removed through absorption of oxygen from the atmosphere.<sup>44</sup>

Since the defect characteristics but not the surface roughness are altered by exposure of the samples to ambient atmosphere, we concluded that point defects play a more important role than surface roughness in altering the photochemical properties of the samples.

Three critical parameters that control hydrophilic and hydrophobic characteristics include  $\sigma_f$  (surface energy of the TiO<sub>2</sub> film),  $\sigma_w$  (water surface energy), and  $\sigma_{fw}$  (TiO<sub>2</sub>/water interfacial free energy). In a hydrophobic surface,  $\sigma_f$  (low) <  $\sigma_w + \sigma_{fw}$  (high). In a hydrophilic surface,  $\sigma_f$  (high) >  $\sigma_w + \sigma_{fw}$  (low). Pulsed laser irradiation makes the surface more reactive by lowering the  $\sigma_{fw}$ ; this process drives the surface to hydrophilicity. The surface smoothness facilitates further lowering of the  $\sigma_{fw}$ . Oxygen absorption and removal of the surface defects increase  $\sigma_{fw}$  and cause the surface to become hydrophobic.

#### 9.4. Conclusions

We integrated single crystalline rutile TiO<sub>2</sub> thin films with silicon (001) substrates and successfully induced dark superhydrophilicity in these films by laser annealing. It was surmised that Ti<sup>3+</sup> and oxygen vacancy defects play critical roles in formation of

dark superhydrophilicity. The  $Ti^{3+}$  point defects introduce mid-band states within the band gap of  $TiO_2$ , leading to a decrease in the effective band gap. Oxygen vacancies were responsible for introducing hydrophilic behavior. The laser-induced enhancement of hydrophilicity can be reversed by exposing the samples to ambient atmosphere; exposing the samples to ambient atmosphere may remove surface oxygen vacancies through absorption of oxygen. Point defects, namely oxygen vacancies or titanium interstitials, are always present in  $TiO_2$ ; these defects play an important role in modification of surface photochemical properties. Indeed, controlling these defects is essential for developing electronic and photonic devices with novel characteristics.

## References

1. M.R. Bayati, A.Z. Moshfegh, and F. Golestani-Fard, *J. Appl. Catal. A* 389, 60 (2010).
2. M.R. Bayati, F. Golestani-Fard, and A.Z. Moshfegh, *Electrochim. Acta* 55, 3093 (2010).
3. M.R. Bayati, A.Z. Moshfegh, and F. Golestani-Fard, *Mater. Lett.* 64, 2215 (2010).
4. M.R. Bayati, F. Golestani-Fard, A.Z. Moshfegh, and R. Molaei, *Mater. Chem. Phys.* 128, 427 (2010).
5. K. Prashant, *J. Phys. Chem. C* 116, 11849 (2012).
6. S. Saehana, P. Arifin, Khairurrijal, and M. Abdullah, *J. Appl. Phys.* 111, 123109 (2012).
7. J. Lee, J. Yoon, M. Jin, and M. Lee, *J. Appl. Phys.* 112, 043110 (2012).
8. P.R. Ohodnicki, C. Wang, S. Natesakhawat, J.P. Baltrus, and T.D. Brown, *J. Appl. Phys.* 111, 064320 (2012).
9. B. Santara, B. Pal, and P.K. Giri, *J. Appl. Phys.* 110, 114322 (2011).

10. M.S. Gabor, T. Petrisor, C. Tiusan, M. Hehn, B.S. Vasile, and T. Petrisor, *J. Appl. Phys.* 111, 083917 (2012).
11. P. Chinnamuthu, J.C. Dhar, A. Mondal, A. Bhattacharyya, and N.K. Singh, *J. Phys. D: Appl. Phys.* 45, 135102 (2012).
12. N. Naseri, M. Amiri, and A.Z. Moshfegh, *J. Phys. D: Appl. Phys.* 43, 105405 (2010).
13. B. Xi, L.K. Verma, J. Li, C.S. Bhatia, A.J. Danner, H. Yang, and H.C. Zeng, *Appl. Mater. Interfaces* 4, 1093 (2012).
14. M.R. Bayati, R. Molaei, H.R. Zargar, A. Kajbafvala, and S. Zanganeh, *Mater. Lett.* 64, 2498 (2010).
15. M.R. Bayati, R. Molaei, A. Kajbafvala, S. Zanganeh, H.R. Zargar, and K. Janghorban, *Electrochim. Acta* 55, 5786 (2010).
16. M.R. Bayati and R. Molaei, *J. Phys. D: Appl. Phys.* 43, 505304 (2010).
17. N. Sakai, A. Fujishima, T. Watanabe, and K. Hashimoto, *J. Phys. Chem. B* 105, 3023 (2011).
18. R. Wang, N. Sakai, A. Fujishima, T. Watanabe, and K. Hashimoto, *J. Phys. Chem. B* 103, 2188 (1999).
19. N. Sakai, R. Wang, A. Fujishima, T. Watanabe, and K. Hashimoto, *Langmuir* 14, 5918 (1998).
20. M.R. Bayati, J. Ding, Y.F. Lee, R.J. Narayan, and J. Narayan, *J. Phys. C: Condens. Mater.* 24, 395005 (2012).
21. P. Gupta, T. Dutta, S. Mal, and J. Narayan, *J. Appl. Phys.* 111, 013706 (2012).
22. S. Mal, S. Nori, J. Narayan, and J.T. Prater, *J. Mater. Res.* 26, 1298 (2011).

23. S. Mal, J. Narayan, S. Nori, J.T. Prater, and D. Kumar, Solid State Commun. 150, 1660 (2010).
24. M.R. Bayati, R. Molaei, R.J. Narayan, J. Narayan, H. Zhou, and S.J. Pennycook, Appl. Phys. Lett. 100, 251606 (2012).
25. M.R. Bayati, S. Joshi, R. Molaei, R.J. Narayan, and J. Narayan, J. Solid State Chem. 187, 231 (2012).
26. A. Gupta, R. Singhal, J. Narayan, and D.K. Avasthi, J. Mater. Res. 26, 2901 (2011).
27. T.H. Yang, S. Mal, C. Jin, R.J. Narayan, and J. Narayan, Appl. Phys. Lett. 98, 022105 (2011).
28. C.H. Chen and Y.C. Lee, Thin Solid Films 518, 4786 (2010).
29. A. Slocombe, and L. Li, Appl. Surf. Sci. 154–155, 617 (2000).
30. C.L. Anderson, G.K. Celler, and G.A. Rozgonyi, Laser and Electron Beam Processing of Electronic Materials; The Electrochemical Society Inc.: Princeton (1980).
31. Z. Guosheng, P.M. Fauchet, and A.E. Siegman, Phys. Rev. B 26, 5366 (1982).
32. J.D. Majumdar and I. Manna, Sadhana 28, 495 (2003).
33. J. Narayan, R.B. James, O.W. Holland, and M.A. Aziz, J. Vac. Sci. Technol. A 3, 1836 (1985).
34. J. Narayan, N. Biunno, R. Singh, O.W. Holland, and O. Auciello, Appl. Phys. Lett. 51, 1845 (1987).
35. M.R. Bayati, P. Gupta, R. Molaei, R.J. Narayan, and J. Narayan, Cryst. Growth Des. 12, 4535 (2012).
36. J. Narayan and B.C. Larson, J. Appl. Phys. 93, 278 (2003).

37. U. Bögli, A. Blatter, S.M. Pimenov, A.A. Smolin, and V.I. Konov, Diamond Relat. Mater. 1, 782 (1992).
38. R.K. Singh and J. Narayan, Mater. Sci. Eng. B 3, 217 (1989).
39. A.P. Shpak, A.M. Korduban, M.M. Medvedskij, and V.O. Kandyba, J. Electron. Spectrosc. Relat. Phenom. 156–158, 172 (2007).
40. T. Bak, J. Nowotny, M. Rekas, and C.C. Sorrell, J. Phys. Chem. Solids 64, 1043 (2003).
41. T.V. Perevalov and V.A. Gritsenko, J. Exp. Theor. Phys. 112, 310 (2011).
42. E. Finazzi, C.D. Valentin, and G. Pacchioni, J. Phys. Chem. C 113, 3382 (2009).
43. S.D. Sharma, D. Singh, K.K. Saini, C. Kant, V. Sharma, S.C. Jain, and C.P. Sharma, Appl. Catal. A 314, 40 (2006).
44. J.C. Yu, J. Yu, W. Ho, and J. Zhao, J. Photochem. Photobiol. A: Chem. 148, 331 (2002).

## **Chapter 10**

# **Enhancement of Photocatalytic Activity of Anatase TiO<sub>2</sub> Single Crystalline Thin Films by Nanosecond Pulsed Excimer Laser Treatment**

We present a novel method for improving the photocatalytic efficiency of epitaxial *c*-axis anatase TiO<sub>2</sub> thin films by a factor of 2 by using pulsed laser irradiation. The anatase films were epitaxially grown by pulsed laser deposition on Si(001) substrates, where a tetragonal yttria-stabilized zirconia (t-YSZ) buffer was used to effectively remove the native SiO<sub>x</sub> layer from the substrates prior to deposition of anatase. With the information from X-ray and TEM diffraction patterns, the epitaxial relationship across the interfaces was shown to be: (001)<sub>anatase</sub>||(001)<sub>t-YSZ</sub>||(001)<sub>silicon</sub> and [110]<sub>anatase</sub>||[110]<sub>t-YSZ</sub>||[001]<sub>silicon</sub>. Performing high temperature XRD, we observed that the anatase epilayers were stable up to 1100 °C, far beyond the normal anatase-to-rutile transition temperature (approximately 600-700 °C). The samples were subsequently laser annealed in air by a single pulse of KrF excimer laser beam at an energy density of approximately 0.3 J.cm<sup>-2</sup>. Based on the detailed HRTEM studies, the interface between the laser annealed and the pristine region as well as the anatase/t-YSZ interface were

crystallographically continuous. The XPS results revealed the presence of point defects and the XRD patterns showed some reduction and broadening after laser treatment. Photocatalytic activity of the pristine and the laser-annealed heterostructures was assessed by measuring the decomposition rate of 4-chlorophenol under UV light. The photocatalytic reaction rate constants were determined to be 0.0077 and 0.0138 min.<sup>-1</sup> for the as-deposited and the laser-treated samples, respectively. Such an appreciable enhancement was attributed to the formation of point defects, in particular oxygen vacancies, near the surface of the anatase thin films. Oxygen vacancies facilitate adsorption of 4-chlorophenol, hydroxyl, and water molecules to the titania surface. In addition, these defects trap the photogenerated electrons, giving rise to charge separation and, hence, improvement of the photocatalytic efficiency. The nanosecond photochemical enhancement may lead to fabrication of smart photocatalytic materials to address the needs of future photochemical devices.

### **10.1. Introduction**

4-Chlorophenol (4CP) is a well-known toxic organic compound, which is found in the waste water of paper, dyestuff, pharmaceutical, and agrochemical industries. It is a non-biodegradable material, which is characterized by high toxicity as well as persistency in both water and soil. So far, different techniques have been employed to degrade and remove 4CP from the environment, including biological treatment, chlorination, and adsorption by activated carbon. However, efficient removal of 4CP by these methods is hindered due to their inherent disadvantages. As an example,

biological treatment usually requires long processing time to decompose 4CP. The carbon adsorption process using granular activated carbon has been commercialized; however, the spent carbon needs to be disposed of safely. The chlorination method generates carcinogenic by-products.<sup>1-5</sup>

Arguably, semiconductor-mediated photodecomposition can be introduced as a more efficient technique to remove 4CP. In this process, 4CP is mineralized to CO<sub>2</sub>, H<sub>2</sub>O, and HCl through the reactions 5-4 to 5-7.<sup>6</sup> According these reactions, e<sup>-</sup>-h<sup>+</sup> pairs are generated by photo-excitation of the catalyst, followed by reaction with oxygen and water molecules from the atmosphere to produce energetic •OH and O<sub>2</sub>•<sup>-</sup> radicals. As is shown in reaction 5-7, 4CP molecules are oxidized to harmless products by reaction of •OH radicals. Generation and separation of the electrons and the holes are the critical steps for any photocatalytic reaction.<sup>7</sup>

The efficiency of any photocatalytic processes is dictated by the initial number of e<sup>-</sup>-h<sup>+</sup> pairs and separation of them. One way to enhance the charge separation is by introducing point defects. The point defects are considered to act as functional traps that reduce the recombination of electrons and holes, resulting in enhancement of the photocatalytic activity of the semiconductor. In particular, the oxygen vacancies are believed to serve as electron traps; holes can freely approach the surface, react with water, and form •OH radicals.<sup>8,9</sup> Of course, the point defects may also act as recombination centers since their energy level within the band gap is influenced by their concentration. That is, there is an optimum concentration beyond which the energy level of the defects shifts toward the middle of the band gap, where both

electrons and holes can get trapped and recombine. Position of the energy bands of the defect is affected by their environment.<sup>10,11</sup>

As of today, various metal oxides (e.g., TiO<sub>2</sub>,<sup>11-15</sup> CeO<sub>2</sub>,<sup>16</sup> CuO,<sup>17</sup> SnO<sub>2</sub>,<sup>18</sup> and WO<sub>3</sub><sup>19,20</sup>) in the pure and mixed forms have been utilized in heterogeneous photocatalytic removal of environmental pollutants. Among these oxides, titanium dioxide (TiO<sub>2</sub>) is an important semiconducting material that is widely used as a photocatalyst. It is chemically and biologically inert, photo-catalytically stable, commercially available, inexpensive, and environmentally safe.<sup>21</sup>

In the field of semiconductor processing, laser treatment has been employed in a variety of applications such as thin film deposition, post-growth processing, rapid thermal annealing, and laser machining. In our previous studies,<sup>22-24</sup> we showed that oxygen vacancies are generated by laser treatment of metal oxides. Hence, it is expected that the charge separation and, hence, the photocatalytic efficiency of TiO<sub>2</sub> can be enhanced by laser annealing due to the formation of oxygen vacancies.

The idea behind the present chapter is improvement of the photocatalytic efficiency of anatase TiO<sub>2</sub> single crystalline thin films by nanosecond laser treatment. We show that the photocatalytic reaction rate constant is increased by a factor of 2 after laser annealing. We also show that anatase, the meta-stable phase of TiO<sub>2</sub>, is stabilized at elevated temperatures by thin film epitaxy and suitable buffering. The epitaxial nature of the anatase film is associated with high photocatalytic efficiency due to the absence of the grain boundaries, which scatter the charge carriers. The grain boundaries may also act as a recombination center for electron-hole pairs. Single

crystalline anatase films were shown to exhibit enhanced photocatalytic activity in comparison with polycrystalline samples.

## 10.2. Experimental

Pulsed laser deposition (PLD) technique was employed to grow epitaxial anatase(001) epilayers on tetragonal yttria-stabilized zirconia (t-YSZ) templates. The ablated material is ejected in a direction normal to the target surface in the form of a forward-directed plume and it is deposited as a film onto a substrate facing the target.<sup>25,26</sup> We used Si(001) wafers as substrates. Before loading into the deposition chamber, the substrates underwent a multistep cleaning procedure including degreasing in hot acetone for 5 min., ultrasonic cleaning in acetone and methanol, each for 5 min. at room temperature. The substrates were, then, chemically etched in HF solution for 30 sec. and dried by high purity nitrogen jet. The PLD chamber was evacuated to a background pressure of  $\sim 8 \times 10^{-7}$  Torr using a turbomolecular pump backed by a rotary pump. The anatase TiO<sub>2</sub> and tetragonal YSZ targets were ablated by a Lambda Physik (LPX200) KrF excimer laser ( $\lambda=248$  nm,  $\tau=25$  ns) at a laser energy density of 3.0-3.5 J.cm<sup>-2</sup> and repetition rate of 5 Hz. To effectively destroy the native oxide layer of the silicon, the t-YSZ films were deposited for 1000 pulses under vacuum followed by a 1000 pulse deposition under the oxygen partial pressure of  $5 \times 10^{-4}$  Torr. More details on the mechanism behind removal of the amorphous SiO<sub>x</sub> layer by YSZ buffer can be found in our previous works.<sup>27</sup> Afterward, the anatase thin films were

deposited for 6000 pulses onto the t-YSZ-buffered Si(001) platform under the oxygen partial pressures of  $5 \times 10^{-2}$  Torr. The substrate temperature was set at 750 and 500 °C for the deposition of t-YSZ and anatase films, respectively. The samples were cooled down inside the PLD chamber under an oxygen pressure of 1 Torr, so the films could be simultaneously annealed to remove the point defects and obtain high crystallinity films. The samples were laser annealed by a single laser pulse at the energy density of 0.30 J.cm<sup>-2</sup> which is below the melting threshold of TiO<sub>2</sub>.

Details of characterization techniques were explained back in chapter 3. A Rigaku diffractometer and a Panalytical X'Pert PRO MRD HR X-Ray diffractometer, both working with a CuK $\alpha$  source at  $\lambda=0.154$  nm, were employed to perform  $\theta$ -2 $\theta$  and  $\varphi$  scan XRD on the anatase/t-YSZ/Si heterostructures to evaluate their in-plane and the out-of-plane orientations. A Siemens D5000 XRD equipped with custom made high temperature furnace<sup>28</sup> and Cu-tube was utilized for high temperature phase analysis. X-ray beam was conditioned by Gobel Mirror and measured using a Bruker Vantec-1 high speed detector. The samples were attached to a high purity alumina strip and placed into the high temperature furnace. Temperature of the samples was ramped at 30 K/min. and the samples were held for 30 min. at each temperature prior to collecting the XRD patterns. A JEOL 2010F transmission electron microscope, operated at 200 kV, with a point-to-point resolution of 1.8 Å, was used to study the atomic and crystallographic arrangements across the interfaces and to confirm the epitaxial growth. The surface stoichiometry of the samples, before and after laser treatment, was studied by a SPECS XPS with an Mg-k $\alpha$  excitation of 1254 eV equipped with a PHOIBIS

150 hemispherical analyzer. C(1s) core level binding energy was set at 285.0 eV, as reference, to interpret the results. Details of photocatalytic studies were already explained in chapter 3.

## 10.3. Results and discussion

### 10.3.1. Microstructure and thin film epitaxy

Fig.10.1 shows the  $\theta$ - $2\theta$  XRD pattern taken from the pristine anatase/t-YSZ/Si(001) heterostructure where growth of the anatase and the t-YSZ films along their [001] direction on the Si(001) substrate is confirmed.

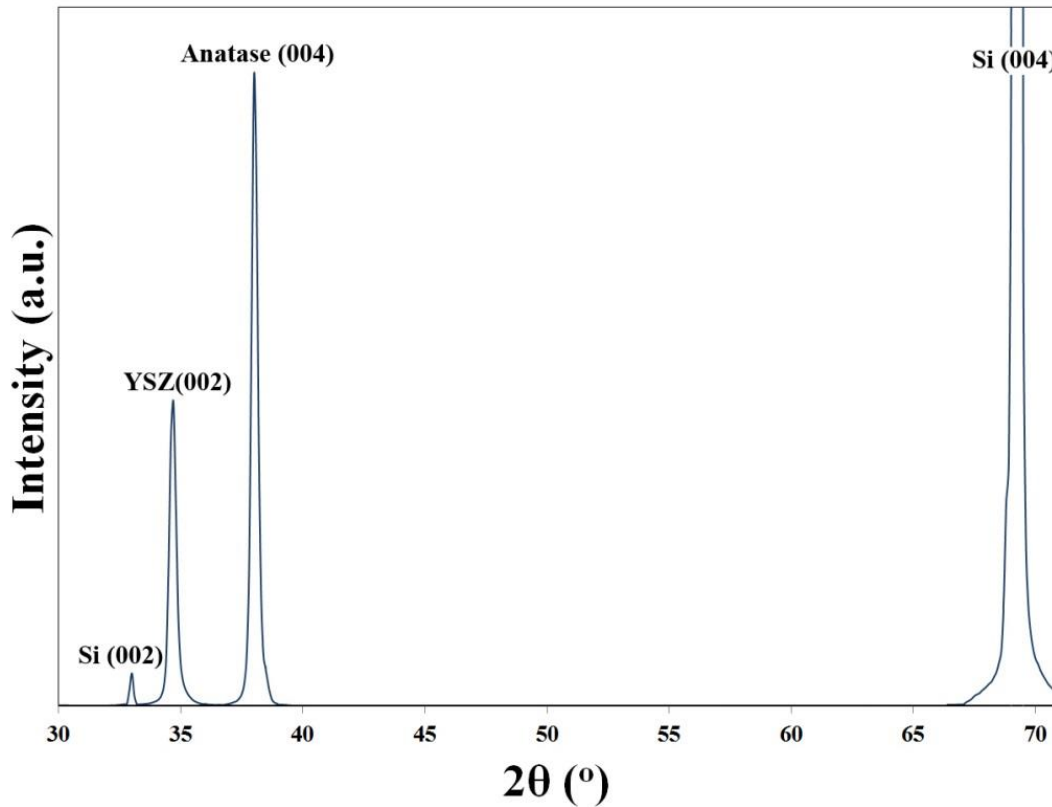


Fig.10.1.  $\theta$ - $2\theta$  XRD pattern of the anatase/t-YSZ/Si(001) epitaxial heterostructure.

Only (00l) peaks of anatase, t-YSZ, and Si were present and rutile peaks were not observed. In order to study the in-plane alignment between the silicon substrate and the t-YSZ buffer layer,  $\varphi$ -scan XRD was performed on the Si(202) reflection at  $2\theta=47.57^\circ$  and  $\psi=45.00^\circ$  and t-YSZ(101) reflection at  $2\theta=30.25^\circ$  and  $\psi=55.20^\circ$  and the corresponding results are displayed in Fig.10.2a.

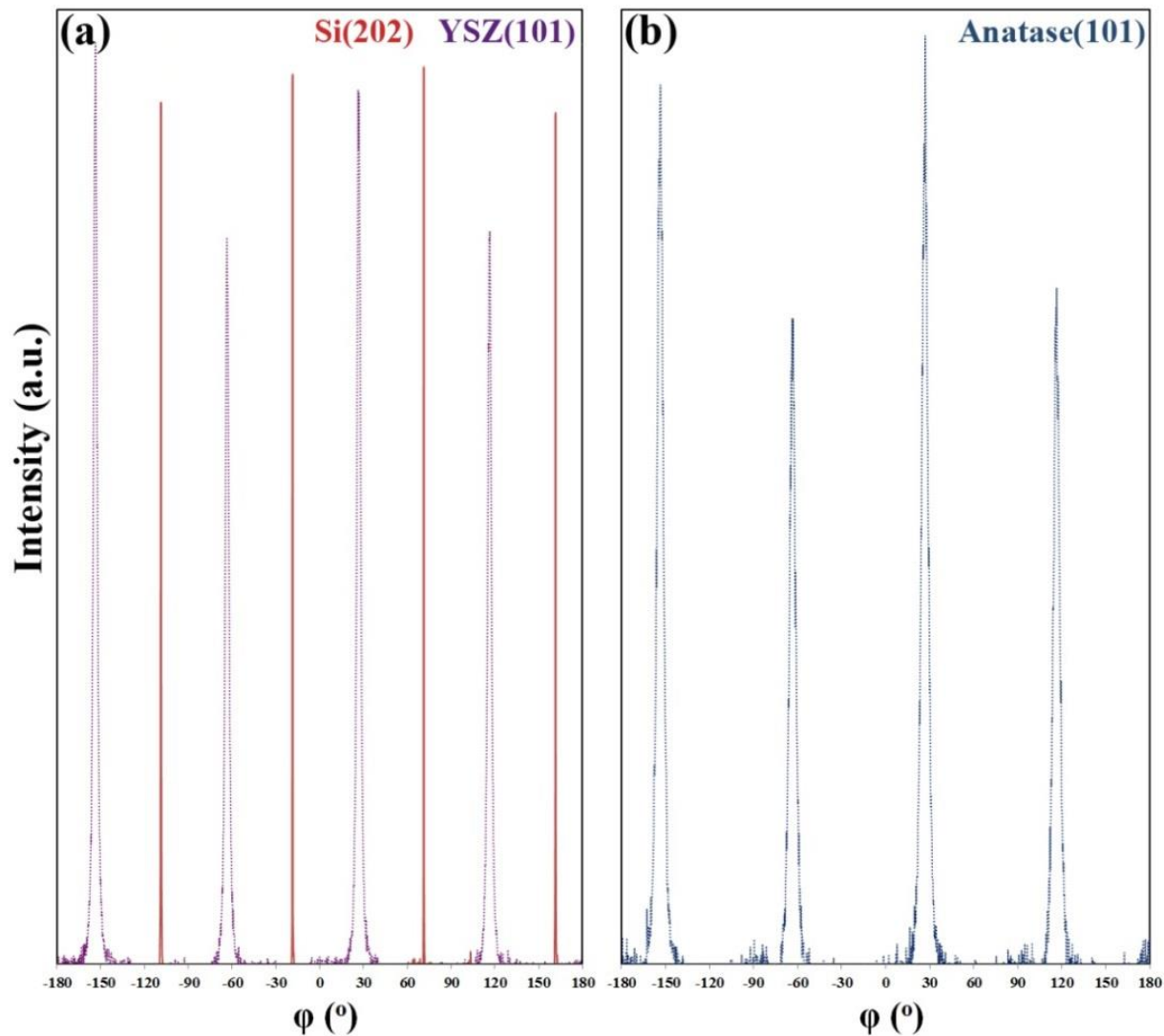


Fig.10.2.  $\varphi$ -scan patterns taken from: (a) Si(202) and t-YSZ(101) and (b) anatase(101) reflection.

A  $45^\circ$  rotation is seen in the t-YSZ layer with respect to the silicon substrate. With this information, the epitaxial relationship was established as  $[110](001)_{\text{t-YSZ}}||<001>\{001\}_{\text{Si}}$ . Based on the domain matching epitaxy paradigm,<sup>30</sup> 16/15 and 15/14 domains alternate with a frequency factor of 0.97 to accommodate the 6.2% misfit strain across the t-YSZ/Si interface. A possible atomic arrangement across the t-YSZ(001)/Si{001} interface is proposed, as shown in Fig.10.3.

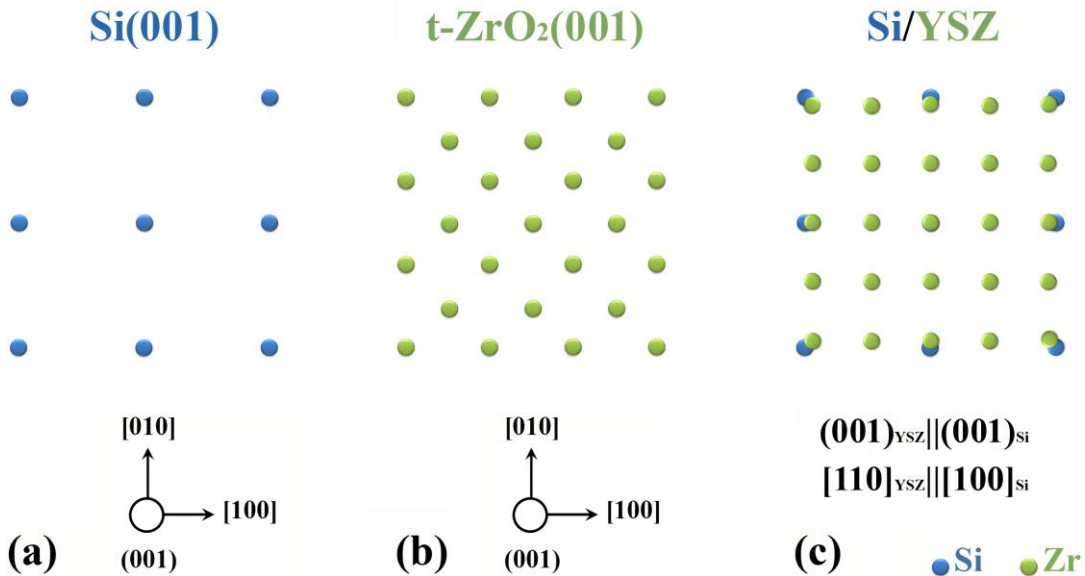


Fig.10.3. Illustration of the crystallographic arrangement across the t-YSZ(001)/Si(001) interface.

The in-plane alignment between the anatase top layer and the t-YSZ buffer was investigated by  $\varphi$ -scan XRD conducted on anatase(101) reflection at  $2\theta=25.28^\circ$  and  $\psi=68.30^\circ$ . It is observed (Fig.10.2b) that there is no in-plane rotation between the anatase and t-YSZ, i.e. a cube-on-cube growth takes place. Taking this information into consideration, the epitaxial relationship was expressed as  $(001)_{\text{anatase}}||(001)_{\text{t-YSZ}}$  and

$[110]_{\text{anatase}} \parallel [110]_{\text{t-YSZ}}$ . A possible atomic arrangement across the anatase/t-YSZ interface is shown in Fig.10.4.

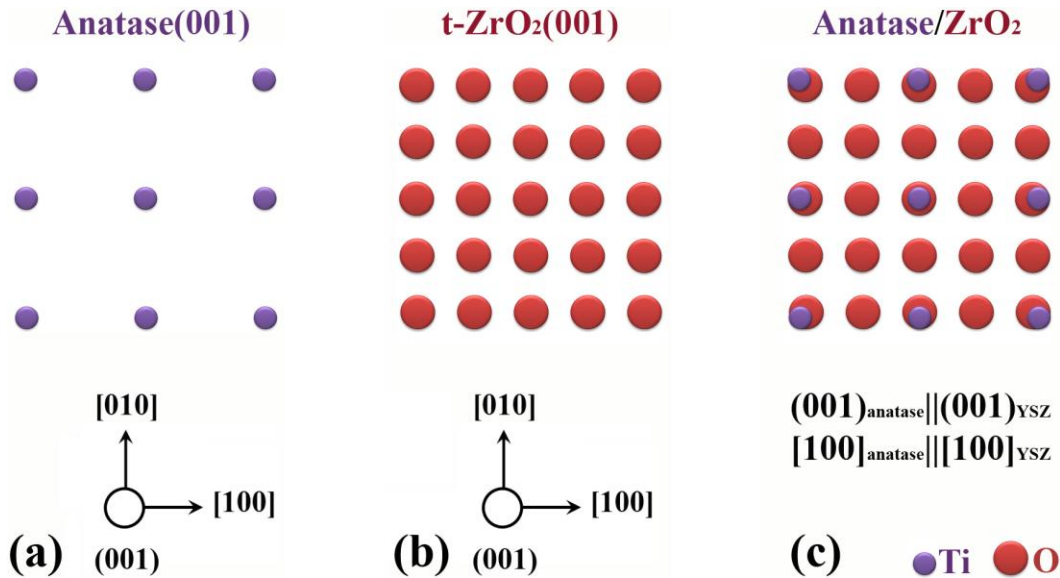


Fig.10.4. Schematic Illustration of the crystallographic arrangement across the anatase/t-YSZ interface.

Cross-section TEM micrograph taken from the as-deposited sample is shown in Fig.10.5a. The selected area diffraction pattern (SAED) is also displayed in the inset which confirms the epitaxial relationships determined from the  $\varphi$ -scans. The SAED pattern in Fig.10.5 belongs to the Si[110], t-YSZ[100], and anatase[100] zones, highlighted in yellow, green, and red. In the epitaxial thin films, domains are separated by low angle boundaries which are crystallographically continuous and atomically sharp. This statement is evident in Fig.10.5b which displays a domain boundary in the anatase epilayer highlighted by the black square and arrows. The highly epitaxial growth of anatase on the t-YSZ[001]/Si<001> platform and continuity of the domain

boundaries are both evident in the high resolution TEM image shown in the inset of Fig.10.5b. The carriers are not trapped or scattered at such boundaries.

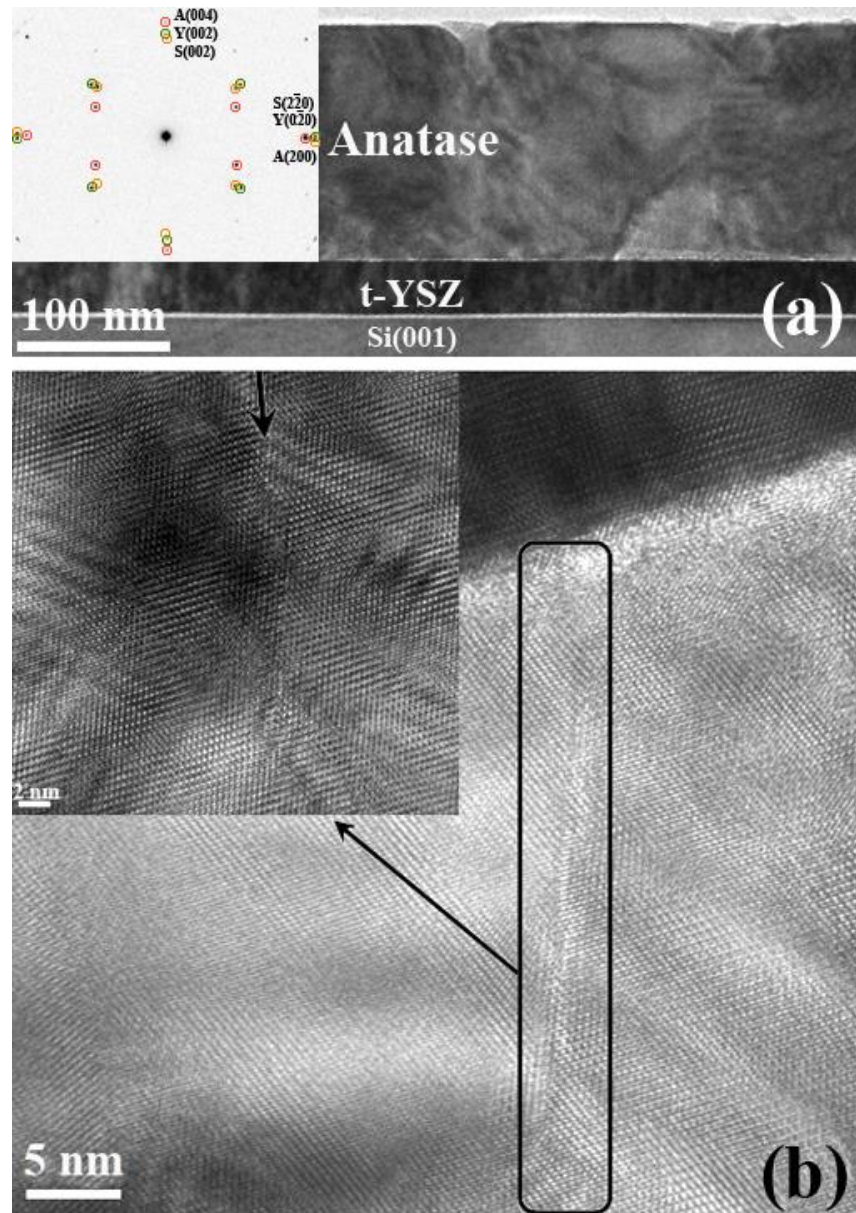


Fig.10.5. (a) Low magnification cross section image from the anatase(001)/t-YSZ(001)/Si(001) heterostructure and the corresponding SAED pattern and (b) A domain boundary in the anatase epitaxial film where an atomically sharp interface is observed.

Fig.10.6a depicts high resolution TEM image taken from the anatase/t-YSZ interface. The inverse FFT image of this interface is shown in Fig.10.6.b.

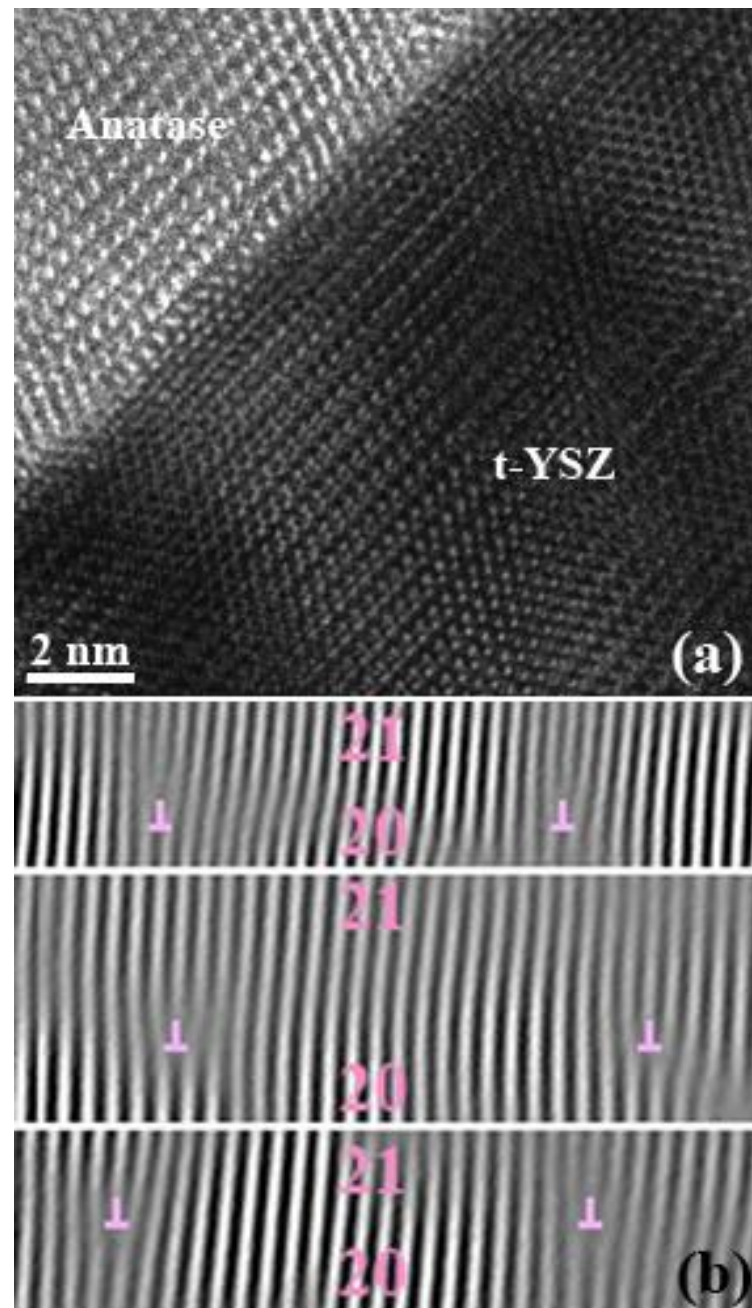


Fig.10.6. (a) High resolution TEM image of the anatase/t-YSZ interface, and (b) Inverse FFT image of the anatase/t-YSZ interface.

It is seen that the interface is clean and atomically sharp with no evidence of interfacial reaction. To relax the 5% misfit strain at the anatase/t-YSZ interface, 20 planes of anatase perfectly match with 21 planes of t-YSZ. It is worth mentioning that lattice constants along the silicon<100>, anatase[001], and t-YSZ[001] directions were considered as 5.43, 3.78, and 3.60 Å, respectively, in all of the above calculations. The inverse Fast Fourier Transform (FFT) of the anatase/t-YSZ interface is presented in Fig.10.6b, where alternating 21/20 domains are observed.

Low magnification cross section TEM micrograph taken from the annealed sample is shown in Fig.10.7a. As is observed, the interface between the laser irradiated and pristine regions is parallel to the free surface of the sample. The reason for such a profile is that the thermal gradient parallel to the interface is much smaller than the gradient perpendicular to the interface to many orders of magnitude, due to the short thermal diffusion distance and the large dimensions of the laser beam compared to the melt depth, in nanosecond laser processing. Hence, one-dimensional heat flow conditions essentially prevail.<sup>31</sup> A high resolution TEM image acquired from the interface between the annealed and pristine regions is depicted in Fig.10.7b. The same structures are observed on both sides of the interface and the interface is crystallographically continuous and atomically sharp. Meanwhile, the tetragonal structure has been preserved after laser annealing, since the laser energy density was below the threshold energy of melting of anatase.

XRD pattern of the anatase/t-YSZ/Si(001) heterostructure after laser annealing is shown in Fig.10.8. Comparing the intensity of the anatase(004) peak with those of the t-

YSZ(002) and Si(004) peaks, it can be deduced that the intensity of anatase peak is reduced in the annealed sample, because the formation of point defects results in a decreasing the structure factor and, consequently, a reduction in the peak intensity.

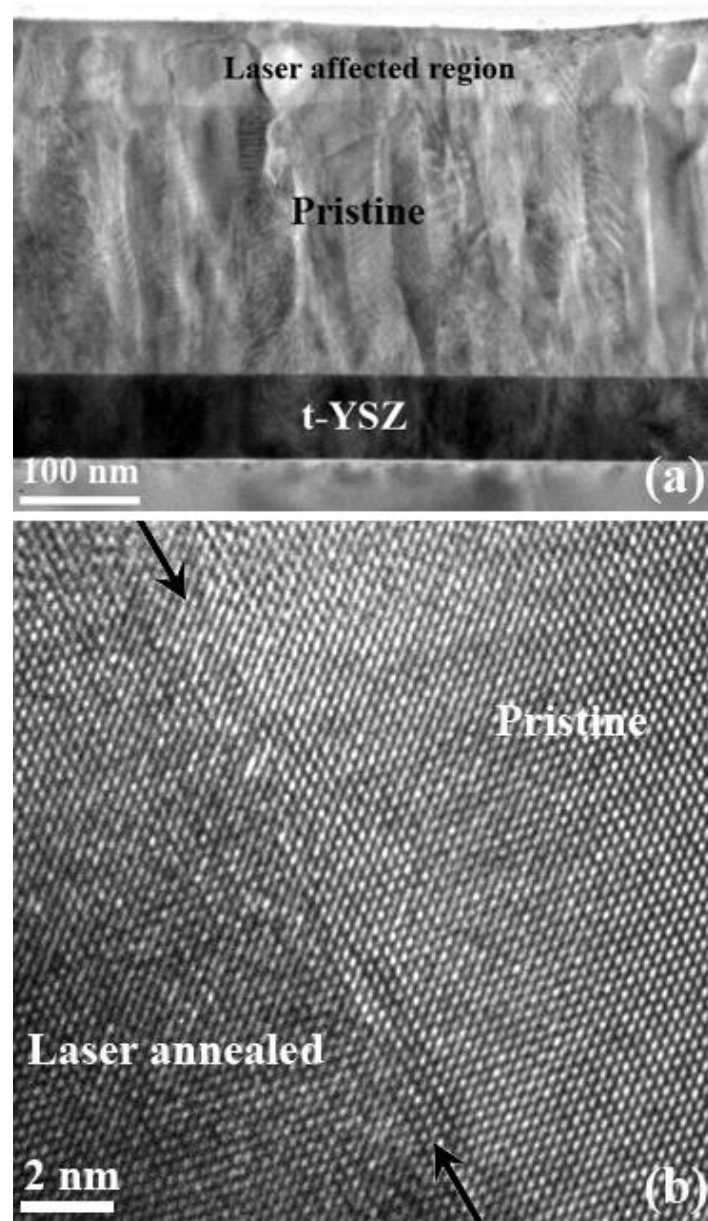


Fig.10.7. (a) Cross section TEM image from the laser treated sample and (b) High resolution micrograph of the interface between the laser affected and the pristine regions. The interface is showed by arrows.

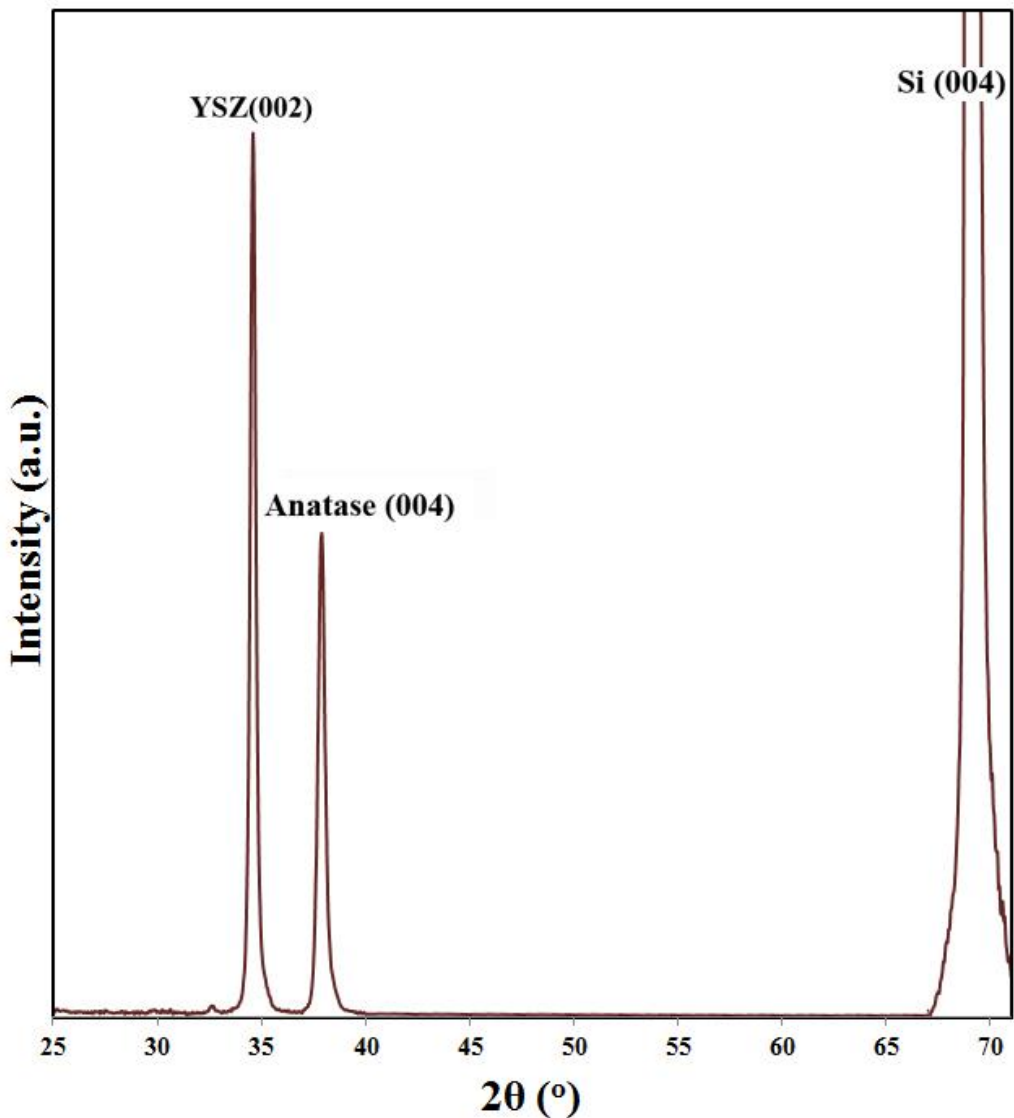


Fig.10.8.  $\theta$ - $2\theta$  scan XRD taken from the laser annealed anatase/t-YSZ/Si(001) heterostructure.

Oxygen vacancies and titanium interstitials result in local distortions of the lattice, which decreases the diffracted intensity as noted for the anatase(004) line. The XRD peak broadening and shift toward higher diffraction angles indicate formation of a defective structure due to the coupling of the laser beam with the anatase film.<sup>11-13</sup>. In our experiment, oxygen vacancies form through two different mechanisms. First,

energy of the laser photons is transferred to titania via photoexcitation of the valence electrons to the conduction band giving rise to the formation of oxygen vacancies, according the reactions 9-1 and 9-2. In addition, temperature of the surface is increased due to the coupling of the high energy laser beam<sup>31</sup> with the surface of the samples leading to the reduction of  $\text{TiO}_2$  and, hence, formation of oxygen vacancies. Oxygen vacancies may convert to titanium interstitials through the reaction 2-1.<sup>32</sup>

### 10.3.2. Stoichiometry

We employed XPS to study stoichiometry and defect characteristics in the near surface regions of the pristine and the laser annealed samples. The O(1s) core level binding energy of the as-deposited and the annealed samples is shown in Fig.10.9a and Fig.10.9b, respectively.

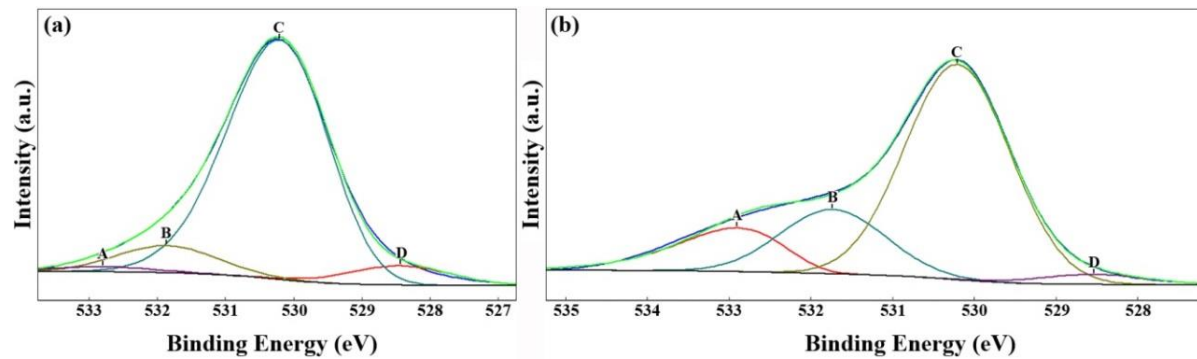


Fig.10.9. XPS O(1s) core level binding energy of the: (a) pristine and (b) laser annealed samples.

Peaks A and B, which are located at the binding energies of about 532.8 and 531.7 eV, are assigned to  $\text{H}_2\text{O}$  and -OH compounds, respectively. The surface oxygen vacancies

are filled by hydroxyl groups originating from dissociative absorption of water at the defect sites. Such a hydroxylated surface usually forms when an oxide material is exposed to the atmosphere.<sup>33</sup> Then, the subsequent water molecules attach to the hydroxyl groups by hydrogen bonds. This is the reason behind formation of peaks A and B. Therefore, concentration of the oxygen vacancies on the surface can be indirectly determined by portion of peak B. Peak C at the binding energy of 530.2 eV represents the perfect TiO<sub>2</sub> structure with Ti-O-Ti bonds. Finally, peak D can be indirectly attributed to the oxygen atoms close to the titanium interstitial defects. The titanium interstitials donate three or four electrons to the host crystal and transforms to Ti<sup>3+</sup> or Ti<sup>4+</sup> ions.<sup>10</sup> The tri-valent Ti interstitial ions remain in equilibrium with four-valent Ti ions.<sup>34</sup> These electrons are trapped by the lattice Ti<sup>4+</sup> cations leading to the formation of lattice Ti<sup>2+</sup> cations. Meanwhile, since the interstitials are positively charged, the oxygen anions relax toward the interstitials resulting in an elongation in the neighboring Ti-O binds and, hence, a decrease in their binding energy. Peak D represents such elongated bonds.

The oxygen vacancies and titanium interstitials are the most probable point defects of TiO<sub>2</sub> which dictate its physical and chemical properties.<sup>35-37</sup> The portion of peak B was determined to be 8.7 and 19.9 % in the as-deposited and laser treated samples, respectively. So, concentration of the oxygen vacancies is noticeably increased by laser irradiation. These results are in agreement with our previous studies on other metal oxides where we observed systematic change in optical, electrical, and magnetic properties of NiO and ZnO epilayers, after laser treatment.<sup>11-13</sup>

### 10.3.3. Thermal stability of anatase in epitaxial heterostructures

Fig.10.10 shows XRD patterns of the anatase/t-YSZ/Si(100) heterostructure at elevated temperatures, between 300 and 950 °C at intervals of 50 °C. For each XRD measurement, the samples were held for 30 min. at each temperature. The inset displays the room temperature XRD pattern of a sample heated to 1100 °C, kept for 4 hours, and, then, cooled to the room temperature inside the furnace. Only anatase XRD peaks are observed with increasing temperature up to 1100 °C, and the epitaxy is maintained at all temperatures.

As shown in Fig.10.11, we note that the intensity of the anatase(004) line increases with temperature starting at about 700 °C, suggesting that the defects are removed by oxidation of the sample and thermal annealing to eliminate oxygen vacancies and titanium interstitials. Fig.10.11 shows that the intensity of the anatase(004) peak, but not the t-YSZ(002) peak increases drastically with the temperature, because oxygen can interact with the anatase top layer directly to remove the point defects; however, the t-YSZ buffer film is shielded by the anatase film and, therefore, cannot be annealed efficiently. This phenomenon leads to increase of the  $I_{\text{anatase}(004)}/I_{\text{t-YSZ}(002)}$  ratio with the temperature, as shown in the inset of Fig.10.11. It is interesting to note that anatase is the metastable phase of  $\text{TiO}_2$  and, in the bulk form, it transforms into the rutile polymorph above 600-800 °C.<sup>38-40</sup> For example, about 80% of anatase should get converted to rutile within only 30 min. at 875 °C.<sup>41</sup> The reason behind the observed thermal stability is thin film epitaxy and use of a proper template. Lattice parameters of tetragonal YSZ along its *c*-axis ( $a=b=3.64 \text{ \AA}$ ) are very close to

those of anatase ( $a=b=3.78$  Å). Therefore, any phase transformation to rutile ( $a=b=4.59$  Å and  $c=2.96$  Å) introduces larger misfit strains. Based on the domain matching epitaxy paradigm,<sup>30</sup> more dislocations are required to relax larger misfits. Taking into account the energy of the misfit dislocations, the strain free-energy makes the phase transformation of anatase to rutile on the t-YSZ/Si platform quite prohibitive.

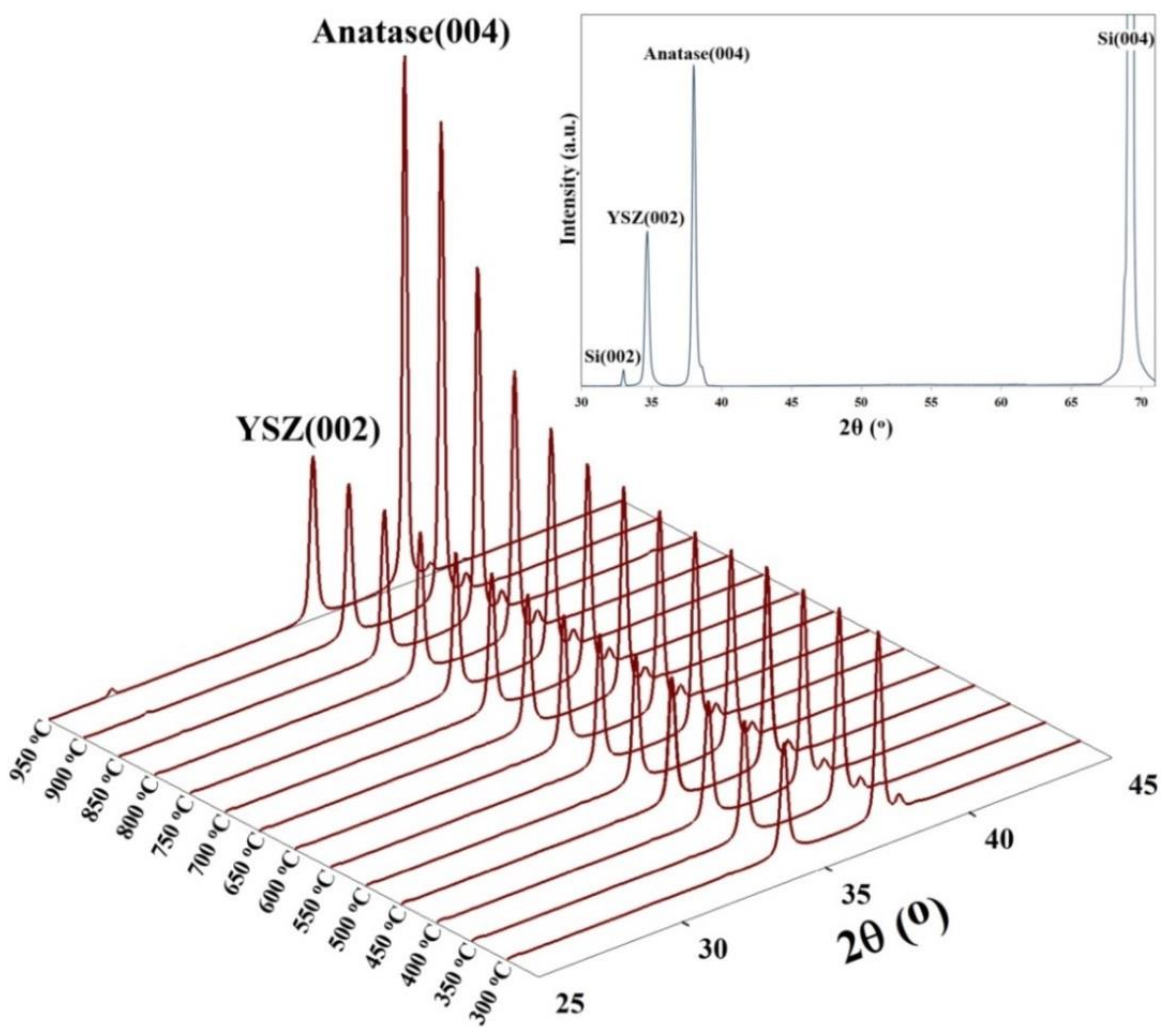


Fig.10.10. XRD patterns collected from the anatase/t-YSZ/Si heterostructure at elevated temperatures.

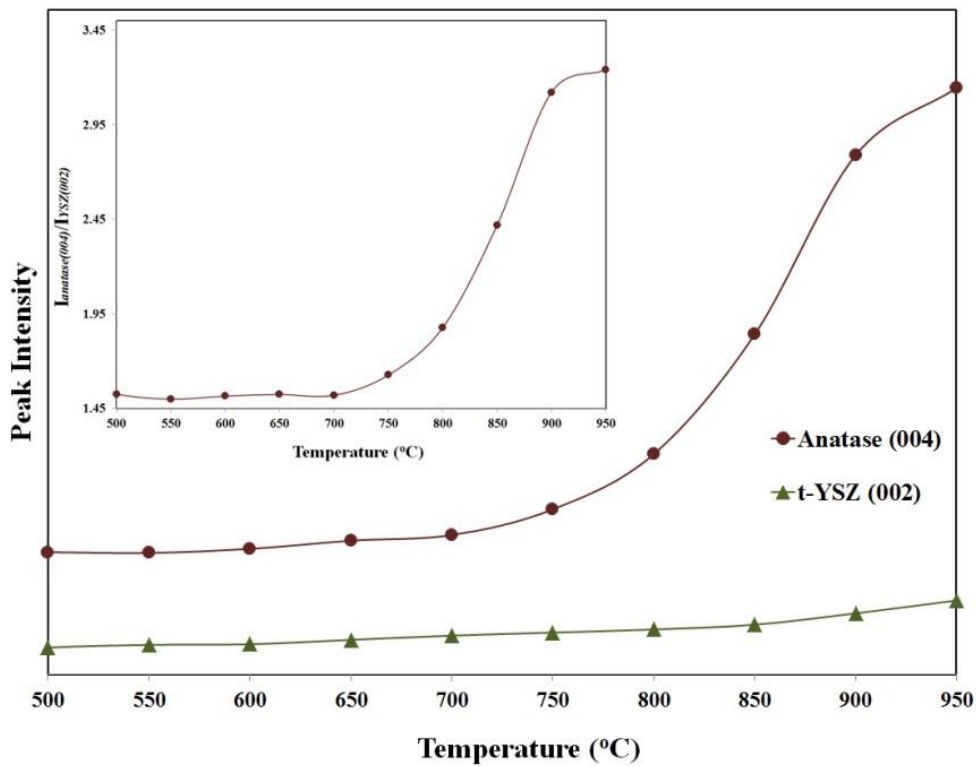


Fig.10.11. Intensity of the anatase(004) and t-YSZ(002) characteristic peaks.

The inset shows  $I_{\text{anatase}(004)}/I_{\text{t-YSZ}(002)}$  ratio at different temperatures.

The stability of the anatase single crystalline thin films deposited onto the t-YSZ/Si(001) platform and maintaining the epitaxy are further ascertained by the TEM image presented in Fig.10.12 and the SAED pattern shown in the inset. This image belongs to the sample annealed at 1100 °C for 4 hours. Formation of a thick SiO<sub>2</sub> layer in between the Si(001) substrate and the t-YSZ buffer is interesting. This layer formed due to the chemical reaction of silicon with the oxygen from the t-YSZ buffer layer or oxygen from the atmosphere at elevated temperatures. However, as the SAED pattern shows, this layer does not alter the epitaxial growth and the structure of the top layers, because those layers have been already formed.

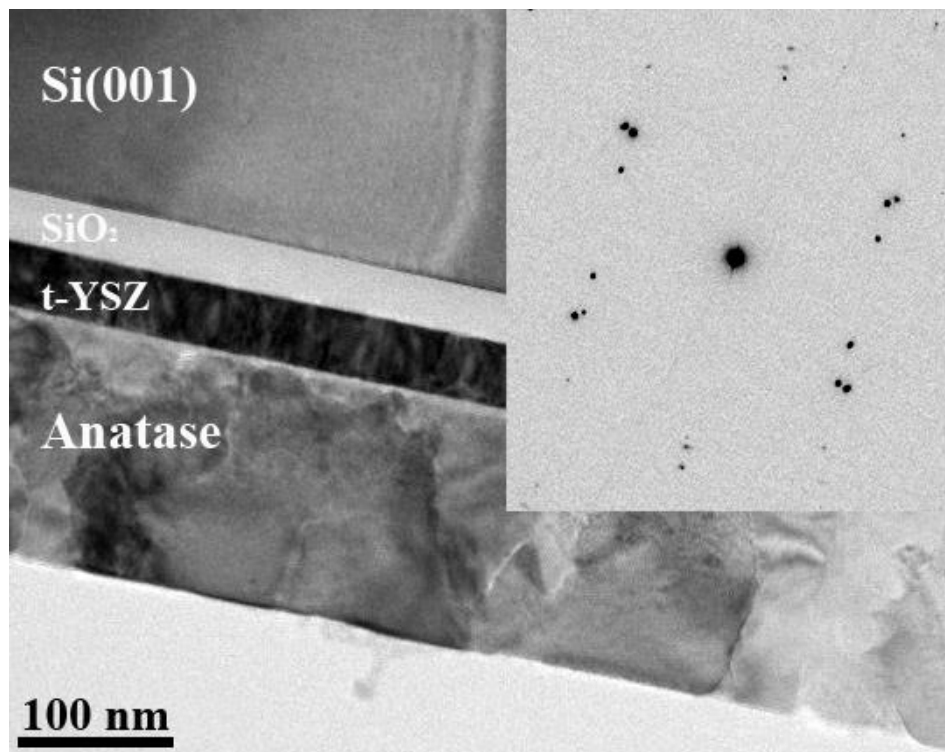


Fig.10.12. Low magnification TEM cross section image and the SAED pattern of the anatase/t-YSZ/Si heterostructure annealed at 1100 °C for 4 hours.

#### 10.3.4. Photocatalytic efficiency

Results of the photocatalytic studies are presented in Fig.10.13. As the inset of this figure shows, the concentration of 4CP decreases over time with ultraviolet irradiation which confirms the decomposition of 4CP. To confirm that the 4CP is degraded by the catalyst and not just the UV light, an experiment was performed without any  $\text{TiO}_2$  sample inside the cell. The curve “No catalyst” represents the results of this experiment where no considerable change is observed in the 4CP concentration. Hence, it is deduced that, in other experiments, 4CP is degraded photocatalytically. To quantitatively compare the photocatalytic efficiency of the anatase films, the

photocatalytic reaction rate constant ( $k$ ) was calculated by the equation  $\ln(C/C_0) = -kt$  where  $C_0$  is the initial concentration of 4CP at  $t=0$  and  $C$  represents the concentration of 4CP at time  $t$ .

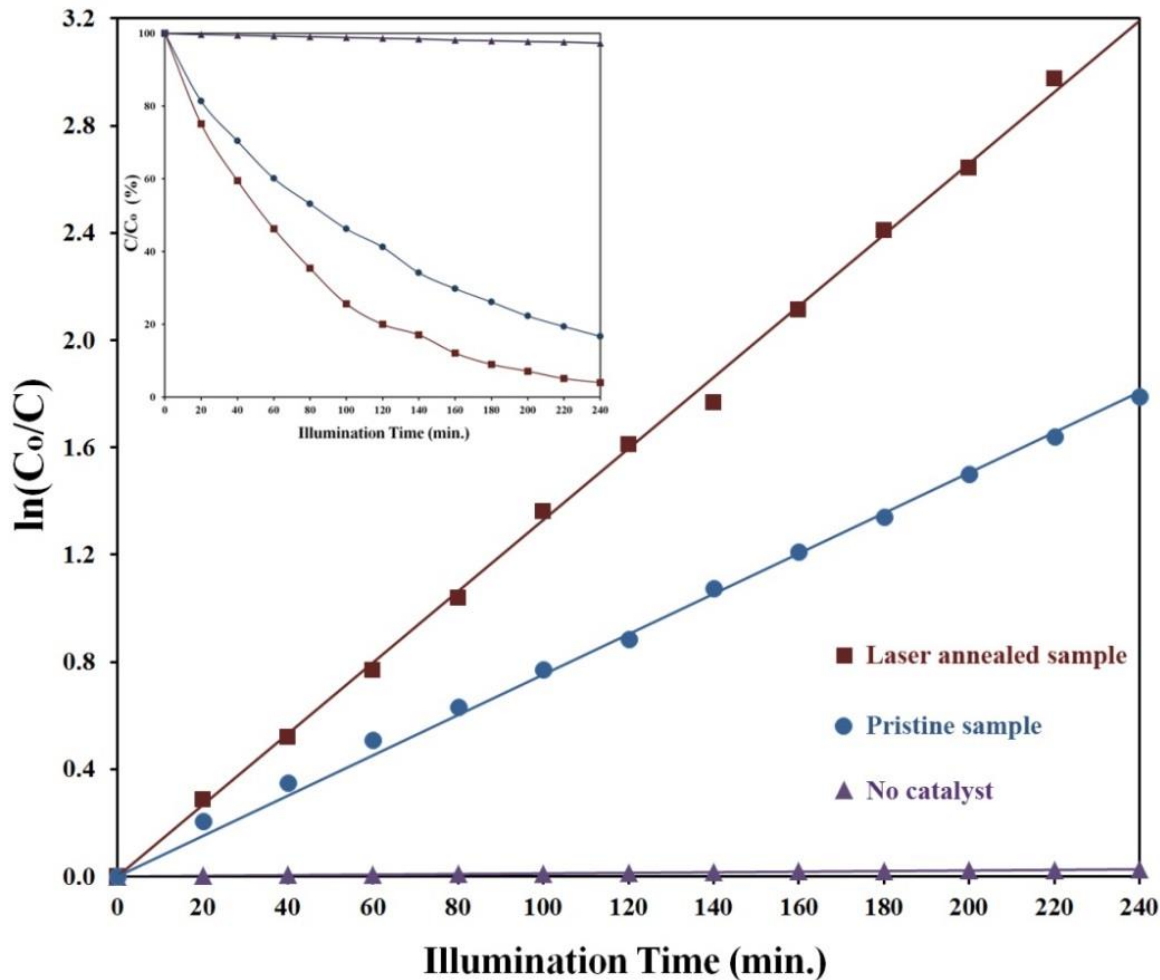


Fig.10.13. Effect of laser annealing on the photocatalytic efficiency of the anatase/t-YSZ/Si(001) thin film heterostructure.

It is worth mentioning that the photocatalytic decomposition of 4CP follows pseudo-first-order kinetics. Fig.10.13 delineates changes of  $\ln(C_0/C)$  as a function of the

irradiation time. Slope of the straight lines express  $k$  which was determined as  $7.7 \times 10^{-3}$  and  $13.8 \times 10^{-3} \text{ min.}^{-1}$  for the pristine and the laser treated samples, respectively. Thus, it is deduced that the photocatalytic activity increases significantly after excimer laser annealing. As already indicated, the concentration of oxygen vacancies in the anatase structure increases after laser treatment. The oxygen vacancies introduce a donor energy level below the conduction band of titania and trap the photogenerated electrons.<sup>8,42,43</sup> Consequently, charge separation is enhanced<sup>41</sup> and the positive holes which are a prerequisite for photocatalytic decomposition of 4CP (reactions 3 and 4) can approach the surface to participate in the chemical reactions without recombination with electrons. Oxygen vacancies have the same role in other metal oxides, such as ZnO, as well.<sup>45</sup> In addition, oxygen vacancies at the TiO<sub>2</sub> surface promote the adsorption of 4CP molecules. It has been demonstrated that the surface of reduced TiO<sub>2</sub> layers is more acidic than that of perfect TiO<sub>2</sub>. The increased acidity can generate a higher affinity for species with unpaired electrons; therefore, these films could absorb more OH<sup>-</sup> or H<sub>2</sub>O, and create more hydroxyl radical necessary for photo-oxidation reactions.<sup>46</sup> These three phenomena give rise to a noticeable increase in photocatalytic efficiency of the anatase thin films after laser annealing.

#### 10.4. Conclusions

The anatase TiO<sub>2</sub> thin films were epitaxially grown on t-YSZ-buffered silicon substrates. The crystallographic alignment between the anatase thin film and t-YSZ layer was determined. The formation of stoichiometric point defects as a result of

interaction of the laser beam with the titania samples was evaluated. We achieved considerable enhancement of the photocatalytic activity of anatase(001) epitaxial thin films by nanosecond laser annealing. It was shown that the laser treatment introduces stoichiometric point defects to the lattice which are surmised to play a critical role in separation of charge carriers and, therefore, improve the catalytic efficiency. Pulsed laser treatment is proposed as an efficient technique for altering the chemical and physical properties of the anatase  $\text{TiO}_2$ . Epitaxial anatase films on t-YSZ/Si(100) substrate also exhibited an increasing thermal stability. No rutile phase was observed after 4 hours heat treatment at elevated temperatures up to 1100 °C.

## References

1. Y. Du, Q.S. Fu, Y. Li, and Y. Su, J. Hazard. Mater. 186, 491 (2011).
2. P.D. Vaidya, and V.V. Mahajani, Appl. Catal. B: Environ. 51, 21 (2004).
3. N. Venkatachalam, M. Palanichamy, B. Arabindoo, and V. Murugesan, J. Molec. Catal. A: Chem. 266, 158 (2007).
4. J. Theurich, M. Lindner, and D.W. Bahnemann, Langmuir 12, 6368 (1996).
5. D. Chen and A.K. Ray, Appl. Catal. B: Environ. 23, 143 (1999).
6. Y. Cheng, H. Sun, W. Jin, and N. Xu, Chem. Eng. J. 128, 127 (2007).
7. A. Fujishima and K. Honda, Nature 238, 37 (1972).
8. J. Zhuang, W. Dai, Q. Tian, Z. Li, L. Xie, J. Wang, and P. Liu, Langmuir 26, 9686 (2010).
9. S.A. Campbell, D.C. Gilmer, X.C. Wang, M.T. Hsieh, H.S. Kim, W.L. Gladfelter, and J. Yan, IEEE Trans. Electron Devices 44, 104 (1997).

10. E. Finazzi, C.D. Valentin, and G. Pacchioni, *J. Phys. Chem. C* 113, 3382 (2009).
11. M.R. Bayati, S. Joshi, R. Molaei, R.J. Narayan, and J. Narayan, *J. Solid State Chem.* 187, 231 (2012).
12. M.R. Bayati, A.Z. Moshfegh, and F. Golestani-Fard, *Mater. Lett.* 60, 2215 (2010).
13. M.R. Bayati, F. Golestani-Fard, A.Z. Moshfegh, and R. Molaei, *Mater. Chem. Phys.* 128, 427 (2011).
14. M.R. Bayati, A.Z. Moshfegh, and F. Golestani-Fard, *Appl. Catal. A: Gen.* 389, 60 (2010).
15. O. Lyandres, D. Finkelstein-Shapiro, P. Chakthranont, M. Graham, and K.A. Gray, *Chem. Mater.* 24, 3355 (2012).
16. X. Fu, W. Tang, L. Ji, and S. Chen, *Chem. Eng. J.* 180, 170 (2012).
17. M. Liu, X. Qiu, M. Miyauchi, and K. Hashimoto, *Chem. Mater.* 23, 5282 (2011).
18. L. Trotochaud, and S.W. Boettcher, *Chem. Mater.* 23, 4920 (2011).
19. Y. Ping, Y. Li, F. Gygi, and G. Galli, *Chem. Mater.* 24, 4252 (2012).
20. M.R. Waller, T.K. Townsend, J. Zhao, E.M. Sabio, R.L. Chamousis, N.D. Browning, and F.E. Osterloh, *Chem. Mater.* 24, 698 (2012).
21. M. Miyauchi, A. Nakajima, T. Watanabe, and K. Hashimoto, *Chem. Mater.* 14, 2812 (2002).
22. P. Gupta, T. Dutta, S. Mal, and J. Narayan, *J. Appl. Phys.* 111, 013706 (2012).
23. S. Mal, S. Nori, J. Narayan, and J.T. Prater, *J. Mater. Res.* 26, 1298 (2011).
24. S. Mal, J. Narayan, S. Nori, J.T. Prater, and D. Kumar, *Solid State Commun.* 150, 1660 (2010).

25. B.C. Riggs, A.D. Dias, N.R. Schiele, R. Cristescu, Y. Huang, D.T. Corr, and D.B. Chrisey, MRS Bull. 36, 1043 (2011).
26. D.B. Chrisey and G.K. Hubler, Pulsed Laser Deposition of Thin Films, John Wiley & Sons (1994).
27. M.R. Bayati, P. Gupta, R. Molaei, R.J. Narayan, and J. Narayan, Cryst. Growth Des. 12, 4535 (2012).
28. S.T. Misture, Measurement Sci. and Tech. 14, 1091 (2003).
29. J.M. Schurr, Chem. Phys. 15, 1 (1976).
30. J. Narayan and B.C. Larson, J. Appl. Phys. 93, 278 (2003).
31. R.K. Singh and J. Narayan, J. Mater. Sci. Eng. B 3, 217 (1989).
32. E. Cho, S. Han, H.S. Ahn, K.R. Lee, S.K. Kim, and C.S. Hwang, Phys. Rev. B: Condens. Matter. 73, 193202 (2006).
33. A.P. Shpak, A.M. Korduban, M.M. Medvedskij, and V.O. Kandyba, J. Electron. Spectrosc. Relat. Phenom. 156–158, 172 (2007).
34. T. Bak, J. Nowotny, M. Rekas, and C.C. Sorrell, J. Phys. Chem. Solids. 64, 1043 (2003).
35. H. Peng, Phys. Lett. A 372, 1527 (2008).
36. M.R. Bayati, J. Ding, Y.F. Lee, R.J. Narayan, and J. Narayan, J. Phys. C: Condens. Mater. 24, 395005 (2012).
37. T. Bak, J. Nowotny, M. Rekas, and C.C. Sorrell, J. Phys. Chem. Solids 64, 1057 (2003).
38. M.R. Bayati, F. Golestani-Fard, and A.Z. Moshfegh, J. Appl. Catal. A: Gen. 382, 322 (2010).
39. D. Yoo, I. Kim, S. Kim, C. Hahn, C. Lee, and S. Cho, Appl. Surf. Sci. 253, 3888 (2007).

40. A.W. Czanderna, C.N. Ramachandra Rao, and J.M. Honig, *Trans. Faraday Soc.* 54, 1069 (1958).
41. S.A. Borkar and S.R. Dharwadkar, *J. Therm. Anal. Calorim.* 78, 761 (2004).
42. M.K. Nowotny, L.R. Sheppard, T. Bak, and J. Nowotny, *J. Phys. Chem. C* 112, 5275 (2008).
43. S.A. Campbell, D.C. Gilmer, X.C. Wang, M.T. Hsieh, H.S. Kim, W.L. Gladfelter, and J. Yan, *IEEE Trans. Electron Devices* 44, 104 (1997).
44. J. Zhuang, W. Dai, Q. Tian, Z. Li, L. Xie, J. Wang, and P. Liu, *Langmuir* 26, 9686 (2010).
45. H. Morkoc and U. Ozgur, Zinc oxide: fundamentals, materials and device technology, Weinheim Wiley-VCH (2009).
46. F. Liu, L. Lu, P. Xiao, H. He, L. Qiao, and Y. Zhang, *Bull. Korean Chem. Soc.* 33, 2255 (2012).

## Chapter 11

# Role of Substrate Crystallographic Characteristics on Structure and Properties of Rutile Epilayers

To investigate heterostructures of interest for catalytic applications, we integrated rutile  $\text{TiO}_2$  epitaxial thin films with  $\text{Al}_2\text{O}_3(0001)$ ,  $\text{Al}_2\text{O}_3(10\bar{1}0)$ , and  $\text{Al}_2\text{O}_3(01\bar{1}2)$  substrates and studied structure and properties of the epilayers as a function of the crystallographic characteristics of the substrate. The epitaxial relationship across the film/substrate interfaces was established as  $(100)_{\text{rutile}}|| (0001)_{c\text{-sapphire}}$  and  $[001]_{\text{rutile}}|| [10\bar{1}0]_{c\text{-sapphire}}$ ,  $(001)_{\text{rutile}}|| (10\bar{1}0)_{m\text{-sapphire}}$  and  $[100]_{\text{rutile}}|| [0001]_{m\text{-sapphire}}$ , and  $(101)_{\text{rutile}}|| (01\bar{1}2)_{r\text{-sapphire}}$  and  $[010]_{\text{rutile}}|| (01\bar{1}2)_{r\text{-sapphire}}$ . The origin and the relaxation mechanism of stress and strain for each heterostructure were studied in detail. It was revealed that large lattice misfit strains relax easily even if the primary slip system is not active due to the epitaxial alignment between the film and substrate and orientation of the in-plane stresses. We also showed that even small misfit strains can relax provided that the primary slip system is active. The origin of the residual strains in the epilayers was found to be primarily due to thermal misfit and defect/impurity strains. In addition, the decomposition rate of 4-chlorophenol by the rutile/sapphire

heterostructures under ultraviolet illumination was measured. The (001)-plane was found to be the most photoactive face of rutile TiO<sub>2</sub>, while the (100)-plane showed the lowest photocatalytic activity. The difference in the photochemical characteristics was attributed to the atomic arrangement on different crystallographic surface planes.

### **11.1. Introduction**

The naturally forming polymorphs of titanium dioxide (TiO<sub>2</sub>) are rutile, anatase, brookite, and TiO<sub>2</sub>(B). All of them are composed of octahedrally coordinated Ti<sup>4+</sup> cations.<sup>1,2</sup> The most thermodynamically stable polymorph of titanium dioxide is rutile, having a tetragonal crystalline structure ( $a=b=4.593$  and  $c=2.959$  Å, P4<sub>2</sub>/mnm space group).<sup>3-5</sup> It has been widely investigated owing to its interesting optical, electrical, photochemical properties. One of the most useful characteristics of rutile TiO<sub>2</sub> is its ability to lose or recover stoichiometry under reduced or increased oxygen pressure; in other words, point defect microstructure and, therefore, properties can be easily manipulated in rutile.<sup>6,7</sup> This is the main reason why this material is technologically important and has been widely used in versatile applications.

TiO<sub>2</sub> based epitaxial heterostructures, with precisely controlled out-of-plane (growth direction) and in-plane orientations over a large area, are of interest due to their scientific and technological importance. Controlled crystallographic structures can be used to manipulate properties of titania based heterostructures. Rutile TiO<sub>2</sub> has three main high symmetry crystalline faces: (110), (100), and (001). These crystallographic planes are depicted in Fig.11.1.

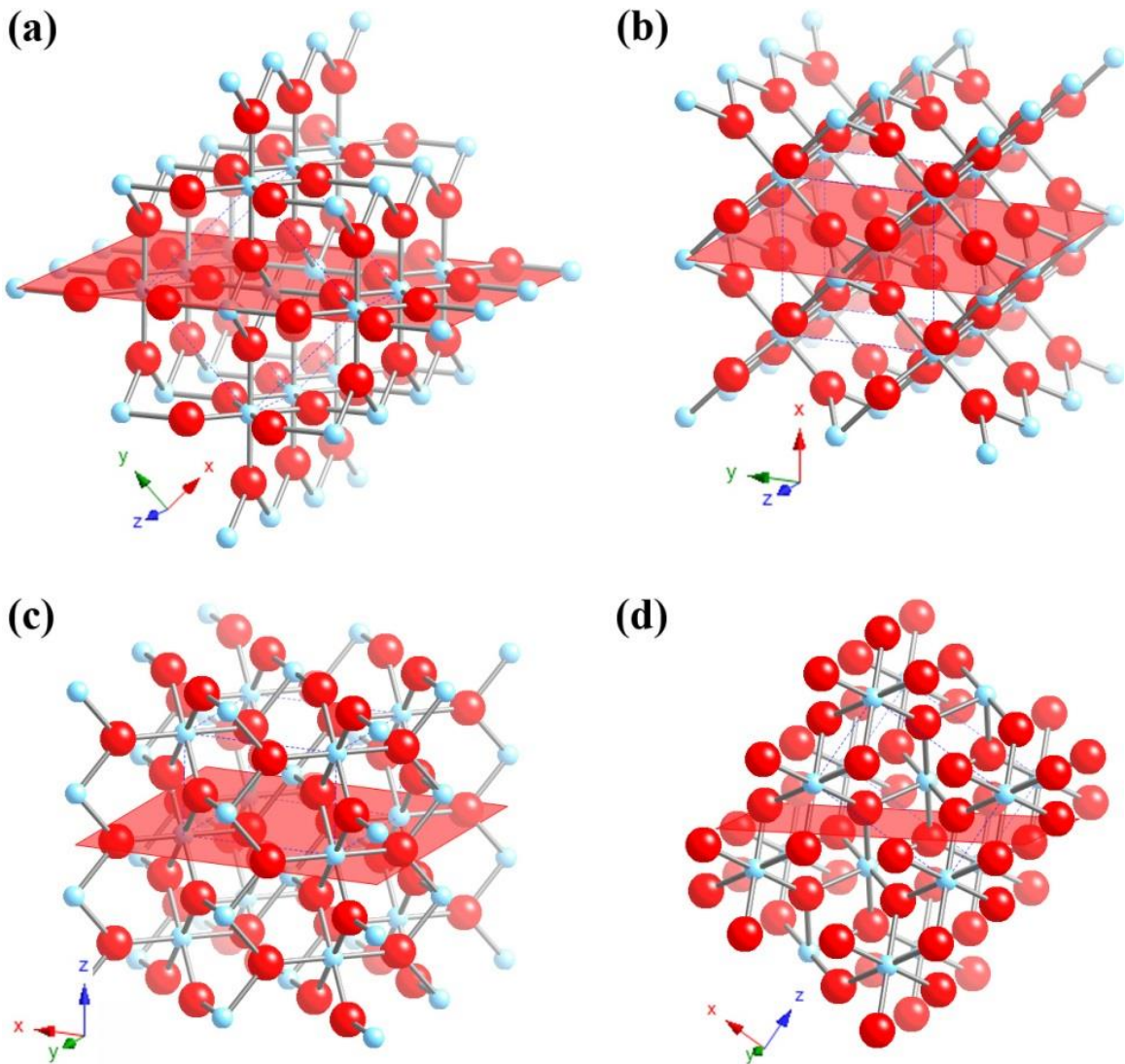


Fig.11.1. Illustration of low-index faces of rutile: (a) (110), (b) (100), (c) (001), and (d) (101).

The most thermally stable face is (110) which has been widely studied. This face (Fig.11.1a) exhibits atoms with different environments. It has rows of bridging oxygen anions connected to two 6-coordinated Ti atoms. Meanwhile, there are rows of 5-coordinated Ti atoms running parallel to the rows of bridging oxygens and alternating with them. In other words, there are also two kinds of oxygen anions on this face. One is

threefold coordinated and is localized in the surface plane. The other one is prominent from the surface around 1 Å and is doubly coordinated. The (100) face, shown in Fig.11.1b, is sometimes called as “sawtooth” orientation of rutile and exhibits the same three kinds of atoms as the (110) face does. It has alternating rows of bridging oxygens and 5-coordinated Ti atoms existing in a different geometric relationship with each other. There are double rows of bridging oxygens alternating with single rows of exposed Ti atoms which are of the equatorial type rather than the axial type. The (100) face is thermally less stable and restructures above 475 °C. As is seen in Fig.11.1c, the (001) face exhibits two kinds of atoms as well: tetracoordinated titanium cations and twofold oxygen anions. The tetracoordinated cations have a high unsaturated valence and, therefore, are very acidic. The (101) face, which is depicted in Fig.11.1d, exhibits two kinds of atoms: pentacoordinated titanium cations and twofold oxygen anions with two different Ti–O bond lengths. These faces have varying surface energies, i.e.  $1.65 \text{ J.m}^{-2}$  for the (001),  $0.89 \text{ J.m}^{-2}$  for the (110),  $1.12 \text{ J.m}^{-2}$  for the (100), and  $1.39 \text{ J.m}^{-2}$  for the (101) face.<sup>3,8,9</sup> It is envisaged that various atomic arrangements and surface energies should result in different physical and chemical characteristics.

As it was pointed out, each face of rutile  $\text{TiO}_2$  shows different characteristics; thus, it is extremely critical to control the in-plane and out-of-plane directions of rutile epilayers for any specific application. In this study, we epitaxially integrated rutile  $\text{TiO}_2$  with *m*-sapphire, *r*-sapphire, and *c*-sapphire substrates and investigated the growth orientation. Thin film epitaxy, microstructure of the epilayers, and film/substrate interfaces were studied in detail. Residual strains were measured and stress values

were calculated. The mechanism of stress relaxation was rationalized based on the crystallographic relationship between titania thin films and sapphire substrates. Photocatalytic properties of the samples were evaluated and a correlation between crystallographic characteristics and photochemical properties has been established and discussed.

## **11.2. Experimental**

Rutile TiO<sub>2</sub> thin films were deposited on *c*-sapphire (Al<sub>2</sub>O<sub>3</sub>(0001)), *m*-sapphire(Al<sub>2</sub>O<sub>3</sub>(10̄10)), and *r*-sapphire (Al<sub>2</sub>O<sub>3</sub>(10̄12)) substrates by pulsed laser deposition (PLD) technique where a KrF excimer laser was used to ablate a high purity TiO<sub>2</sub> target. The photon energy and pulsed duration of the laser beam were about 5.0 eV ( $\lambda=248$  nm) and  $2.5\times10^{-8}$  sec., respectively. Using an optics system, the laser beam was focused onto the target surface to provide an energy density of about 3.0-3.5 J.cm<sup>-2</sup>. The repetition rate was set at 5 Hz. The deposition chamber was pumped down to a background pressure of better than  $8\times10^{-7}$  Torr. The rutile films were deposited under an oxygen partial pressure of  $5\times10^{-4}$  Torr at a substrate temperature of 750 °C for 15 min. Subsequently, the samples were cooled down to room temperature in the deposition chamber under an oxygen pressure of 1 Torr. Details on the substrate pretreatment and cleaning procedure can be found in our previous works.<sup>6,10,11</sup>

The microstructure of the rutile/sapphire heterostructures was studied in detail by X-ray diffraction where a 4-circle Huber diffractometer with a Cu-K $\alpha$  source ( $\lambda_{ave} = 1.5418$  Å) was employed. A graphite monochromator was placed between the X-ray

tube and sample to analyze the incident X-ray beam. We also used Soller slits, between the sample and detector, to analyze the diffracted beam. A JEOL 2010F transmission electron microscope with 0.18 nm resolution and Gatan image filter (GIF) attachment was used to carry out the microstructural studies. The microscope was operated at 200 kV. Electron transparent samples were fabricated by a FEI Quant 3D FEG focused ion beam instrument. Stoichiometry of the samples was examined by X-ray photoelectron spectrometry using an SPECS instrument equipped with an Mg-K $\alpha$  source ( $\lambda=1254$  eV) and a PHOIBIS 150 hemispherical analyzer. The results were interpreted by SDP 4.1 software. The binding energy of the C(1s) peak was set to 285.0 eV as a reference. Photocatalytic activity of the layers was evaluated according to the procedure explained in chapter 3.

### **11.3. Results and discussion**

#### **11.3.1. Microstructural studies**

##### *11.3.1.1. Rutile TiO<sub>2</sub>/m-sapphire heterostructure*

Fig.11.2a shows a log-scale  $\theta$ - $2\theta$  pattern acquired from the rutile TiO<sub>2</sub> thin film deposited on *m*-sapphire substrate (Al<sub>2</sub>O<sub>3</sub>(10 $\bar{1}$ 0)) where the growth of epitaxial or highly textured rutile TiO<sub>2</sub> along its *c*-axis is clearly evident. Prior to the  $\theta$ - $2\theta$  scan, the sample was aligned with the surface normal of Al<sub>2</sub>O<sub>3</sub>(30 $\bar{3}$ 0) reflection along the diffractometer  $\varphi$ -axis within 0.01°. Rocking curves through the TiO<sub>2</sub>(002) reflection for different  $\varphi$  positions (Fig.11.2b) reveal that TiO<sub>2</sub>(001) planes are almost parallel to Al<sub>2</sub>O<sub>3</sub>(10 $\bar{1}$ 0) planes with a tilt of about 0.15° in one direction. Laser reflection from the

substrate surface showed a  $0.26^\circ$  miscut. The observed tilt in the rutile film originates from a small deviation between the actual normal of the substrate surface and  $\text{Al}_2\text{O}_3[10\bar{1}0]$  orientation.

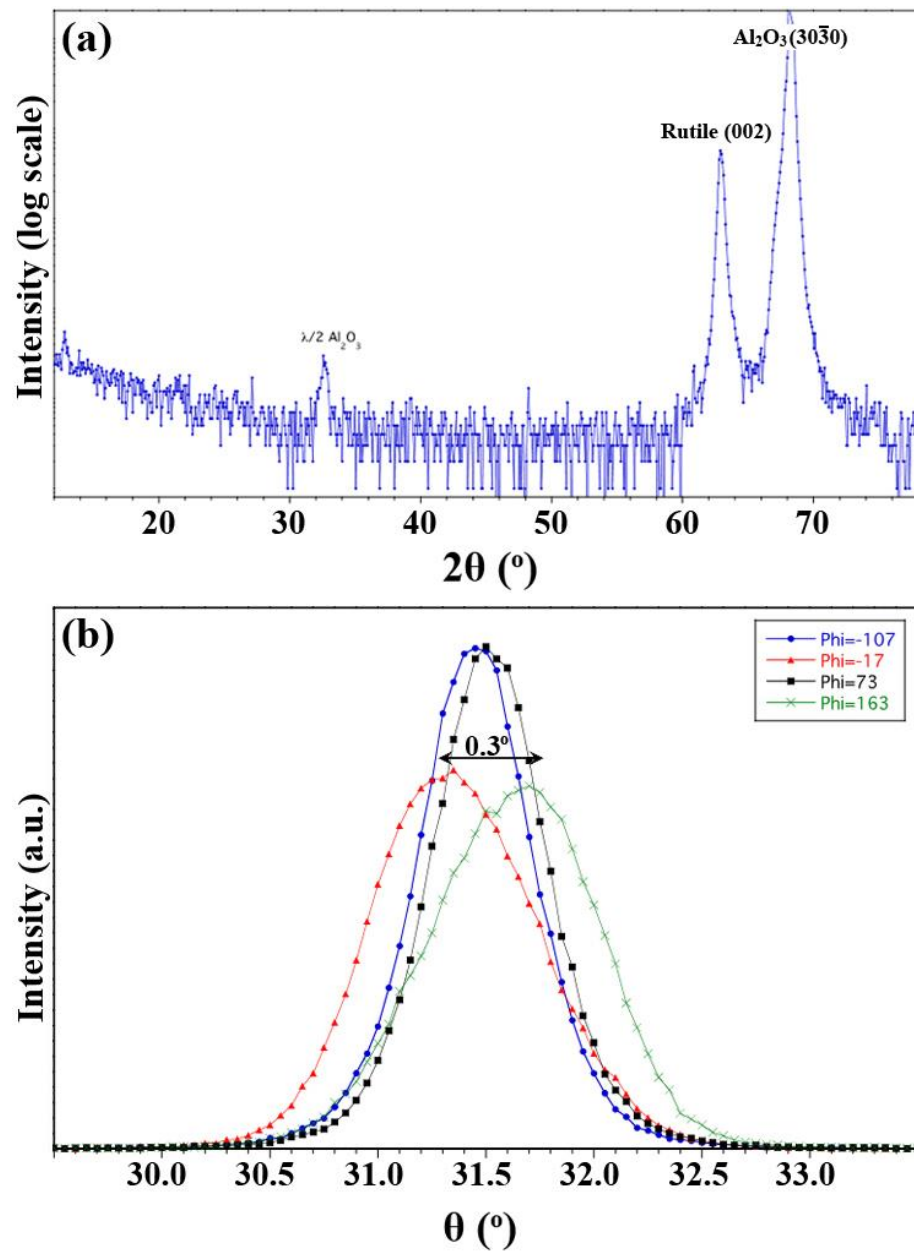


Fig.11.2. (a)  $\theta$ - $2\theta$  pattern acquired from the rutile  $\text{TiO}_2(001)/\text{Al}_2\text{O}_3(10\bar{1}0)$  heterostructure and (b) Rocking curves taken from (002) reflection of rutile  $\text{TiO}_2$  using several  $\varphi$ -angles.

To confirm the epitaxial growth and determine the in-plane alignment between the rutile thin film and the sapphire substrate,  $\varphi$ -scan XRD was conducted on (101) reflection of rutile at  $2\theta=36.1^\circ$  and  $\psi=32.8^\circ$  and (10 $\bar{1}$ 4) reflection of alumina at  $2\theta=35.13^\circ$  and  $\psi=51.77^\circ$  and the corresponding results are depicted in Fig.11.3.

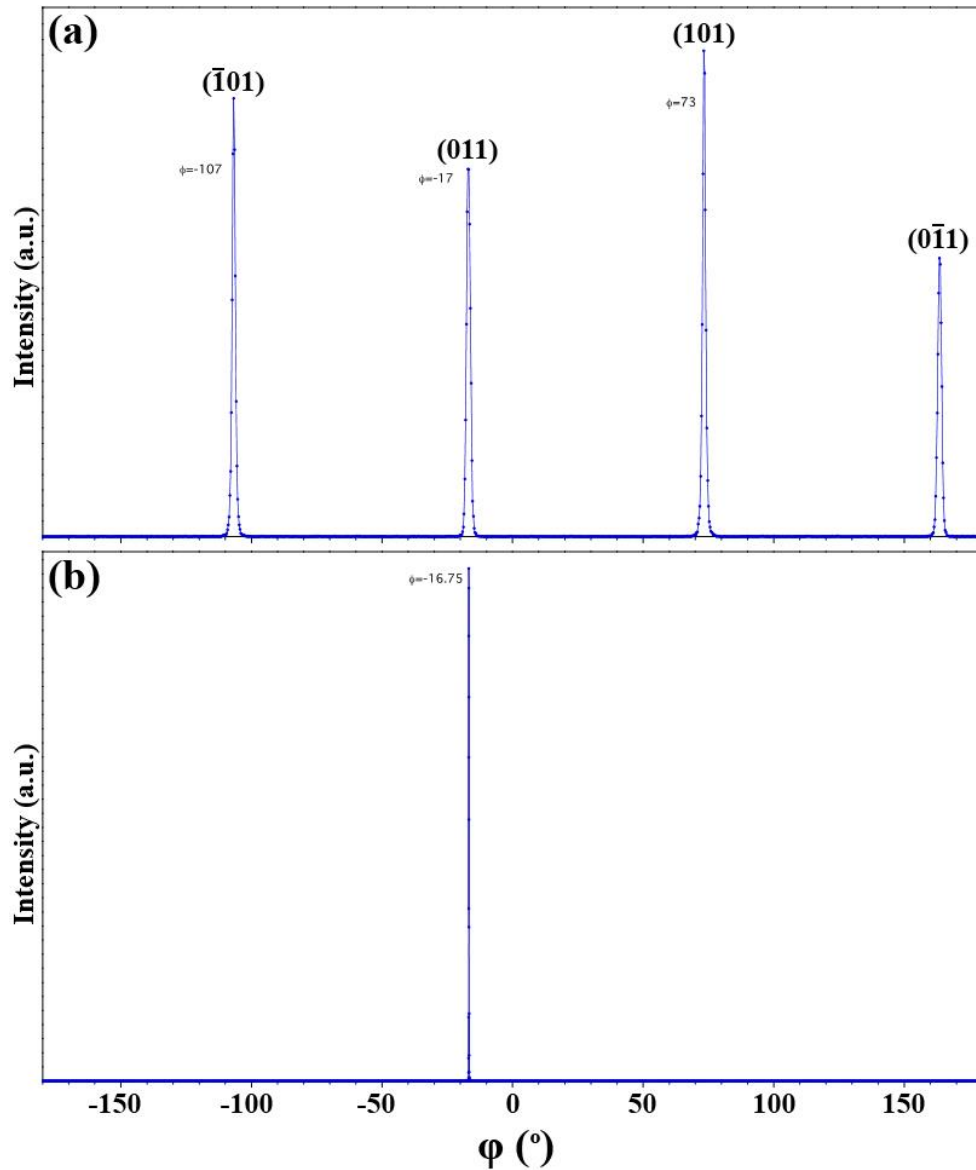


Fig.11.3. Results of  $\varphi$ -scan XRD performed on rutile  $\text{TiO}_2(001)/\text{Al}_2\text{O}_3(10\bar{1}0)$  heterostructure:  
 (a) Rutile(101) reflection and (b) Alumina(10 $\bar{1}$ 4) reflection.

The reason why only a single  $\varphi$ -peak from  $\text{Al}_2\text{O}_3(10\bar{1}4)$  is seen is that the trigonal (R3c) symmetry of the alumina crystal means that the  $(10\bar{1}\bar{4})$  reflection is absent. However, rutile  $\text{TiO}_2$  has 4-fold symmetry about its [001] axis, so 4 strong  $\varphi$ -peaks from nominally identical  $(\bar{1}01)$ ,  $(011)$ ,  $(101)$ , and  $(0\bar{1}1)$  reflections with azimuthal separations of  $90^\circ$  are observed.

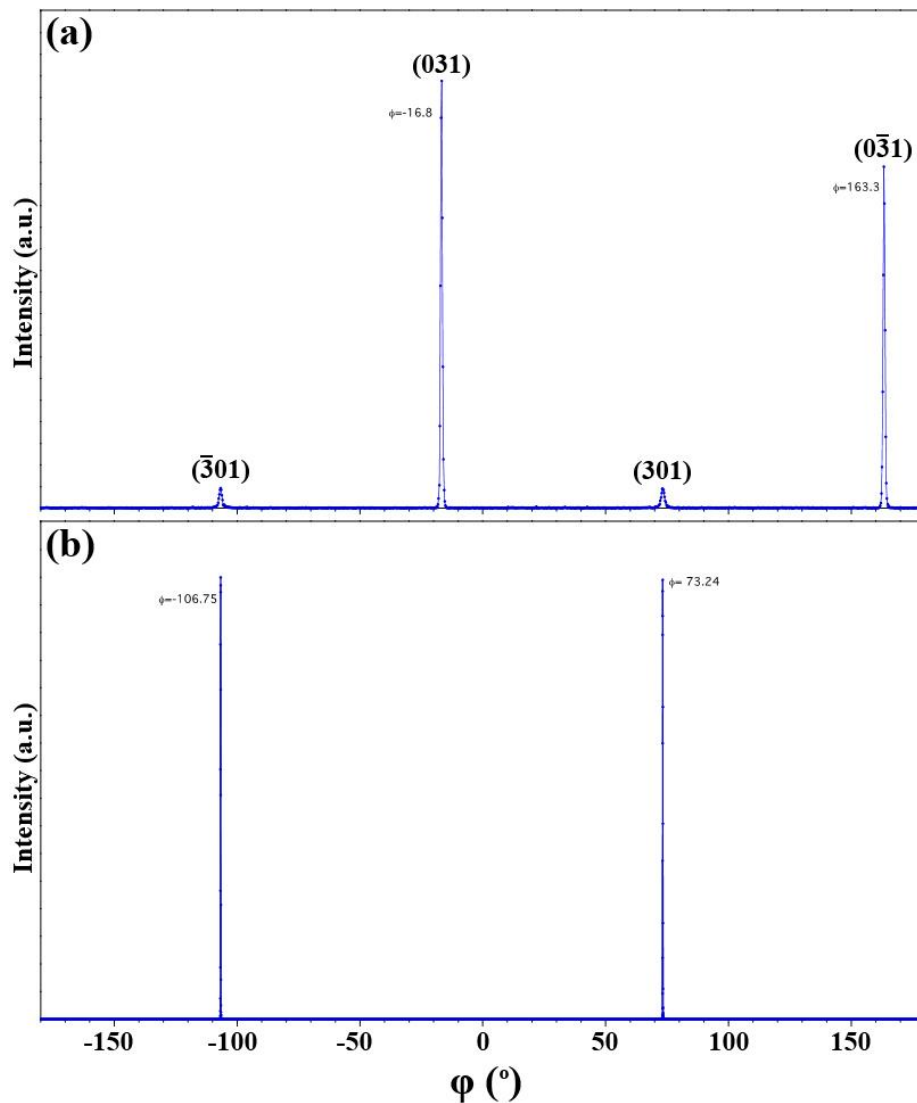


Fig.11.4. Results of  $\varphi$ -scan XRD performed on rutile  $\text{TiO}_2(001)/\text{Al}_2\text{O}_3(10\bar{1}0)$  heterostructure:  
 (a) Rutile(301) reflection and (b) Alumina(033̄0) reflection.

Taking this information into consideration, the epitaxial relationship across the rutile  $\text{TiO}_2/m$ -sapphire interface is established as  $[100](001)_{\text{rutile}}||[0001](10\bar{1}0)_{\text{alumina}}$  and  $[100]_{\text{rutile}}||[\bar{1}2\bar{1}0]_{\text{alumina}}$ . We also performed  $\varphi$ -scan XRD on rutile (301) plane at  $2\theta=69.4^\circ$  and  $\psi=62.6^\circ$  and (03 $\bar{3}$ 0) plane of alumina at  $2\theta=68.26^\circ$  and  $\psi=60.0^\circ$ . The results, presented in Fig.11.4, shows a  $0^\circ$  and  $90^\circ$  in-plane rotation of  $\text{TiO}_2(301)$  with respect to  $\text{Al}_2\text{O}_3(03\bar{3}0)$  which is in agreement with the established epitaxial relationship. The reason why (301) and (301) reflections from rutile  $\text{TiO}_2$  have much lower intensity than (031) and (0 $\bar{3}$ 1) reflections is that the presence of a biaxial strain in the film shifts the positions of the diffraction peaks. As will be explained later, the two orthogonal  $\text{TiO}_2$  in-plane directions have different lattice parameters, i.e.  $[100]\neq[010]$ . To acquire the  $\varphi$ -scan pattern shown in Fig.11.4, the diffractometer was aligned using the  $2\theta$  value of the (031) plane rather than the (301) plane; therefore,  $\varphi$ -peaks from the (301) reflections have a weaker intensity. The stereographic projection (Fig.11.5) shows the alignment between other planes of rutile and  $m$ -sapphire.

Based on the domain matching epitaxy paradigm,<sup>12</sup> the misfit strain along the [100] axis of rutile is calculated to be  $1 - \frac{4.59}{4.76} = +3.57\%$  which can be accommodated by almost perfect matching of 28 planes of film with 27 planes of substrate. Along the [010] axis of rutile, 17/18 and 18/19 matching domains alternate with a frequency factor of about 0.36 to relax the -5.76% misfit strain ( $1 - \frac{4.59}{4.34}$ ). For the sake of clarification, 4.34 Å is the distance between two neighboring oxygen anions on the  $\text{Al}_2\text{O}_3(10\bar{1}0)$  plane running along [0001] direction. Fig.11.6a shows a low magnification

cross section TEM micrograph taken from the rutile(001)/sapphire( $10\bar{1}0$ ) heterostructure.

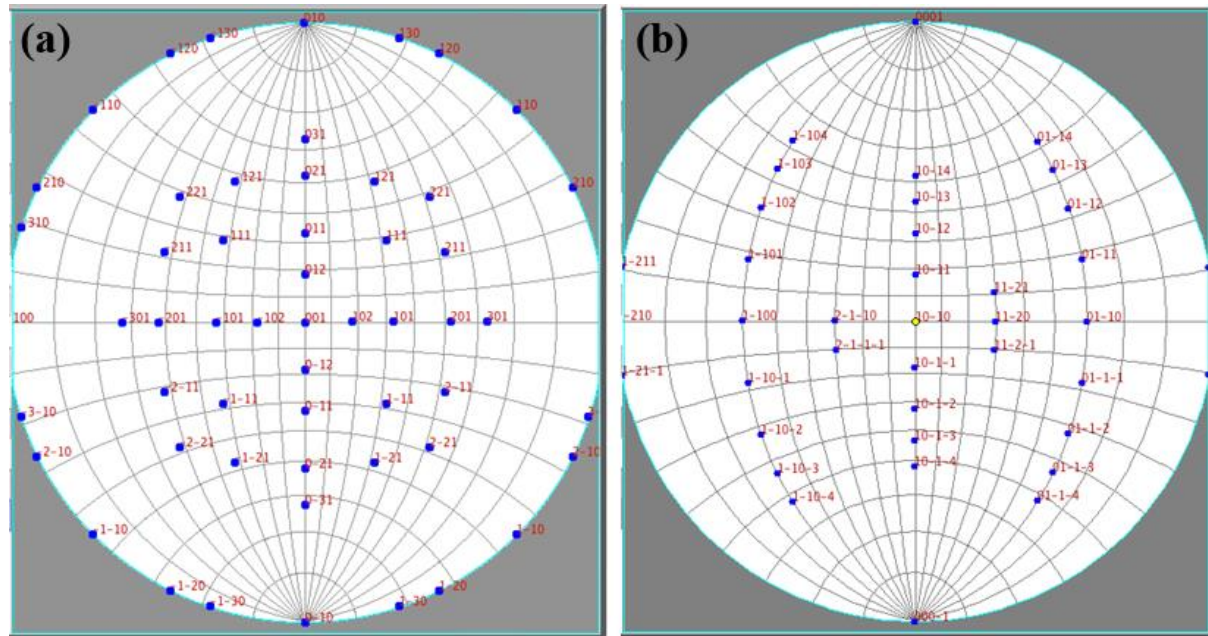


Fig.11.5. Stereographic projection showing: (a) Rutile  $\text{TiO}_2(001)$  and (b)  $\text{Al}_2\text{O}_3(10\bar{1}0)$  poles.

The indexed selected area electron diffraction (SAED) pattern, displayed in the inset of Fig.11.6a, confirms the proposed epitaxial relationship. The pattern belongs to the [100] and [0001] zones of rutile and sapphire, respectively. A high resolution image acquired from the  $\text{TiO}_2/\text{Al}_2\text{O}_3$  interface is displayed in Fig.11.6b where formation of an atomically sharp interface and absence of any interfacial reaction are evident. Besides, alternation of 19/18 and 18/17 domains to relax the lattice misfit strain is observed in the inverse fast Fourier transform (FFT) image which is shown in the inset of Fig.11.6b. Please note that the FFT image has been rotated and its orientation does match with the high resolution image.

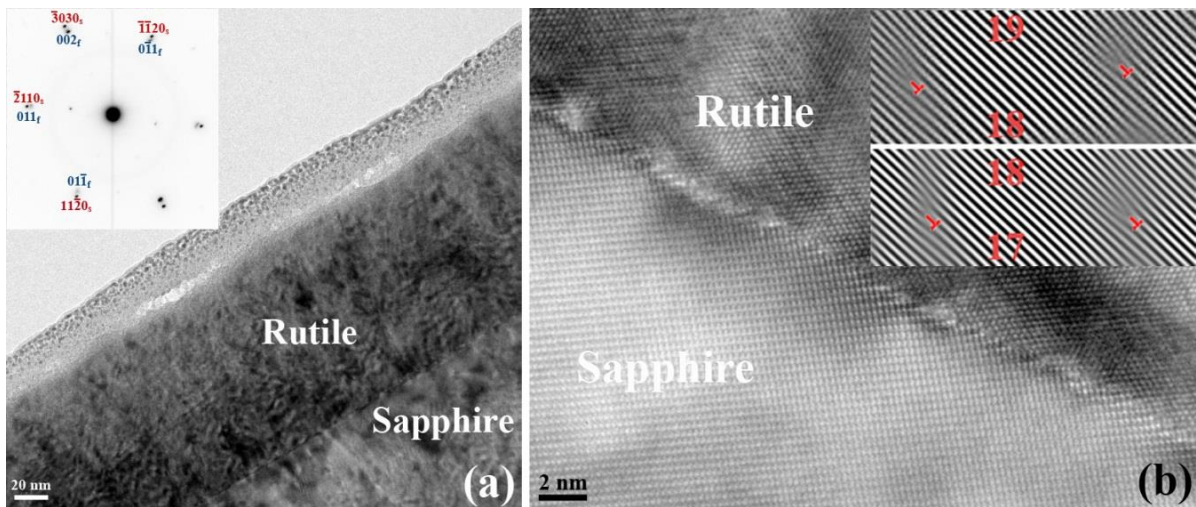


Fig.11.6. (a) Cross section TEM micrograph and indexed SAED pattern acquired from rutile/*m*-sapphire heterostructure. The SAED pattern belongs to rutile[100] and sapphire[0001] zones, (b) High resolution TEM image from the rutile/*m*-sapphire interface. Alternation of 19/18 and 18/17 domains across the film/substrate interface is shown in the inset.

High resolution  $\theta$ - $2\theta$  scans were obtained from (002), (111), (301), and (101) planes of rutile  $\text{TiO}_2$  in order to calculate the residual strain along several orientations of the film, and the resulting lattice parameters are shown in Fig.11.7 and Tab.11.1.

Tab.11.1. Interplanar spacing for several family of planes of rutile(001)/*m*-sapphire heterostructure obtained from high resolution  $\theta$ - $2\theta$  scans (Fig.11.7).

Plane	Measured ( $\text{\AA}$ )	Calculated ( $\text{\AA}$ )	Strain
002	1.4770	1.4796	-0.0018
111	2.1874	2.1874	0.0000
$\bar{3}01$	1.3679	1.3599	+0.0059
031	1.3545	1.3599	-0.0039
101	2.4907	2.4876	+0.0012
011	2.4812	2.4876	-0.0026

Lattice parameters of the rutile thin film are calculated to be  $a=4.630 \text{ \AA}$ ,  $b=4.573 \text{ \AA}$ , and  $c=2.954 \text{ \AA}$ . Comparing these values with those of bulk rutile  $\text{TiO}_2$  (JCPDS 21-1276:  $a=b=4.5933 \text{ \AA}$  and  $c=2.9592 \text{ \AA}$ ), the residual strains along  $a$ ,  $b$ , and  $c$  axes of rutile are obtained as 0.80% (expansion), 0.45% (contraction), and 0.18% (contraction), respectively. Even though bulk rutile, with its tetragonal unit cell, has equivalent symmetries and structures along its [100] and [010] directions, different symmetries along the [0001] and [ $\bar{1}2\bar{1}0$ ] orientations of  $m$ -sapphire substrate leads to a biaxial strain condition in the rutile  $\text{TiO}_2$  thin film.

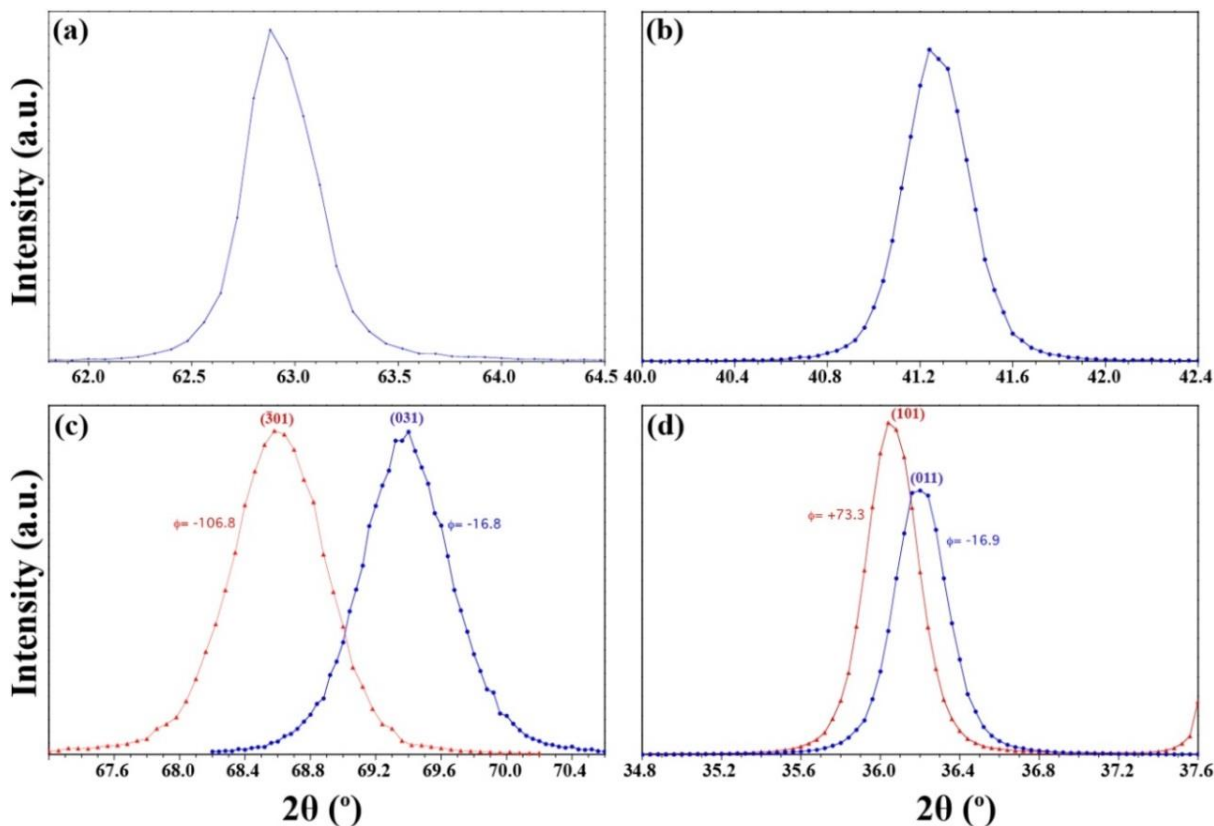


Fig.11.7. High resolution  $\theta$ - $2\theta$  scans through: (a)  $\text{TiO}_2(002)$ , (b)  $\text{TiO}_2(111)$ , (c)  $\text{TiO}_2(301)$ , and (d)  $\text{TiO}_2(101)$  faces of rutile epilayer deposited on  $\text{Al}_2\text{O}_3(10\bar{1}0)$  substrate.

Thermal strains, which appear after cooling from the growth temperature down to the room temperature, are different along different orientations of sapphire due to the different thermal expansion coefficients. In the absence of dislocation relaxation, the thermal strain can be calculated via the following equation:<sup>13</sup>

$$\epsilon_T = (T_{\text{growth}} - \text{Room Temperature}) \times (\alpha_{\text{film}} - \alpha_{\text{substrate}}) \quad (11-1)$$

where  $\alpha$  is the thermal expansion coefficient. The thermal expansion coefficient of rutile along its [100] direction is about  $6.99 \times 10^{-6} \text{ K}^{-1}$ .<sup>14</sup> The thermal expansion coefficient of alumina equals  $5.3 \times 10^{-6}$  and  $4.5 \times 10^{-6} \text{ K}^{-1}$  for the directions parallel and perpendicular to the *c*-direction, respectively. With this information, the thermal strain is calculated to be 0.18% along the *a*-axis and 0.12% along the *b*-axis of rutile. The thermal strains are small, but very difficult to relax. In fact, managing the thermal strains in thin film heterostructures has been one of the scientific challenges for technological applications. Smaller strains are more difficult to relax, since the critical thickness beyond which the system (thin layer) can, from a thermodynamic point of view, accommodate misfit dislocations becomes larger; as such, the dislocations, which nucleate at the free surface of the growing film, cannot reach the film/substrate interface to relax the strain due to the large glide distance, i.e. the distance between the free surface of the film and the film/substrate interface. This issue is more critical in the highly ionic materials such as TiO<sub>2</sub> because of large lattice friction stress needed for dislocation glide. In contrast, in large misfit systems, the critical thickness is in an order

of a couple of monolayers through which misfit dislocations are able to glide and reach the interface easily. Ease of dislocation glide is also governed by the slip systems of the material; however, the slip systems are not determined within the first couple of monolayers of the material, so the dislocations can approach the interface even if the primary slip system is not active due to the growth direction of the film. Another reason for the different strains along [100] and [010] axes of the rutile epilayer is the miscut on the substrate surface. Surface miscut leads to surface steps with a spacing of  $L=d/\theta$  where  $d$  and  $\theta$  are step height and the projected angle in radians, respectively. Dislocation nucleation is easier in one direction, i.e. the miscut direction.

From the unrelaxed residual strains along orthogonal orientations of the rutile unit cell and assuming isotropic characteristics, Poisson's ratio ( $\nu$ ) can be obtained as following:<sup>13</sup>

$$\varepsilon_{zz} = \frac{-2\nu}{1-\nu} \times (\varepsilon_{xx} + \varepsilon_{yy}) \quad (11-2)$$

where  $\varepsilon_{zz}$  is the strain along the out-of-plane orientation of the rutile film and  $\varepsilon_{xx}$  and  $\varepsilon_{yy}$  are the in-plane strains. The Poisson's ratio is obtained as 0.22 for the rutile TiO<sub>2</sub> epilayer deposited on *m*-sapphire substrate. It is worth mentioning that the Poisson's ratio equals 0.28 for bulk rutile TiO<sub>2</sub>.<sup>15</sup> The lattice misfit stress in the rutile TiO<sub>2</sub> epilayer was calculated by the following formula:

$$\sigma_{xx(yy)} = \frac{2\mu(1+\nu)}{1-\nu} \times \varepsilon_{xx(yy)} \quad (11-3)$$

where  $\sigma_{xx(yy)}$  and  $\varepsilon_{xx(yy)}$  are the stress and strain along the  $x(y)$ -direction,  $\mu$  represents the shear modulus (118 GPa for rutile  $TiO_2^{16}$ ), and  $\nu$  is the Poisson's ratio. The lattice misfit stresses are calculated to be  $\sigma_a = 13.29$  GPa and  $\sigma_b = -21.44$  GPa. It should be mentioned that the stress along the  $c$ -axis of rutile (out-of-plane orientation) is zero, although the strain does not equal zero. For a dislocation to be able to glide, the critical resolved shear stress ( $\tau_r = \sigma \times \cos\varphi \times \cos\lambda$ , where  $\varphi$  is the angle between normal of the slip plane and stress ( $\sigma$ ) direction and  $\lambda$  is the angle between the slip direction and direction of the stress ( $\sigma$ )) has to be larger than the yield stress of the material. The yield stress of rutile  $TiO_2$  is considered to be about 3.0 GPa.<sup>17</sup> The primary slip system in rutile  $TiO_2$  has been found to be  $\frac{1}{2}\langle\bar{1}01\rangle\{101\}$ .<sup>7</sup> Taking the  $[10\bar{1}](101)$  slip system as an example, as is shown Fig.11.8,  $\cos\varphi \times \cos\lambda$  is calculated to be about 0.453 for  $\sigma_a$  and zero for  $\sigma_b$ . Thus,  $\tau_r$  is obtained as 6.02 GPa for the stress along the  $a$ -axis. Similar calculations can be done for the  $[01\bar{1}](011)$  slip system. In this case,  $\cos\varphi \times \cos\lambda$  is obtained as zero and about 0.455 for  $\sigma_a$  and  $\sigma_b$ , respectively. With this information,  $\tau_r$  is obtained as -9.76 GPa for the stress along the  $b$ -axis. As is seen, in both cases, the critical resolved shear stress is larger than the yield stress of rutile  $TiO_2$ ; consequently, the misfit dislocations nucleating onto the free surface of the growing rutile epilayer should be able to glide and reach the film/substrate interface to fully relax the misfit strain. Hence, the lattice misfit strains get fully relaxed.

The lattice misfit strain along the  $b$ -axis relaxes more easily. The compressive strains are easier to relax, as nucleation of the misfit dislocations is easier under the compressive conditions.<sup>18</sup> Dislocation nucleation/glide phenomena are followed by the

formation of surface steps. The step formation energy can be negative, giving rise to a decrease in the surface energy, if the dislocation relaxes a compressive stress, while it is always positive if the dislocation relaxes a tensile stress.<sup>18</sup>

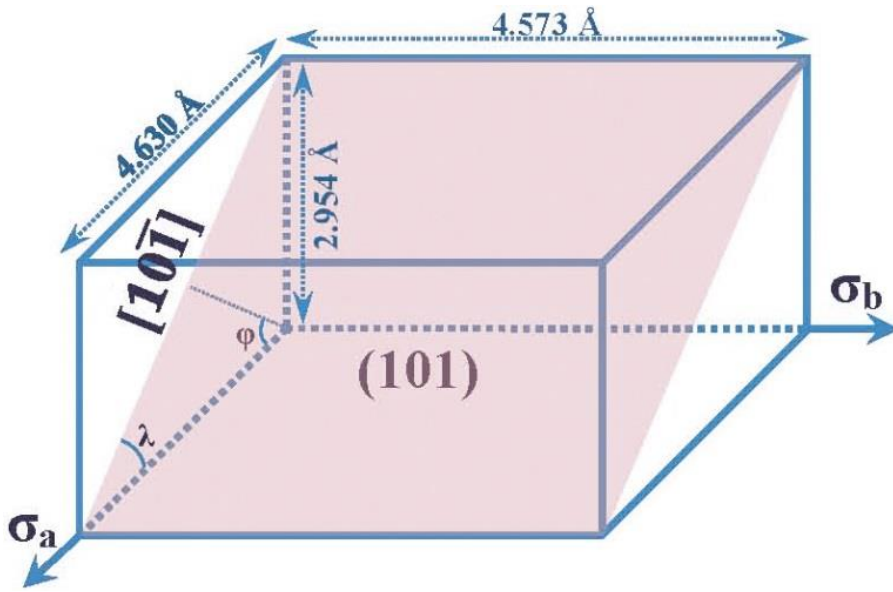


Fig.11.8. Schematic illustration of the rutile TiO<sub>2</sub> unit cell and the  $\frac{1}{2}[10\bar{1}](101)$  slip system.

Under compressive strain conditions, the step formation process decreases the number of dangling bonds and, therefore, the surface energy. On the other hand, the number of surface dangling bonds increases when the strain is tensile. To relax a tensile strain, one extra half plane, i.e. misfit dislocation, needs to be inserted in the lattice; hence, one extra row of dangling bonds is added to the surface. However, one atomic plane and one row of dangling bonds are missing when a compressive strain relaxes.<sup>19</sup> As was explained earlier, the misfit strain is tensile along the *a*-axis and compressive along the *b*-axis of rutile, so the misfit strain along the *b*-axis is relaxed more easily.

### 11.3.1.2. Rutile $TiO_2$ /r-sapphire heterostructure

A  $\theta$ - $2\theta$  XRD scan was performed to study the out-of-plane alignment for the rutile  $TiO_2$  thin film grown on an *r*-sapphire substrate ( $Al_2O_3(01\bar{1}2)$ ). The result is displayed in Fig.11.9a which confirms the growth of rutile  $TiO_2$  with its  $(101)$  planes parallel to the surface on *r*-cut sapphire.

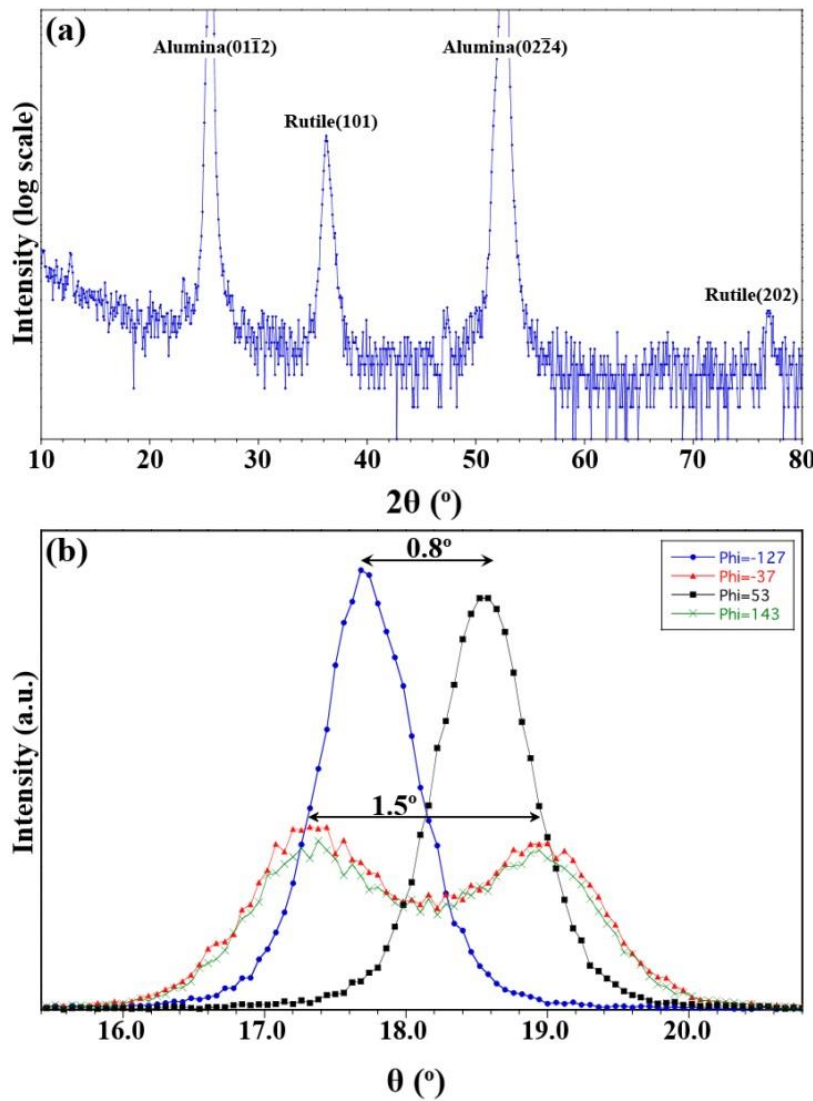


Fig.11.9. (a)  $\theta$ - $2\theta$  pattern of the rutile  $TiO_2(101)/Al_2O_3(01\bar{1}2)$  heterostructure and (b) Rocking curve taken from  $(101)$  reflection of rutile  $TiO_2$  along different  $\varphi$ -angles.

Fig.11.9b shows rocking curves conducted on the  $\text{TiO}_2$  (101) peak using several orthogonal  $\varphi$ -angles. As is seen, the  $\text{TiO}_2$ (101) planes are not exactly parallel to  $\text{Al}_2\text{O}_3(01\bar{1}2)$  planes and there is a small tilt ( $\sim 0.4^\circ$ ) in one direction as well as a peak splitting ( $\pm 0.75^\circ$ ) into two orientations in the orthogonal directions. This tilting will be shown in a later stereographic projection. Laser reflection measurement from the sample surface showed a miscut of  $0.12^\circ$  of the substrate surface.

In order to confirm the epitaxial growth and determine the in-plane alignment between the  $\text{TiO}_2$ (101) thin film and the *r*-sapphire substrate,  $\varphi$ -scan XRD was carried out on several reflections. The results are depicted in Fig.11.10. With the information obtained from  $\varphi$ -patterns, the epitaxial relationship across the film/sapphire interface is determined to be  $(101)_{\text{rutile}} \parallel (01\bar{1}2)_{\text{alumina}}$  and  $[010]_{\text{rutile}} \parallel [2\bar{1}\bar{1}0]_{\text{alumina}}$ . The stereographic projection of  $\text{TiO}_2[101]$  and  $\text{Al}_2\text{O}_3[01\bar{1}2]$  poles (Fig.11.11) shows the angular relation between other directions of the rutile epilayer and the sapphire substrate. In particular, the approximate position of the orthogonal *a* and *c* axes of the rutile tetragonal unit cell with respect to the substrate unit cell are as follows:  $[100]_{\text{rutile}} \parallel [0001]_{\text{alumina}}$  and  $[001]_{\text{rutile}} \parallel [01\bar{1}0]_{\text{alumina}}$ . As discussed earlier, there is a small tilt in the rutile thin film with respect to the substrate giving rise to  $\text{TiO}_2$  peak orientation splitting. The inset of Fig.11.11 displays the enlarged stereographic projection. The  $\text{TiO}_2$ (101) peak is actually a split peak shown by the two red circles. From the  $\text{TiO}_2$ (101) rocking curves shown in Fig.11.9b, the horizontal tilt is  $\sim 0.4^\circ$  and the vertical splitting is  $\sim \pm 0.75^\circ$ . Therefore, there are some small deviations in the actual epitaxial relationships from the nominal alignments described above.

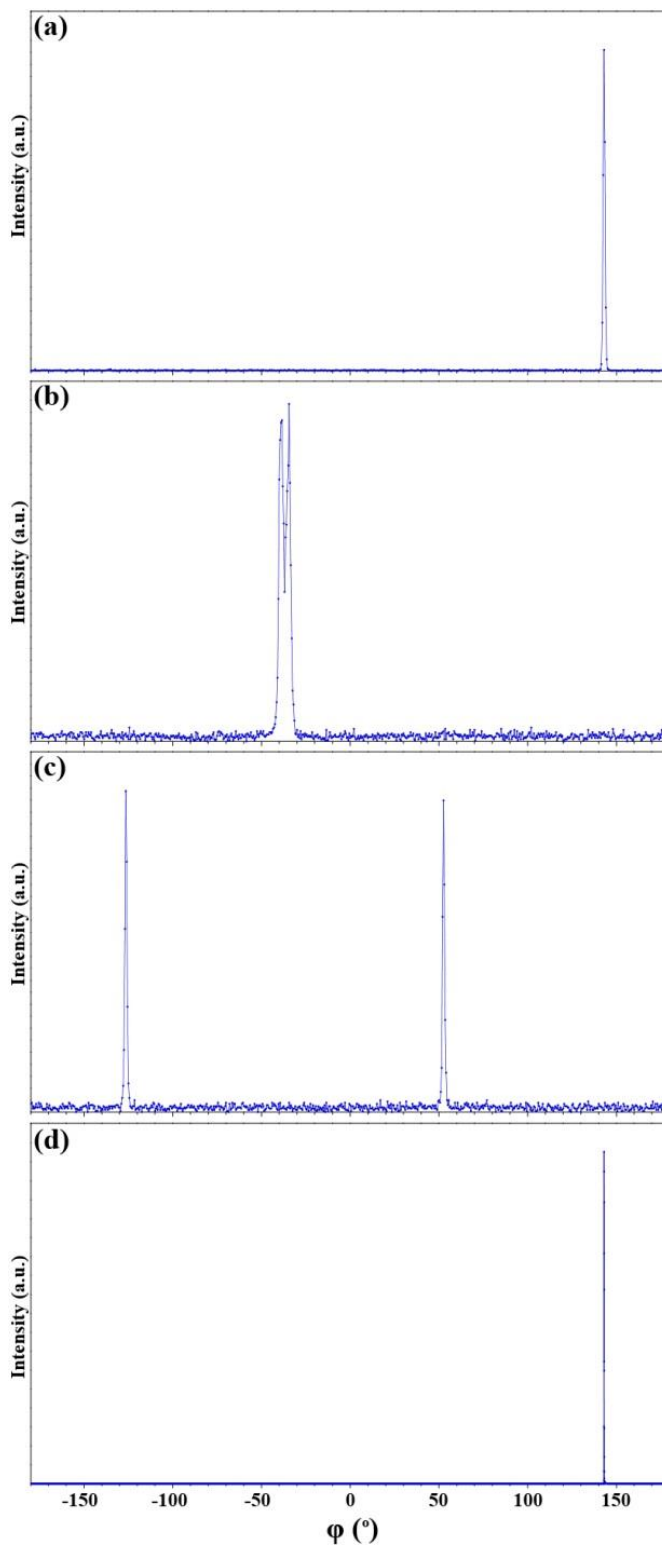


Fig.11.10.  $\varphi$ -scan patterns taken from rutile  $\text{TiO}_2(101)/\text{Al}_2\text{O}_3(01\bar{1}2)$  heterostructure: (a) Rutile(200), (b) Rutile(002), (c) Rutile(121), and (d) Alumina(0006) reflections.

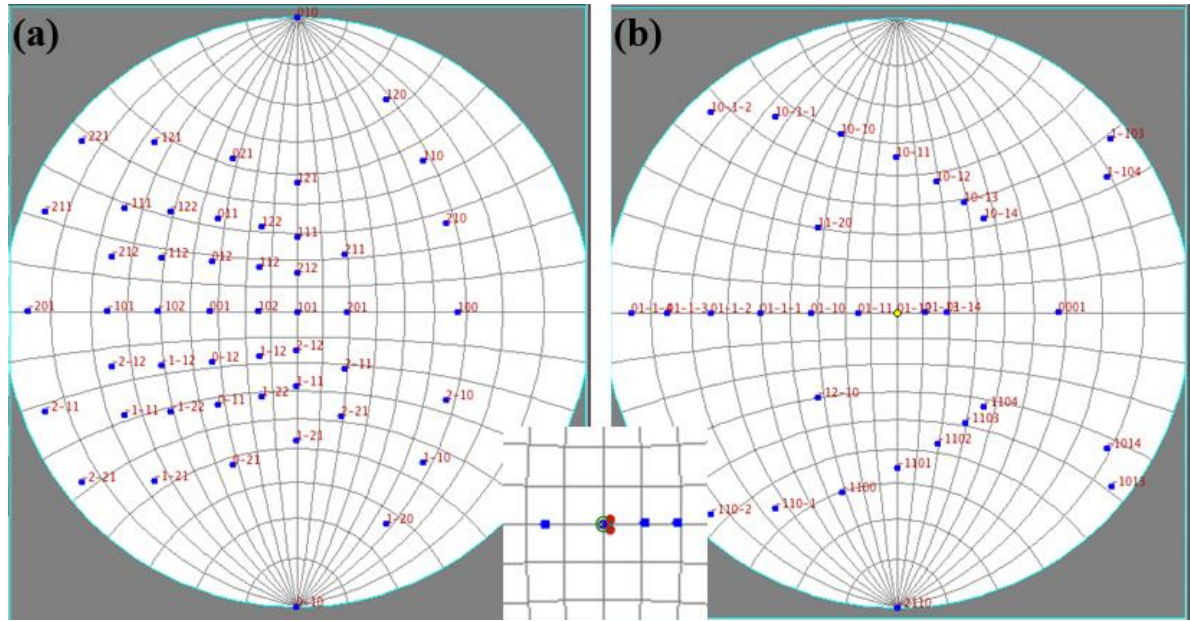


Fig.11.11. Stereographic projection showing: (a) Rutile TiO<sub>2</sub>(101) and (b) Al<sub>2</sub>O<sub>3</sub>(011̄2) poles.

The misfit strain along the *b*-axis of rutile is calculated to be  $1 - \frac{4.59}{4.76} = +3.75\%$  which is relaxed through a perfect matching of 28 planes of TiO<sub>2</sub> with 27 planes of sapphire. The in-plane direction perpendicular to the *b*-axis of rutile on the (101) face, is [1̄01]. The misfit strain along this direction is calculated as  $1 - \frac{5.46}{5.13} = -6.43\%$  which is accommodated by alternation of 15/16 and 16/17 domains with a frequency factor of about 0.54. A cross-section TEM image as well as the indexed SAED pattern taken from the rutile(101)/*r*-sapphire heterostructure is depicted in Fig.11.12a where the established epitaxial alignment between the rutile TiO<sub>2</sub> thin film and the *r*-sapphire substrate is ascertained. The high resolution TEM micrograph, shown in Fig.11.12b, reveals formation of a sharp interface with no evidence of chemical reaction. Meanwhile, the arrangement of misfit dislocations across the film/substrate interface to

fully relax the lattice misfit strain is evident in the inset of Fig.11.12b. As is seen, 28 planes of rutile match with 27 planes of sapphire to accommodate the misfit strain. It should be mentioned that the inverse FFT image has been rotated and has different orientation with respect to the high resolution image of the interface.

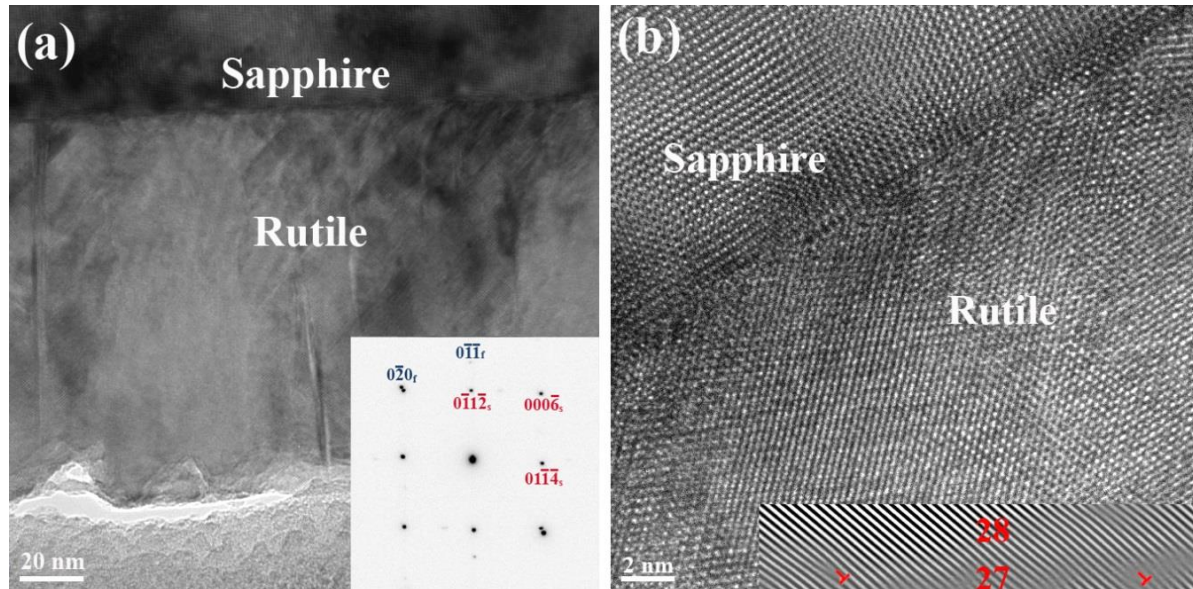


Fig.11.12. (a) Cross section TEM image taken from rutile/r-sapphire heterostructure. The inset shows the indexed SAED pattern belonging to typical rutile[100] and sapphire[2 $\bar{1}$  $\bar{1}$ 0] zones, (b) High resolution micrograph of the rutile/r-sapphire interface. Matching of 28 planes of rutile with 27 planes of sapphire to accommodate the lattice misfit strain is evident in the inset.

To calculate the lattice parameters and the residual strain along several directions in the rutile  $TiO_2$  epilayer, high resolution  $\theta$ - $2\theta$  scans were obtained from (101), (002), and (121) planes of rutile. Results are shown in Fig.11.13 and Tab.11.2. The lattice parameters obtained are  $a=4.590 \text{ \AA}$ ,  $b=4.617 \text{ \AA}$ , and  $c=2.950 \text{ \AA}$ . Compared with bulk rutile  $TiO_2$ , the film residual strains are generally small, with contraction in the out-of-

plane surface normal as well as in the in-plane  $[\bar{1}01]$  direction, and expansion in the in-plane  $[010]$  direction. As is listed in Tab.11.2, the residual strains for  $(\bar{1}01)$  and  $(101)$  families of planes are about -0.20% and -0.28%, respectively. Moreover, the residual strain for the  $(020)$  family of planes is found to be about +0.51%. With these data and using eq.11.2, the Poisson's ratio is obtained as 0.3.

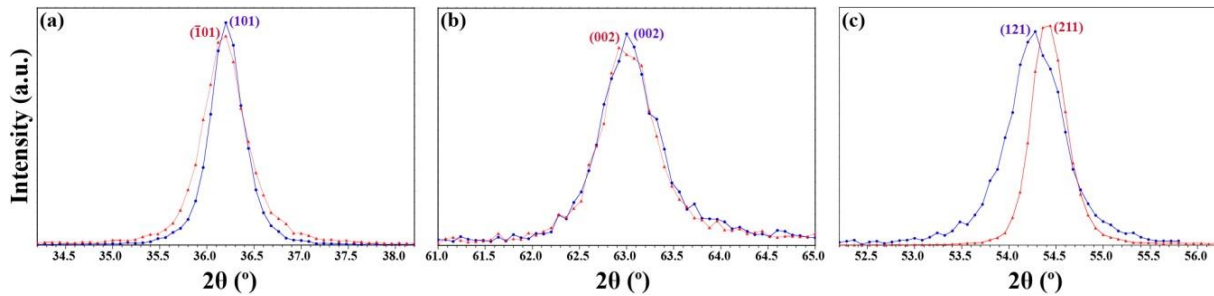


Fig.11.13. High resolution  $\theta$ - $2\theta$  scan obtained from: (a)  $\text{TiO}_2(101)$ , (b)  $\text{TiO}_2(002)$ , and (c)  $\text{TiO}_2(121)/(211)$  faces of rutile epilayer grown on  $\text{Al}_2\text{O}_3(01\bar{1}2)$  substrate.

Considering eq.11.3, the misfit stress for the  $(101)$  and  $(010)$  planes are calculated to be 15.78 and -28.42 GPa, respectively. Taking the  $\frac{1}{2}[01\bar{1}](011)$  slip system, the resolved shear stress for the  $[010]$  direction is obtained as -12.94 GPa which is compressive and larger than the yield stress of rutile; therefore, the misfit strain should fully relax. The resolved shear stress for the  $[\bar{1}01]$  direction is calculated to be about 4.41 GPa. This value is slightly larger than the yield stress. Hence, the residual strain has its origin in thermal and defect strains, as pointed out earlier.

There are three primary sources of strains during the growth of thin film heterostructures, namely lattice misfit strain, thermal misfit strain, and strains coming

from dopants, impurities, and defects. These strains are additive during thin film growth.<sup>13</sup> In view of the above analysis, the residual strain in the rutile epilayer is attributed primarily to the thermal strain and defect strain.

Tab.11.2. Interplanar spacing for several family of planes of rutile(101)/*r*-sapphire heterostructure obtained from high resolution  $\theta$ - $2\theta$  scans (Fig.11.13).

Plane	Measured ( $\text{\AA}$ )	Calculated ( $\text{\AA}$ )	Strain
101	2.481	2.4876	-0.0028
$\bar{1}01$	2.483	2.4876	-0.0020
200	2.295	2.2967	-0.0009
002	1.475	1.4796	-0.0030
121	1.690	1.6875	+0.0014
211	1.686	1.6875	-0.0009

### 11.3.1.3. Rutile $\text{TiO}_2/c$ -sapphire heterostructure

Fig.11.14 displays results of  $\theta$ - $2\theta$  XRD scan taken from the rutile  $\text{TiO}_2$  thin film deposited on a *c*-cut sapphire substrate. As was already shown by our group,<sup>20,21</sup> rutile grows along its [100] orientation on a sapphire(0001) platform. Rocking curves acquired from rutile(200) peak using different  $\varphi$ -angles show no tilt in the film. Therefore, it is found that the  $\text{TiO}_2$ (100) family of planes are quite parallel to the  $\text{Al}_2\text{O}_3$ (0001) planes. To determine the in-plane alignment between the  $\text{TiO}_2$  layer and the *c*-sapphire substrate, detailed  $\varphi$ -scan XRD was conducted on several reflections of

titania results of which are depicted in Fig.11.15. Fig.11.15a shows the  $\varphi$ -pattern from (110) planes of rutile where the diffractometer was set at  $2\theta=27.4^\circ$  and  $\psi=44.7^\circ$  prior to the data acquisition.

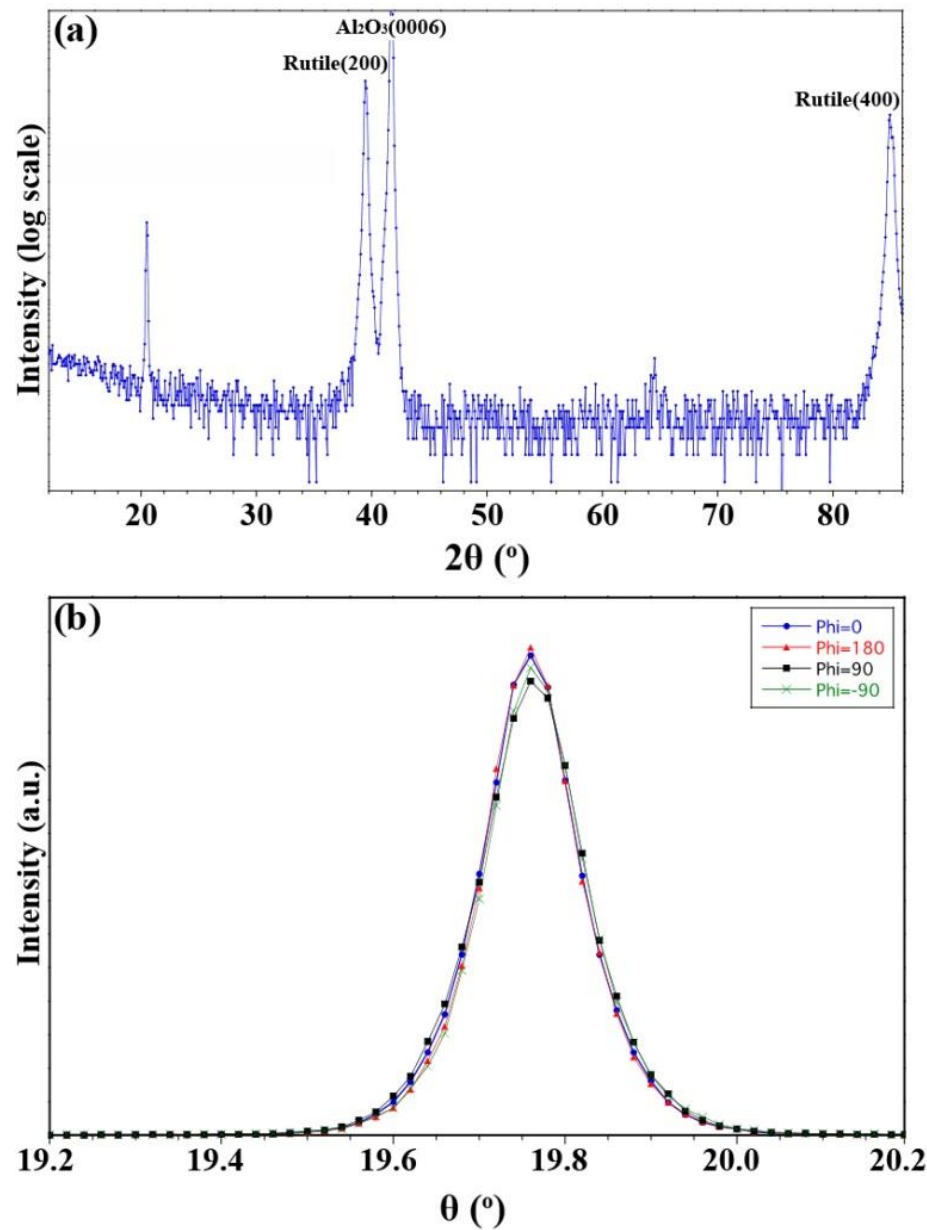


Fig.11.14. (a)  $0-2\theta$  pattern taken from the rutile  $\text{TiO}_2(001)/\text{Al}_2\text{O}_3(0001)$  heterostructure and (b) Rocking curve acquired from (200) reflection of rutile  $\text{TiO}_2$  along several  $\varphi$ -angles.

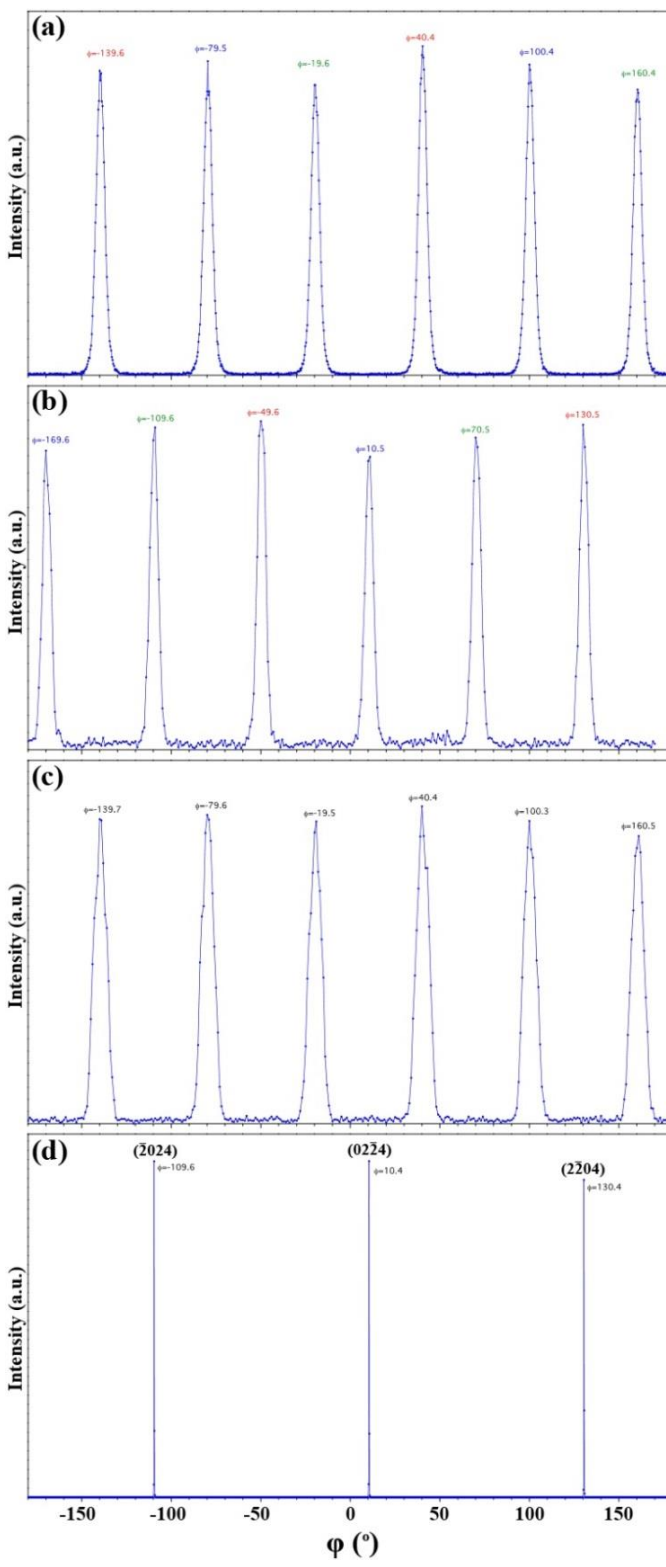


Fig.11.15. Results of  $\varphi$ -scan XRD from rutile  $\text{TiO}_2(001)/\text{Al}_2\text{O}_3(0001)$  heterostructure: (a) Rutile(110), (b) Rutile(101), (c) Rutile(111), and (d) Alumina(02 $\bar{2}$ 4) reflections.

The reason behind appearance of 6  $\varphi$ -peaks is the 2-fold symmetry in the rutile unit cell along its  $a$ -axis superposed on the 3-fold symmetry in the trigonal structure of the  $c$ -sapphire substrate. As is seen, the  $\varphi$ -signal from rutile(110) reflection rotates by 30° with respect to that of alumina(02 $\bar{2}$ 4) reflection. To record the  $\varphi$ -pattern from Al<sub>2</sub>O<sub>3</sub>(02 $\bar{2}$ 4) reflection, the diffractometer was aligned at  $2\theta=52.6^\circ$  and  $\psi=57.6^\circ$ . The epitaxial alignment between the rutile TiO<sub>2</sub> thin film and  $c$ -sapphire substrate is written as [001](100)<sub>rutile</sub>||[10 $\bar{1}$ 0](0001)<sub>alumina</sub>, plus the symmetry-equivalent domains; moreover,  $b$ -axis of rutile aligns with sapphire[1 $\bar{2}$ 10] direction.

Comparing the patterns presented in Fig.11.15 shows that the  $\varphi$ -peaks from {111} reflections are broader (Full width half maximum= ~8.1°) than those of the (110) or (101) peaks (FWHM= ~5.5°). The reason for this difference can be seen by examining the azimuthal alignments in the TiO<sub>2</sub> and Al<sub>2</sub>O<sub>3</sub> stereographic projections. Azimuthally, the TiO<sub>2</sub>(111) reflection is 32.8° from the TiO<sub>2</sub>(001) reflection, not 30°; or equivalently stated, TiO<sub>2</sub>(111) and TiO<sub>2</sub>(1 $\bar{1}$ 1) reflections should be azimuthally separated by 65.6°, not 60° in a  $\varphi$ -scan. We now assume that the film's in-plane orientation is driven by the azimuthal alignment of TiO<sub>2</sub>(001) and TiO<sub>2</sub>(010) planes with Al<sub>2</sub>O<sub>3</sub>(10 $\bar{1}$ 0) and (1 $\bar{2}$ 10) planes, i.e. the horizontal and vertical axes in the stereographic projections. Then, since the surface normal combines a twofold TiO<sub>2</sub>(100) axis with a threefold substrate(0001) axis, symmetry equivalent domains will be created corresponding to all ±60° rotations about the normal. The presence of these symmetry equivalent ±60° domains will azimuthally broaden the TiO<sub>2</sub>{111} reflections. Thus, our observation of larger FWHM widths in the {111}  $\varphi$ -scan confirms our assumption that epitaxy is driven by low-index

plane alignment at the interface. Alignment between other reflections can be determined from the stereographic projections in Fig.11.16.

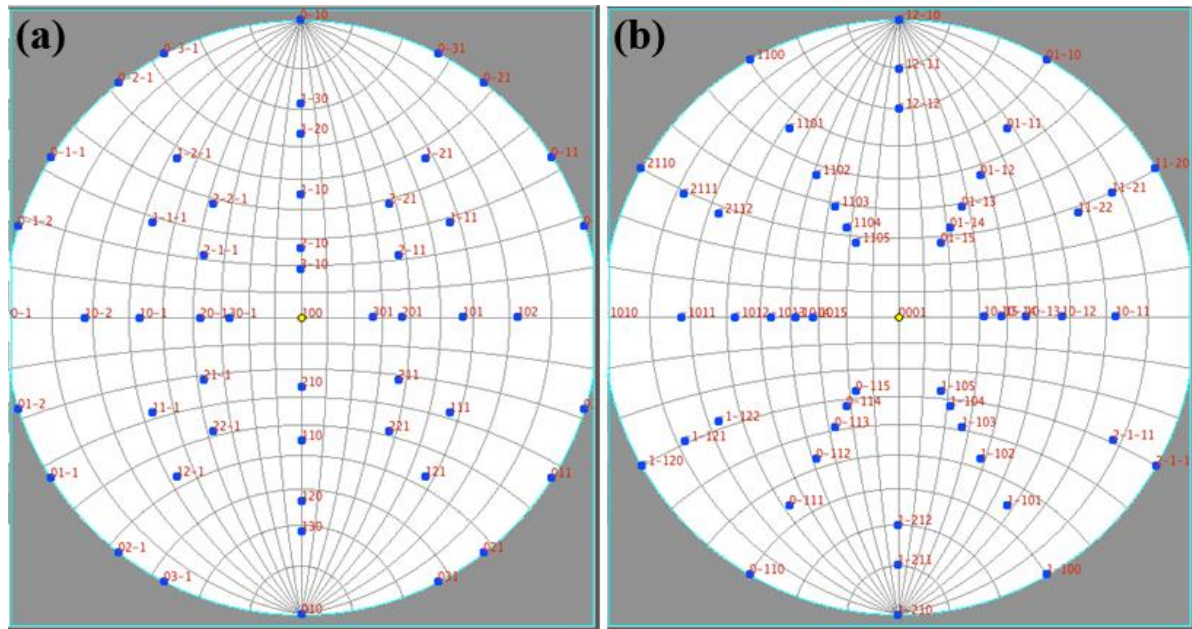


Fig.11.16. Stereographic projection showing: (a) Rutile  $\text{TiO}_2(100)$  and (b)  $\text{Al}_2\text{O}_3(0001)$  poles.

It was already revealed by our group<sup>11</sup> that the rutile film initially grows pseudomorphically on *c*-sapphire as  $Ti_2O_3$  and, after reaching the critical thickness, it grows tetragonally on the  $Ti_2O_3$ /sapphire platform. Formation of the  $Ti_2O_3$  pseudomorphic layer originates from the symmetry and chemistry mismatch between the tetragonal structure of  $TiO_2$  and trigonal structure of  $Al_2O_3$ . More details on thin film epitaxy in the rutile  $TiO_2(100)/c$ -sapphire heterostructure can be found in our previous works.<sup>10,11</sup> The lattice misfits across the film/substrate interface are calculated to be +3.57% and +28.15% along the [010] and [001] directions of the rutile film. The misfit along the *b*-axis is accommodated by matching of 28 planes of the film with 27

planes of the substrate. The misfit strain along the *c*-axis of rutile is relaxed via alternation of 4/3 and 3/2 domains with a frequency factor of 0.55. To further confirm the abovementioned epitaxial relationship, we did  $\varphi$ -scan XRD on rutile(101) and rutile(111) reflections as well, and the corresponding results are presented in Fig.11.15b and Fig.11.15c. The angular distances between those reflections of rutile and sapphire(02 $\bar{2}$ 4) reflection agrees with the established epitaxial relationship. For example, the azimuthal separation between rutile(101) plane and typical sapphire(02 $\bar{2}$ 4) plane is zero which is completely identical with the 30° angular separation between rutile(110) and sapphire(02 $\bar{2}$ 4) planes.

Bright field TEM image and the indexed SAED patterns taken from [10 $\bar{1}$ 0] and [2 $\bar{1}$ 10] zones of sapphire (Fig.11.17a) confirm the proposed epitaxial alignment between the rutile thin film and the *c*-sapphire substrate. The high resolution image in Fig.11.17b manifests formation of a clean interface with no interfacial reaction.

High resolution  $\theta$ -2 $\theta$  patterns were taken from different family of planes of rutile TiO<sub>2</sub> in order to measure the interplanar spacing, lattice parameters, and the residual strain in the lattice (Fig.11.18a through Fig.11.18j and Tab.11.3). The lattice parameters are obtained to be  $a = 4.566 \text{ \AA}$ ,  $b = 4.622 \text{ \AA}$ , and  $c = 2.952 \text{ \AA}$ , showing that the residual strain can be approximately described as an 0.6% in-plane expansion along TiO<sub>2</sub>[010], an 0.2% in-plane contraction along TiO<sub>2</sub>[001], and an 0.6% out-of-plane contraction along TiO<sub>2</sub>[100] direction. Using eq.11.2, the Poisson's ratio is calculated as about 0.43 which is much larger than that of the bulk rutile TiO<sub>2</sub>. The results indicate that the film is not relaxed. Comparing the residual strains in the systems which are under

consideration in this chapter reveals that the rutile(100)/sapphire(0001) heterostructure contains the largest residual strain, the reason behind which is the thermal strains and unrelaxed lattice misfit strains, as will be discussed later. Taking eq.11.3 into account, the lattice misfit stress along the *b*-axis and *c*-axis of rutile is obtained to be 21.32 and 168.08 GPa, respectively.

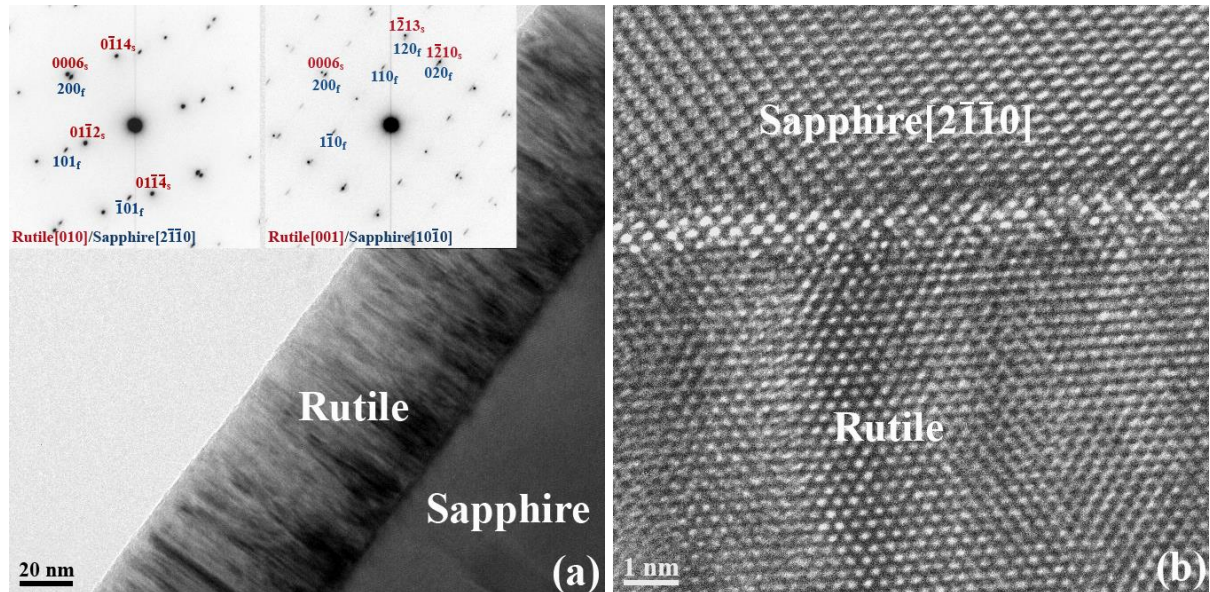


Fig.11.17. (a) Cross section TEM image taken from the rutile/*c*-sapphire heterostructure. The inset shows SAED patterns from two different zones of the TiO<sub>2</sub> film and sapphire substrate and (b) High resolution image from the rutile/*c*-sapphire interface along [2̄1̄0] direction.

As discussed earlier, the critical resolved shear stress ( $\tau_r$ ) must be larger than the yield stress of the material to enable the misfit dislocations to glide from the free surface of the TiO<sub>2</sub> epilayer toward the film/substrate interface to relax the strain. Considering a  $\frac{1}{2}[10\bar{1}](101)$  slip system,  $\tau_r$  is calculated to be 0 and 76.25 GPa for the stress along the [010] and [001] axes, respectively. As is seen, the critical resolved shear

stress for  $\sigma_c$  is far beyond the yield stress of rutile  $\text{TiO}_2$ . Furthermore, the critical thickness is of order of a couple of monolayers for  $\sigma_c$ , due to the large misfit along the [001] orientation ( $\varepsilon_c=28.15\%$ ), so the lattice misfit strain should fully relax. However, there is no primary slip system where the critical resolved shear stress along the *b*-axis does not equal zero; the critical thickness is also large in this case due to the small misfit strain. Consequently, the lattice misfit strain along the *b*-axis of rutile does not get relaxed, and, hence, the residual strain along [010] direction is larger, although the misfit strain is much smaller than that along [001] direction.

Tab.11.3. Interplanar spacing for several family of planes of rutile(100)/*c*-sapphire heterostructure obtained from high resolution  $\theta$ -2 $\theta$  scans (Fig.11.18).

Plane	Measured (Å)	Calculated (Å)	Strain
200	2.2830	2.2966	-0.0058
111	2.1819	2.1874	-0.0025
101	2.4853	2.4876	-0.0010
110	3.2564	3.2480	0.0026
130	1.4595	1.4525	0.0048
210	2.0486	2.0542	-0.0027
220	1.6291	1.6240	0.0032
121	1.6912	1.6875	0.0022
211	1.6804	1.6875	-0.0042

The thermal expansion coefficient of rutile  $\text{TiO}_2$  in the *c*-axis direction is about  $9.36 \times 10^{-6} \text{ K}^{-1}$ .<sup>14</sup> This coefficient for different orientations of sapphire and rutile was already introduced. Using eq.11.1, thermal strain along [010] and [001] orientations of

the rutile epilayer is calculated to be 0.18% and 0.35%, respectively. The thermal strain along the *c*-axis of rutile is relatively large. The larger thermal strain and unrelaxed lattice misfit strain leads to the uneven Poisson's ration in the rutile(100)/*c*-sapphire heterostructure. The difference between the thermal strain and the residual strain is related to the defect strain or unrelaxed lattice misfit strains.

### **11.3.2. Photocatalytic characteristics**

Results of photocatalytic decomposition of 4CP by the UV-excited rutile epilayers are shown in Fig.11.19. To quantitatively study the influence of the crystallographic orientation on photocatalytic efficiency of the rutile TiO<sub>2</sub> thin films, the photocatalytic reaction rate constant (*k*) was calculated. The photocatalytic decomposition of 4CP on the oxide surfaces follows pseudo-first-order kinetics. Therefore, the photocatalytic reaction rate constant can be obtained via the equation  $\ln(C/C_0) = -kt$ . In this equation, *C* represents the concentration of 4CP at time *t*, and *C*<sub>0</sub> is the initial concentration of 4CP at the beginning of the experiments (*t*=0). The curve "No catalyst" represents results of the experiment where no catalyst was used during the photocatalytic measurements and the 4CP solution was lonely irradiated by the UV light. Since no considerable change is observed in the 4CP concentration, it is deduced that 4CP was decomposed photocatalytically, and not by the UV light only.

It was found that the (001) face of rutile has the highest photocatalytic activity among the crystallographic faces under consideration in this study. The [001] direction of rutile titania is the crystallographic direction of highest conductivity.

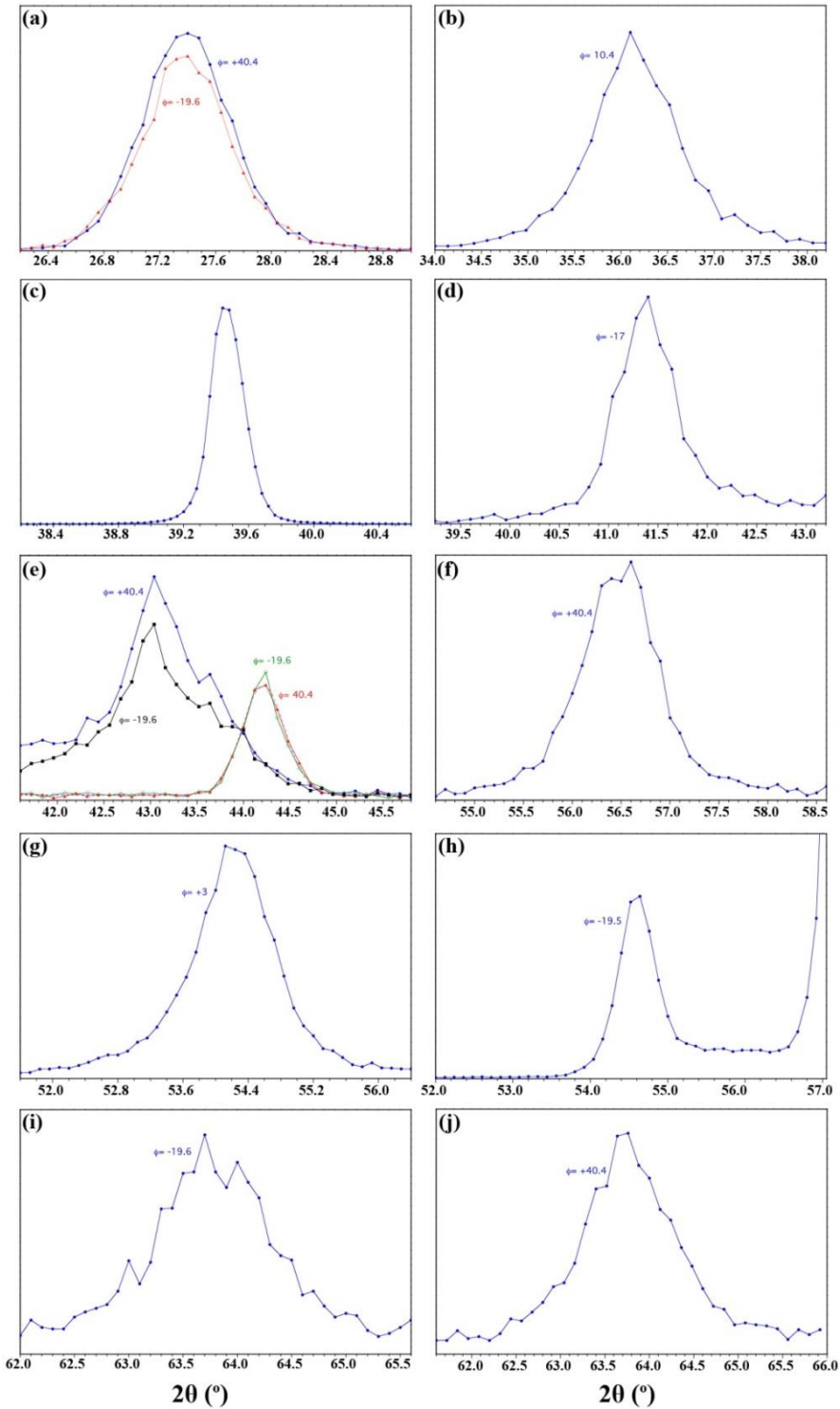


Fig.11.18. High resolution  $\theta$ - $2\theta$  scans performed through: (a)  $\text{TiO}_2(110)$ , (b)  $\text{TiO}_2(101)$ , (c)  $\text{TiO}_2(200)$ , (d)  $\text{TiO}_2(111)$ , (e)  $\text{TiO}_2(210)/(120)$ , (f)  $\text{TiO}_2(220)$ , (g)  $\text{TiO}_2(121)$ , (h)  $\text{TiO}_2(211)$ , (i)  $\text{TiO}_2(130)$ , and (j)  $\text{TiO}_2(130)$  faces of rutile epilayer grown on  $\text{Al}_2\text{O}_3(0001)$  substrate.

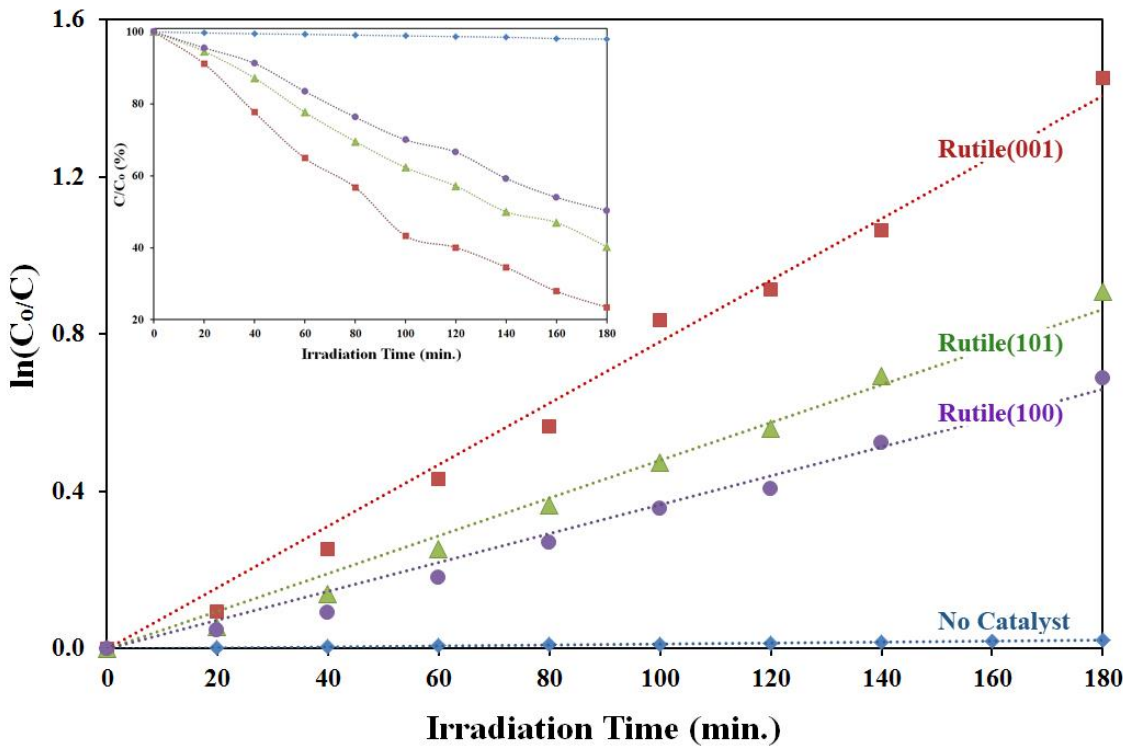


Fig.11.19. Role of out-of-plane orientation of rutile thin film on decomposition rate of 4CP.

The *c*-axis of rutile is the crystallographic direction with the highest conductivity, because the rutile(001) face is more open comparing to the rutile(110) and rutile (100) faces. In fact, there is a network of channels perpendicular to the (001) surface, with a radius of about 0.8 Å. The increased conductivity of this face leads to a higher charge mobility; therefore, the photogenerated  $e^-$ - $h^+$  pairs can reach the surface more easily and participate in the photocatalytic reactions. In contrast, the (100) face has less mobile surface charges, due to the presence of the bridging oxygen atoms, shown in Fig.11.1b, and the jagged surface structure inhibiting charge mobility across the surface.<sup>20-22</sup> In addition, as it was shown back in Fig.11.1c, all oxygen anions are 2-fold-coordinated and all titanium cations are 4-fold coordinated. This situation, which is

exclusively present on the rutile(001) surface, reveals that the (001) face of rutile has the highest number of broken bonds among low-index planes of rutile  $\text{TiO}_2$ . It is worth remembering that (110) and (100) surfaces contain a mixture of 2-fold and 3-fold oxygen sites. The highest number of dangling bonds on the surface results in a large surface energy and, thus, higher chemical activity.<sup>21,23</sup>

We compared surface chemical composition of rutile(001), rutile(101), and rutile(100) faces by XPS technique. O(1s) core level binding energies of rutile  $\text{TiO}_2$  epilayers grown on different substrates are shown in Fig.11.20.

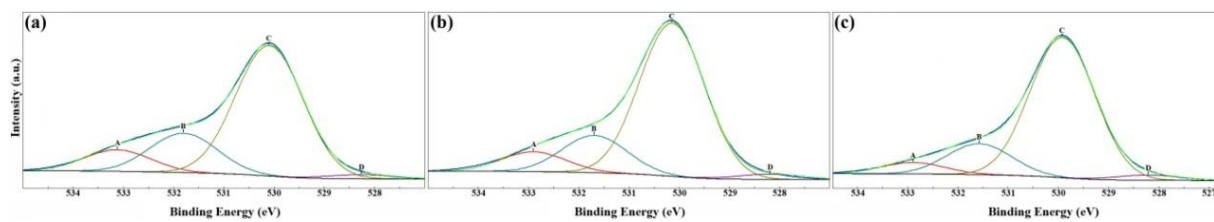


Fig.11.20. XPS O(1s) core level binding energy in: (a)Rutile/*m*-sapphire, (b) Rutile/*r*-sapphire, and (c) Rutile/*c*-sapphire heterostructures.

Peaks A and B, with the binding energies of about 532.9 and 531.6 eV, are assigned to water ( $\text{H-O-H}$ ) and hydroxyl ( $-\text{OH}$ ) compounds, respectively. Oxygen vacancies on the surface are filled by hydroxyl groups which have their origin in dissociative absorption of water at the defect sites. Such a hydroxylated surface usually forms when an oxide material is exposed to the atmosphere.<sup>24</sup> Then, the subsequent water molecules attach to the hydroxyl groups by hydrogen bonds. Peak C at the binding energy of 530.0 eV represents the perfect  $\text{TiO}_2$  structure, i.e.  $\text{Ti-O-Ti}$  bonds. Finally, peak D can be indirectly attributed to the regions with oxygen deficiency. In other words, it represents the  $\text{TiO}$

compound. The portion of peak B was determined to be about 24.2, 17.3, and 16.1 % for the rutile(100), rutile(101), and rutile(100) surfaces. These values show that the *c*-plane of rutile TiO<sub>2</sub> has the highest number of dangling bonds where the hydroxyl groups are attached. Besides, this face has the highest chemical reactivity compared to the (101) and (100) faces.

#### 11.4. Conclusions

Epitaxial rutile TiO<sub>2</sub> thin films were grown on *m*-cut, *r*-cut, and *c*-cut sapphire substrates by pulsed laser deposition technique. Structural and photochemical characteristics of heterostructures were investigated in detail. The out-of-plane alignment between the rutile thin layers and sapphire substrates was established as (100)<sub>rutile</sub>||(0001)<sub>c-sapphire</sub>, (001)<sub>rutile</sub>||(10̄10)<sub>m-sapphire</sub>, and (101)<sub>rutile</sub>||(01̄12)<sub>r-sapphire</sub>. The in-plane alignment was also shown to be [001]<sub>rutile</sub>||[10̄10]<sub>c-sapphire</sub>, [010]<sub>rutile</sub>||[0001]<sub>m-sapphire</sub>, and [100]<sub>rutile</sub>||[2̄1̄10]<sub>r-sapphire</sub>. The unrelaxed strains in the thin films were calculated. The thermal and defect strains were found to be the primary origin of the residual strains in the epilayers, and the lattice misfit strains were shown to be relaxed via matching of domains across the film/substrate interfaces. The relative photocatalytic activity of different faces of rutile TiO<sub>2</sub> was shown to be in the following sequence: (001) > (101) > (100).

#### References

1. A.W. Czanderna, C.N.R. Rao, and J.M. Honig, Trans. Faraday Soc. 54, 1069 (1958).

2. C.N.R. Rao, S.R. Yoganarasimhan, and P.A. Faeth, *Trans. Faraday Soc.* 57, 504 (1961).
3. A. Fujishima and X. Zhang, *C.R. Chimie* 9, 750 (2006).
4. A. Fahmi, C. Minot, B. Silvi, and M. Causa, *Phys. Rev. B* 47, 11717 (1993).
5. G.B. Song, J.K. Liang, F.S. Liu, T.J. Peng, and G.H. Rao, *Thin Solid Films* 491, 110 (2005).
6. M.R. Bayati, J. Ding, Y.F. Lee, R.J. Narayan, and J. Narayan, *J. Phys. C: Cond. Mater.* 24, 395005 (2012).
7. Y. Motohashi, M.G. Blanchi, E. Vicario, G. Fontain, and S. Otake, *Phys. Stat. Sol. A* 64, 355 (1979).
8. H. Perron, C. Domain, J. Roques, R. Drot, E. Simoni, and H. Catalette, *Theor. Chem. Acc.* 117, 565 (2007).
9. M. Ramamoorthy, D. Vanderbilt, and R.D. King-Smith, *Phys. Rev. B* 49, 16721 (1994).
10. M.R. Bayati, S. Joshi, R.J. Narayan, and J. Narayan, *J. Mater. Res.* 28, 1 (2013).
11. M.R. Bayati, R. Molaei, R.J. Narayan, J. Narayan, H. Zhou, and S.J. Pennycook, *Appl. Phys. Lett.* 100, 251606 (2012).
12. J. Narayan, and B.C. Larson, *J. Appl. Phys.* 93, 278 (2003).
13. J. Narayan, *Acta Mater.* 61, 2703 (2013).
14. D.R. Hummer, P.J. Heaney, and J.E. Post, *Powder Diffraction* 22, 352 (2007).
15. R. Riedel and I.W. Chen (Ed.), *Ceramics Science and Technology, Materials and Properties*, John Wiley & Sons (2011).
16. M. Iuga, G. Steinle-Neumann, and J. Meinhardt, *Eur. Phys. J. B* 58, 127 (2007).
17. T. Mashimo, K. Nagayama, and A. Sawaoka, *J. Appl. Phys.* 54, 5043 (1983).
18. M. Ichimura and J. Narayan, *Mater. Sci. Eng. B* 31, 299 (1995).

19. M. Ichimura and J. Narayan, *Philos. Mag. A* 72, 281 (2006).
20. H.O. Finklea (Ed.), *Semiconductor Electrodes*, New York: Elsevier (1988).
21. U. Diebold, *Surf. Sci. Rep.* 48, 53 (2003).
22. J.W. Bullard and M.J. Cima, *Langmuir* 22, 10264 (2006).
23. X. Han, Q. Kuang, M. Jin, Z. Xie, and L. Zheng, *J. Am. Chem. Soc.* 131, 3152 (2009).
24. A.P. Shpak, A.M. Korduban, M.M. Medvedskij, V.O. Kandyba, *J. Electron. Spectrosc. Relat. Phenom.* 156–158, 172 (2007).

## Chapter 12

# Semiconductor to Metal Transition Characteristics in VO<sub>2</sub>/TiO<sub>2</sub>/Al<sub>2</sub>O<sub>3</sub> Thin Film Heterostructures

This chapter sheds light on the role of strain and thin film epitaxy on the semiconductor to metal transition (SMT) characteristics of single crystalline VO<sub>2</sub> thin films. The VO<sub>2</sub>/TiO<sub>2</sub> heterostructures of controlled orientations were epitaxially grown on *m*-cut, *r*-cut, and *c*-cut sapphire substrates. Detailed structural investigations were performed using high resolution XRD ( $2\theta$ - $\theta$  and  $\varphi$  scans) and high resolution transmission electron microscopy techniques to correlate SMT properties with microstructural characteristics. Monoclinic ( $M_1$ ) VO<sub>2</sub> thin films with (100), (001), and ( $\bar{2}01$ ) out-of-plane orientations were grown on TiO<sub>2</sub>(101)/*r*-sapphire, TiO<sub>2</sub>(100)/*c*-sapphire, and TiO<sub>2</sub>(001)/*m*-sapphire platforms, respectively. The in-plane alignments across the interfaces was established to be [010](100)<sub>VO2</sub>||[010](101)<sub>TiO2</sub>, [100](001)<sub>VO2</sub>||[001](100)<sub>TiO2</sub>, and [010]( $\bar{2}01$ )<sub>VO2</sub>||[010](001)<sub>TiO2</sub> for *r*-sapphire, *c*-sapphire, and *m*-sapphire substrates, respectively. We were able to tune the SMT temperature of VO<sub>2</sub> epilayers from about 313 K to 354 K (bulk  $T_c \approx 340$  K). The SMT characteristics were interpreted based upon the residual strain in the VO<sub>2</sub> lattice,

particularly along the *c*-axis of tetragonal VO<sub>2</sub>. This research introduces the VO<sub>2</sub> based single crystalline heterostructures as a potential candidate for a wide range of applications where different transition temperatures are required.

## 12.1. Introduction

Vanadium dioxide (VO<sub>2</sub>) is an *n*-type semiconductor with a band gap of 0.5-0.7 eV at room temperature. Bulk single crystals of VO<sub>2</sub> exhibit an extremely sharp and ultrafast first-order phase transformation from a low temperature monoclinic state into a high temperature tetragonal state at about 340 K in the absence of internal and external stresses. This phase transformation results in a significant change in electrical and optical characteristics and is called a semiconductor to metal transition (SMT). The SMT phenomenon in VO<sub>2</sub> is characterized by an abrupt change in resistivity and reflectivity within the infrared region of the spectrum by several orders of magnitude. The tetragonal polymorph (space group P4<sub>2</sub>/mnm) with a metallic electrical behavior is stable at temperatures higher than about 340 K. The lattice constants of bulk tetragonal VO<sub>2</sub> just above the transition are *a*=*b*=4.555 and *c*=2.851 Å. Upon cooling below 340 K, the regular V<sup>4+</sup>-V<sup>4+</sup> pairs along the *c*-axis of the tetragonal structure transforms to alternating V<sup>4+</sup>-V<sup>4+</sup> pairs along the *a*-axis of the monoclinic phase with separations of 0.265 and 0.312 nm leading to a doubling of the unit cell. As discussed earlier, the room temperature polymorph of VO<sub>2</sub> has a monoclinic structure (*a*=5.752, *b*=4.538, *c*=5.382 Å, and  $\beta=122.65^\circ$ ) and belongs to the space group of P2<sub>1</sub>/c.<sup>1-9</sup> This phase is called M<sub>1</sub>. However, in the presence of internal and external stresses and strains, the formation of

a transient monoclinic phase M<sub>2</sub> ( $a=9.06$ ,  $b=5.80$ ,  $c= 4.25 \text{ \AA}$ ,  $\beta=91.8^\circ$ ) which is an intermediate of the M<sub>1</sub> and rutile phases, often broadens the transition characteristics. The formation of the M<sub>2</sub> phase in thin film heterostructures is caused by internal stresses and constraints imposed by substrates, which can be controlled by epitaxial growth orientations and relaxation of stresses and strains.<sup>10</sup>

The semiconductor to metal transition (SMT) is strongly influenced by the strain along the  $a_{\text{monoclinic}}$  or  $c_{\text{tetragonal}}$  axes, which needs to be controlled for reliable device performance [8]. The SMT characteristics in VO<sub>2</sub> thin films, namely  $\Delta T$  (SMT sharpness),  $\Delta A$  (SMT amplitude), and  $\Delta H$  (SMT thermal hysteresis), are influenced by the nature of the microstructure. Based on the model developed by Narayan et al.<sup>5</sup> these features of the SMT are affected by the defect content, grain size, and nature of boundaries. As was explained earlier, the  $c$ -axis of the tetragonal unit cell undergoes a large change during SMT, so any expansion or contraction along the tetragonal [001]-direction significantly alters the SMT temperature. In other words, the SMT temperature is dictated by the strain in the VO<sub>2</sub> films. Basically, there are three kinds of strains in thin films: misfit strain, defect strain, and thermal strain which are cumulative.<sup>11</sup> The misfit strain is believed to get relaxed, in accordance with the domain matching epitaxy paradigm where the misfit dislocations and matching of the integral multiples of the atomic rows are the key factors to release this strain.<sup>12</sup> However, small misfits are very hard to relax and have been one of the challenges in thin film based heterostructures. The strain from cooling the film from the growth temperature down to room temperature and the difference in the thermal expansion coefficients of the film and the substrate is normally

below 1%. Such small strains do not relax easily and remain in the lattice as residual strain. The unrelaxed strains control the SMT temperature. In addition, defects affect the sharpness and width of SMT. They might also impact the SMT temperature through introduction of strain along the c-direction. In this research, we study the effect of microstructure, epitaxy, and residual strains on SMT characteristics of VO<sub>2</sub> single crystalline thin films in detail.

This chapter addresses the effect of strain on SMT characteristics by controlling growth orientations of VO<sub>2</sub> thin films. This VO<sub>2</sub> orientation control has been achieved by TiO<sub>2</sub> buffer layers on *m*-, *r*-, and *c*- sapphire substrates, and correlation established with electrical properties and SMT characteristics. We first successfully grew rutile TiO<sub>2</sub> epilayers with various out-of-plane orientations on sapphire substrates. Subsequently, VO<sub>2</sub> thin films with different out-of-plane directions were epitaxially grown on TiO<sub>2</sub> platforms. We were able to tune the SMT temperature over a wide temperature range both above and below the unstrained value through thin film epitaxy and control of growth orientation. These findings provide insight into the role of defects and strain in VO<sub>2</sub> thin film heterostructures and open new opportunities for advanced applications of VO<sub>2</sub>-based devices where different SMT characteristics are required.

## 12.2. Experimental

Pulsed laser deposition (PLD) was employed to grow epitaxial VO<sub>2</sub>/TiO<sub>2</sub>/sapphire thin film heterostructures. Details on substrate cleaning procedure can be found in our previous works.<sup>13,14</sup> The chamber was evacuated to a background pressure of about

$8 \times 10^{-7}$  Torr. To ablate the targets, a Lambda Physik (LPX200) KrF excimer laser, with  $\lambda = 248$  nm and  $\tau = 25$  ns, was employed. The laser beam was incident at an angle of  $45^\circ$  on the surface of the targets which were rotated during the deposition to achieve uniform ablation characteristics on the target surface. The laser energy density and repetition rate were set at  $3.0\text{-}3.5 \text{ J.cm}^{-2}$  and 5 Hz for all layers. The rutile  $\text{TiO}_2$  thin films were deposited at  $700^\circ\text{C}$  under an oxygen partial pressure of  $5 \times 10^{-4}$  Torr for 2500 pulses. Afterward, the  $\text{VO}_2$  films were grown onto the  $\text{TiO}_2$ /sapphire platforms under a pressure of  $5 \times 10^{-2}$  Torr for 4500 pulses at  $500^\circ\text{C}$ .

The  $\text{TiO}_2$  and  $\text{VO}_2$  targets were made by pressing the  $\text{TiO}_2$  (Sigma Aldrich) and  $\text{VO}_2$  (Sigma Aldrich) pellets under a pressure of  $>5 \text{ ton.cm}^{-2}$  for 40 min. followed by 5 hrs. sintering at  $1100^\circ\text{C}$  under an oxygen atmosphere for  $\text{TiO}_2$  and at  $900^\circ\text{C}$  under an argon atmosphere for  $\text{VO}_2$ .

High resolution  $\theta\text{-}2\theta$  X-ray diffraction was performed by a Rigaku diffractometer with Cu-K $\alpha$  radiation ( $\lambda=0.154$  nm) to study the out-of-plane alignment of the films. A Philips X'Pert Pro X-ray diffractometer was also employed to collect high resolution  $\varphi$  and  $\theta\text{-}2\theta$  patterns. Some of the high-resolution XRD measurements were done by using a 4-circle Huber diffractometer. Further microstructural studies were performed by a JEOL 2010F transmission electron microscope with 0.18 nm resolution and Gatan image filter (GIF) attachment. The microscope was operated at 200 kV. Semiconductor-to-metal transition properties of the heterostructures were studied using a Keithley 2400 sourcemeter and labview program. The measurements were done in the temperature range of 280-370 K.

## 12.3. Results and discussion

### 12.3.1. SMT characteristics

Fig.12.1 displays the role of growth orientation on SMT characteristics of  $\text{VO}_2/\text{TiO}_2/\text{sapphire}$  heterostructures. Sharp transitions in the heterostructures were observed with amplitude of over 4 orders of magnitude in all of the samples.

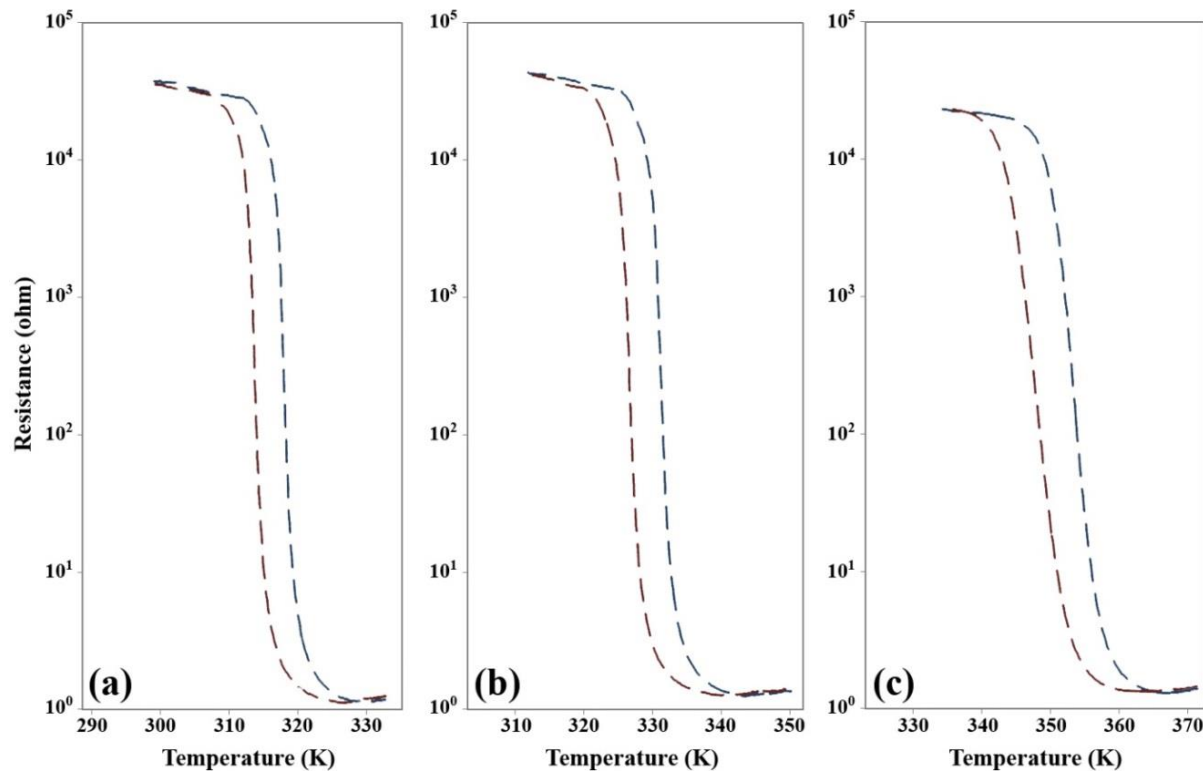


Fig.12.1. Resistance versus temperature in: (a)  $\text{VO}_2/\text{TiO}_2/m\text{-sapphire}$ , (b)  $\text{VO}_2/\text{TiO}_2/r\text{-sapphire}$ , and (c)  $\text{VO}_2/\text{TiO}_2/c\text{-sapphire}$  heterostructures.

The hysteresis is about 5 K. It is interesting to note that the SMT temperature changes significantly from about 313 K to about 354 K for different substrates (Tab.12.1). This shift of the transition temperature toward higher or lower

temperatures has been attributed to tensile or compressive strains along the *c*-axis of tetragonal VO<sub>2</sub>, respectively.<sup>8,15-17</sup> Longer V<sup>4+</sup>-V<sup>4+</sup> spacing along the [001] orientation leads to a high activation barrier for direct overlapping of *d*-orbitals which, in turn, stabilizes the covalent monoclinic phase and hinders the phase transformation of monoclinic state to rutile structure. This phenomenon gives rise to the observation of higher SMT temperatures. In contrast, the SMT takes place at lower temperatures, with respect to the bulk SMT temperature, if the V<sup>4+</sup>-V<sup>4+</sup> distance decreases due to a compressive residual strain along the *c*-axis of VO<sub>2</sub>. In the following sections, we present the details of epitaxy and strain characteristics and their correlations with SMT.

Tab.12.1. SMT characteristics of VO<sub>2</sub> epilayers grown on several TiO<sub>2</sub>/sapphire platforms.

Heterostructure	TiO <sub>2</sub> out-of-plane orientation	VO <sub>2</sub> out-of-plane orientation	SMT temperature (K), Cooling	SMT temperature (K), Heating
VO <sub>2</sub> /TiO <sub>2</sub> /Al <sub>2</sub> O <sub>3</sub> (1̄100)	(001)	(̄201)	312.8	318.1
VO <sub>2</sub> /TiO <sub>2</sub> /Al <sub>2</sub> O <sub>3</sub> (1̄102)	(101)	(100)	326.7	331.6
VO <sub>2</sub> /TiO <sub>2</sub> /Al <sub>2</sub> O <sub>3</sub> (0001)	(100)	(001)	348.6	353.9

### 12.3.2. Microstructural studies

#### 12.3.2.1. VO<sub>2</sub>/TiO<sub>2</sub>/m-sapphire heterostructure

Results of a θ-2θ XRD scan conducted on a VO<sub>2</sub>/TiO<sub>2</sub>/m-sapphire heterostructure is shown in Fig.12.2 confirming growth of the TiO<sub>2</sub> thin film along its [001] axis; therefore, a 4-fold symmetry exists on the TiO<sub>2</sub> platform. The peak labeled “VO<sub>2</sub>” can be assigned to either tetragonal VO<sub>2</sub>(002) reflection (JCPDS 76-0675) or monoclinic M<sub>1</sub> VO<sub>2</sub>(̄402) reflection (JCPDS 76-0456).

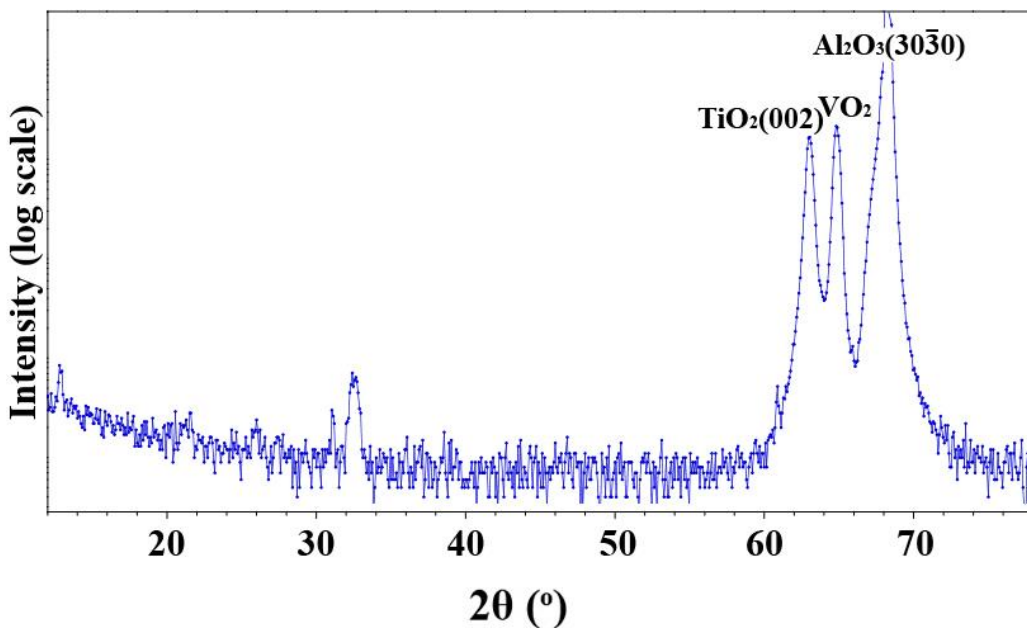


Fig.12.2. Results of  $\theta$ - $2\theta$  scan conducted on  $\text{VO}_2/\text{TiO}_2/m$ -sapphire heterostructure.

In order to determine the origin of this peak, high resolution  $\theta$ - $2\theta$  XRD scans were performed on several planes of  $\text{VO}_2$  along different  $\varphi$  and  $\psi$  angles to test two different possibilities: first, stabilization of tetragonal rutile  $\text{VO}_2$  at room temperature due to a templating effect of rutile  $\text{TiO}_2$  and, second, formation of  $\text{M}_1$  phase of  $\text{VO}_2$ . The results are presented in Fig.12.3. If rutile  $\text{VO}_2$  is epitaxially stabilized, all  $\theta$ - $2\theta$  scans should show two distinct peaks, one from  $\text{TiO}_2$  located at lower  $2\theta$  values due to larger lattice constants, and one from  $\text{VO}_2$  at higher  $2\theta$  values due to smaller lattice constants. As is seen in Fig.12.3, two separate peaks are observed only in four  $\theta$ - $2\theta$  scans and not in all of them; on the other hand, those 4 peaks can be indexed based on both tetragonal and monoclinic  $\text{M}_1$  structures. In addition, rutile  $\text{VO}_2$  does not have any reflection with  $d$ -spacings of 4.845 Å (Fig.12.3a), 3.317 Å (Fig.12.3b), and 2.686 Å (Fig.12.3c), but monoclinic  $\text{VO}_2$  does. Hence, the  $\text{VO}_2$  peak in Fig.12.2 belongs to  $(\bar{4}02)$  reflection of

monoclinic  $\text{VO}_2$ ; i.e. the larger monoclinic unit cell is revealed by the presence of additional  $\text{VO}_2$  diffraction peaks in particular directions.

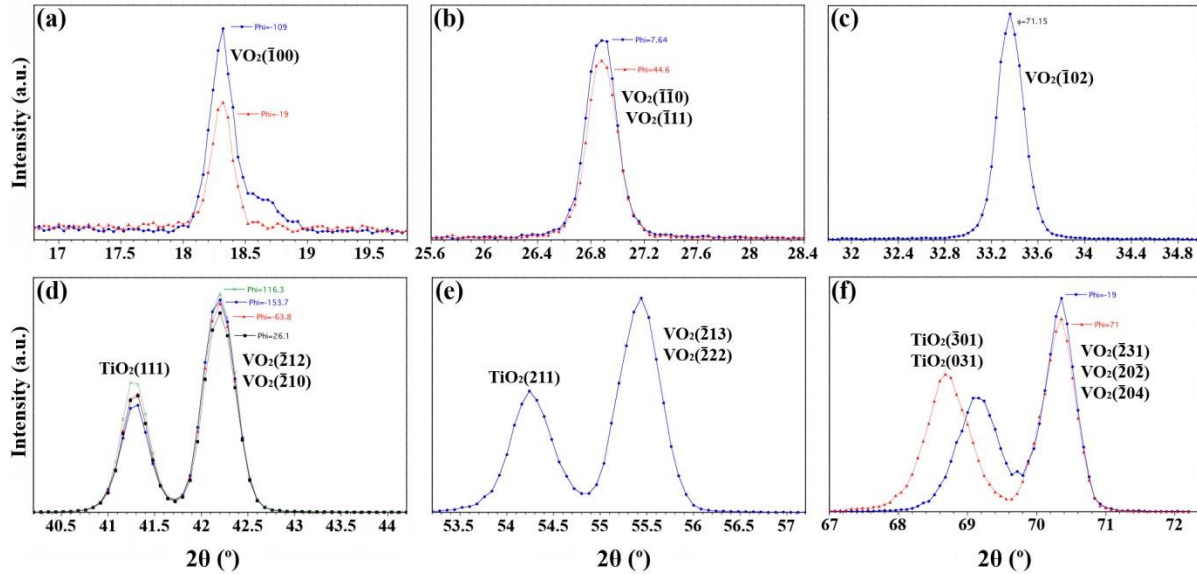


Fig.12.3. High resolution  $\theta$ - $2\theta$  scans performed on: (a)  $\text{VO}_2(\bar{1}00)$ , (b)  $\text{VO}_2(\bar{1}\bar{1}0)+\text{VO}_2(\bar{1}\bar{1}1)$ , (c)  $\text{VO}_2(\bar{1}02)$ , (d)  $\text{TiO}_2(111)$  and  $\text{VO}_2(\bar{2}12)+\text{VO}_2(\bar{2}10)$ , (e)  $\text{TiO}_2(211)$  and  $\text{VO}_2(\bar{2}13)+\text{VO}_2(\bar{2}22)$ , and (f)  $\text{TiO}_2(031)$  and  $\text{VO}_2(\bar{2}31)+\text{VO}_2(\bar{2}0\bar{2})+\text{VO}_2(\bar{2}04)$  reflections in  $\text{VO}_2/\text{TiO}_2/m$ -sapphire heterostructure.

Although other researchers have indexed the  $\text{VO}_2$  peak with a  $2\theta$  of about  $65^\circ$  as (002) reflection of tetragonal  $\text{VO}_2$ <sup>18-21</sup>, we showed that this peak should be indexed for ( $\bar{4}02$ ) reflection of monoclinic  $\text{VO}_2$  (Fig.12.2). We believe the main reason leading to such a disagreement is the thickness of the  $\text{VO}_2$  thin film. The thickness of our thin films is  $\sim 100$ - $150$  nm which is about ten times larger than the thickness in other works (10-15 nm). Phase transformation and strain relaxation phenomena follow totally different kinetics in thin and thick layers. With increasing the film thickness, the stored energy, originating from strains, increases and relaxes after the film reaches a critical thickness. The critical thickness is the thickness at which the misfit dislocations are generated to

relax the film and form the equilibrium phase. These dislocations, which are prerequisites for strain relaxation, nucleate at the free surface of the film and glide toward the interface. In very thin films, if the thickness does not exceed the critical value, misfit dislocations are not generated and, hence, strains do not relax. As it is shown in Tab.12.2, the lattice misfit strain across the  $\text{VO}_2^{\text{tetragonal}}/\text{TiO}_2^{\text{tetragonal}}$  interface is very small. In such small misfit systems, the critical thickness is larger than 10 nm; therefore, the misfit strain does not relax and it generates residual strains which affect the SMT characteristics. However, in our experiments, the  $\text{VO}_2$  films are thick enough to accommodate misfit dislocations. In other words, the thickness of the  $\text{VO}_2$  layers is much larger than the critical thickness. Of course, small strains are hard to relax, because the critical thickness beyond which the growing thin layer can accommodate misfit dislocations becomes larger in small misfit systems, so the misfit dislocations need to glide a larger distance to the interface, i.e. across the critical thickness. This issue is more critical in partially ionic materials such as  $\text{VO}_2$  where lattice friction stress of dislocation glide is very large. In contrast, in large misfit systems, the critical thickness is about a couple of monolayers, so dislocations can glide and reach the interface easily. Due to the large critical thickness, the misfit dislocations might not be able to reach the interface, so the lattice misfit is envisaged to partially relax. This difference in relaxation results in the different SMT characteristics that were observed.

To confirm the epitaxial growth and determine the crystallographic alignment across the  $\text{VO}_2(\bar{2}01)/\text{TiO}_2(001)$  interface,  $\varphi$ -scan XRD was conducted on several reflections of  $\text{VO}_2$  and  $\text{TiO}_2$  thin films, and the sapphire substrate (Fig.12.4).

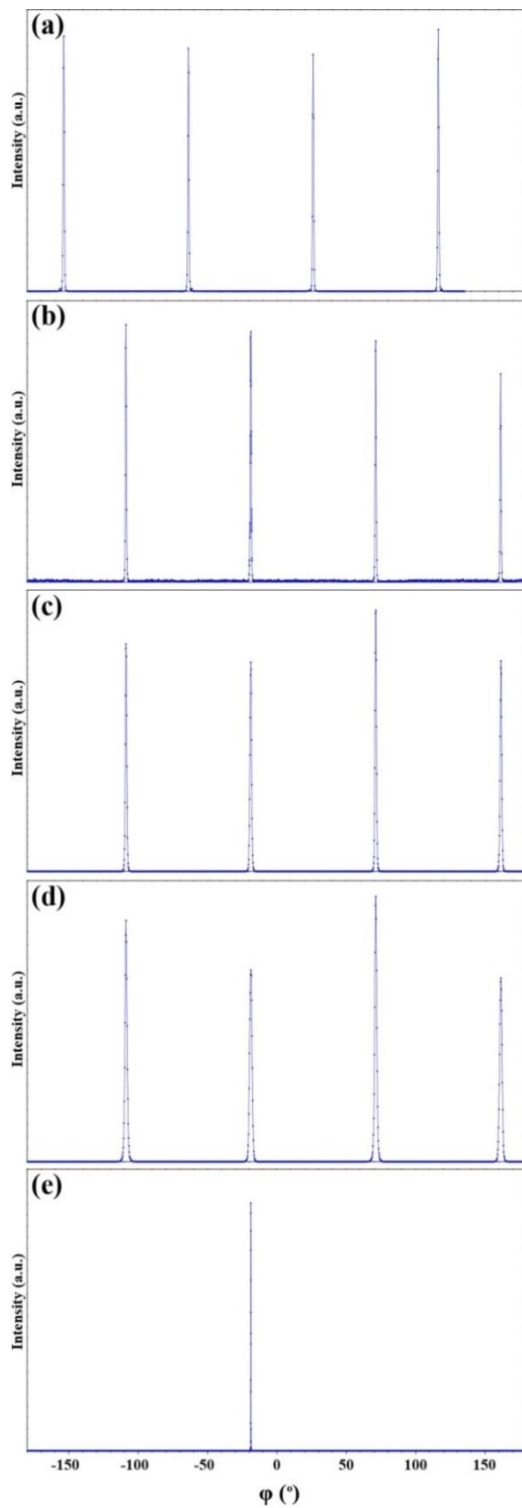


Fig.12.4.  $\varphi$ -scan patterns acquired from several reflections in  $\text{VO}_2/\text{TiO}_2/m\text{-sapphire}$  heterostructure: (a)  $\text{VO}_2(\bar{2}12)+\text{VO}_2(\bar{2}10)$ , (b)  $\text{VO}_2(\bar{1}02)$ , (c)  $\text{VO}_2(\bar{2}11)+\text{VO}_2(\bar{2}00)$ , (d)  $\text{TiO}_2(101)$ , and (e)  $\text{Al}_2\text{O}_3(10\bar{1}4)$ .

As expected, only a single azimuthal peak is observed from  $\text{Al}_2\text{O}_3(10\bar{1}4)$  planes because the  $(10\bar{1}\bar{4})$  reflection is not an allowed reflection in the trigonal symmetry of alumina. Taking the information shown in Fig.12.4 into closer considerations, the epitaxial relationship in  $\text{VO}_2/\text{TiO}_2/m$ -sapphire system is established to be  $(\bar{2}01)_{\text{VO}_2}||(001)_{\text{TiO}_2}||(\bar{1}0\bar{1}0)_{\text{Al}_2\text{O}_3}$  and  $[010]_{\text{VO}_2}||[010]_{\text{TiO}_2}||[0001]_{\text{Al}_2\text{O}_3}$ .

#### 12.3.2.2. $\text{VO}_2/\text{TiO}_2/r$ -sapphire heterostructure

A  $\theta$ - $2\theta$  XRD log-scale pattern taken from the  $\text{VO}_2$  thin films grown on  $\text{TiO}_2(101)/r$ -sapphire template is shown in Fig.12.5 where growth of monoclinic  $\text{M}_1\text{VO}_2$  such that its  $(100)$  planes are parallel to the substrate surface is evident.

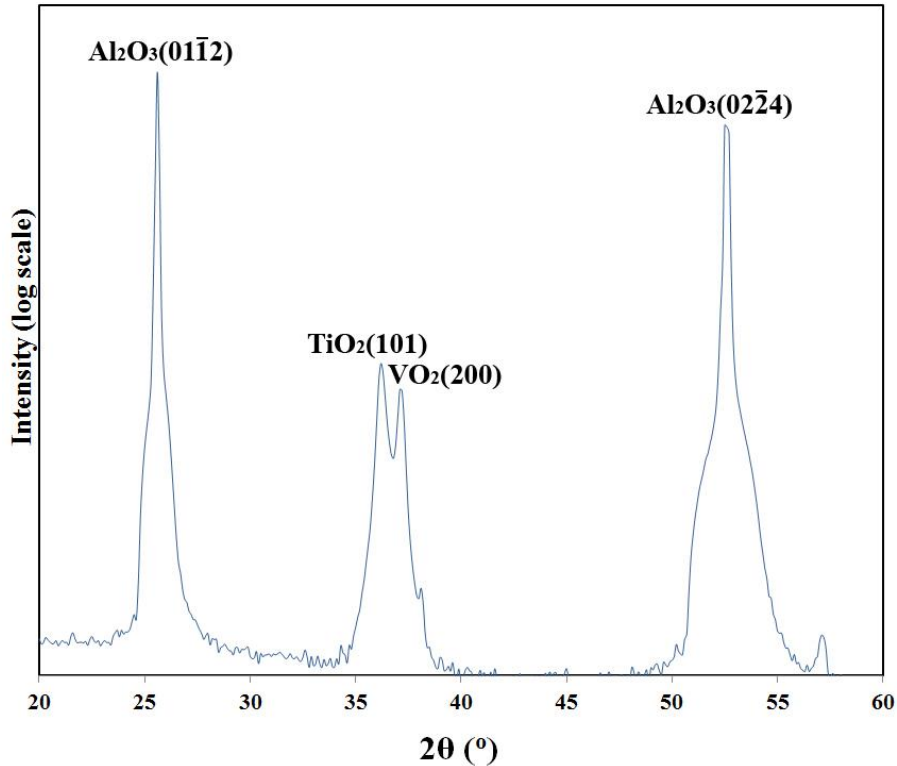


Fig.12.5. Result of  $\theta$ - $2\theta$  scan performed on  $\text{VO}_2/\text{TiO}_2/r$ -sapphire heterostructure.

Considering the SMT transition of this sample (Fig.12.1) and discussions in section 12.3.2.1, this peak cannot be assigned to the rutile  $\text{VO}_2(101)$  reflection. We performed detailed  $\theta$ - $2\theta$  scans along several  $\varphi$  and  $\psi$  angles on  $\text{VO}_2/\text{TiO}_2/r$ -sapphire heterostructure. The results, presented in Fig.12.6, are in complete agreement with our discussion in section 12.3.2.1 on  $\theta$ - $2\theta$  patterns in Fig.12.3. Rutile  $\text{VO}_2$  does not have any reflection with  $2\theta$  values of  $26.83^\circ$  and  $33.38^\circ$ , but  $M_1 \text{VO}_2$  does. As seen in Fig.12.7, only a single peak is present in Fig.12.6a and Fig.12.6c. Therefore, the  $2\theta$  peak in Fig.12.5 should be assigned to the monoclinic  $\text{VO}_2(200)$  reflection.

The XRD  $\varphi$ -scan was conducted on the  $\text{VO}_2(100)/\text{TiO}_2(101)/r$ -sapphire heterostructure to establish crystallographic alignment across the interfaces. The results are displayed in Fig.12.7.

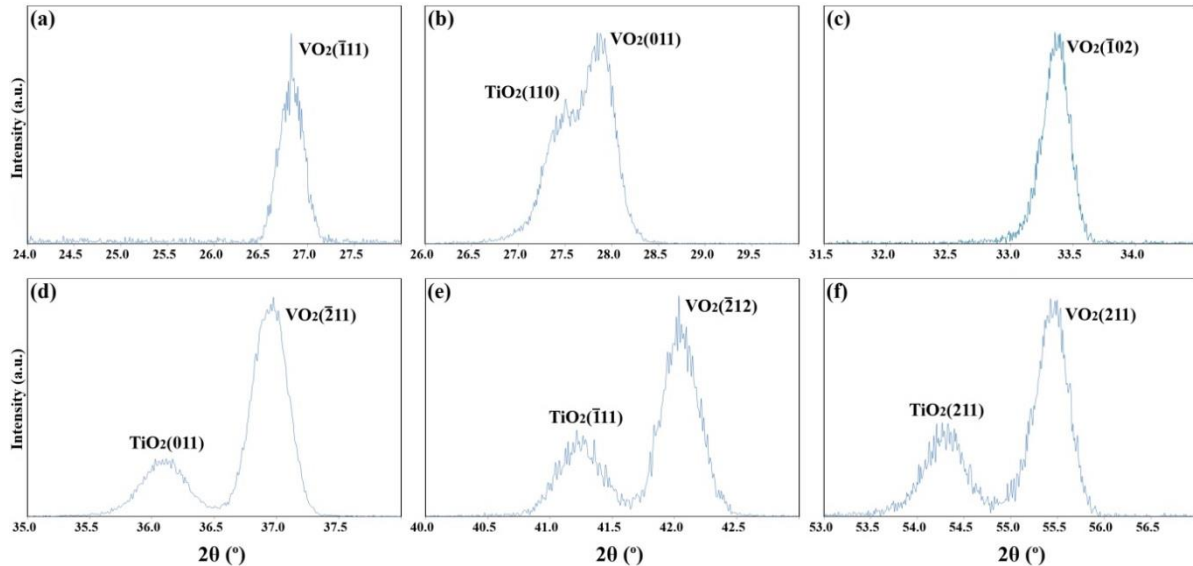


Fig.12.6. High resolution  $\theta$ - $2\theta$  patterns acquired from  $\text{VO}_2/\text{TiO}_2/r$ -sapphire heterostructure: (a)  $\text{VO}_2(\bar{1}11)$ , (b)  $\text{TiO}_2(110)$  and  $\text{VO}_2(011)$ , (c)  $\text{VO}_2(\bar{1}02)$ , (d)  $\text{TiO}_2(011)$  and  $\text{VO}_2(\bar{2}11)$ , (e)  $\text{TiO}_2(\bar{1}11)$  and  $\text{VO}_2(\bar{2}12)$ , and (f)  $\text{TiO}_2(211)$ , and  $\text{VO}_2(211)$  reflections.

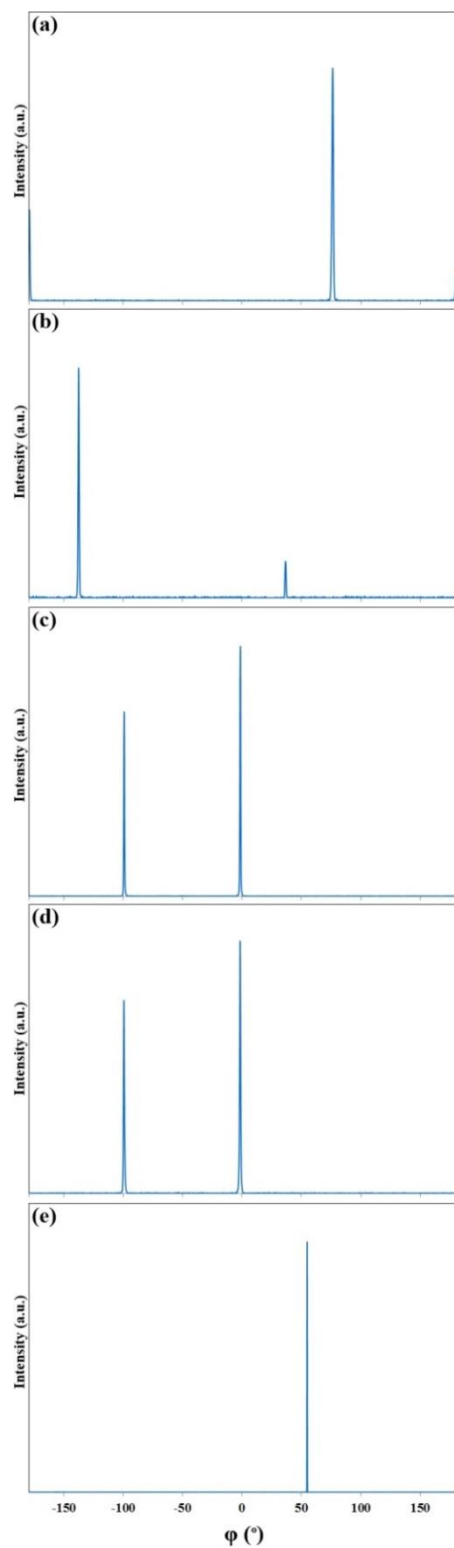


Fig.12.7. Results of  $\varphi$ -scan XRD conducted on: (a)  $\text{VO}_2(\bar{2}11)$ , (b)  $\text{VO}_2(220)$ , (c)  $\text{VO}_2(011)$ , (d)  $\text{TiO}_2(110)$ , and (e)  $\text{Al}_2\text{O}_3(0006)$  reflections in  $\text{VO}_2/\text{TiO}_2/r$ -sapphire heterostructure.

The results confirm the growth of highly epitaxial VO<sub>2</sub> and TiO<sub>2</sub> thin films on the Al<sub>2</sub>O<sub>3</sub>(10̄12) substrate. Fig.12.7a shows  $\varphi$ -pattern acquired from (220) reflection of monoclinic VO<sub>2</sub> at  $2\theta=55.45^\circ$  and  $\psi=46.86^\circ$ . It should be noted that rutile TiO<sub>2</sub> has two reflections, namely (211) and (220), with  $2\theta$  angles near to that of (220) reflection of VO<sub>2</sub>; however,  $\psi$ -angle between (211) and (220) planes and (101) plane of TiO<sub>2</sub> are approximately  $29.25^\circ$  and  $53.32^\circ$ , respectively, which are far away from the  $\psi$ -angle between (220) and (100) planes of monoclinic VO<sub>2</sub>; thus, it is deduced that the obtained  $\varphi$ -pattern is certainly from VO<sub>2</sub> crystal. To determine the epitaxial alignment between VO<sub>2</sub>(100) and TiO<sub>2</sub>(101) thin films, VO<sub>2</sub>(011) and TiO<sub>2</sub>(110) reflections are taken into account (Fig.12.7b and Fig.12.7c) whose  $\varphi$ -peaks appeared at the same angles. The azimuthal distance between  $\varphi$ -peaks of each crystal is about  $99.3^\circ$ . The geometrical intersection between (011) and (100) planes of VO<sub>2</sub> is the [0̄11] vector; furthermore, the [̄111] vector represents the intersection between the (110) and (101) planes in TiO<sub>2</sub>. Since the  $\varphi$ -patterns from two crystals completely overlap one another, the [0̄11]<sub>VO2</sub> and [̄111]<sub>TiO2</sub> vectors have to be parallel, while the (100)<sub>VO2</sub> and (101)<sub>TiO2</sub> planes are kept parallel. Under these circumstances, the epitaxial relationship is written as  $(100)_{VO2}||(101)_{TiO2}||(01\bar{1}2)_{Al_2O_3}$  and  $[010]_{VO2}||[010]_{TiO2}||[2\bar{1}\bar{1}0]_{Al_2O_3}$ . The misfit strains which are calculated and shown in Tab.12.2 for the VO<sub>2</sub><sup>rutile</sup>/TiO<sub>2</sub><sup>rutile</sup> interface remain in the lattice, as explained earlier. The misfit strain across the VO<sub>2</sub><sup>monoclinic</sup>/TiO<sub>2</sub><sup>rutile</sup> interface will be discussed later. The reflections for  $\varphi$ -scan on VO<sub>2</sub> thin film were selected in such a way that the  $2\theta$  and  $\psi$  would be different from those of TiO<sub>2</sub> buffer; thus, presence of M<sub>1</sub> phase of VO<sub>2</sub> in this sample is further ascertained.

Our results clearly showed that VO<sub>2</sub> exists in its monoclinic (M<sub>1</sub>) state in the VO<sub>2</sub>/TiO<sub>2</sub>(101)/r-sapphire heterostructure. In the work by Y. Cui et al.<sup>21</sup>, where VO<sub>2</sub> thin films were grown in a TiO<sub>2</sub>(101) single crystalline substrate, the VO<sub>2</sub> peak at about 37.1° was indexed as tetragonal VO<sub>2</sub>(101). Our results clearly established that this peak belongs to the monoclinic VO<sub>2</sub>(200) reflection. In their work, the SMT takes place at temperatures above 50 °C; thus, it is not possible to have tetragonal VO<sub>2</sub> at room temperature. They also grew VO<sub>2</sub> thin films epitaxially on TiO<sub>2</sub>(002) single crystalline substrate and assigned the 2θ peak from VO<sub>2</sub> to tetragonal (002) reflection. On this sample, they performed φ-scan XRD on the (101) reflections of VO<sub>2</sub> where the diffractometer needs to be set at 2θ and ψ angles of 37.08° and 32.78°, respectively. However, assuming a monoclinic structure with an out-of-plane normal to (2̄01) plane, these values approximately equal to 2θ and ψ values of the (200) reflection. It should be noticed that φ-patterns can be obtained even if the diffractometer is misaligned slightly.

#### 12.3.2.3. VO<sub>2</sub>/TiO<sub>2</sub>/c-sapphire heterostructure

Fig.12.8 and Fig.12.9 show θ-2θ and φ X-ray patterns acquired from the VO<sub>2</sub>/TiO<sub>2</sub>/c-sapphire heterostructure. In this case, we chose another approach to prove that VO<sub>2</sub> exists in its monoclinic and not in its tetragonal polymorph. First of all, based on the SMT behavior of this sample, it is deduced that VO<sub>2</sub> exists in its monoclinic phase at room temperature. Secondly, we performed detailed φ-scan XRD studies on the reflections having different 2θ and ψ values in tetragonal and monoclinic states. In Fig.12.8, the peak from VO<sub>2</sub> can be assigned to either (020) or (002) planes of M<sub>1</sub> phase.

The (020) and (002) family of planes of monoclinic VO<sub>2</sub> have similar interplanar spacings and, therefore, close 2θ values.

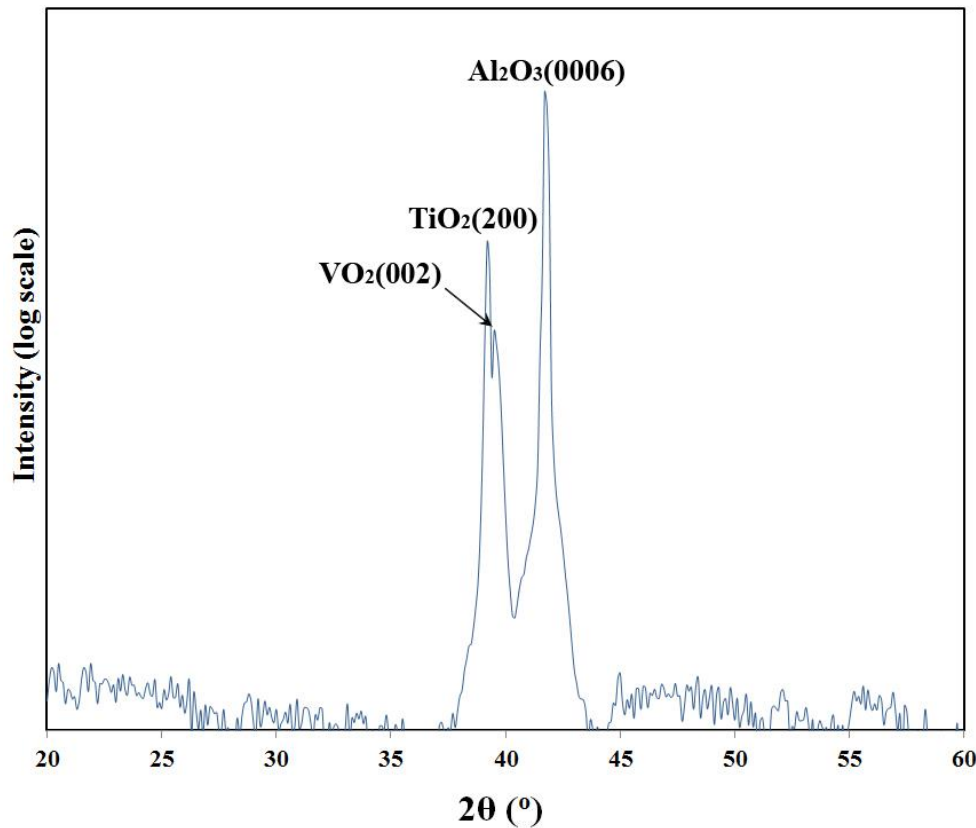


Fig.12.8. θ-2θ pattern taken from VO<sub>2</sub>/TiO<sub>2</sub>/c-sapphire heterostructure.

To distinguish the origin of this peak, φ-scan XRD was performed on (220) reflection of monoclinic VO<sub>2</sub> which has ψ-angles of  $43.14^{\circ}$  with (020) face and  $68.35^{\circ}$  with (002) face. The results are shown in Fig.12.9a and Fig.12.9b. Since no φ-peak was observed when the  $2\theta$  and ψ angles were set at  $55.45^{\circ}$  and  $43.14^{\circ}$  and φ-peaks emerged when the diffractometer was set at  $2\theta=55.45^{\circ}$  and  $\psi=68.35^{\circ}$ , the VO<sub>2</sub> peak in Fig.12.8 is assigned to the (002) reflection and not to the (020) reflection.

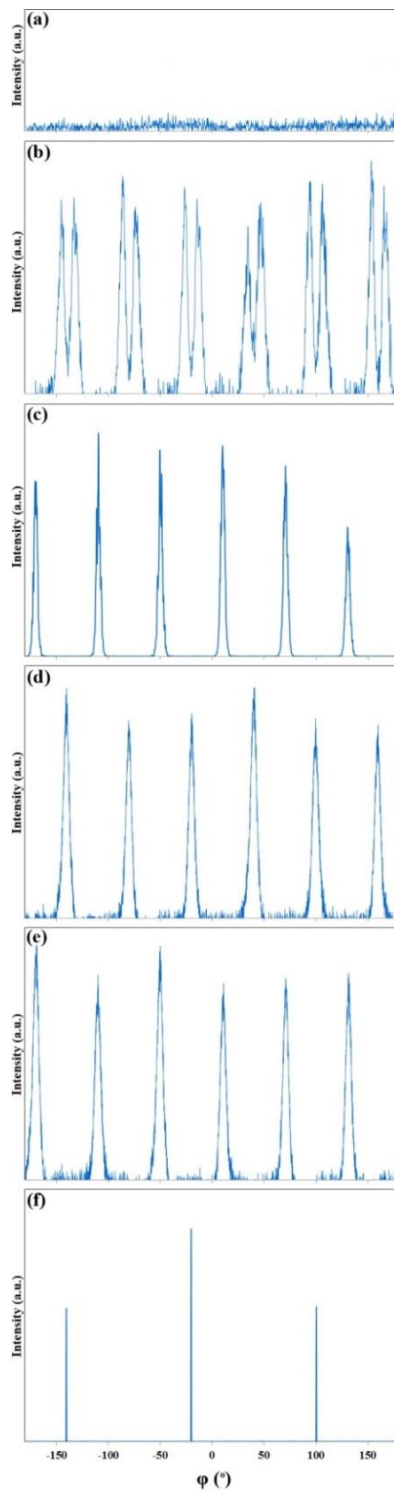


Fig.12.9. Results of  $\varphi$ -scan XRD conducted on different reflections in  $\text{VO}_2/\text{TiO}_2/c\text{-sapphire}$  heterostructure: (a)  $\text{VO}_2(220)$  at  $\psi=43.14^{\circ}$ , (b)  $\text{VO}_2(220)$  at  $\psi=68.35^{\circ}$ , (c)  $\text{VO}_2(211)$ , (d)  $\text{VO}_2(200)$ , (e)  $\text{TiO}_2(110)$ , and (f)  $\text{Al}_2\text{O}_3(01\bar{1}2)$ .

As depicted in Fig.12.9c,  $\varphi$ -scan XRD conducted on the (200) reflection of monoclinic  $\text{VO}_2$  further confirms the proposed out-of-plane alignment. The (200) planes of  $\text{VO}_2$  have an angular separation of  $57.354^\circ$  with (002) planes and  $90^\circ$  with (020) planes. Because the  $\varphi$ -peaks are clearly observed in this pattern, it is, once again, deduced that the  $2\theta$  peak in Fig.12.8 originates from the  $\text{VO}_2(002)$  reflection. To investigate the epitaxial growth and relationship across the  $\text{VO}_2(001)/\text{TiO}_2(100)/c$ -sapphire interface, we performed  $\varphi$ -scan XRD on several reflections whose results are presented in Fig.12.9. From the results in this figure, the crystallographic alignment in the  $\text{VO}_2/\text{TiO}_2/c$ -sapphire heterostructure is established to be  $(001)_{\text{VO}_2}||(100)_{\text{TiO}_2}||(0001)_{\text{Al}_2\text{O}_3}$  and  $[100]_{\text{VO}_2}||[001]_{\text{TiO}_2}||[10\bar{1}0]_{\text{Al}_2\text{O}_3}$ . Details on thin film epitaxy across the  $\text{TiO}_2/c$ -sapphire interface can be found in our other works.<sup>13,22</sup> According to these  $\varphi$  patterns, it is further ascertained that  $\text{VO}_2$  exists in its monoclinic polymorph in this sample at room temperature. In contrast to the study by X. Zhong et al.,<sup>23</sup> our results clearly show that  $\text{VO}_2$  grows on  $\text{TiO}_2(100)$  buffer such that its (001) planes align with  $\text{TiO}_2(100)$  planes. In their work, where  $\text{VO}_2$  epilayers were grown on a rutile  $\text{TiO}_2(200)$  substrate, the  $2\theta$  peak at about  $40^\circ$  was assigned to the  $\text{VO}_2(200)$  reflection.

### 12.3.3. Structure-property correlation characteristics

As it was expected, the SMT temperature increases as the lattice parameter along the [001]-direction of rutile  $\text{VO}_2$  (length of  $\text{V}^{4+}$ - $\text{V}^{4+}$  bonds) increases. Now, the question is why the misfit strain across the  $\text{VO}_2^{\text{tetragonal}}/\text{TiO}_2^{\text{tetragonal}}$  interface does not relax and

how the residual strain influences the SMT temperature. According to Tab.12.2, the lattice misfit strains in all the heterostructures which are under consideration in this study are very small.

Tab.12.2. Details on thin film epitaxy of  $\text{VO}_2/\text{TiO}_2$ /sapphire heterostructures.

Heterostructure	Epitaxy at $\text{VO}_2^{\text{rutile}}/\text{TiO}_2^{\text{rutile}}$ interface	Lattice misfit strain (%)	Epitaxy at $\text{VO}_2^{\text{monoclinic}}/\text{TiO}_2^{\text{rutile}}$ interface	Lattice misfit strain (%)
$\text{VO}_2/\text{TiO}_2/m$ -sapphire	(001) $_{\text{VO}2}$   (001) $_{\text{TiO}2}$	$\varepsilon_1=+0.81$	( $\bar{2}01$ ) $_{\text{VO}2}$   (001) $_{\text{TiO}2}$	$\varepsilon_1=+1.21$
	[100] $_{\text{VO}2}$   [100] $_{\text{TiO}2}$	$\varepsilon_2=+0.81$	[010] $_{\text{VO}2}$   [010] $_{\text{TiO}2}$	$\varepsilon_2=+5.25$
$\text{VO}_2/\text{TiO}_2/r$ -sapphire	(101) $_{\text{VO}2}$   (101) $_{\text{TiO}2}$	$\varepsilon_1=+0.81$	(100) $_{\text{VO}2}$   (011) $_{\text{TiO}2}$	$\varepsilon_1=+1.21$
	[010] $_{\text{VO}2}$   [010] $_{\text{TiO}2}$	$\varepsilon_2=+1.55$	[010] $_{\text{VO}2}$   [010] $_{\text{TiO}2}$	$\varepsilon_2=+1.49$
$\text{VO}_2/\text{TiO}_2/c$ -sapphire	(100) $_{\text{VO}2}$   (100) $_{\text{TiO}2}$	$\varepsilon_1=+3.36$	(001) $_{\text{VO}2}$   (100) $_{\text{TiO}2}$	$\varepsilon_1=+2.82$
	[001] $_{\text{VO}2}$   [001] $_{\text{TiO}2}$	$\varepsilon_2=+0.81$	[100] $_{\text{VO}2}$   [001] $_{\text{TiO}2}$	$\varepsilon_2=+1.21$

As it was discussed earlier, large misfit strains are easier to relax, since the critical thickness beyond which the system can accommodate misfit dislocations becomes smaller, namely in the order of a couple of monolayers, so the dislocations can reach the interface even if the primary slip system is not active. However, in small misfit systems where the critical thickness is large, glide of dislocations toward the interface is very difficult, especially in materials such as  $\text{VO}_2$  and  $\text{TiO}_2$ .<sup>12,24,25</sup> Meanwhile, all in-plane lattice misfit strains for  $\text{VO}_2$  on  $\text{TiO}_2$  are tensile which are more difficult to relax as compared to compressive strains. Nucleation of the misfit dislocations on the free surface of the growing  $\text{VO}_2$  film is easier under the compressive strains. Dislocation

nucleation/glide phenomenon is followed by the formation of surface steps. The step formation, when the strain is compressive, leads to decreasing the number of dangling bonds and, therefore, the surface energy of the system. The step formation energy is always positive, when the strain is tensile. Actually, the number of surface dangling bonds increases under the tensile strain.<sup>24,25</sup> In summary, the tensile misfit strain at the  $\text{VO}_2^{\text{tetragonal}}/\text{TiO}_2^{\text{tetragonal}}$  interface does not fully relax and alters the SMT temperature.

Considering Tab.12.2, the lattice misfit strains at the  $\text{VO}_2^{\text{tetragonal}}/\text{TiO}_2^{\text{tetragonal}}$  interface are all positive; that is, the  $\text{VO}_2$  thin films are under tensile strains. Taking the epitaxial alignments in the  $\text{VO}_2/\text{TiO}_2/m$ -sapphire heterostructure into consideration, it is found that *a*-axis and *b*-axis of rutile  $\text{VO}_2$  are under tension and, hence, its *c*-axis is under compression. The compressive strain along the *c*-axis leads to stabilization of tetragonal phase corresponding to SMT at lower temperatures. Thermal strains at the  $\text{VO}_2/\text{TiO}_2$  interface can be obtained from  $\epsilon_T = (T_{\text{growth}} - T_{\text{SMT}}) \times (\alpha_{\text{VO}_2} - \alpha_{\text{TiO}_2})$ , where  $\alpha$  is the thermal expansion coefficient. The thermal expansion coefficient of rutile  $\text{TiO}_2$  along its [100] and [001] directions are about  $6.99 \times 10^{-6}$  and  $9.36 \times 10^{-6} \text{ K}^{-1}$ , respectively.<sup>26</sup> The thermal expansion coefficient of tetragonal  $\text{VO}_2$  equals  $4.9 \times 10^{-6}$  and  $26.0 \times 10^{-6} \text{ K}^{-1}$  for [100] and [001] directions, respectively.<sup>27</sup> It is necessary to mention that the thermal strain across the  $\text{TiO}_2/\text{sapphire}$  interface has been neglected due to the large thickness of the titania buffer. In the case of  $\text{VO}_2/\text{TiO}_2/m$ -sapphire heterostructure, the thermal strains along two orthogonal in-plane orientations are calculated as  $(500-14.8) \times (6.99 - 4.9) \times 10^{-6} = 0.1\%$  which is compressive, but small and cannot compensate the tensile in-plane lattice misfit strain. A similar approach is applicable for the  $\text{VO}_2/\text{TiO}_2/c$ -

sapphire heterostructure. In this case, the *b*-axis and *c*-axis of rutile VO<sub>2</sub> are under a tensile strain and its *a*-axis is under a compressive strain; the lengthened V-V bond along the *c*-axis is in a complete agreement with the SMT characteristics shown in Fig.12.1c. The thermal strains along [100]-orientation is calculated as  $(500-50.6) \times (6.99 - 4.9) \times 10^{-6} = 0.09\%$  which is compressive. This strain in the [001]-direction is obtained to be  $(500-50.6) \times (9.36 - 26.0) \times 10^{-6} = -0.75\%$  which is tensile. This tensile thermal strain along the *c*-axis of rutile VO<sub>2</sub> is another reason for the transition occurring at temperatures higher than the strain-free transition temperature.

All the above discussions involved the VO<sub>2</sub><sup>tetragonal</sup>/TiO<sub>2</sub><sup>tetragonal</sup> interface during the cooling cycle. Now, the VO<sub>2</sub><sup>monoclininc</sup>/TiO<sub>2</sub><sup>tetragonal</sup> interface is considered which is present during the heating cycle. Taking the established epitaxial relationships into account, the VO<sub>2</sub><sup>monoclininc</sup>/TiO<sub>2</sub><sup>tetragonal</sup> interface is shown schematically in Fig.12.10 for the heterostructures which are studied here. From Goodenough's model,<sup>28</sup> we know that the *a*-axis of monoclinic VO<sub>2</sub> changes to the *c*-axis of tetragonal VO<sub>2</sub> and the *b*-axis of monoclinic VO<sub>2</sub> changes to the *a*-axis of tetragonal VO<sub>2</sub>. In the case of the VO<sub>2</sub>/TiO<sub>2</sub>/*m*-sapphire heterostructure (Fig.12.10a), we know that the (2̄01) planes of monoclinic VO<sub>2</sub> align with TiO<sub>2</sub>(001) planes. Two perpendicular directions that lie in the VO<sub>2</sub>(2̄01) plane are monoclinic [010] and [102] which align with rutile [100] and [010] orientations of TiO<sub>2</sub>. With this information, the misfit strain was calculated and shown in Tab.12.2. As seen, both in-plane orientations of the VO<sub>2</sub> thin film are under tensile strain; as such, the out-of-plane orientation, i.e. normal of (2̄01) face, is under a compressive strain. Because the angle between the VO<sub>2</sub>(2̄01) plane normal and the

[100] direction is very small ( $0.35^\circ$ ), it is deduced that the  $a_{\text{monoclinic}}$  is also under a compressive strain. A smaller  $a_{\text{monoclinic}}$  leads to a smaller  $c$ -axis in the tetragonal polymorph of  $\text{VO}_2$  which, in turn, results in an SMT below 340 K.

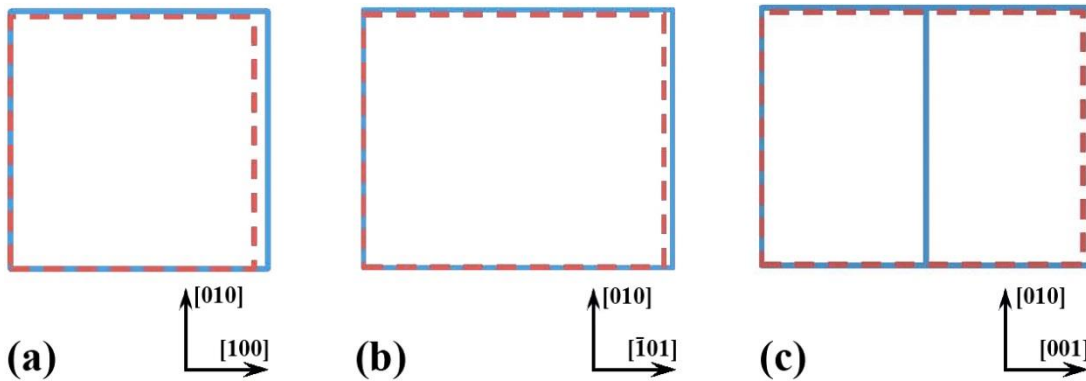


Fig.12.10. Schematic illustration of  $\text{VO}_2^{\text{monoclinic}}/\text{TiO}_2^{\text{tetragonal}}$  interface in: (a)  $\text{VO}_2/\text{TiO}_2/m$ -sapphire, (b)  $\text{VO}_2/\text{TiO}_2/r$ -sapphire, and (c)  $\text{VO}_2/\text{TiO}_2/c$ -sapphire heterostructures.  $\text{TiO}_2$  and  $\text{VO}_2$  unit cells are displayed in blue and red, respectively. The arrows show crystallographic orientations of  $\text{TiO}_2$  lattice.

According to Fig.12.10b where the  $\text{VO}_2/\text{TiO}_2$  interface in  $\text{VO}_2/\text{TiO}_2/r$ -sapphire heterostructure is illustrated, the (100) planes of  $\text{VO}_2^{\text{monoclinic}}$  align with  $\text{TiO}_2(101)$  planes. Two orthogonal directions within the monoclinic  $\text{VO}_2(100)$  plane are [010] and [001] which align with [010] and [ $\bar{1}01$ ] directions of  $\text{TiO}_2$ . Based on the calculated misfit strains in Tab.12.2, the lattice of monoclinic  $\text{VO}_2$  is under a tensile strain along the in-plane [010] and [001] orientations, so it experiences a compressive strain along the out-of-plane normal to the (100) planes. A shortened  $a$ -axis in monoclinic  $\text{VO}_2$  results in a shortened  $c$ -axis in rutile  $\text{VO}_2$  and, hence, a decreased SMT temperature.

Considering Fig.12.10c which shows the interface between  $\text{VO}_2$  and  $\text{TiO}_2$  in  $\text{VO}_2/\text{TiO}_2/c$ -sapphire heterostructure, the [100] direction of monoclinic  $\text{VO}_2$  matches

with [001] direction of  $\text{TiO}_2$  and, hence, is under tension. Since  $a_{\text{monoclinic}}$  is lengthened,  $c_{\text{tetragonal}}$  will be larger than the equilibrium conditions. Therefore, the SMT shifts toward temperatures higher than 340 K. Another feature of Fig.12.1 is the larger SMT width in  $\text{VO}_2/\text{TiO}_2/c$ -sapphire heterostructure. In our other works,<sup>13,22</sup> we showed that the rutile  $\text{TiO}_2$  epilayer grown on *c*-cut sapphire substrate has a very small domain size increasing the domain boundaries. More domain boundaries results in a wider transition.

Cross-section TEM images acquired from  $\text{VO}_2/\text{TiO}_2/m$ -sapphire,  $\text{VO}_2/\text{TiO}_2/r$ -sapphire, and  $\text{VO}_2/\text{TiO}_2/c$ -sapphire heterostructures are shown in Fig.12.11a, Fig.12.11b, and Fig.12.11c, respectively. The SAED pattern, shown in Fig.12.11a, belongs to  $\text{VO}_2[010]$ , rutile[100], and sapphire[0001] zones. The SAED pattern for  $\text{VO}_2/\text{TiO}_2/r$ -sapphire, which is displayed in Fig.12.11b, belongs to  $\text{VO}_2[010]$ , rutile[ $\bar{1}00$ ] and sapphire[ $2\bar{1}\bar{1}0$ ] zones. The SAED patterns further confirm existence of monoclinic  $M_1$  phase of  $\text{VO}_2$  in our samples.

As it was shown in Fig.12.3 and Fig.12.6, a single  $\theta$ -2 $\theta$  high resolution peak were measured for several reflections of  $\text{VO}_2$ , so interplanar spacings and lattice strain cannot be accurately calculated. However, interplanar spacings can also be measured using selected SAED patterns. The lattice parameter of  $\text{VO}_2$  monoclinic unit cell along the [100] direction was measured to be 5.710 and 5.723 Å in  $\text{VO}_2/\text{TiO}_2/m$ -sapphire and  $\text{VO}_2/\text{TiO}_2/r$ -sapphire heterostructures, respectively. Considering the relaxed lattice parameter of 5.752 Å along the *a*-direction of monoclinic  $\text{VO}_2$ , a compressive strain of about 0.72 and 0.49% is revealed which is responsible for the observed shift in the SMT temperature toward lower temperatures.

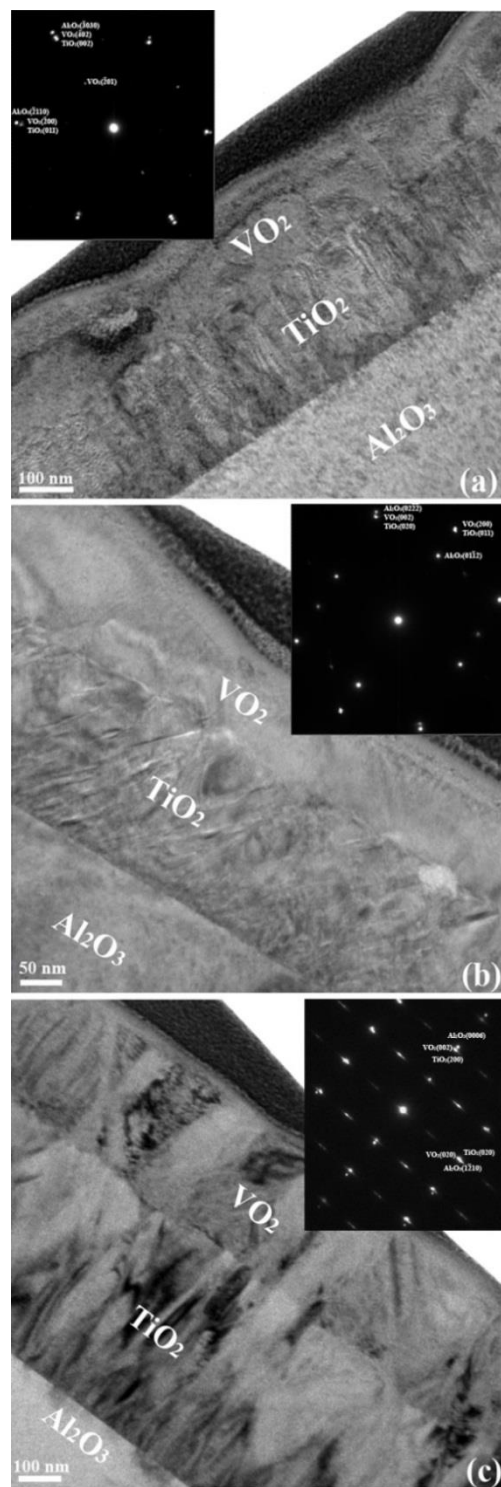


Fig.12.11. Cross section bright field TEM micrographs taken from: (a)  $\text{VO}_2/\text{TiO}_2/m$ -sapphire, (b)  $\text{VO}_2/\text{TiO}_2/r$ -sapphire, and (c)  $\text{VO}_2/\text{TiO}_2/c$ -sapphire heterostructure. The insets show corresponding SAED patterns.

Fig.12.11c depicts the cross-section view of  $\text{VO}_2/\text{TiO}_2/c$ -sapphire heterostructure where the corresponding indexed SAED pattern is shown in the inset. The pattern belongs to typical  $\text{VO}_2[100]$ , rutile[001], and sapphire[10 $\bar{1}$ 0] zones and confirms the established epitaxial relationship and existence of  $\text{VO}_2$  in its  $M_1$  phase. The lattice parameter along the [100] orientation was measured as 5.763 Å which shows a 0.21% tensile strain. This tensile strain resulted in a SMT temperature higher than 340 K.

High resolution TEM micrographs acquired from the  $\text{VO}_2/\text{TiO}_2$  interface in  $\text{VO}_2/\text{TiO}_2/m$ -sapphire and  $\text{VO}_2/\text{TiO}_2/r$ -sapphire heterostructures are displayed in Fig.12.12a and Fig.12.12b, respectively. The interfaces are clean with no evidence of interfacial reaction. As is seen, there is no distinct interface in Fig.12.12b. The reason behind this observation is the crystallographic alignment between two crystals and close interplanar spacings, as schematically illustrated in Fig.12.13.

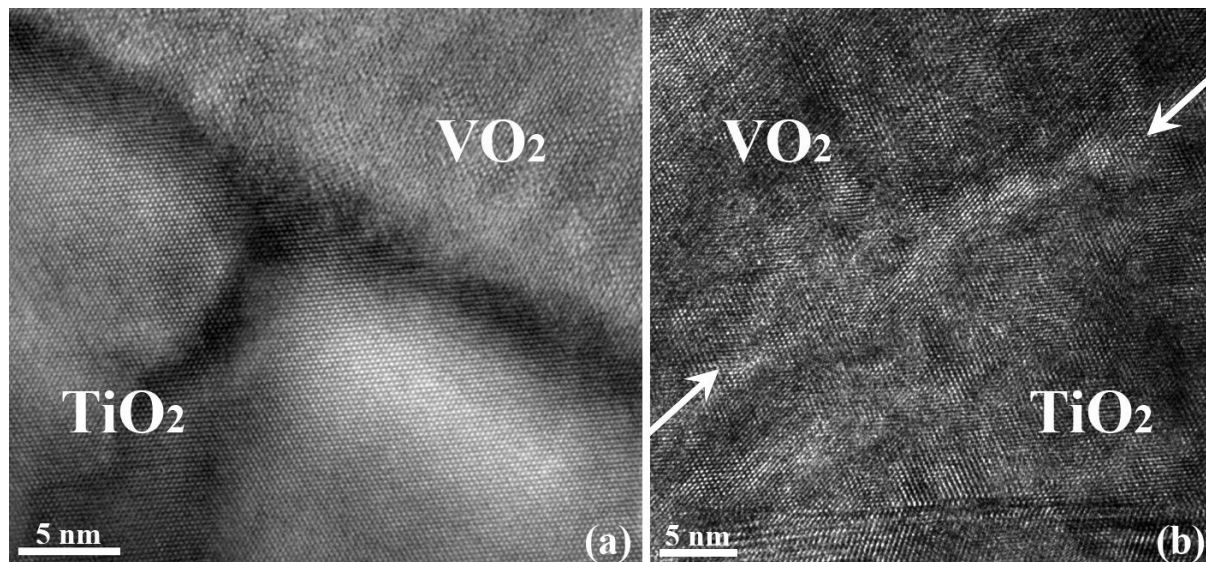


Fig.12.12. High resolution TEM image acquired from  $\text{VO}_2/\text{TiO}_2$  interface in:  
(a)  $\text{VO}_2/\text{TiO}_2/m$ -sapphire (b)  $\text{VO}_2/\text{TiO}_2/r$ -sapphire heterostructures.

According to Fig.12.13, VO<sub>2</sub> and TiO<sub>2</sub> unit cells are drawn such that TiO<sub>2</sub>(011) planes get aligned with VO<sub>2</sub>(100) planes. These two planes are highlighted in red. The reason why no clear interface is seen in Fig.12.12b is that the angle between TiO<sub>2</sub>(011) and TiO<sub>2</sub>(010) planes ( $57.18^\circ$ ) are close to the angle between VO<sub>2</sub>(100) and VO<sub>2</sub>(001) planes ( $57.35^\circ$ ). Meanwhile, the interplanar spacing between TiO<sub>2</sub>(010) planes along [011] orientation equals 5.46 Å which is very close to the interplanar spacing of VO<sub>2</sub>(001) planes which is about 5.38 Å.

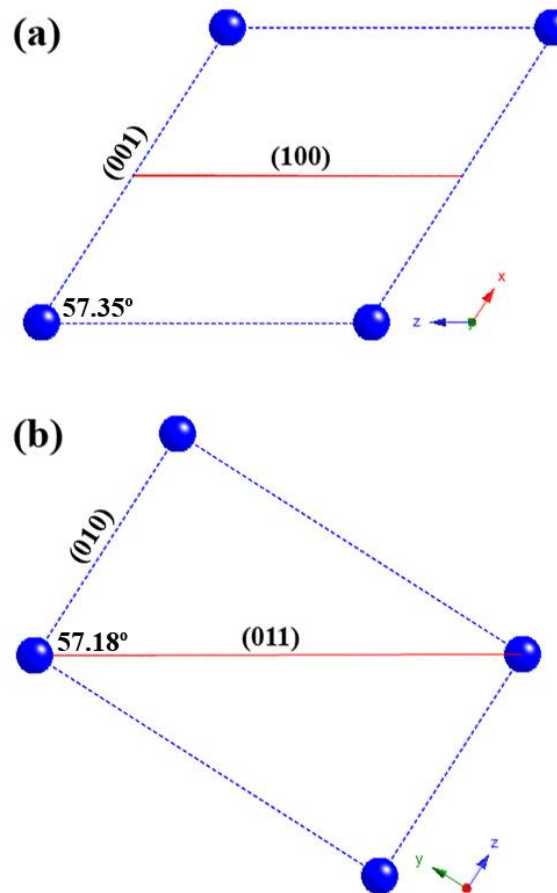


Fig.12.13. Schematic delineation of: (a) VO<sub>2</sub> and (b) TiO<sub>2</sub> unit cells along their [010] and [100] orientations.

## 12.4. Conclusions

VO<sub>2</sub> thin films, with controlled out-of-plane orientations, were epitaxially grown on TiO<sub>2</sub>(001)/*m*-sapphire, TiO<sub>2</sub>(101)/*r*-sapphire, and TiO<sub>2</sub>(100)/*c*-sapphire platforms to establish detailed structure-property correlations. Characteristics of Thin film epitaxy and defect microstructure of the samples were studied in detail by high-resolution XRD and TEM techniques. Our results clearly established that VO<sub>2</sub> exists in its monoclinic (M<sub>1</sub>) polymorph in all heterostructures of concern in this study. Epitaxial relationships were determined to be [010](100)<sub>VO2</sub>||[010](101)<sub>TiO2</sub>||[2̄1̄0](01̄2)<sub>r</sub>-sapphire, [100](001)<sub>VO2</sub>||[001](100)<sub>TiO2</sub>||[10̄10](0001)<sub>c</sub>-sapphire, and [010](2̄01)<sub>VO2</sub>||[010](001)<sub>TiO2</sub>||[0001](10̄10)<sub>m</sub>-sapphire. The SMT temperature of the VO<sub>2</sub> epilayers was tuned from about 313 to 354 K. The SMT characteristics were correlated with the residual strains and crystallographic characteristics of epitaxial VO<sub>2</sub> thin films.

## References

1. B. Fisher, J. Phys. C: Solid State Phys. 9, 1201 (1976).
2. J.F. Morin, Phys. Rev. Lett. 3, 34 (1959).
3. W. Burkhardt, T. Christmann, S. Franke, W. Kriegseis, D. Meister, B.K. Meyer, W. Niessner, D. Schalch, and A. Scharmann, Thin Solid Films, 402, 226 (2002).
4. D. Ruzmetov and S. Ramanathan, Thin Film Metal Oxides: Fundamentals and Applications in Electronics and Energy, New York: Springer (2010).
5. J. Narayan and V.M. Bhosle, J. Appl. Phys. 100, 103524 (2006).
6. V. Eyert, Ann. Phys. Lpz, 11, 650 (2002).

7. D.B. McWhan, M. Marezio, J.P. Remeika, and P.D. Dernier, Phys. Rev. B 10, 490 (1974).
8. J.P. Pouget, H. Launois, J.P. D'Haenens, P. Merenda, and T.M. Rice, Phys. Rev. Lett. 35, 873 (1975).
9. K. Rogers, Powder Diffr. 8, 240 (1993).
10. J.D. Budai, A. Tselev, J.Z. Tischler, E. Strelcov, A. Kolmakov, W.J. Liu, A. Gupta, and J. Narayan, Acta Mater. 61, 2751 (2013).
11. J. Narayan, Acta Mater. 61, 2703 (2013).
12. J. Narayan and B.C. Larson, J. Appl. Phys. 93, 278 (2003).
13. M.R. Bayati, S. Joshi, R.J. Narayan, and J. Narayan, J. Mater. Res. 28, 1 (2013).
14. M.R. Bayati, J. Ding, Y.F. Lee, R.J. Narayan, and J. Narayan, J. Phys. C: Cond. Mater. 24, 395005 (2012).
15. Y. Muraoka and Z. Hiroi, Appl. Phys. Lett. 80, 583 (2002).
16. A. Gupta, R. Aggarwal, P. Gupta, T. Dutta, R.J. Narayan, and J. Narayan, Appl. Phys. Lett. 95, 111915 (2009).
17. A. Gupta, J. Narayan, and T. Dutta, Appl. Phys. Lett. 97, 151912 (2010).
18. K. Nagashima, T. Yanagida, H. Tanaka, and T. Kawai, Phys. Rev. B 74, 172106 (2006).
19. Y. Muraoka and Z. Hiroi, Appl. Phys. Lett. 80, 583 (2002).
20. K. Nagashima, T. Yanagida, H. Tanaka, and T. Kawai, J. Appl. Phys. 101, 026103 (2007).
21. Y. Cui and S. Ramanathan, J. Vac. Sci. Technol. A 29, 041502-1 (2011).
22. M.R. Bayati, R. Molaei, R.J. Narayan, J. Narayan, H. Zhou, and S.J. Pennycook, Appl. Phys. Lett. 100, 251606 (2012).
23. X. Zhong, P. LeClair, S.K. Sarker, and A. Gupta, Phys. Rev. B 86, 094114 (2012).

24. M. Ichimura and J. Narayan, *Mater. Sci. Eng. B* 31, 299 (1995).
25. M. Ichimura and J. Narayan, *Philos. Mag. A* 72, 281 (2006).
26. D.R. Hummer, P.J. Heaney, and J.E. Post, *Powder Diffraction* 22, 352 (2007).
27. Y. Hazony and H.K. Perkins, *J. Appl. Phys.* 41, 5130 (1970).
28. J.B. Goodenough, *J. Solid State Chem.* 3, 490 (1971).

## **Chapter 13**

# **Summary and Suggestions for Future Works**

### **13.1. Concluding remarks**

TiO<sub>2</sub> and VO<sub>2</sub> thin films were epitaxially grown on Si(001), Al<sub>2</sub>O<sub>3</sub>(0001), Al<sub>2</sub>O<sub>3</sub>( $\bar{1}010$ ), and Al<sub>2</sub>O<sub>3</sub>(01 $\bar{1}2$ ) substrates using pulsed deposition techniques. The effect of laser, vacuum, and oxygen annealing on structure and properties was investigated. Detailed microstructural investigations were performed by XRD, HRTEM, and STEM techniques. Optical properties of the samples were studied employing UV-Vis and room PL spectrophotometry at room temperature. XPS was employed to determine stoichiometry and defect content. We also studied the surface morphology by AFM. Photochemical properties were assessed through measuring surface wettability characteristics and photocatalytic reaction rate constant of degradation of 4-chlorophenol under ultraviolet and visible irradiations. Electrical properties of thin film heterostructures were evaluated using a self-made labview program employing a Keithley 2400 sourcemeter where a closed cycle helium cryostat was employed to cool the samples down.

The following briefly reviews the obtained results:

1. Rutile is the dominant polymorph at higher substrate temperatures and lower oxygen pressures. Anatase forms at lower temperatures and higher pressures.
2. The epitaxial relationship across the rutile  $\text{TiO}_2$ /sapphire interfaces was established to be  $[001](100)_{\text{rutile}} \parallel [10\bar{1}0](0001)_{c\text{-sapphire}}$ ,  $[010](001)_{\text{rutile}} \parallel [0001](10\bar{1}0)_{m\text{-sapphire}}$ , and  $[010](101)_{\text{rutile}} \parallel [2\bar{1}\bar{1}0](01\bar{1}2)_{r\text{-sapphire}}$ .
3. Integration with silicon was achieved using cubic zirconia buffer. The epitaxial relationship between  $\text{Si}(100)$  substrate and the zirconia buffer layer was shown to be:  $[100](001)_{c\text{-YSZ}} \parallel [100](001)_{\text{Si}}$ . The epitaxial relationships at the rutile/zirconia and the anatase/zirconia interfaces were established as  $[0\bar{1}1](100)_{\text{rutile}} \parallel [010](001)_{c\text{-YSZ}}$  and  $[110](001)_{\text{anatase}} \parallel [100](001)_{c\text{-YSZ}}$ , respectively.
4. Tetragonal zirconia was also used as buffer to integrate anatase epilayers with silicon. The epitaxial relationship across the interfaces was shown to be:  $[110](001)_{\text{anatase}} \parallel [110](001)_{t\text{-YSZ}} \parallel [001](001)_{\text{Si}}$ .
5. In all these cases, DME calculations were performed and arrangement of misfit dislocations across the interfaces was revealed by inverse FFT images.
6. In  $\text{TiO}_2/c\text{-sapphire}$  heterostructures, the films exhibited a transmittance of 75-90% over the visible region. The absorption edge was observed to shift toward longer wavelengths at higher deposition temperatures or lower pressures.
7. Concentration of lattice point defects, namely oxygen vacancies and titanium interstitials, increased at lower oxygen pressures.
8. The rutile film initially grew pseudomorphically on  $c\text{-sapphire}$  as  $\text{Ti}_2\text{O}_3$  and, after a few monolayers, it grew tetragonally on the  $\text{Ti}_2\text{O}_3/\text{sapphire}$  platform.

9. The separation between the  $\frac{1}{2}[10\bar{1}](101)$  misfit dislocations was dictated by  $Ti_2O_3$  and was determined to be 9.7 Å which was consistent with 4/3 and 3/2 alternating domains across the film/substrate interface.
10. The rutile  $TiO_2$  films grown on *c*-sapphire substrates at higher repetition rates showed higher photocatalytic efficiency.
11. The effect of vacuum and oxygen annealing on structure and properties of rutile  $TiO_2/c$ -sapphire samples was studied. It was shown that rutile  $TiO_2$  can be photo-responsive even under low energy visible light after annealing in vacuum where we envisage the point defects, i.e. oxygen vacancies and titanium interstitials, serve an important role.
12. Increasing the annealing pressure resulted in formation of larger grains.
13. Electrical resistivity of the rutile films strongly increased by about three orders of magnitude when annealing pressure increased from  $5 \times 10^{-4}$  to  $5 \times 10^{+1}$  Torr.
14.  $TiO_2$  epilayers were integrated with silicon substrates. Phase structure of  $TiO_2$  epilayers was tuned from pure rutile to pure anatase by manipulating the substrate temperature and oxygen partial pressure.
15. AFM results revealed that the finest grain size and the smoothest surfaces were obtained at the intermediate deposition temperatures.
16. The  $TiO_2/c$ -YSZ/Si(001) heterostructures deposited at 500 °C were more conductive than those grown at 300 and 700 °C. The maximum photocatalytic reaction rate constants were determined as 0.0124 and 0.0087 min.<sup>-1</sup> for the anatase and the rutile films grown at 500 °C.

17. In  $\text{TiO}_2/c\text{-YSZ/Si}(001)$  heterostructures, dark hydrophilicity was demonstrated where nanosecond switching from a hydrophobic surface to a hydrophilic surface was achieved using excimer laser irradiation.
18. It was envisaged that the concurrent formation of oxygen vacancies and  $\text{Ti}^{3+}$  defects from laser annealing and, therefore, introduction of mid-band states is responsible for a dark hydrophilicity phenomenon. The samples exhibited hydrophobic behavior after being placed in ambient atmosphere.
19. The effect of excimer laser treatment on photocatalytic activity of anatase/t-YSZ/Si(001) thin film heterostructures was studied. The photocatalytic efficiency was improved by a factor of 2 after laser irradiation.
20. It was observed that the anatase epilayers were stable up to 1100 °C.
21. In addition to *c*-sapphire substrate, rutile  $\text{TiO}_2$  epitaxial thin films were deposited on *m*-cut and *r*-cut sapphire substrates to study structure and properties of the epilayers as a function of the crystallographic characteristics of the substrates.
22. It was revealed that large lattice misfit strains relax easily even if the primary slip system is not active due to the epitaxial alignment between the film and substrate and orientation of the in-plane stresses.
23. We also showed that even small misfit strains can relax provided that the primary slip system is active.
24. The origin of the residual strains in the epilayers was found to be primarily due to thermal misfit and defect/impurity strains.

25. The relative photocatalytic activity of different faces of rutile TiO<sub>2</sub> was shown to be in the following sequence: TiO<sub>2</sub>(001)/*m*-sapphire > TiO<sub>2</sub>(101)/*r*-sapphire > TiO<sub>2</sub>(100)/*c*-sapphire.
26. VO<sub>2</sub>/TiO<sub>2</sub> heterostructures were epitaxially deposited on *m*-cut, *r*-cut, and *c*-cut sapphire substrates and detailed structural investigations were performed using XRD and electron microscopy techniques to correlate SMT properties with microstructural characteristics.
27. Monoclinic (M<sub>1</sub>) VO<sub>2</sub> thin films with (100), (001), and (2̄01) out-of-plane orientations were obtained on TiO<sub>2</sub>(101)/*r*-sapphire, TiO<sub>2</sub>(100)/*c*-sapphire, and TiO<sub>2</sub>(001)/*m*-sapphire platforms.
28. The in-plane alignments across the interfaces was established to be [010](100)<sub>VO2</sub>||[010](101)<sub>TiO2</sub>, [100](001)<sub>VO2</sub>||[001](100)<sub>TiO2</sub>, and [010](2̄01)<sub>VO2</sub>||[010](001)<sub>TiO2</sub>.
29. The SMT temperature of VO<sub>2</sub> epilayers was tuned from about 313 K to 354 K.
30. The SMT characteristics were interpreted based upon the residual strain in the VO<sub>2</sub> lattice, particularly along the *c*-axis of tetragonal VO<sub>2</sub>.

### **13.2. Suggestions for future works**

Taking the achievements of this research into account, following topics are recommended for future studies:

1. The effect of thickness on electrical and photochemical properties of anatase and rutile TiO<sub>2</sub> epilayers.

2. The effect of thickness on SMT characteristics of VO<sub>2</sub> epilayers grown on *c*-cut, *r*-cut, and *m*-cut sapphire substrates.
3. Direct integration of TiO<sub>2</sub> epilayers with silicon through deposition of TiN buffer followed by oxygen annealing to convert TiN to TiO<sub>2</sub>, or deposition of TiN initially under vacuum followed by deposition under an oxygen atmosphere.
4. Photochemical characteristics of VO<sub>2</sub>/TiO<sub>2</sub> multilayer heterostructures.